REACTOR MATERIALS

A Quarterly Technical Progress Review

Prepared for DIVISION OF TECHNICAL INFORMATION, USAEC, by
E. M. SIMONS, D.L. KELLER, and ASSOCIATES, BATTELLE MEMORIAL INSTITUTE

Winter 1966-1967

● VOLUME 9

● NUMBER 4

TECHNICAL PROGRESS REVIEWS

To meet the needs of industry for concise summaries of current atomic developments, the Atomic Energy Commission is publishing this series, Technical Progress Reviews. Issued quarterly, each of the reviews digests and evaluates the latest findings in a specific area of nuclear technology and science.

The journals published in this series are:

Isotopes and Radiation Technology P. S. Baker, A. F. Rupp, and associates
Oak Ridge National Laboratory

Nuclear Safety Wm. B. Cottrell, W. H. Jordan, J. P. Blakely, and associates
Nuclear Safety Information Center, Oak Ridge National Laboratory

Power Reactor Technology
Argonne National Laboratory

Reactor Materials E. M. Simons and associates
Battelle Memorial Institute

See the back cover for availability information.

The views expressed in this publication do not necessarily represent those of the United States Atomic Energy Commission, its divisions or offices, or of any Commission advisory committee or contractor.

Availability of Reports Cited in This Review

Unclassified AEC reports are available for inspection at AEC depository libraries and are sold by the Clearinghouse for Federal Scientific and Technical Information, National Bureau of Standards, U. S. Department of Commerce, 5285 Port Royal Road, Springfield, Va., 22151. Some of the reports cited are not available owing to their preliminary nature; however, the information contained in them will eventually be made available in formal progress or topical reports.

Unclassified reports issued by other Government agencies or private organizations should be requested from the originator.

Unclassified British and Canadian reports may be inspected at AEC depository libraries. British reports are sold by the British Information Service, 45 Rockefeller Plaza, New York, N. Y.; Canadian reports (AECL series) are sold by the Scientific Document Distribution Office, Atomic Energy of Canada, Ltd., Chalk River, Ontario, Canada.

Classified U. S. and foreign reports identified in this journal as Classified may be purchased by properly cleared Access Permit Holders from the Division of Technical Information Extension, U. S. Atomic Energy Commission, P. O. Box 1001, Oak Ridge, Tenn., 37830. Such reports may be inspected at classified AEC depository libraries.

Contents

Reactor Materials

Vol. 9, No. 4

I Fuel and Fertile Materials 203
Uranium Metal and Alloys 203
Plutonium 205
Thorium 207
Metal–Ceramic Fuels 207
Coated-Particle Fuel Materials 209
Uranium Oxide Fuels 210
Intermetallic Compound Fuels 211
Mechanism of Corrosion of Fuel Alloys . . . 212
Basic Studies of Irradiation Effects in Fuel Materials 213
References 214

II Moderator Materials 217
Graphite 217
Beryllium Metal and Alloys 218
Beryllium Oxide 221
Solid Hydrides 224
References 225

III Nuclear Poisons 226
Metallic Poison Materials 226
Dispersion and Nonmetallic Poison Materials 226

IV Cladding and Structural Materials 229
Corrosion 229
Metal–Water Reactions 237
Radiation Effects in Nonfuel Materials 239
Selected Metallurgical Aspects of Cladding and Structural Materials . . . 243
Diffusion Studies 248
Selected Mechanical Properties of Cladding and Structural Materials. . . . 249
Ceramic Technology 251
References 251

V Special Fabrication Techniques . . . 255
Melting, Casting, and Fabrication 255
Pressure Bonding. 257
Canning of Particulate Fuels 257
Plating 258
Explosive Forming 260
Welding and Brazing 260
Nondestructive Testing 263
References 264

Index, Volume 9 267

Issued quarterly by the U. S. Atomic Energy Commission. Use of funds for printing this publication approved by the Director of the Bureau of the Budget on July 8, 1966.

Reactor Materials is one of a series of quarterly technical progress reviews broadly covering the field of nuclear science and technology. Under the auspices of the USAEC Division of Technical Information, *Reactor Materials* is prepared by Battelle personnel from worldwide literature. It covers properties, behavior, and fabrication processes of materials applicable to nuclear reactor components and associated equipment.

The reader will recognize that the scope of this Review is too broad to permit detailed coverage of every topic. Rather, the authors and editors attempt to combine the highlights of significant new developments into an information summary of current research for both management and the technical specialist. As a rule, enough of the results are presented to define the research and summarize the findings. For readers desiring more information on any particular topic, a complete set of references is provided at the end of each section.

Each quarter a number of bibliographies, monographs, and books appear on subjects within the scope of *Reactor Materials*. Although the main purpose of this Review is to call attention to findings that are new and significant, such publications are noted in the text because they often represent excellent compilations of available information on important materials topics.

E. M. SIMONS
S. W. POREMBKA, JR.
D. L. KELLER
Battelle Memorial Institute

Section

I

Reactor Materials

Fuel and Fertile Materials

Uranium Metal and Alloys

Unalloyed Uranium

The purification of uranium by zone melting has been reported by the French.[1] Because of the high affinity of uranium for elements such as oxygen, contamination was avoided by adopting the floating-zone technique and by working under high vacuum. The deformation of the uranium rod caused by the anisotropy of dilation of the alpha and beta phases and the allotropic transformations of $\alpha \rightarrow \beta$ and $\beta \rightarrow \alpha$ was overcome by the use of electron bombardment stabilized by feedback. Electrical-resistivity measurements at 20°K were used to determine the degree of purity obtained.

The French[2] have also reported on the annealing of uranium from 100 to 412°K. Zone-melted uranium quenched from 100°K in liquid helium shows important increases in resistivity that disappear after annealing at very low temperatures (5 to 30°K). This phenomenon is explained by the existence of a very mobile defect of interstitial nature, and this is confirmed by neutron irradiation at 415°K and electron irradiation at 6°K.

The British[3] report that the ductile–brittle transition temperature of alpha uranium increases from 25 to 120°C when the strain rate applied during tensile testing is raised from 0.005/sec to 150/sec. This increase appears to be similar in both vacuum- and salt-annealed material. Anomalous behavior has been noticed in the effect of vacuum annealing on the ductile–brittle transition in rod and cross-rolled plate; however, texture differences are suggested as a cause of this.

Enhancement of the ductility of alpha uranium has been demonstrated by the British.[4] Superplastic flow was achieved in which the specimen underwent approximately 170% elongation. To accomplish this they held the uranium specimen under constant stress (1.15 g/mm^2), and the temperature was changed from 400 to 600°C and then back to 400°C every 20 min for 7 days. Under stresses of about 1% of the yield strength and irradiation at 100°C, alpha uranium exhibited a steady-state creep rate of about 10^{-7}/hr and obeyed a pseudo-creep law of the form $\epsilon' \approx (\sigma/Y)\,\epsilon' g$, where Y is the yield strength of the material and $\epsilon' g$ is the irradiation growth rate of individual crystals.

The French[5] have studied the tensile deformation in monocrystalline and polycrystalline uranium between 20 and −196°C.

The effect of temperature, crystal orientation, and neutron irradiation on the plastic deformation of alpha-uranium monocrystals was investigated by the Russians.[6] Small single crystals of uranium grown by $\beta \rightarrow \alpha$ recrystallization were given neutron exposures up to 4×10^{20} neutrons/cm^2 at temperatures not exceeding 100°C and were then subjected to tensile tests. X-ray and metallographic examinations showed that exposures of up to 1.6×10^{18} neutrons/cm^2 do not change the plastic deformation mode. In crystals in which initial deformation occurred by slip along the plane (0 1 0), the yield point increased rapidly at low neutron exposures, reaching saturation at 10^{17} neutrons/cm^2. Irradiation caused a threefold to fivefold increase in critical shear stress and decreased elongation from about 65% to about 40%. Annealing at 450°C restored the mechanical properties of samples that had undergone exposures of up to 5.5×10^{17} neutrons/cm^2.

A report detailing the procedures and standards used for the metallographic preparation and evaluation of uranium has been issued by the National Lead Co. of Ohio.[7] Other publications of interest include uranium property studies by Lloyd and Barrett[8] and by Fisher.[9]

Alpha-Phase Uranium Alloys

The solid solubility of iron in uranium has been determined by British investigators.[10] They found that alpha uranium at 660°C can dissolve 0.003 wt.% iron; whereas the maximum solubility of iron in beta uranium (at 763°C) is 0.085 wt.%. The solubilities of iron in gamma uranium at 780 and 800°C are 0.223 and 0.305 wt.%, respectively. The eutectoid point for the beta phase was determined to be at 661°C and 0.027 wt.% iron, and that for the gamma phase, at 0.15 wt.% iron.

The examination of two irradiated fuel elements from the organic-cooled Piqua Reactor Core 1 has been reported by Atomics International.[11] The fuel elements consist of a uranium–3.5 wt.% molybde-

num–0.1 wt.% aluminum alloy that is enriched to 1.94 wt.% ^{235}U. The aluminum cladding has a finned surface to increase the heat-transfer area. It is metallurgically bonded to the uranium fuel, using an intermediate nickel diffusion barrier with a thickness of 0.0010 to 0.0015 in. Each fuel element consists of fuel tubes stacked in two concentric tiers. The outer tubes have a mean diameter of 4.63 in., and the inner tubes have a mean diameter of 3.60 in. The fuel alloy in each tube is 0.208 in. thick and is covered on the inner and outer surfaces with finned aluminum.

The overall general condition of the fuel elements was excellent. Fuel dimensional increases were small; the outside diameter of the outer fuel elements increased $0.2 \pm 0.09\%$ per 4.65×10^{19} fissions/cm^3 (1000 Mwd/metric ton of uranium). The peak cladding temperature for one of the fuel elements examined was 720°F (382°C). Assuming that fuel dimensional changes continue to be linear with burnup, firm contact between the fuel-cylinder cladding and the outer process tube would be expected at a burnup of $2.8 \times 10^{20} \pm 0.9 \times 10^{20}$ fissions/cm^3 (6000 ± 1900 Mwd/metric ton of uranium). The nickel diffusion barrier between the cladding and fuel did not show a significant increase in its interdiffusion rates as a result of irradiation, and it performed successfully as a diffusion barrier. No fuel-cladding separation was found in either fuel element.

The results of phase studies in the uranium–vanadium–chromium system have been reported by the Portuguese.[12]

Gamma-Phase Uranium Alloys

Further investigation of the physical and mechanical properties of a uranium–7.5 wt.% niobium–2.5 wt.% zirconium alloy has been reported by Livermore.[13] The mechanical properties obtained are given in Table I-1. This gamma-phase alloy develops high strength on low-temperature (150 to 200°C) aging, presumably by an ordering mechanism, while maintaining its body-centered cubic structure. Physical properties measured include: specific heat (RT to 200°C) – 0.035 to 0.038 cal/(g)(°C); density (gamma phase) – 16.3 to 16.6 g/cm^3.

In further studies on this alloy, the same laboratory[14] determined the effect of strain rate on the tensile strength and reduction in area at various temperatures. The data obtained are presented in Figs. I-1 and I-2. Also the TTT curve for this alloy was determined both by means of hardness and by electrical-resistance measurements. These data are presented in Fig. I-3.

The specific heat of gamma-phase uranium–10 wt.% molybdenum alloy has been determined by investigators at Battelle–Columbus.[15] The results are given in Table I-2.

Table I-1 MECHANICAL PROPERTIES[13] OF URANIUM–7.5 WT.% NIOBIUM–2.5 WT.% ZIRCONIUM

Room-temperature property	Condition of alloy				
	Gamma annealed + water quench	Aged at 150°C 1 hr*	Aged at 200°C 1 hr*	Aged at 200°C 20 hr	Aged at 350°C 4 hr*
Yield strength (0.2% offset), 1000 psi	52–70	92.25	100.5–117	143	215
Yield strength (0.2% offset) at 1% strain, 1000 psi	60.6–85.4		103.3		
Ultimate tensile strength, 1000 psi	121.5–123.7	129.3	150–159	170	228.5
Ultimate tensile strength (1% prestrain),† 1000 psi	125–130				
Elongation, %	20–23.5	20.5	12.5	10	3.5
Elongation (1% prestrain), %	16.5–21.5				
Reduction in area, %	50–53.5	50	42	35	7.5
Reduction in area (1% prestrain), %	48–51				
Young's modulus, 10^6 psi	7.5–8.5	8.5	8.8	9.5	12.7
Young's modulus (1% prestrain), 10^6 psi	7.5–8.8				
Diamond pyramid hardness (measured near fracture)	245	247	260	295	450
Charpy V notch at 25°C, ft-lb	15.0–15.5	13.7	10.8	8.0	4.5

*Average of three determinations.
†Prestrain to 1% total strain, unload, and then reload to failure.

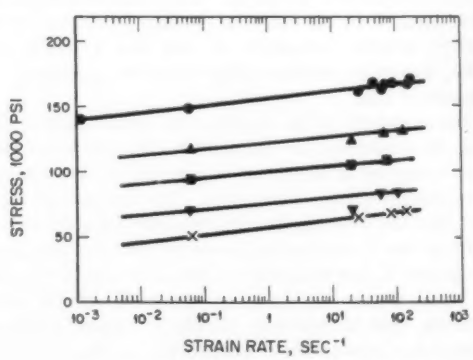

Fig. I-1 Effect of strain rate on the tensile strength of gamma-phase uranium–7.5 wt.% niobium–2.5 wt.% zirconium alloy.[14] ●, 23°C; ▲, 200°C; ■, 300°C; ▼, 400°C; and ×, 500°C.

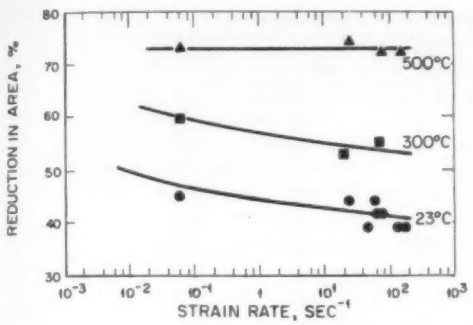

Fig. I-2 Effect of strain rate on ductility (reduction in area) of gamma-phase uranium–7.5 wt.% niobium–2.5 wt.% zirconium alloy.[14] ●, 23°C; ■, 300°C; ▲, 500°C.

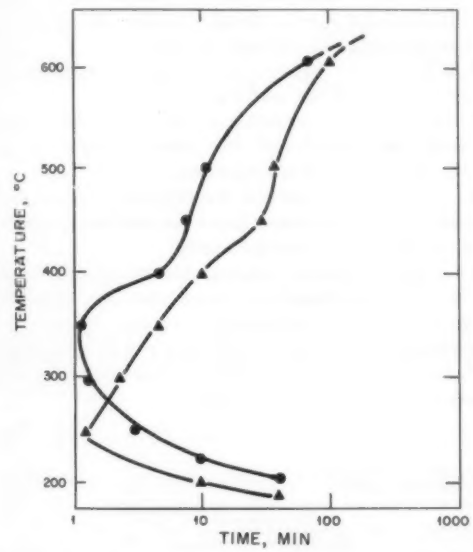

Fig. I-3 Time–temperature–transformation (TTT) curves for gamma-phase uranium–7.5 wt.% niobium–2.5 wt.% zirconium alloy.[14] ●, determined by hardness measurements; ▲, determined by electrical-resistance measurements. The hardness curve is considered the more accurate.

Table I-2 INTERPOLATED SPECIFIC HEAT VALUES FOR A GAMMA-PHASE URANIUM–10 WT.% MOLYBDENUM ALLOY[15]

Temp., °C	Specific heat, cal/(g)(°C)
0	0.0322
100	0.0339
200	0.0357
300	0.0375
400	0.0393
500	0.0410
600	0.0428
700	0.0446
800	0.0463
900	0.0481
1000	0.0499

Dilute Uranium Alloys

The specific heat of a niobium–20 wt.% uranium alloy was determined by Battelle–Columbus investigators.[15] The results are given in Table I-3.

(M. S. Farkas)

Table I-3 INTERPOLATED SPECIFIC HEAT VALUES FOR A NIOBIUM–20 WT.% URANIUM ALLOY[15]

Temp., °C	Specific heat, cal/(g)(°C)
0	0.0580
100	0.0595
200	0.0610
300	0.0625
400	0.0639
500	0.0654
600	0.0669
700	0.0684
800	0.0699
900	0.0714
1000	0.0729

Plutonium

Plutonium Metal and Alloys

Argonne National Laboratory[16] is continuing the development of metallic plutonium-containing fuel alloys. Rates at which molten uranium–plutonium–zirconium and uranium–plutonium–titanium alloys penetrate potential cladding materials are being investigated. Molten uranium–15 wt.% plutonium–10 wt.% zirconium penetrated type 304 stainless steel at rates of 0.076 mm/sec and 0.136 mm/sec at 1350 and 1400°C, respectively. Vanadium–20 wt.% titanium in uranium–15 wt.% plutonium–6.5 wt.% titanium was penetrated at rates of 0.0027 mm/sec at 1300°C and 0.027 mm/sec at 1450°C.

Compatibility tests[17] showed that the uranium–plutonium–zirconium alloys were compatible with type 304 stainless steel at temperatures up to 800°C, and uranium–plutonium–zirconium alloys reacted with type 304 stainless steel at temperatures above 650°C. The good compatibility of the uranium–plutonium–zirconium with stainless steel is believed to be partially dependent on the oxygen content of the alloys because a phase containing zirconium and oxygen apparently forms a barrier film between the fuel and the stainless steel. Compatibility becomes progressively poorer as the nickel content of the clad material increases, and the composition of the phases present in the alloys at the test temperatures probably influences compatibility.

Thermal-conductivity values for a uranium–13 at.% plutonium–22 at.% zirconium alloy ranged from 0.100 watt/(cm)(°C) at 100°C to 0.301 watt/(cm)(°C) at 800°C.

Several uranium–plutonium–fizzium and uranium–plutonium–fissium alloy specimens have been examined after being irradiated to burnups of up to 8.7 at.% at maximum temperatures[18] up to 740°C. Results of measurements of fuel-volume increase and

Table I-4 RELEASE OF FISSION GAS FROM METAL-FUEL SPECIMENS[18]

Specimens	Composition (balance uranium), wt.%	Maximum fuel-irradiation temp., °C	Burnup, at.% Pu + U	Fuel-volume increase, %	Fission-gas release, %
33-1	10 Pu–10 Fz	590	7.1	20	3.2
33-6	10 Pu–10 Fz	610	7.1	21	3.7
33-2	15 Pu–10 Fz	610	8.7	26	9.6
23-5	20 Pu–10 Fs	650	1.4	25	14.8
23-6	20 Pu–10 Fs	650	1.4	21	9.2
32-1	20 Pu–10 Fs	690	4.2	25	10.9
32-3	20 Pu–10 Fs	690	4.2	22	8.2
32-4	20 Pu–10 Fs	720	4.2	26	14.1
32-5	20 Pu–10 Fs	720	4.2	22	2.6
32-6	20 Pu–10 Fs	720	4.2	24	4.5
39-2	15 Pu–10 Fz	740	3.0	30	33
39-4	15 Pu–10 Fz	740	3.0	57	63
39-5	15 Pu–10 Fz	740	3.0	97	76
39-6	15 Pu–10 Fz	740	3.0	133	83

fission-gas release are tabulated in Table I-4. The data suggest that fission-gas release does not become appreciable until volume increases exceed about 30%.

Argonne has also continued investigations of uranium–plutonium-base alloys for use in zero-power experiments.[18] Thermal-expansion characteristics of uranium–25 wt.% plutonium–2.5 wt.% molybdenum and uranium–28 wt.% plutonium–2.5 wt.% molybdenum alloys were measured in the as-cast condition. For both alloys the thermal-expansion curves have a gradually increasing slope to about 200°C. The slope of the curves shows a decided increase slightly above 200°C. From this point up to 540°C, the curves are nearly linear. A transformation occurs between 540 and 630°C, and the curves are again linear in the range from 630 to 780°C. The data obtained on the as-cast specimens are presented in Table I-5.

Results of French studies of the kinetics of plutonium $\alpha \rightleftharpoons \beta$ transformations suggest that the transformations may proceed by either of two mechanisms.[19] Near the equilibrium temperature, transformation proceeds by diffusion; under other conditions, it proceeds by shear. The activation energy for the $\alpha \rightarrow \beta$ transformation is 33 kcal/mole and that for the $\beta \rightarrow \alpha$ transformation is 4.6 kcal/mole.

Battelle–Northwest has also devoted considerable effort to studies of the $\alpha \rightleftharpoons \beta$ transformations in plutonium.[20] Significant observations made during these studies are as follows:

1. The kinetic data show conclusively that the $\beta \rightarrow \alpha$ transformation in high-purity plutonium can proceed isothermally.
2. Plastic deformation of the stable beta phase retards the subsequent $\beta \rightarrow \alpha$ transformation.
3. Plastic deformation of the stable alpha phase accelerates the $\alpha \rightarrow \beta$ transformation; the acceleration is attributed to residual stresses.
4. The $\alpha \rightarrow \beta$ and $\beta \rightarrow \alpha$ volume changes occur anisotropically in the textured plutonium.
5. An apparent crystallographic relation exists between the parent and the product phase of the $\alpha \rightarrow \beta$ and $\beta \rightarrow \alpha$ transformations.
6. Both applied uniaxial compressive stresses and uniaxial tensile stresses raise the starting temperature for the $\beta \rightarrow \alpha$ transformation.
7. A given applied uniaxial tensile stress favors the $\alpha \rightarrow \beta$ transformation more than an equivalent applied uniaxial compressive stress opposes the transformation. These observations of the $\beta \rightarrow \alpha$ and $\alpha \rightarrow \beta$ phase changes in plutonium are consistent with known martensitic transformations.

Table I-5 EXPANSION CHARACTERISTICS OF URANIUM–PLUTONIUM–MOLYBDENUM ALLOYS FOR ZPPR[18]

Composition (balance uranium), at.%	Mean expansion coefficient, 10^{-6}/°C			Transformation	
	25–200°C	200–540°C	630–780°C	Temperature range, °C	Expansion (Δl), %
24 Pu–6 Mo 25 Pu–2.5 Mo	16.6	26.8	24.0	540–630	0.52
27 Pu–6 Mo 28 Pu–2.5 Mo	15.4	26.2	25.3	540–630	0.46

On the basis of measurements of changes[21] in electrical resistivity when high-purity plutonium was thermally cycled near the alpha–beta transformation temperature, investigators at Los Alamos Scientific Laboratory determined that the alpha–beta transformation occurs at 117.0° ± 0.5°C. (V. W. Storhok)

Plutonium Compounds

For the preparation of plutonium microspheres by the sol-gel process, Oak Ridge reports that the nitrate-to-plutonium ratio of the sol can be reduced to an acceptable level for most fuel-cycle applica-

tions by a drying and baking operation prior to preparing the final sol. Plutonia microspheres prepared in this manner have yielded a product of 95 to 99% of theoretical density and a crushing strength in excess of 600 for 150-μ-diameter spheres.[22]

PuO_2 was found to be compatible with an 80 wt.% nickel–20 wt.% chromium alloy at 1093°C (2000°F) for up to 400 hr. No evidence of PuO_2 diffusion through a 0.15-mm-thick nickel–chromium foil was observed. Compatibility is impaired by silicon as an impurity in the nickel–chromium alloy.[23]

Battelle–Columbus is continuing the preparation of (U,Pu)N by a hydride–nitride–vacuum outgas cycle on arc-cast uranium–plutonium alloy ingots, followed by consolidation of the powders by isostatic hot pressing or uniaxial hot pressing. Product characteristics of a typical isostatically hot-pressed $(U_{0.2}Pu_{0.8})N$ are given in Table I-6. Thermal stability, chemical compatibility, and thermal conductivity of the mixed nitride fuels are being determined. Irradiation of (U,Pu)N fuels has been initiated in the high-flux facility of the Engineering Test Reactor (ETR).[24]

Table I-6 CHARACTERIZATION[24] OF (U,Pu)N

Density, % of theoretical	99.4
Microhardness, DPHN (1000-g load)	622
Nitrogen content, wt.%	5.29
Oxygen content, ppm	2261 ± 184
Hydrogen content, ppm	29 ± 23
Lattice parameter, A	4.8920 ± 0.0002

Los Alamos reports thermodynamic properties[25] of PuN obtained from emf cell measurements. For the reaction

$$Pu\ (solid) + 0.5N_2\ (gas,\ p = 1\ atm) = PuN\ (solid)$$

the free energy $\Delta G_T^\circ = 99 + 0.55T$ kcal per mole of PuN. This corresponds to a free energy of formation of -60 ± 1 kcal per mole of PuN at 700°K. At this temperature the free energy of formation of UN is −56 kcal/mole, for comparative purposes.

Homogeneous solid solutions of (U,Pu)S have been prepared by workers at Argonne[18] by reaction-sintering US and PuS powders at 1700 and 1900°C. Lattice constants and melting-point determinations were made on compositions of US with 20, 40, 60, and 80 at.% PuS.

Investigators at Los Alamos,[26] using X-ray analysis and metallography, have defined a portion of the plutonium–carbon–oxygen ternary phase diagram at 1250°C. A single phase Pu(C,O) field was found with a range of lattice parameters from 4.954 to 4.972 A. Three two-phase fields containing Pu + Pu(C,O), Pu_2O_3 + Pu(C,O), and Pu_2C_3 + Pu(C,O) and a three-phase field containing Pu + Pu_2O_3 + Pu(C,O) were also delineated.

Argonne is developing[16] two fluidized-bed processes for preparing mixed carbides: (1) carburization of hydrided uranium–plutonium alloy with hydrocarbon–hydrogen gas mixtures to form (U,Pu)C and (2) conversion of $(U,Pu)O_2$ to (U,Pu)C by reaction with carbon or methane. On the basis of current thermobalance and fluidized-bed studies, it is believed that mixed-carbide powders of low oxygen content and near-stoichiometric carbon content can be routinely prepared by the fluidized-bed process.

A study of the changes in lattice parameters of several plutonium compounds due to self-induced radiation damage over periods up to 4 years has been continued at Battelle–Northwest.[27] The following equations have been derived as a result of this study (time in days):

For carbon-rich Pu_2C_3,

$$\frac{\Delta a}{a_0} = 1.59 \times 10^{-3}\ [1 - \exp\ (-1.99 \times 10^{-3} t)]$$

For stoichiometric Pu_2C_3,

$$\frac{\Delta a}{a_0} = 1.65 \times 10^{-3}\ [1 - \exp\ (-1.99 \times 10^{-3} t)]$$

For carbon-poor Pu_2C_3,

$$\frac{\Delta a}{a_0} = 1.68 \times 10^{-3}\ [1 - \exp\ (-1.99 \times 10^{-3} t)]$$

For PuC,

$$\frac{\Delta a}{a_0} = 4.65 \times 10^{-3}\ [1 - \exp\ (-1.45 \times 10^{-3} t)]$$

For PuO_2–10 mole % UO_2,

$$\frac{\Delta a}{a_0} = 1.84 \times 10^{-3}\ [1 - \exp\ (-2.00 \times 10^{-3} t)]$$

(D. F. Askey)

Thorium

Several methods for producing kilogram quantities of high-purity thorium metal are being investigated at Ames Laboratory:[28] (1) triple distillation of $ThCl_4$ under a pressure of 25 torrs of argon; (2) heating by internal resistance with direct current and producing the electrotransport phenomenon; (3) improving the purity of thorium oxalate, oxide, or nitrate as starting materials. Thus far the electrotransport process appears to be quite effective in reducing the impurity content of thorium. However, chemical analyses have not been obtained as yet, and the effectiveness of the purification process is being measured by electrical-resistance techniques. (R. L. Martin)

Metal–Ceramic Fuels

Dispersion Fuels (Less Than 50 Vol.% Ceramic Phase)

General Electric Company reports that thermal conductivity was measured for 20 and 40 vol.% UO_2–

tungsten dispersions. Specimens of both dispersions were prepared by a Dynapak process, and the measurements were made in a plane perpendicular to the direction of compaction. Final densities of the 20 and 40 vol.% UO_2–tungsten dispersions were 97.4 and 95% of theoretical, respectively. The data for these compositions are compared with those for tungsten, UO_2, and a 60 vol.% UO_2–tungsten cermet (Fig. I-4). The influence of composition on the thermal conductivity of the UO_2–tungsten specimens is readily apparent in Fig. I-4. Studies conducted to date have not been sufficient to determine the mechanisms of heat transport in these materials or the effects of shape and orientation of the oxide particles on thermal conductivity.[29,30]

Metallographic examination of a 38 wt.% PuO_2–Nichrome specimen, after a 300-hr heat-treatment at 1093°C, at Phillips Petroleum Company, revealed that the PuO_2 particles adjacent to the Nichrome foils which sealed the ends of a Nichrome tube containing the PuO_2–Nichrome cermet were darkened in appearance. Microprobe analysis[31] revealed silicon pickup in these darkened PuO_2 particles and suggested that the temperature was sufficiently high to allow appreciable mobility of the silicon in the Nichrome matrix and foil, which in turn was scavenged by the PuO_2.

Fabrication studies at Phillips Petroleum on the uranium–aluminum intermetallic compounds indicate that UAl_2 and UAl_3 can be prepared by several methods. A solid–solid reaction, using uranium hydride, however, yields the highest purity compounds. Irradiation tests have shown lower swelling rates for UAl_x–aluminum dispersions to fission densities of 1.6×10^{21} fissions/cm^3 than for corresponding UO_2, U_3O_8, and UN–aluminum dispersions. Postirradiation annealing tests have also shown the superiority of the UAl_x intermetallic fuels in terms of blister resistance. Metallography of the irradiated fuel particles did not reveal the fission-induced porosity in the UAl_3 fuels observed in the oxide (UO_2 and U_3O_8) fuels irradiated to equivalent burnups.[32] Oak Ridge National Laboratory[33] has successfully fabricated 30 wt.% UAl_3–aluminum dispersions. These plates were assembled as prototype fuels for irradiation testing in the Oak Ridge Research Reactor. Visual examination of these specimens after 30% ^{235}U burnup showed no evidence of damage. Steps are currently in progress to continue the fabrication of large quantities of similar 30 wt.% UAl_3–aluminum compacts.

Argonne reports[34] that ETR irradiations were performed on 37 wt.% UO_2–type 347 stainless-steel dispersion fuels prepared by Battelle and by Martin Co. These two dispersion fuels differ mainly in the technique used to disperse the UO_2 fuel within the matrix. Briefly, Battelle blends spherical UO_2 particles and type 347 stainless-steel powders into mixtures with

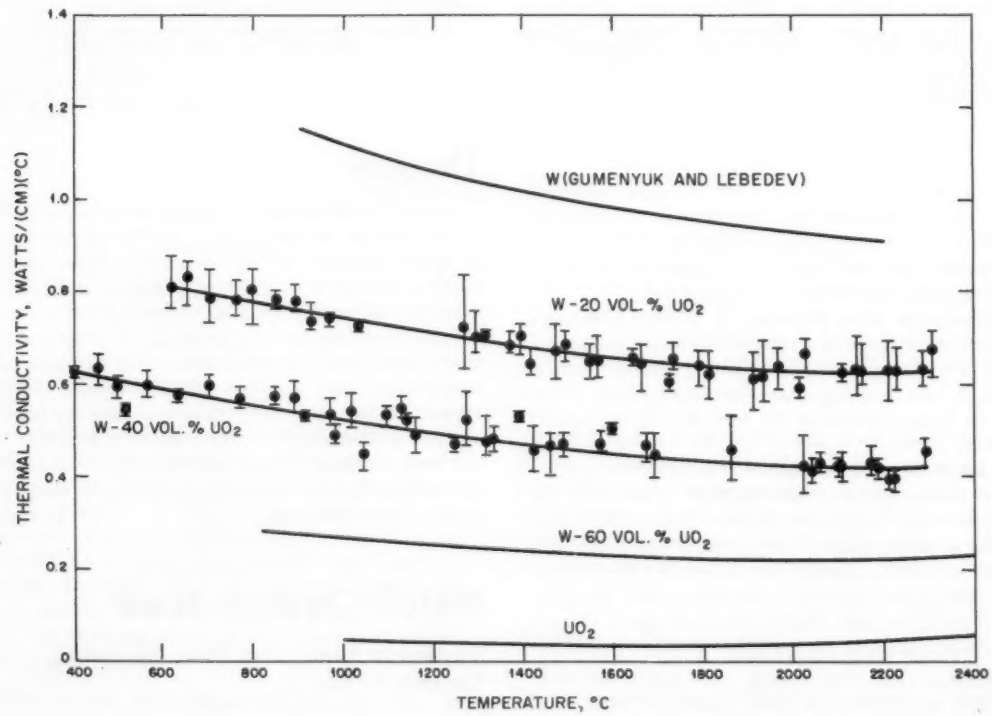

Fig. I-4 Thermal conductivity vs. temperature for tungsten–UO_2 and composites.[30]

adequate homogeneity to provide matrix soundness, whereas Martin utilizes spherical UO_2 particles vapor coated with a type 347 stainless-steel layer. The test conditions are listed in Table I-7. In the table, B-6 and M-1 represent fuel plates prepared by Battelle and Martin, respectively. The net measured swelling in the fuel plates having the highest burnups was less than 3%. The highest burnups in these tests correspond roughly to twice the average burnup in the 37 wt.% UO_2–type 347 stainless-steel fuel at the end of the core life in the Argonne Advanced Research Reactor (AARR). Extensive postirradiation examination of the specimens is planned.

A sandwich type fuel-element structure of depleted UO_2 dispersed in a stainless-steel "picture frame" was tested at Argonne.[16] The core consisted of 37 wt.% UO_2 particles dispersed in type 304B stainless steel and had been fabricated by pressing and sintering. The fuel element was machined into test specimens oriented longitudinally and transversely to the direction of rolling. Tensile, bending, and dynamic tests were conducted. Data indicated that Young's modulus for the longitudinal specimens was 21.5×10^6 psi, and that for the transverse specimens was 23.5×10^6 psi. Young's moduli for the transverse and longitudinal cores were calculated to be 21.4 and 18.5×10^6 psi, respectively. The ratio of the modulus value in the transverse direction to that in the longitudinal direction (1.14) is not enough to justify the assumption of anisotropy for these 37 wt.% UO_2–type 304B stainless-steel cores. Therefore the sandwich material was assumed to be isotropic, with a Poisson's ratio of 0.25.

General Electric reports[35] that the excellent thermal stability of the iron–chromium–aluminum–yttrium clad UO_2 dispersions was shown by the large number of samples that achieved many thousands of hours of testing at 950 and 1100°C without failure. The lower chromium content of the 1541 alloy made it no less effective as an oxidation-resistant cladding than the 2541 alloy for 10,000-hr operation at temperatures to 1100°C. The iron-matrix core with 40 vol.% UO_2 content was favored over the chromium and iron–chromium alloy matrices since it exhibited less uranium diffusion to the cladding surface as determined by X-ray fluorescence analysis. Metallography indicated that the cladding materials gettered the oxygen from the cores, possibly by the reduction of the UO_2 or other oxides. The amount of internal oxidation varied, and in some specimens a continuous Al_2O_3 layer was formed at the core–cladding interface. Such an oxide layer inhibited further reaction between the cladding and the fuel and prevented uranium diffusion to the surface. Evidence of Y_2O_3 particles in the grain boundaries of the cladding, however, suggested that this Al_2O_3 layer can be reduced by the yttrium present in the cladding. For instance, at 1100°C the Y_2O_3 particles were present in the grain boundaries, whereas at 950°C the Y_2O_3 particles were distributed at the previous sites of YFe_9 particles. Possible reduction of the Al_2O_3 layer by the yttrium suggests that over a long time the initial Al_2O_3 layer could be reduced and result in a reaction between the core and cladding. Consequently the stability of the specimens is believed to be enhanced primarily by the use of hyperstoichiometric UO_2 rather than by the type of matrix material or by fuel-particle size. (D. L. Stoltz)

Coated-Particle Fuel Materials

Particle Coating

A report that correlates separate phases of the development of ceramic-coated nuclear fuel particles has been compiled at Battelle–Columbus.[36] Separate reports have been issued on numerous phases of the broad-scoped program. However, a single final report summarizing all phases was written to supply the reader with an overall perspective. The report includes work on the deposition of PyC (pyrolytic carbon), Al_2O_3, BeO, MgO, SiC, ZrC, NbC, WC, and TaC coatings on nuclear fuel particles in fluidized-bed apparatus. The coating material identified as being of most general utility was PyC.

Table I-7 CALCULATED ETR IRRADIATION TEST CONDITIONS FOR AARR FUEL-PLATE SPECIMENS CONTAINING 37 WT.% UO_2 IN A TYPE 347 STAINLESS-STEEL MATRIX[34]

(Nominal Oxide Density = 80 to 85% of Theoretical)

	Cycle 70					Cycle 71				
				Av./max. surface temp.,					Av./max. surface temp.,	
Plate	Av. fission rate, fissions/(g)(sec)	Av. heat flux,* Btu/(hr)(sq ft)	Av. burnup, % ^{235}U	°F	°C	Av. fission rate, fissions/(g)(sec)	Av. heat flux,* Btu/(hr)(sq ft)	Av. burnup, % ^{235}U	°F	°C
M-1-926	1.49×10^{14}	1.37×10^6	8.6	240/282	116/139	1.57×10^{14}	1.33×10^6	21†	226/295	108/146
M-1-923	1.49×10^{14}	1.37×10^6	8.6	240/282	116/139					
M-1-933						1.57×10^{14}	1.45×10^6	~13	233/306	112/152
M-1-925	1.49×10^{14}	1.37×10^6	8.6	240/282	116/139	1.57×10^{14}	1.33×10^6	21†	226/295	108/146
B-6-947	2.11×10^{14}	1.69×10^6	12.8	314/368	157/187	2.17×10^{14}	1.56×10^6	27†	295/327	146/164
B-6-952						2.17×10^{14}	1.67×10^6	~15	304/343	151/173
B-6-943	2.11×10^{14}	1.69×10^6	12.8	314/368	157/187					
B-6-945	2.11×10^{14}	1.69×10^6	12.8	314/368	157/187	2.17×10^{14}	1.56×10^6	27†	295/327	146/164

*Maximum heat flux = 2×10^6 Btu/(hr)(sq ft).
†Total burnup for both cycles.

Workers at Oak Ridge are continuing an investigation of PyC coatings. They report[37] that the same type of PyC coating can be deposited on 530-μ-diameter particles as on 200-μ-diameter particles in either 1- or 2-in.-diameter fluidized-bed units. At General Atomic[38] the emphasis is on the study of high-density isotropic coatings since earlier irradiation tests of various PyC structures indicate that the dense isotropic coating should have the greatest radiation stability of the structures tested to date. In a systematic study, particles were coated at 2000 and 2200°C with PyC having CH_4 concentrations of 5 to 20 vol.%. Evaluation of these coatings is pending. (N. D. Veigel)

Irradiation and Evaluation of Coated-Particle Fuels

Workers at General Atomic[39] have ascribed the improvement obtained in high-temperature gas-cooled reactor fuel-element design through the use of coated fuel particles with good fission-product retention. This improvement has been made possible by continued studies to characterize quantitatively the factors that influence the coated-particle stability under irradiation conditions at high burnup, high fast flux, and reactor temperatures. The application of this knowledge has resulted in improved PyC-coated particles with greater integrity. Major interest has been given to Triplex (inner porous buffer layer, intermediate isotropic layer, and outer columnar layer) and BISO (inner buffer layer and outer high-density isotropic layer) coatings. Those parameters having the greatest effect on the stability of PyC coatings are: coating structure, fuel particle size, coating thickness, temperature of irradiation, burnup, burnup rate, and fast-neutron exposure. Isotropic, high-density, crystalline PyC coatings have been shown to be most stable under irradiation.

An extensive study of the effect of density on coating stability has shown that, as the density of the isotropic coating increases, the failure decreases. Improved Triplex-coated particles were operated unpurged in the GAIL IV Loop for 9700 hr with an accumulated power of 670 Mw-hr with low fission-product release. The circulating activity in the coolant was 1 μc/cm³, and the ^{85m}Kr release fraction *(R/B)* leveled at approximately 2×10^{-5}.

A new series of experiments by Oak Ridge[40] is being conducted to evaluate a large number of batches of two-layer PyC-coated UO_2 and UC_2 particles. These tests are being used to evaluate their mathematical model for predicting the performance of coated fuel particles. The results of these studies show at least three important criteria for the successful performance of PyC-coated fuel particles:

1. An adequate free-void volume must be provided by the inner coating and/or fuel particle to accommodate fuel swelling, fission-gas release, and fast-neutron-induced shrinkage of the outer coating.

2. The outer layer must not be subject to fission recoils either from a contaminated inner layer or direct recoils from the fuel.

3. The outer layer must be mechanically decoupled from the inner layer so that recoil-induced shrinkage of the inner layer does not impose excessive stresses on the outer coating.

Triplicate specimens of each of 25 lots of PyC-coated fuel particles were irradiated by Battelle-Columbus[41] in the ETR at temperatures of nominally 550, 1100, and 1300°C to burnups on the order of 2×10^{21} fissions/cm³. The samples included coatings of monolithic laminar PyC, duplex PyC (laminar over porous), and composite PyC (PyC over BeO or SiC) applied to uranium- or (thorium–uranium) base fuel particles. Postirradiation fission-gas-release measurements and metallographic examinations were used to study the effects of coating composition and thickness, fuel composition and density, and irradiation temperatures. No definite effects of fuel composition and irradiation temperature were observed. Duplex and composite coatings showed the best performance, with some additional improvement noted when used on fuel cores of lower density. Of the monolithic coatings, only the thick coating showed no failure.

Irradiations at Harwell[42] of $(Th_{0.84}-Pu_{0.16})C_2$ and $(Th_{0.95}-Pu_{0.05})C_2$ at 800 to 1400°C to 26% burnup (Fifa) showed no change in the integrity of Triplex PyC or PyC–SiC–PyC coatings by the replacement of ^{235}U with ^{239}Pu in the fuel particle. (N. E. Miller)

Uranium Oxide Fuels

Properties and Behavior

The Japanese have reported results of studies of fission-product release from UO_2. Takagi[43] has made measurements of nongaseous fission-product diffusion from UO_2 over the temperature range from 750 to 1600°C, taking into account surface evaporation. The results are summarized in Table I-8, where D_0 and Q give the diffusion coefficients in terms of

$$D = D_0 \exp(-Q/RT) \quad \text{cm}^2/\text{sec}$$

where T is the absolute temperature and R is the gas constant. Oi[44] has reported data for xenon diffusion

Table I-8 DIFFUSION PARAMETERS[42] FOR RELEASE OF NONGASEOUS FISSION PRODUCTS FROM UO_2

Nuclide	D_0, cm²/sec	Q, cal/gram atom
^{106}Ru	5.5×10^{-7}	27,000
^{144}Ce	1.2×10^{-4}	50,000
^{90}Sr	1.0×10^{-6}	27,000
^{95}Zr, ^{95}Nb	2.4×10^{-2}	92,000
^{131}I, ^{132}I	1.5×10^{-3}	59,000
^{99}Mo	3.9×10^{-4}	54,000
^{132}Te	6.6×10^{-3}	70,000
^{140}La	2.2×10^{-6}	35,000

from single-crystal UO_2 at high temperatures in helium. These data followed the relation

$$D = 3 \times 10^{-3} \exp(-Q/RT) \quad cm^2/sec$$

at temperatures ranging from 600 to 2400°C, where Q, the activation energy, is equal to 63,000 cal/gram mole. These results were not corrected for evaporation, which may be a significant factor at the higher temperatures.

Armstrong, Causey, and Sturrock[45] have investigated the initial stages of creep in single-crystal UO_2 over the temperature range 1340 to 1685°C and the stress range 3600 to 8000 psi. The stationary deflection rate $\dot{d}_s$ was found to follow the expression

$$\dot{d}_s = K\sigma^{3.3} \exp(-5.1/kT) \quad mm/hr$$

where k = Boltzmann's constant in electron volts
σ = stress in pounds per square inch
T = absolute temperature
K = a constant

Amato, Colombo, and Balzari[46] have studied the reaction between tantalum metal and hyperstoichiometric uranium oxide. For heating times of about 5 min, reactions were observed at temperatures of about 2150°C. The tantalum reaction product appears to be an oxide that disappears after prolonged heating at high temperatures, probably owing to the high volatility of the oxide.

Eash[47] performed studies of the compatibility of tungsten with molten UO_2 at 3000°K. After heating periods of 168 hr, large amounts of free alpha uranium were detected as a grain-boundary network in the tungsten and as dispersed particles within the UO_2. Although the extent of the reaction was minor considering the amount of time involved, the regions experiencing the most rapid attack were the grain boundaries and subgrain boundaries. A test performed at a lower temperature of 2750°C showed no evidence of any reaction. Use of either helium or hydrogen atmospheres had no effect on the results. It appears that the uranium was formed by dissociation of the UO_2, with the free oxygen diffusing into the tungsten.

Ohse[48] has reported measurements of the vapor pressure of UO_2. Over the temperature range from 2200 to 2800°K, the vapor pressure followed the relation

$$\log p\,(mm) = 12.426 - 3.318 \times 10^4 \frac{1}{T}$$

The latent heat of sublimation at 298°K was calculated to be 148.6 kcal/gram mole.

Baldock, Spindler, and Baker[49] have investigated the thermal expansion of uranium oxide samples having compositions between $UO_{1.98}$ and $UO_{2.00}$ using a high-temperature X-ray diffractometer. The expansion coefficient was linear above 400°C, and the mean coefficient of thermal expansion was $(10.8 \pm 0.1) \times 10^{-6}$ °C over the range from 20 to 2300°C.

(R. H. Barnes)

Fabrication

The preparation of porous UO_2 compacts having high fission-gas retention capabilities and swelling resistance is the subject of a recently issued British patent.[50] Hyperstoichiometric UO_2 granules are dispersed in a matrix of highly sinterable, stoichiometric UO_2 powder, and the mixture is green pressed. During the sintering operation in a reducing atmosphere, the oxygen-rich granules are reduced to UO_2 prior to fusion, and as a result they shrink more than does the UO_2 matrix. The resulting body exhibits a dense matrix containing discrete regions of internal porosity. (T. R. Wright)

Intermetallic Compound Fuels

Properties and Behavior

The French have added some details to the uranium–carbon–nickel ternary diagram.[51] The melting point of $UNiC_2$ is about 1400°C. Ties radiate from $UNiC_2$ to UC_2, graphite, nickel, UNi_5, UNi_3, and to "U_2C_3Ni" at 1000°C. The "U_2C_3Ni" is described as a new phase, melting above 1800°C, with ties radiating to UC, U_2C_3, $UNiC_2$, and UNi_3. A tie exists between UC and UNi_3. The experimental basis for postulating the existence of "U_2C_3Ni" is not clear, and it seems possible that this phase is a eutectic between UC and $UNiC_2$.

The thermal conductivity[52] of an arc-cast UC specimen was measured in the NRX reactor. Over the temperature range 280 to 830°C, the measured conductivities were about 40% lower than values reported elsewhere for out-of-reactor conductivity.[61] The sample was in good condition after one cycle in the NRX.

The thermal conductivities at room temperature of UC, UP, and US were measured by a heat-pulse technique and found to be 0.055, 0.025, and 0.019 cal/(sec)(cm)(°C), respectively.[53] The thermal conductivity[54] of 93% dense UP increased from 0.030 to 0.043 cal/(sec)(cm)(°C) between 100 and 900°C.

In good agreement with previous attempts to determine the solubilities of tungsten and UWC_2 in UC, Atomics International[55] reports that the maximum solubility of tungsten in UC is 1.7% at 1950°C, 2.0% at 2100°C, and 1.9% at 2300°C. The decrease from 2100°C to 2300°C is probably associated with the fact that 2300°C is above the solidus temperature of the UC–tungsten system. In excellent agreement with other data[56] are the findings[55] that the self-diffusion coefficients of carbon and uranium in UC at 1700°C are 2.5×10^{-8} and 4.8×10^{-11} cm^2/sec, respectively.

The British[57] obtained the following results for the self-diffusion of carbon in UC:

Carbon content, wt.%	A, cm²/sec	Q, kcal/mole	Diffusion coefficient, $D_c = A \exp(-Q/RT)$, at 1400°C, cm²/sec
4.82	1.75	63	1×10^{-9}
5.0	3.21×10^{-2}	55	2×10^{-9}
5.1	2.95×10^{-2}	54	2.5×10^{-9}

These results obtained between 1266 and 1684°C are in excellent agreement with the data mentioned above and data in the literature. For the self-diffusion of uranium in UC, it is reported that $D_u = 4.5 \times 10^3 \exp(-128{,}000/RT)$ and $D_u = 8.5 \exp(-104{,}000/RT)$ over the temperature range from 1500 to 1850°C. These equations result in good agreement above 1600°C with the above data for D_u and with data in the literature for D_u that were obtained above 1600°C only.

The British also report[66] that up to 2 wt.% oxygen dissolved in UC has no marked effect on the thermal conductivity of UC. However, the creep rates of UC alloyed with up to 2 wt.% oxygen were about 500 times faster than would be expected of cast, hypostoichiometric carbides. On the other hand, an alloy of UC–10 mole % NbC showed a creep rate 100 times slower than that of unalloyed UC at 1400°C and 6000 psi.

It has also been determined by British investigators[58] that at 1410°C that slip in UC occurs in a [1 1 0] direction, probably on planes other than [1 1 1].

At Harwell[57] 12 samples of UC–15 wt.% PuC have been irradiated at an estimated central temperature of about 850°C to burnups ranging from 5.4 to 10.6% of the metal atoms. The specimens were 1.0 in. long and 0.1 in. in diameter and were clad in 0.020-in.-thick stainless steel. Five samples having carbon contents from 4.4 to 4.65 wt.% had gas releases ranging from 0.47 to 18.8%. Five samples having carbon contents of 4.72 wt.% had gas releases ranging from 0.19 to 2.1%. Two hyperstoichiometric samples had gas releases ranging from 0.17 to 0.70%. Dimensional measurements on the stainless-steel cans showed no gross swelling.

Dumas and Mansard[59] found traces of CO in the fission gases over a UC sample containing 2000 ppm oxygen and irradiated to a low burnup at a temperature below 1000°C. Although no information is supplied relative to the quantity of gas, the system pressure, or the equilibrium constant for the proposed reaction to form the CO, it is suggested that some of the density change observed in the UC may have derived from the production of CO gas.

Between 340 and 420°C, UN reacts quantitatively with two molecules of water to give UO_2 and ammonia and half a molecule of hydrogen.[60] The reaction proceeds with an activation energy of 21,000 cal per molecule of UN.

A preliminary assessment of the compatibility of UP with various metals is shown in the following tabulation:[16]

Metal in contact with UP	Temperature, °C	
	Some melting	Complete melting
Titanium	1800	2110
Zirconium	1800	2055
Niobium	2000	2380
Molybdenum	2000	2395
Tantalum	2200	2405
Tungsten		2574

Nuclear pulse heating[61] of US in TREAT produced no gross cracking of the samples under conditions that would produce violent cracking of UO_2. This difference is attributed to the facts that (1) the thermal conductivity of US is three to five times greater than that of UO_2 and (2) the US contained a low-melting intergranular eutectic mixture of UOS–US. This eutectic apparently inhibited the propagation of extensive microcracks into macrocracks. Melting of this eutectic was observed in samples heated above 2060°C. (W. Chubb)

Fabrication

The papers presented at the symposium on Carbides in Nuclear Energy held at Harwell in November 1963 were published in book form.[62] Twenty-two papers were presented, covering the synthesis and fabrication of uranium carbide, uranium–plutonium carbides, and uranium carbide–zirconium carbide fuels.

The carbothermic reduction of uranium oxide in vacuum has been used to prepare UC suitable for fabrication of near-stoichiometric, dense carbide bodies with low oxygen (<0.1 wt.%) and nitrogen (<0.05 wt.%) contents.[63] Carbide feed material having known carbide contents in the range of 4.2 to 5.2 wt.% carbon can be provided to a predictable value of ±0.05 wt.% using the stable oxide U_3O_8 and vacuum-degassed graphite powders as raw materials. These latter materials are mixed and compacted for reacting at high temperatures in a vacuum furnace, the temperature at which the reaction to carbide is carried out being shown to influence the composition of the product. According to the amount of carbon content required, corresponding oxygen contents may range between 0.7 and 0.01 wt.% as the reaction temperature is varied from 1500 to 2000°C. The process is good for producing UC in batches up to 1 kg.

(D. S. Acuncius)

Mechanism of Corrosion of Fuel Alloys

The mechanism of oxidation of uranium was studied at 75°C in moist nitrogen, oxygen, and nitrogen–

oxygen mixtures at The Ohio State University.[64] The final oxidation product was UO_{2+x}, and uranium hydride was formed at the metal surface as a transitory, intermediate product. (The hydrogen was a by-product of the corrosion reaction.) The oxidation rate in moist oxygen was $^1/_{20}$ that in moist nitrogen. The inhibiting effect of oxygen was believed to result from its reaction with by-product hydrogen to form water at the uranium hydride–oxide interface, thereby restricting the supply of hydrogen to the metal-surface reaction. (W. E. Berry)

Basic Studies of Irradiation Effects in Fuel Materials

Metals

At Harwell[65] the production of irradiation damage in alpha uranium has been investigated by observing the ejection of atoms from single crystal and polycrystalline specimens during irradiation with 80-kev Kr^+ ions.

Ejection from the single crystals was found to occur preferentially near the [1 0 0], [1 1 0], and [4 8 7] type directions. This was interpreted in terms of focused collision sequences traveling along these directions which on intersecting the surface cause ejection in the same direction. The possible focusing mechanisms were discussed for each sequence, and an estimate was made of their focusing energies.

Atom ejection from the polycrystals was measured as a function of temperature. The sputtering ratio (the average number of atoms ejected per ion) remained effectively constant from room temperature up to about 400°C; however, between 400 and 600°C, an approximately exponential increase was observed. The increase is explained in terms of evaporation from thermal spikes created by the individual bombarding ions, and analysis of the results has provided information as to the spike's size, lifetime, and temperature.

In the light of the present results, the spatial distribution of interstitials and vacancies produced in alpha uranium as a result of recoils from direct collisions with fast neutrons is discussed qualitatively. Some of the main conclusions are also appropriate to a better understanding of the damage produced by fission fragments.

In Japan[66] the diffusion coefficient for xenon in uranium was obtained by measuring the concentration distribution of xenon in the uranium. The specimens were irradiated to a total dose of 2×10^{18} neutrons/cm^2 and heated at 950 and 1000°C for 100 hr. The diffusion coefficients at 950 and 1000°C were about 3×10^{-15} and 1×10^{-14} cm^2/sec, respectively.

Ceramics

At the University of California,[67] isothermal post-irradiation anneal experiments have been extensively used to determine diffusion coefficients for fission gases in nuclear fuel bodies. Several of these experiments have been carried out at temperatures sufficiently high for an appreciable evaporation rate of the fuel body, but the effect of this evaporation upon the release of the fission gas and upon the determination of diffusion coefficients has not heretofore been analyzed.

The time-dependent lattice diffusion of a radioactive gas contained in solids of simple shapes (sphere, slab, cylinder, and certain partially unbounded media) was analyzed. The solid sublimes into a vacuum, and as a result the boundary surface regresses. This regression is assumed to be a linear function of time. It is shown that the effect of the moving boundary increases the rate of diffusion of the gas through the boundary because the regression of the interface steepens the surface concentration gradient as compared with a stationary interface. If the surface evaporation is ignored, the predicted diffusion coefficient in a postirradiation-anneal experiment can be erroneously high by several orders of magnitude.

At Harwell[68] hyperstoichiometric uranium carbide single-crystal specimens have been irradiated to doses of up to 5.4×10^{16} fissions/cm^3 at about 130°C. A transmission electron-microscope examination of thin films has shown that a dose of 1.4×10^{16} fissions/cm^3 results in the formation of observable clusters in the uranium carbide matrix, the size and number of which increase with dose. Observable point-defect clusters are formed in the uranium dicarbide platelets only after exposure to the highest dose studied. On annealing, the point-defect clusters in both phases start to disappear above 700°C. However, on annealing at 1200 and 1300°C, the clusters in the uranium carbide matrix grow and become resolvable as loops.

The results are explained on the hypothesis that the point-defect clusters in the irradiated material are interstitial in nature. It is suggested that the vacancies become mobile at 700°C and produce the observed annealing effects by recombining with the interstitial clusters. A model is proposed for the formation of interstitial loops which is consistent with the observed loop behavior.

Bloch and Mustelier[69] studied the variation in the lattice parameters of UC irradiated at a flux of from 7×10^{11} to 2×10^{12} neutrons/(cm^2)(sec) for periods of 1 to 15 days. The irradiated UC was then annealed for 10 hr at temperatures to 1000°C in 50° increments. The relative variation in the parameters attained its maximum value after about 1.1×10^{17} fissions/cm^3. The effects of annealing on the lattice-parameter recovery are plotted and tabulated. The results show that the effect of the fission products is negligible. An interpretation is given of the three stages of the observed lattice-parameter recovery.

At Argonne[70] the surface-diffusion migration of an isolated pore in a solid was analyzed in detail. The results, which are similar to earlier results, are

applied in analyses of bubble coalescence during postirradiation annealing. Coalescence is considered, first, as a result of random migration of bubbles, in which case the results confirm earlier results that the mean bubble radius should be proportional to $(\text{time})^{1/3}$, and second, as a result of biased migration of bubbles. In the latter case the predicted mean radius increases linearly with time; in both cases the bubble-size distribution is calculated and used to predict the swelling of the solid, which is about 15% greater in the first case and up to 65% greater in the second case than predicted by approximate calculations on the basis of change in the mean bubble radius with time.

In work at Oak Ridge,[71] it was found that, according to the defect-trap theory for fission-gas release, the rate of escape of gas from UO_2 is controlled by the number of defects in the UO_2 structure. Defects are created by fission and may also be inherent flaws, such as grain boundaries and pores. This theory was tested by a comparison of the release rate of gas from single-crystal UO_2 to that from fine-grained UO_2. It was found that the single crystal released much more gas (a factor of 17 at 1000°C) than did the fine-grained material. Postirradiation examination showed that the grain boundaries trapped fission products. The theory further states that the number of radioinduced traps at a given temperature will be roughly proportional to the fission rate, under the conditions of this experiment. At a high fission rate, therefore, there will be more fission gas but also a higher probability of trapping the gas atoms, and a change in fission rate should not produce much change in the fission-gas-release rate. In a fine-grained material, a change in fission rate by a factor of 4.5 did not produce a detectable change in the rate of gas release. These results confirmed the defect-trap model for fission-gas release and are directly opposed to any gas-release mechanism that is diffusion controlled.

At Bettis Atomic Power Laboratory,[72] plates of ZrO_2–36.8 wt.% UO_2 and ZrO_2–46 wt.% UO_2, consisting initially of two phases, were clad in Zircaloy and irradiated to various burnups from 1 to 6×10^{20} fissions/cm^3. X-ray diffraction showed that the axial ratio of the zirconia-rich tetragonal phase decreased toward unity with irradiation and that the cell volume of the tetragonal phase increased until it reached the value appropriate for a single homogeneous phase. These changes proceeded more rapidly in ZrO_2–46 wt.% UO_2 than in ZrO_2–36.8 wt.% UO_2. The process of homogenization can be satisfactorily defined by a diffusion equation, if a value for the diffusion constant, D, of 3.32×10^{-14} cm^2/sec is used. This D value indicates that a single fission homogenizes a volume containing 1.66×10^7 atoms. This number is two orders of magnitude too large to be explained by Brinkman's displacement-spike hypothesis. Calculations based on Konobeevsky's hypothesis of a thermal pulse show that the liberation of 23 Mev of thermal energy at the center of such a volume is sufficient to cause homogenization. This seems well within the capabilities of a fission event. (F. A. Rough)

References

1. J. L. Pascal, Applications of Electrical Resistivity Measurements to Research into Purification of Uranium Using Floating Zone Melting by Electronic Bombardment [Thesis], French Report CEA-R-2740, 1965.
2. J. C. Jousset, Annealing of Uranium Quenched From 100 to 4.2°K, USAEC Report ANL-Trans-273 [from *Acta Met.*, 14: 193-200 (1966)].
3. P. D. Tilbury, Impact Tensile Testing of Uranium, British Report AWRE-O-36/66, March 1966.
4. R. H. Johnson and E. C. Sykes, Enhancement of Ductility in α-Uranium, *Nature*, 209: 192-193 (Jan. 8, 1966).
5. A. Lemogne, Tensile Deformation in Mono- and Polycrystalline Uranium Between 20 and −196°C [Thesis], French Report CEA-R-2819, 1966.
6. F. P. Butra, Z. F. Yevkina, O. L. Fufayeva, I. A. Korobeynikov, and L. M. Lebedev, The Effect of Temperature and Neutron Irradiation on Plastic Deformation of Alpha Uranium Monocrystals (in Russian), *At. Energ. USSR*, 19(4): 372-380 (1965).
7. M. H. Cornett, Metallography of Uranium: Procedures and Standards, USAEC Report NLCO-954, National Lead Co. of Ohio, Mar. 25, 1966.
8. L. T. Lloyd and C. S. Barrett, Thermal Expansion of Alpha Uranium, *J. Nucl. Mater.*, 18: 55-59 (1966).
9. E. S. Fisher, Temperature Dependence of the Elastic Moduli in Alpha Uranium Single Crystals, Part IV (298 to 923 K), *J. Nucl. Mater.*, 18: 39-54 (1966).
10. N. Swindells, The Solubility of Iron in Solid Uranium Between 0.003 Wt.% and 0.3 Wt.% Iron, *J. Nucl. Mater.*, 18: 261-271 (1966).
11. J. L. Arnold, Irradiation Performance of Piqua Core 1 Fuel Elements, USAEC Report NAA-SR-11712, Atomics International, May 25, 1966.
12. A. Sampaio and M. Pinto, Study of the Ternary System U–V–Cr (in Portuguese), Portuguese Report LFEN-24, 1964.
13. C. A. W. Peterson and W. E. Elkington, Physical and Mechanical Properties of U-7.5 Wt.% Nb-2.5 Wt.% Zr Alloy, USAEC Report UCRL-14724, University of California, Lawrence Radiation Laboratory, Feb. 17, 1966.
14. K. G. Hoge, Mechanical Properties of Gamma-Phase Uranium-7.5 Wt.% Niobium-2.5 Wt.% Zirconium Alloy Under Dynamic Loading, USAEC Report UCRL-14805, University of California, Lawrence Radiation Laboratory, Apr. 6, 1966.
15. M. S. Farkas and E. A. Eldridge, Battelle Memorial Institute, Columbus Laboratories, personal communication, July 15, 1966.
16. Argonne National Laboratory, Reactor Development Program Progress Report, February 1966, USAEC Report ANL-7176, Mar. 23, 1966.
17. Argonne National Laboratory, Reactor Development Program Progress Report, March 1966, USAEC Report ANL-7193, Apr. 22, 1966.
18. Argonne National Laboratory, Reactor Development Program Progress Report, April 1966, USAEC Report ANL-7204, May 31, 1966.
19. B. Spriet, Kinetics of the $\alpha \rightarrow \beta$ Transformation of Plutonium in the Vicinity of Equilibrium, Report MLM-1303 (tr) [translated from *J. Nucl. Mater.*, 16: 59-67 (1965)].
20. Battelle Memorial Institute, Pacific Northwest Laboratory, Metallurgy Research Section, Quarterly Progress Report, October–December 1965, USAEC Report BNWL-207, Jan. 17, 1966.
21. J. W. Anderson, Studies on the Equilibrium Temperature for the Plutonium Alpha-Beta Transformation,

USAEC Report LA-DC-7278 (Suppl.), Los Alamos Scientific Laboratory, 1964.

22. R. G. Haire and M. H. Lloyd, Development of a Sol-Gel Process for the Preparation of Dense-Oxide Forms of PuO_2, *Trans. Amer. Nucl. Soc.*, 9(1): 20 (June 1966).
23. D. F. Carroll, Compatibility Between PuO_2 and 80 Ni/20 Cr, USAEC Report BNWL-18, Battelle Memorial Institute, Pacific Northwest Laboratory, Jan. 29, 1965.
24. W. M. Pardue, R. A. Smith, and F. A. Rough, Uranium-Plutonium Mononitride Fuel Materials for Fast Reactors, *Trans. Amer. Nucl. Soc.*, 9(1): 37 (June 1966).
25. Los Alamos Scientific Laboratory, Quarterly Status Report on Advanced Reactor Technology (ART) for Period Ending January 31, 1966, USAEC Report LA-3482, February 1966.
26. R. N. R. Mulford et al., The Plutonium-Carbon-Oxygen System, *J. Nucl. Mater.*, 17: 324-329 (1965).
27. Battelle Memorial Institute, Pacific Northwest Laboratory, Ceramics Research and Development Quarterly Report, July–September 1965, USAEC Report BNWL-198.
28. A. F. Voigt (Ed.), Reactor Materials Development Quarterly Report, January–March 1966, USAEC Report IS-RD-5, Ames Laboratory.
29. General Electric Company, Nuclear Materials and Propulsion Operation, High-Temperature Materials Program Progress Report No. 55, Part A, USAEC Report GEMP-55A, Jan. 21, 1966.
30. General Electric Company, Nuclear Materials and Propulsion Operation, High-Temperature Materials Program Progress Report No. 59, Part A, USAEC Report GEMP-59A, May 31, 1966.
31. Phillips Petroleum Company, Nuclear Technology Branches Quarterly Report, January 1–March 31, 1965, USAEC Report IDO-17104, December 1965.
32. W. C. Francis (Ed.), Annual Progress Report on Reactor Fuels and Materials Development for FY 1965, USAEC Report IDO-17154, Phillips Petroleum Company, February 1966.
33. Oak Ridge National Laboratory, unpublished, May 5, 1966.
34. Argonne National Laboratory, Reactor Engineering Division Annual Report, July 1, 1964–June 30, 1965, USAEC Report ANL-7190, March 1966.
35. General Electric Company, Nuclear Materials and Propulsion Operation, High Temperature Materials Program, Part A, Fifth Annual Report, USAEC Report GEMP-400A, Feb. 28, 1966.
36. C. W. Townley (Ed.), Development of Ceramic-Coated-Particle Nuclear Fuels, Summary Report, USAEC Report BMI-1768, Battelle Memorial Institute, Columbus Laboratories, Apr. 25, 1966.
37. J. H. Coobs and O. Sisman (Comps.), Coated-Particle Fuels Development at Oak Ridge National Laboratory for Period May 15–November 15, 1965, USAEC Report ORNL-TM-1331, Oak Ridge National Laboratory, December 1965.
38. General Atomic Division, General Dynamics Corp., High-Temperature Gas-Cooled Reactor Research and Development Program, Quarterly Progress Report for the Period Ending December 31, 1965, USAEC Report GA-6950, Mar. 21, 1966.
39. General Atomic, Division of General Dynamics Corp., Advances in Fuel Element Design and Materials, USAEC Report GA-7183, June 17, 1966.
40. J. H. Coobs and J. G. Morgan (Comps.), Coated-Particle Fuels Development at Oak Ridge National Laboratory for Period November 15, 1965–May 15, 1966, USAEC Report ORNL-TM-1528, Oak Ridge National Laboratory, May 1966.
41. N. E. Miller, R. L. Martin, R. B. Price, H. S. Rosenberg, and C. W. Townley, ETR Irradiations of Pyrolytic-Carbon-Coated Fuel Particles, USAEC Report BMI-1772, Battelle Memorial Institute, Columbus Laboratories, May 11, 1966.
42. B. Riley and J. H. Worth, The Fabrication and Irradiation Behavior of Plutonium-Thorium Carbide Coated Fuels, British Report DP-Report-414, March 1966.
43. J. Takagi, Evaporation Behavior of Nongaseous Fission Products from UO_2, *Z. Naturforsch.*, 202: 1566-1568 (1965).
44. N. Oi, Xenon Diffusion in UO_2 Single Crystals, *Z. Naturforsch.*, 202: 1569-1571 (1965).
45. W. M. Armstrong, A. R. Causey, and W. R. Sturrock, Creep of Single-Crystal UO_2, *J. Nucl. Mater.*, 19: 42-49 (1966).
46. I. Amato, R. L. Colombo, and A. M. P. Balzari, On the Reaction Between Tantalum Metal and Uranium Dioxide, *J. Nucl. Mater.*, 19: 190-192 (1966).
47. D. T. Eash, On the Compatibility of Tungsten with Molten UO_2, *J. Nucl. Mater.*, 19: 196-197 (1966).
48. R. W. Ohse, High Temperature Vapor Pressure Studies of UO_2 by the Effusion Method and Its Thermodynamic Interpretation, *J. Chem. Phys.*, 44: 1375-1378 (Feb. 15, 1966).
49. P. J. Baldock, W. E. Spindler, and T. W. Baker, The X-Ray Thermal Expansion of Near-Stoichiometric UO_2, *J. Nucl. Mater.*, 18: 305-313 (1966).
50. B. R. Steele, Improvements in or Relating to Fuel for Nuclear Reactors, British Patent No. 1,015,004, Dec. 31, 1965.
51. F. Anselin, D. Calais, and J. -C. Passefort, Survey of Uranium-Carbon-Nickel Ternary Diagrams, French Report CEA-R-2845, August 1965.
52. Atomic Energy of Canada Ltd., unpublished, 1965.
53. J. B. Moser and O. L. Kruger, Heat Pulse Measurements on Uranium Compounds, *J. Nucl. Mater.*, 17: 153-158 (1965).
54. Argonne National Laboratory, Reactor Development Program Progress Report, December 1965, USAEC Report ANL-7132, Jan. 25, 1966.
55. Atomics International, AEC Unclassified Programs, Quarterly Technical Progress Report, October–December, 1965, USAEC Report NAA-SR-11805, Feb. 15, 1966.
56. W. Chubb, R. W. Getz, and C. W. Townley, Diffusion in Uranium Monocarbide, *J. Nucl. Mater.*, 3(1): 63-74 (1964).
57. L. E. J. Roberts and J. Williams, U. K. Atomic Energy Authority, February 1966.
58. B. L. Eyre and A. F. Bartlett, Determination of the Burgers Vector of Dislocations in Deformed Uranium Carbide, British Report AERE-M-1668, November 1965.
59. J. P. Dumas and B. Mansard, The Shaping and Irradiation of Uranium Monocarbide, Quarterly Report No. 15, July 1, 1964–March 31, 1965, USAEC–Euratom Report EURAEC-1455, Commissariat à l'Énergie Atomique, January 1966.
60. R. M. Dell, V. J. Wheeler, and E. J. McIver, The Hydrolysis of Uranium Mononitride, British Report AERE-R-4984, November 1965.
61. L. E. Robinson et al., Behavior of Uranium Sulfide Fast-Reactor-Type Fuel Specimens Under Transient Heating in TREAT, *Nucl. Appl.*, 1/2: 168-175 (April 1965).
62. L. E. Russell, B. T. Bradbury, J. D. L. Harrison, H. J. Hedger, and P. G. Mardon (Eds.), *Carbides in Nuclear Energy*, Symposium Proceedings, Harwell, England, November 1963, Vol. 2, Macmillan & Co. Ltd., London, 1964.
63. N. R. Williams, Preparation of Uranium Monocarbide of Controlled Composition by Carbothermic Reduction of the Oxides in Vacuum, British Report AERE-R-5098, December 1965.
64. Ellis D. Verink, Jr., A Study of the Oxidation Mechanism of Uranium in Moist, Flowing Nitrogen and in Nitrogen-Oxygen Mixtures, Thesis, The Ohio State University, 1965.
65. R. S. Nelson, An Investigation of Atomic Collision Sequences and Thermal Spikes in α-Uranium, *J. Nucl. Mater.*, 18: 348-356 (Oct. 27, 1965).

66. R. Nagasaki and S. Kawasaki, Diffusion of Xenon in Metals, *J. Nucl. Mater.*, 19: 90-92 (April 1966).

67. P. L. Chambre, On the Release of Fission Gas From an Evaporating Fuel Body, *J. Nucl. Mater.*, 18: 167-175 (Feb. 10, 1965).

68. B. L. Eyre and M. J. Sole, On the Formation and Behaviour of Point Defect Clusters in Neutron Irradiated Uranium Carbide, *J. Nucl. Mater.*, 18: 314-322 (Oct. 15, 1965).

69. J. Bloch and J. P. Mustelier, Variation of the Parameters of Weakly Irradiated Uranium Monocarbide, *J. Nucl. Mater.*, 17: 350-355 (December 1965).

70. E. E. Gruber, On the Theory of Migration and Coalescence of Bubbles in Solids, USAEC Report ANL-7079, Argonne National Laboratory, November 1965.

71. R. M. Carroll and O. Sisman, In-Pile Fission-Gas Release from Fine-Grain UO_2, *J. Nucl. Mater.*, 17: 305-312 (December 1965); ORNL-P-793.

72. R. M. Berman, Homogenization of Two-Phase Mixtures of ZrO_2-UO_2 by Irradiation, *J. Nucl. Mater.*, 17: 313-323 (December 1965).

Section

II

Reactor Materials

Moderator Materials

Graphite

Additional experimental data on the effects of cold preirradiation and intermittent thermal anneals upon subsequent high-temperature irradiation behavior of graphites are reported by Battelle–Northwest.[1] The seeding of graphite with radiation-produced defects at low temperature is of particular interest in reactor design and operation because it results in enhanced contraction. The ability of intermittent thermal anneals to reduce subsequent radiation-induced contraction is likewise important.

The graphites investigated for cold-seeding effects were: KC, CSF, and TSGBF. Cold (30°C) exposures were 0.8×10^{20} to 2.9×10^{20} neutrons/cm^2 ($E > 0.18$ Mev), and hot (550 to 700°C) exposures were to 11.1×10^{20} neutrons/cm^2. The cold-seeded samples were thermally annealed (to 750°C) after the irradiation. Cold-seeding increased the contraction rate of all the graphites. The contraction rate, independent of orientation, increased by a factor of about 3. On the basis of the wide experimental range of both cold and hot exposures, it appears that the factor of 3 is the upper limit for the temperatures investigated. The minimum cold exposure required to reach this limit was not established.

Samples of TSX graphite were irradiated at temperatures greater than 500°C to exposures up to 3.0×10^{21} neutrons/cm^2. Samples were annealed at 2500°C after each increment of exposure. In every case the contraction upon subsequent irradiation was less in annealed samples than in unannealed standard samples irradiated under the same condition.

The functional dependence of the radiation-induced dimensional changes on the density and the degree of preferred orientation of pyrolytic carbons has been examined by General Atomic researchers.[2] The carbons of interest in this study are those used as coatings on nuclear fuel particles. The conclusions drawn from this study are:

1. The neutron-induced densification of carbons at 520, 670, and 1000°C is a simple first-order rate process in which the density defect (difference between theoretical and experimental unirradiated density) is removed by rearrangement of the point defects generated by the irradiation.

2. For isotropic carbons with c values in the range 100 to 200 A, the densification constant, k_d, in the relation

$$\frac{d\rho}{d\gamma} = k_d\,(\rho_{th} - \rho_0)e^{-k_d\gamma}$$

where ρ = density
ρ_{th} = theoretical density
ρ_0 = initial unirradiated density
γ = neutron dose

has the values of 1.0×10^{-22}, 1.4×10^{-22}, and 2.8×10^{-22} cm^2/neutron at 520, 670, and 1000°C, respectively.

3. The apparent activation energy calculated from the temperature dependence of k_d is very low (~ 0.2 ev), suggesting that the densification process is controlled by the thermal migration of single interstitial carbon atoms displaced by fast neutrons during the irradiation.

The authors used the results of this study to estimate the densities and degrees of preferred orientation that a restrained carbon coating must have to sustain the radiation-induced dimensional changes without a failure at 1000°C. Figure II-1 presents calculated maximum stresses when stress is partially relieved by creep.

Test results have been reported for a BeO–graphite compatibility experiment.[3] Test samples were irradiated at 1250 to 1500°C to an exposure of about 1.5×10^{21} neutrons/cm^2 ($E > 0.18$ Mev). Post-irradiation examination showed no reaction between the two materials. Dimensionally, the BeO expanded about 0.5%, and the graphite contracted about 1.3% in the parallel direction and 0.8% in the perpendicular direction.

New data on the effects of irradiation at very high temperatures on graphite and carbons were obtained at Battelle–Northwest.[4] The research was performed to provide information for predicting behavior in the Ultra-High Temperature Reactor Experiment (UHTREX). The materials irradiated are described in Table II-1. Included as a reference material was CSF. Grade B260 was a substitute for the insulating carbon (not available at the experimental time) to be used in the UHTREX. All samples were heat-treated

prior to irradiation since, at the irradiation temperatures, the temperature alone may cause significant changes, particularly for carbon.

The results of heat-treatment are summarized in Table II-2.

Irradiations were conducted at Battelle–Northwest[4] to maximum exposures of 7×10^{20} neutrons/cm^2 ($E > 0.18$ Mev) at sample temperatures between 900 and 1800°C. The results are presented in Fig. II-2. At irradiation temperatures of 1000 and 1800°C, CGL graphite behaved about the same as CSF, and the length changes were less than −0.06% in both orientations at the maximum exposures. The CGL is an isotropic material, having a preirradiation CTE ratio of 1.02. At 1300 to 1400°C the amount of CGL contraction increased sharply to about 1%. This increase in contraction over that for CSF was attributed to the impregnation treatment that CGL received. In all cases the carbons contracted more than the CGL, and the more dense impregnated carbon, CGM, contracted most. (M. C. Brockway)

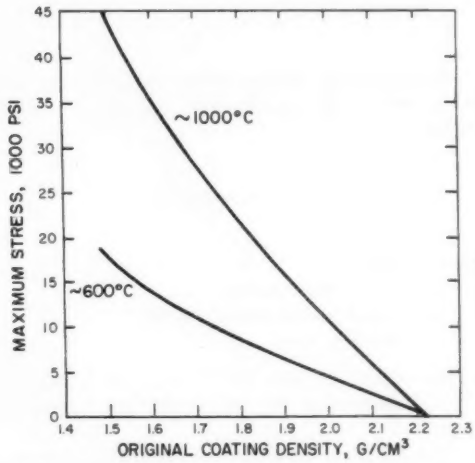

Fig. II-1 Maximum stress generated by neutron-induced shrinkage of carbon coatings onto an unyielding support as a function of density of the carbon.[2] The relation was calculated for irradiation at approximately 1000°C using densification constant $k_d = 2.8 \times 10^{-22}$ cm^2/neutron and creep constant $k_c = 1 \times 10^{-27}$ cm^2/(neutron) (psi) and at approximately 600°C using $k_d = 1.1 \times 10^{-22}$ cm^2/neutron and $k_c = 1 \times 10^{-27}$ cm^2/(neutron)(psi).

Beryllium Metal and Alloys

Physical Metallurgy

A comprehensive report on the mechanical behavior of beryllium as a structural material has been presented by Conrad and Perlmutter.[5] The mechanical characteristics of single-crystal and polycrystalline beryllium are reported and are compared with those of other close-packed-hexagonal materials. Possible means for improving low-temperature ductility are discussed. Texture in wrought beryllium and hot-shortness problems are considered. The effect of surface defects on mechanical properties is also covered.

Table II-1 GRAPHITE AND CARBON MATERIALS IRRADIATED AT BATTELLE–NORTHWEST[4]

Material designation	Block	Block size, in.	Remarks	Approximate service conditions in UHTREX: Maximum exposure, 10^{20} neutrons/cm^2 ($E > 0.18$ Mev)	Temperature °F	Temperature °C
CGL	CL-1	5⅛ dia. × 6	UHTREX core graphite; graphitized petroleum coke, maximum particle size, 0.032 in.; coal-tar-pitch binder; molded; baked at 800°C; impregnated; graphitized at 2800°C; very isotropic ($CTE_\perp/CTE_\parallel \cong 1.05$ up to 1600°C); density, 1.76 g/cm^3	5	2000 to 3000	1090 to 1650
CGM	CM-2	5⅛ dia. × 6	High-density reflector carbon; petroleum-coke filler, maximum particle size, 0.065 in.; coal-tar-pitch binder; molded; baked at 800°C; impregnated; rebaked at 900°C; very isotropic ($CTE_\perp/CTE_\parallel \cong 1.1$ up to 1600°C); density, 1.73 g/cm^3	2.5	1800 to 2000	980 to 1090
CGN	CN-2	5⅛ dia. × 6	Normal-density support-column carbon; same as CGM except not impregnated or rebaked; very isotropic ($CTE_\perp/CTE_\parallel \cong 1.1$ up to 1600°C); density, 1.61 g/cm^3	2	1300 to 2000	900 to 1090
B260	PC	5 dia. × 12	Insulating carbon; density, 0.59 g/cm^3	0.2*	550 to 1800*	290 to 980*
CSF	222	4 × 4 × 50	Reactor grade; Cleves petroleum coke, conventional type; standard coal-tar-pitch binder; extruded; F purified; graphitized at 2800°C; anisotropic ($CTE_\perp/CTE_\parallel \cong 2.4$ at 400°C); density, 1.66 g/cm^3			

*Conditions for insulating carbon used.

Table II-2 EFFECTS OF HEAT-TREATMENT ON DIMENSIONS OF IRRADIATED GRAPHITE AND CARBON MATERIALS[4]

Material	Maximum temperature, °C	Weight change, %	Length change, %
CGL	1700	−0.09 ± 0.02	+0.01 ± 0.005
CGM	1700	−1.54 ± 0.10	+0.07 ± 0.05
CGN	1700	−0.93 ± 0.18	+0.09 ± 0.02
PC	1300	−7.39 ± 0.33	−1.69 ± 0.51
CSF		−0.006 ± 0.002	−0.002 ± 0.001

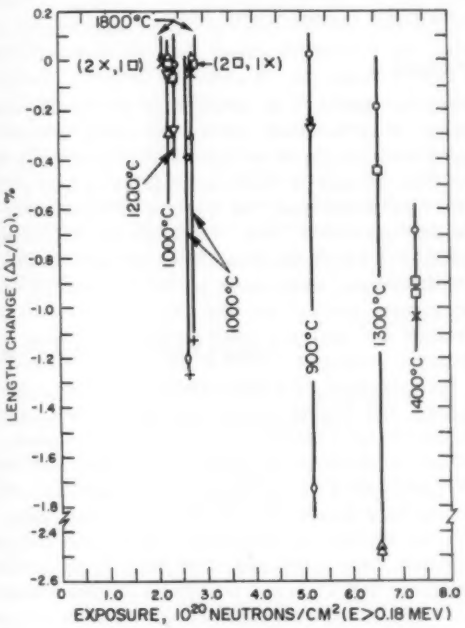

Fig. II-2 Physical distortion of UHTREX materials as a function of exposure.[4] ○, *CSF* ⊥; ●, *CSF* ∥; □, *CGL* ⊥; ×, *CGL* ∥; △, *CGM* ⊥; +, *CGM* ∥; ▽, *CGN* ⊥; ◁, *CGN* ∥; ▷, *PC* ⊥; ◇, *PC* ∥.

The mechanical behavior of single crystals is discussed in terms of dislocation theories. On this basis the behavior of beryllium was found to be similar to that of other close-packed-hexagonal metals. For example, the slip behavior and strain hardening during slip are much the same. Much is known about the effect of substitutional elements but nothing about the effect of interstitials.

The low ductility of polycrystalline beryllium is apparently due to easy cleavage and a few deformation modes. Generally, properties increase with decreasing grain size according to the Hall–Petch relation. It is believed that the effect of purity on ductility of polycrystalline beryllium has not been well established. Several methods are proposed for improving the ductility of beryllium. For example, decreasing the grain size of wrought materials, increasing purity, and alloying with elements such as copper would be expected to improve ductility. Also, modifying texture by controlling the fabrication history should contribute to increased ductility.

The relation of hot shortness in beryllium with respect to the forging problem is discussed briefly. The iron–aluminum reaction in beryllium and its relation to hot shortness is described in some detail. Mention is made of a possible connection between impurities and the forgeability of beryllium. A theory is advanced for a possible mechanism to explain the loss of grain-boundary cohesion resulting from aluminum–beryllium eutectic formation.

Splat cooling was employed by Nuclear Metals to produce fine-grain high-purity beryllium with a minimum of texturing.[6] By means of this technique, fine-grain materials of SSR-grade purity were produced. Splats of beryllium, beryllium–0.15 wt.% iron, beryllium–1 wt.% nickel, and beryllium–4 wt.% copper were consolidated and then remachined and consolidated to eliminate layering. Cracking was pronounced in the iron alloy in the as-hot-pressed condition.

Tensile and bend tests were performed on flats that were extruded from the various alloys. In all cases, ductility was low and the strength was very high, especially for materials of these purities. Post-fabrication heat-treatments decreased tensile properties for all alloys and increased the elongation in the unalloyed beryllium and the beryllium–nickel alloy. Grain size was stable even after annealing 1 hr at 1100°C, which was surprising for an alloy of this purity. Highest strengths were obtained with the iron and copper alloys, but these were very brittle even after thermal treatments.

The authors suggested that the high thermal stability and strength and the low ductilities were associated with one or more of the following:

1. Unique distribution of dispersed phases because of splatting
2. A high degree of cold work due to chip machining and low-temperature processing
3. An atypical extrusion texture that inhibited ductility in both testing directions

The British[7] determined the angular relations between the crystallographic faces of grain-boundary holes which were formed at elevated temperature during low-strain-rate testing of irradiated beryllium. The angles of these faces were determined by measuring electron micrographs using stereoscopic techniques. The results indicate that the orientation of the holes (and the adjacent matrix) can be determined to better than 5°. The holes were practically equiaxed. This method is suggested as a possible means for measuring grain-boundary orientations and relative surface-energy relations after suitable treatment to induce cavitation. However, the material must have low-temperature fracture characteristics suitable for revealing the grain-boundary holes.

Fabrication

Investigators at Franklin Institute have recently reported on the effect of prior history on properties of beryllium.[8] High-purity (SR-grade) powder was used to produce sheet by compression rolling, upset forging of powder, and upset forging of hot-pressed block. Bend properties and preferred orientation were determined after various thermal treatments. The overall properties were compared with commercial powder-metallurgy sheet.

In compression-rolled sheets the material having the lowest reduction appears to have the highest bend ductility. In the hot-upset sheet, bend ductility tended to increase with increased reduction. Hot-forged block showed the best bend properties in the study. This suggested to the authors that the upsetting caused a banding together of the particles which would cause some basal-plane disorientation.

Bend properties of commercial sheet were approximately the same as those of the compression-rolled SR beryllium. Since the reduction ratios are approximately the same, it appears that there might be no effect of purity on the properties in this range. However, it was noted that lack of an optimized fabrication schedule for the high-purity sheet might contribute to this occurrence.

Texturing was greatest in the compression-rolled sheets and least in the forged material. However, no significant difference was noted in the bend ductility of the two materials. From this, it was concluded that preferred orientation alone is not the key factor in determining bend ductility.

A joint report was issued by Union Carbide Corporation and Dow Chemical Co. concerning the processing of ingot-source beryllium.[9] (Ingot beryllium is defined as metal prepared from cast ingots by conventional metalworking procedure.) The Union Carbide portion of the report describes techniques for casting, rolling, forming, and joining of ingot beryllium and the preparation of beryllium honeycomb.

Thermally reduced beryllium in the form of scrap from hot-pressed block is vacuum cast into ingots. The machined ingots are canned in mild steel and hot rolled to sheet measuring 0.300 to 0.025 in. thick. Forming of bare ingot sheet is accomplished at 400 to 750°C. The thin (0.025 in.) sheet is formed in a rubber pack.

Ingot sheet is also rolled to 2.5-mil-thick foil for the manufacture of honeycomb. Strips of foil can be corrugated and welded to make the honeycomb core. Brazing and epoxy bonding are used to join the honeycomb foils.

Similar techniques are employed at Rocky Flats for sheet production. Castings up to 100 lb which are suitable for sheet production are produced from scrap powder-metallurgy material. Sheets up to 28 by 48 in. are rolled from these large castings. A process is described for the production of wrought beryllium shapes from ingot sheet. Both conventional deep drawing and marforming are used.

Special techniques employed during the extrusion of beryllium were reviewed in a paper by Siergiej.[10] It was shown that extrusions of long lengths could be produced in many complex shapes. A limitation of the process is that the cross section of the shape must have such width and wall-thickness dimensions as to enable it to be circumscribed by a circle having an area 12 to 40 times the area of the shape. Also, a practical die design is required that will allow flow of the metal without breakthrough.

Analysis

Nuclear Metals[11] is attempting to develop techniques for determining carbon and nitrogen levels in high-purity beryllium of sufficient simplicity so that they can be used in various facilities without elaborate equipment. Also, an attempt is being made to prepare standards that would allow the various facilities to verify the capabilities of the technique.

Modifications were made in the combustion–conductometric method so that the amount of carbon released for analysis could be increased. The best technique employed consisted in burning the sample in the presence of copper rings that were used as coupling and fluxing agents. By this method, carbon contents on the order of 25 ppm were determined.

Reliable methods of analyzing for nitrogen were developed using a modified micro-Kjeldahl still. Results were consistent even in the 10-ppm range.

Three batches of beryllium carbon and nitrogen standards were prepared. The first, from distilled beryllium, had 25 ppm carbon and 11 ppm nitrogen. The other two were from SR-grade material and contained 101 and 120 ppm carbon and 55 and 56 ppm nitrogen, respectively.

Corrosion

Corrosion of beryllium in aqueous-salt environments was studied by Pronchko, Myers, and Saxer.[12] Rates for intermittent total-immersion testing at 15°C were: 0.8 mil/year in distilled water, 13.7 mils/year in 3% NaCl solution, and 33.4 mils/year in 3.5% NaCl. Continuous-immersion rates in natural seawater measured on both pickled and anodized beryllium were 6.4 mils/year and 0.3 mil/year, respectively. The anodized treatment afforded considerable protection in this environment.

In addition to the general attack experienced in the various environments, pitting was shown to be serious in the chloride-containing environments. Pits measuring nearly 8 mils deep were noted after 30 days in 3% salt solution. Anodizing appeared to impede pitting, but it was not effective in eliminating it.

Limited stress–corrosion studies were also performed in natural seawater. Time to failure for pickled specimens was 190 hr at 20,000 psi and 100 hr at 30,000 psi. The anodized specimens were

insensitive to the different stress levels since they both failed in approximately 360 hr. Failure was generally associated with the pitting attack. Pitting occurred continuously during the test, and the pits acted as stress concentrations that caused premature failure.

General

Proceedings of the 1963 Gatlinburg Conference on the Physical Metallurgy of Beryllium have been published recently.[13] This conference was sponsored by the AEC through Oak Ridge National Laboratory, with participants from the United States and the United Kingdom. Several reports in the general area of purification and its effect on properties of beryllium were presented. Also, some information is given on the properties of polycrystalline materials, especially ingot sheet. A review of structural applications in the United Kingdom is included. Much of the work in this publication has been supplemented by later conferences and publications, but it is of value to those interested in this field. (H. D. Hanes)

Beryllium Oxide

The utility of the diametral compression test to measure the strength of BeO has been demonstrated by General Electric researchers.[14] The use of this test to obtain tensile strengths of ceramics, principally MgO, has previously been developed and reported by Rudnick et al.* The present research clearly demonstrates the test applicability to BeO and determines effects of loading rate, specimen cushioning, and specimen length-to-diameter ratio on strength data.

The BeO test specimens were cut from centerless-ground 0.6-cm-diameter cylinders. Specimen length for most tests was 0.3 cm. When padding was used between the test cylinder and the loading tungsten carbide platens, it consisted of a business-machine card (0.017 cm thick). Most of the tests were made at a loading rate of 0.152 cm/min (0.060 in./min). The test results and comparison with modulus-of-rupture strength data are given in Table II-3 and Figs. II-3 to II-6. The conclusion from these test results is that the diametral compression test appears as useful in defining the strength behavior of BeO as does the modulus-of-rupture test, and perhaps it has some advantages in defining the strength dependence on porosity. The major significance of this conclusion is that the diametral compression

*A. Rudnick, A. R. Hunter, and F. C. Holden, An Analysis of the Diametral-Compression Test, *Materials, Research and Standards*, 3(4): 283 (1963).

Table II-3 STRENGTH OF BeO MATERIALS AS DETERMINED IN DIAMETRAL COMPRESSION TEST[14]

Specimen description				Modulus of rupture at room temperature					
				Diametral compression test†					
				Cushioned‡			Uncushioned§		
Composition	Grain size, μ	Density, g/cm³	Bending test,* 10^3 kg/cm²	No. of samples	Average strength, 10^3 kg/cm²	Standard deviation, 10^3 kg/cm²	No. of samples	Average strength, 10^3 kg/cm²	Standard deviation, 10^3 kg/cm²
AOX	8	2.88	2.12	21	2.40	0.43	11	2.16	0.23
	6	2.75	2.12	21	1.87	0.38	11	1.78	0.22
	5	2.56	2.04	45	1.74	0.18	31	1.42	0.15
	10	2.88	2.72	19	2.64	0.26	9	2.05	0.33
	9	2.76	2.32	21	2.16	0.36	11	1.78	0.23
	12	2.58	1.88	19	1.22	0.32	8	0.64	0.17
	16	2.88	2.54	19	2.29	0.34	9	1.53	0.38
	16	2.77	2.09	21	1.55	0.33	10	1.20	0.36
	22	2.57	1.50	20	1.15	0.10	8	0.77	0.08
	50	2.97	1.26	10	1.20	0.14	10	0.89	0.17
	38	2.76	1.54	9	1.25	0.16	9	0.98	0.07
	37	2.65	1.24	11	0.92	0.11	11	0.74	0.14
	74	2.86	1.07	8	0.93	0.04	8	0.76	0.04
	66	2.74	1.00	11	0.87	0.07	11	0.74	0.11
	100	2.94	1.00	10	0.86	0.06	9	0.64	0.06
UOX–MgO	4	2.92	2.16	10	2.52	0.37			
	4	2.77	2.25	10	1.86	0.26			
	4	2.46	2.23	10	1.39	0.05			
	10	2.91	2.40	10	2.22	0.44	9	1.93	0.17
	10	2.78	2.50	10	1.88	0.27			
	10	2.66	1.98	10	1.38	0.14			
	17	2.89	2.24	10	2.02	0.20			
	21	2.78	1.72	10	1.62	0.26	11	1.20	0.16
	15	2.59	1.87	10	1.18	0.17			
	42	2.86	1.69	16	1.37	0.13			
	57	2.76	1.22	10	1.00	0.08	10	0.48	0.13
	39	2.65	1.24	10	0.82	0.04			
	79	2.93	0.90	10	0.82	0.21			
	61	2.75	1.34	10	0.98	0.05	9	0.65	0.15
	93	2.96	1.14	10	1.15	0.10	8	0.94	0.10

*Standard bending modulus-of-rupture test using four-point bending over a 7.5-cm span at a loading rate of 0.15 cm/min.
†Specimens 0.6 cm in diameter by 0.3 cm long were loaded across the diameter at the rate of 0.15 cm/min until fracture.
‡Cushions were IBM cards placed on each platen of testing machine.
§Specimens were in direct contact with platens of the testing machine.

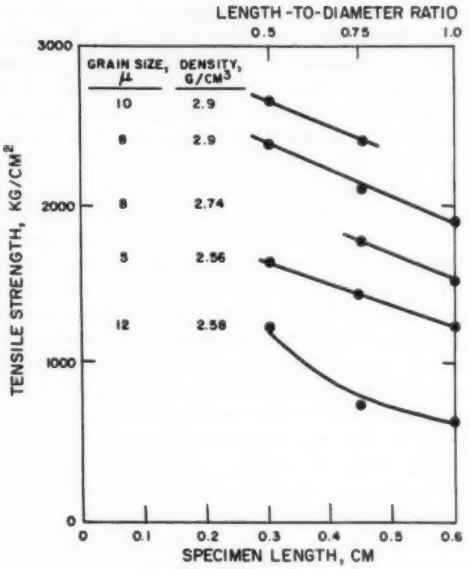

Fig. II-3 Effect of specimen length on the tensile strength of BeO as measured by diametral compression.[14]

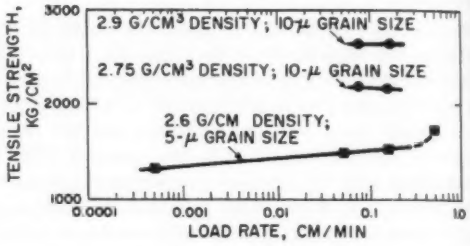

Fig. II-4 Effect of load rate on the tensile strength of BeO as measured by diametral compression.[14]

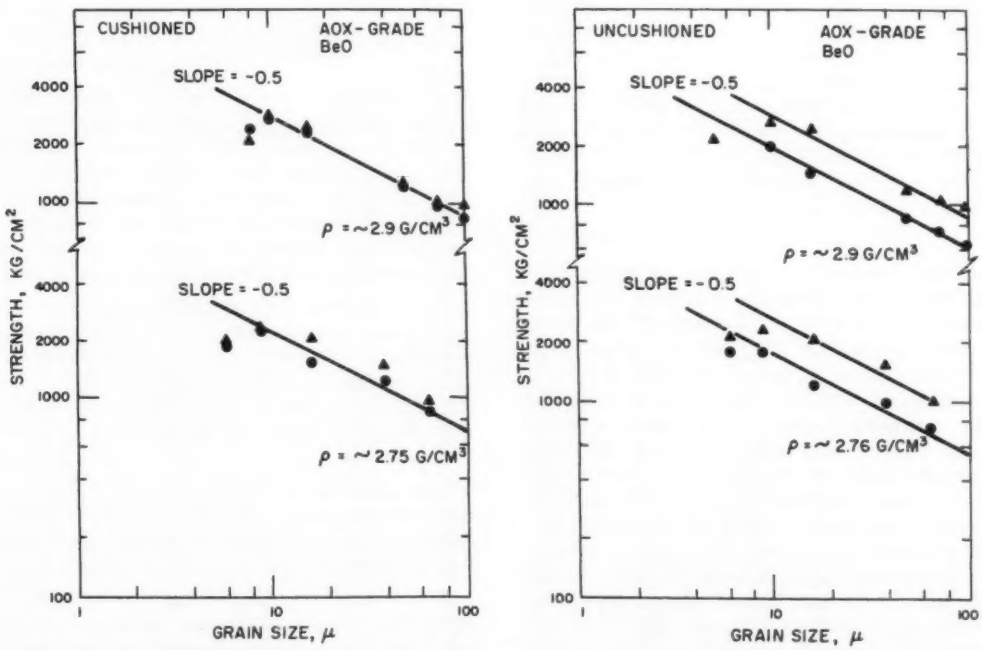

Fig. II-5 Comparison of the strength vs. grain-size relation in BeO as determined by diametral compression and by transverse bending.[14] ▲, transverse bending; ●, diametral compression.

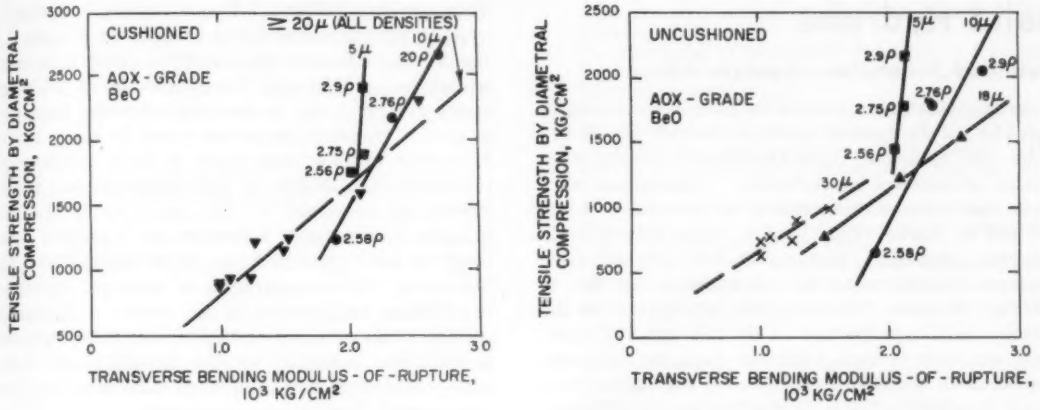

Fig. II-6 Comparison of the strength of BeO as measured by diametral compression and by transverse bending. Solid curves show the greater porosity dependence of the diametral compression test for fine-grain material.[14] ■, approximately 5-μ grain size; ●, approximately 10-μ grain size; ▲, approximately 18-μ grain size; ▼, greater than or equal to 20-μ grain size; ×, 30-μ grain size; ρ = density, g/cm³.

test may be used to test small samples and sample quantities often utilized in materials-irradiation programs.

General Electric investigators reported[14] additional information on the effect of additives on resistance to radiation-induced microcracking of BeO. Previous data indicated that 0.4 wt.% Al_2O_3 + 0.1 wt.% SiO_2 in BeO (Thermalox 995A fabricated by The Brush Beryllium Co.) and 1 wt.% bentonite in small-grain-size BeO improved resistance to microcracking. Three glass additives were investigated in this study; their compositions are given in Table II-4.

Table II-4 COMPOSITION OF GLASSES TO BE USED AS ADDITIVES* IN BeO (REF. 14)

Compound	Silica-glass composition, wt.%		
	High	Medium	Low
SiO_2	82	53	30
Al_2O_3	4	22	20
CaO		10	20
MgO		7	10
BeO		8	10
Na_2O	10		
ZrO_2	4		10

*Additives used in 1 wt.% concentration in UOX-grade BeO. Specimen density 92 to 95% of theoretical.

Only the low-silica glass appeared to have a significant influence on microcracking. It was most effective in BeO of 4-μ grain size but also improved a 17-μ material. At the highest dosage to which this material was exposed, 2.3×10^{20} neutrons/cm² (≥ 1 Mev) at 100°C, the volume changes were less than 1%, and changes in open porosity were not indicative of microcracking. The strength changes in the 4-μ material were the greatest observed by the researchers to date, ranging up to 170 to 180% of that for unirradiated material. The highest previous strength increases were approximately 50% in Thermalox 995A (0.4 wt.% Al_2O_3 + 0.1 wt.% SiO_2 in BeO). Assuming that the strength change at higher exposures would follow the same general curve as other compositions, it was predicted that the fine-grain-size, low-silicon-glass BeO material would probably withstand 3 to 4 × 10^{20} neutrons/cm² before the strength decreased to a value less than that of the unirradiated material.

British investigators have studied the grain-growth inhibition and resulting properties of SiC additions to BeO (Ref. 15). In order to achieve densification in the BeO–SiC materials, a third constituent was added — MgO in the amount of ½ to 1 wt.% was found most successful. In such BeO–SiC–MgO systems, the use of submicron (0.1 to 0.5 μ) SiC permitted the achievement of densities greater than 97% of theoretical while retaining small (5 to 8 μ) grain size stable for long periods at high temperature.

Strengths in three-point bending of 35,000 to 67,000 psi, with a mean of 50,200 psi, were obtained on BeO–1 wt.% MgO–8 wt.% SiC fabricated by sintering and by hot pressing. Pronounced scatter in results was found in all groups of specimens.

Although the absolute values of bend strength of BeO–MgO–SiC bodies were higher at high density than those of BeO bodies, for equivalent grain size the mean modulus of rupture of SiC-containing bodies was only approximately 75% of the value for pure BeO. Several possible causes of the lower strength were considered: the presence of magnesia or silica, a plastic-flow effect during fracture propagation, and the presence of residual stresses due to thermal mismatch. On the basis of agreement between calculated and observed strengths, it was concluded that the thermal mismatch between the BeO and SiC grains was the most likely cause. (M. C. Brockway)

Solid Hydrides

Hydrided Zirconium–Uranium Alloys

Analytical studies have been made of the transient behavior of zirconium–uranium hydride SNAP-reactor fuel elements, under atmospheric reentry conditions, at Atomics International.[16] Calculations were made for fuel-element release between 200,000 and 400,000 ft. Aerodynamic heating, transpiration cooling, and chemical reactions of fuel with air were analyzed to determine the net surface heat flux to the fuel elements. The available information on the thermophysical properties of the fuel was evaluated. With the best of such available data, the minimum fuel-element ejection altitudes were estimated, from which complete ablation of the fuel can be achieved. The optimum release altitude to attain melting and ablation of the fuel elements was calculated to be around 300,000 ft. The probability of initial ablation was found to be greatest for a random tumbling motion of the fuel elements.

Hydrided Zircaloy

When zirconium alloys oxidize in hot water or steam, the hydrogen released is absorbed by the metal, often to an amount beyond the solubility limit of hydrogen at that temperature. This phenomenon in Zircaloy-2 was investigated by Westerman.[17] Samples coated with zirconium hydride were held isothermally and also were thermally cycled. The maximum temperatures employed were in the vicinity of 400°C. After the treatments, the hydrogen concentration in the bulk metal was determined. It was found that long-term isothermal holding of a zirconium hydride–alpha-phase Zircaloy-2 system at 400°C did not result in supercharging of the alpha phase with hydrogen beyond a terminal solubility characteristic of the material employed and the maximum temperature attained. Thermal cycling such a specimen did result in supercharging the bulk metal beyond the classical terminal solubility. Fast thermal cycling was found to result in less supercharging than slow thermal cycling. However, the degree of supercharging is likely to be highly dependent on heating rate, cooling rate, and sample geometry. In addition, thermal cycling cannot produce sufficient supercharging to explain the high hydrogen concentrations found in corrosion samples. Possibly the presence of an oxide film on the free surface may prevent hydride formation there and bring about higher hydrogen activity, with supercharging, within the bulk metal. This concept would be difficult to verify experimentally.

Strontium Hydride

The strontium–strontium hydride phase diagram has been studied by thermal analysis, chemical analysis of equilibrated phases, and X-ray diffraction by Peterson and Colburn.[18] The maximum solubility of SrH_2 in strontium metal was found to be 38 mole % at the peritectic temperature of 880°C. Strontium metal undergoes an allotropic transformation at 555°C and melts at 768°C, but, in samples containing hydrogen, a second transformation was found at about 240°C. Strontium hydride was found to have an allotropic transformation at 855°C. The phase diagram for the system is presented in Fig. II-7. As is true for calcium and barium, hydrogen has a greater solubility in solid strontium than in the liquid phase, and increasing the concentration of hydrogen increases the melting temperature of the metal. Also characteristic of the alkaline-earth hydrides is the extensive endothermic solubility of the hydride in the metal phase. Strontium fits in between barium and calcium with respect to all of these properties.

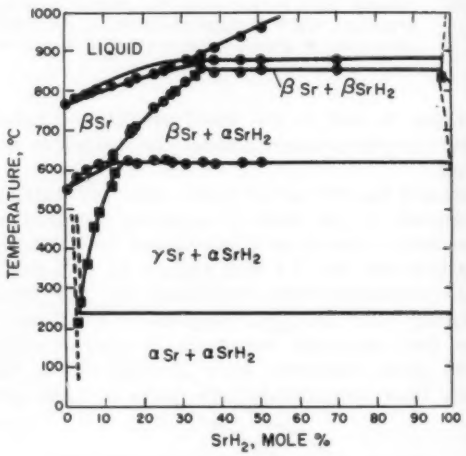

Fig. II-7 The strontium–strontium hydride phase system.[18] ●, thermal analysis; ■, isothermal equilibration.

Rare-Earth Hydrides

A literature review on the structure and properties of the rare-earth hydrides has been published by Bos and Gayer.[19] Cited are 118 references, and the review includes an extensive discussion of the stoichiometry and bonding in these hydrides. In Table II-5 the dissociation pressures at 600 and 800°C are

Table II-5 DISSOCIATION PRESSURES OF SEVERAL RARE-EARTH HYDRIDES[19]

Hydride	Constants*		$P_{diss.}$, mm		ΔH,†
	A	B	600°C	800°C	kcal/mole H_2
LaH_{2-x}	10,850	10.64	0.0166	3.44	−49.6
CeH_{2-x}	10,760	10.63	0.0202	4.01	−49.2
PrH_{2-x}	10,870	10.53	0.0119	2.50	−49.7
NdH_{2-x}	11,030	10.48	0.0070	1.60	−50.5
SmH_{2-x}	11,700	11.4	0.010	3.8	−53.3
GdH_{2-x}	10,250	9.72	0.011	1.56	−46.9
ErH_{2-x}	11,900	11.0	0.0027	0.93	−54.2

*For equation $\log P$, mm $= -(A/T, °K) + B$.
†Heat of dissociation.

shown for several of the more common rare-earth hydrides. Calculated heats of dissociation are given also. The crystal structures and the lattice parameters of 14 rare-earth hydrides are given in Table II-6. (H. H. Krause)

Table II-6 CRYSTAL STRUCTURES AND LATTICE PARAMETERS* OF RARE-EARTH DI- AND TRIHYDRIDES[18]

Metal	Dihydride		Trihydride	
	Structure	Parameters, A	Structure	Parameters, A
La	Fcc	$a = 5.663$	Fcc	$a = 5.604$
Ce	Fcc	$a = 5.575$	Fcc	$a = 5.539$
Pr	Fcc	$a = 5.518$	Fcc	$a = 5.483$
Nd	Fcc	$a = 5.464$	Fcc	$a = 5.435$
Sm	Fcc	$a = 5.374$	Hcp	$a = 3.782$ $c = 6.779$
Eu	Orthorhombic	$a = 6.21$ $b = 3.77$ $c = 7.16$		
Gd	Fcc	$a = 5.303$	Hcp	$a = 3.73$ $c = 6.71$
Tb	Fcc	$a = 5.246$	Hcp	$a = 3.700$ $c = 6.658$
Dy	Fcc	$a = 5.201$	Hcp	$a = 3.671$ $c = 6.615$
Ho	Fcc	$a = 3.642$	Hcp	$a = 3.642$ $c = 6.560$
Er	Fcc	$a = 5.123$	Hcp	$a = 3.621$ $c = 6.526$
Tm	Fcc	$a = 5.090$	Hcp	$a = 3.599$ $c = 6.489$
Yb	Orthorhombic	$a = 5.871$ $b = 3.561$ $c = 6.763$	Fcc	$a = 5.191$
Lu	Fcc	$a = 5.033$	Hcp	$a = 3.558$ $c = 6.443$

*Except for Eu ($EuD_{1.98}$) and Yb ($YbD_{1.98}$), the parameters are given for the stoichiometric dihydrides. The parameters given for the trihydrides are for compositions above $MH_{2.0}$ with the exception of ytterbium; the highest composition for which data are available is $YbH_{2.55}$.

References

1. J. H. Cox and E. M. Woodruff, Irradiation-Induced Contraction of Graphites at High Temperature Following Cold Preirradiation and Intermittent Thermal Anneals, USAEC Report BNWL-215, Battelle Memorial Institute, Pacific Northwest Laboratory, January 1966.
2. J. C. Bokros and A. S. Schwartz, Irradiation-Induced Densification of Pyrolytic Carbon Coatings, USAEC Report GA-7146, General Atomic Division, General Dynamics Corp., May 27, 1966 (to be published in *Trans. Met. Soc. AIME*).
3. General Atomic Division, General Dynamics Corp., HTGR Base Program Quarterly Progress Report for Period Ending May 31, 1966, USAEC Report GACD-7181.
4. J. W. Helm, Effect of Neutron Irradiation on UHTREX Graphite and Carbon, USAEC Report BNWL-191, Battelle Memorial Institute, Pacific Northwest Laboratory, February 1966.
5. H. Conrad and I. Perlmutter, Beryllium as a Technological Material, Report AFML-TR-65-310, Franklin Institute, August 1965.
6. W. C. Muller, A. K. Wolff, and A. R. Kaufmann, Study of Methods to Control Grain Size, Purity, and Texture in Beryllium and Beryllium Alloys, Report NMI-8001.6, Nuclear Metals Division of Textron Inc., Mar. 1, 1966.
7. R. M. Haines, Application of Stereo Metallography to Determination of Crystal Orientation, British Report TRG-Report-1161, Dec. 16, 1965.
8. D. B. Hoover, V. V. Damiano, and M. Herman, Effects of Thermo-Mechanical Variables on the Texture and Bend Ductility of High-Purity Beryllium Sheet, Report AFML-TR-65-309(Vol. I), Franklin Institute, August 1965.
9. J. L. Frankeny, V. C. Hemperly, W. J. Hulsey, R. J. Ludwig, and W. J. Yaggi, Fabrication of Wrought Beryllium, Parts I and II, USAEC Report TID-22797, Union Carbide Corporation, Nuclear Division, and Dow Chemical Co., Rocky Flats Division, Apr. 22, 1966.
10. J. M. Siergiej, *Extrusion of Beryllium Structural Shapes*, American Society for Testing and Materials, Special Technical Publication No. 379, pp. 106-118, 1965.
11. L. R. Aronin, F. A. Bauman, and A. K. Wolff, Preparation of Standard Samples and Development of Analytical Techniques for Carbon and Nitrogen in High-Purity Beryllium, Report AFML-TR-65-195 (AD-626987), Nuclear Metals Division of Textron Inc., October 1965.
12. R. J. Pronchko, J. R. Myers, and R. K. Saxer, Corrosion of Beryllium Sheet Material by Chloride-Containing Aqueous Environments, paper presented at the 21st Annual NACE Conference, March 15–19, 1965.
13. Conference on the Physical Metallurgy of Beryllium Held at Gatlinburg, Tennessee, April 30–May 1, 1963, USAEC Report CONF-170.
14. General Electric Company, Nuclear Materials and Propulsion Operation, High-Temperature Materials Program Progress Report No. 58, Part A, USAEC Report GEMP-58A, Apr. 29, 1966.
15. N. A. Hill, J. S. O'Neill, and D. T. Livey, An Investigation of the Properties of Beryllia Containing Up to 15 Wt.% Silicon Carbide and Up to 2 Wt.% Magnesia, British Report AERE-R-5056, January 1966 (to be published in *Trans. Brit. Ceram. Soc.*).
16. A. W. Barsell, L. D. Montgomery, and J. E. Arnold, Thermal Behavior of SNAP Reactor Fuel Elements During Atmospheric Reentry, USAEC Report NAA-SR-11502, Atomics International, Mar. 25, 1966.
17. R. Westerman, Charging Zircaloy-2 with Hydrogen Beyond the Solubility Limit, *J. Nucl. Mater.*, 18(1): 31-38 (January 1966).
18. D. T. Peterson and R. P. Colburn, The Strontium-Strontium Hydride Phase System, *J. Phys. Chem.*, 70(2): 468-471 (February 1966).
19. W. G. Bos and K. H. Gayer, The Rare Earth Hydrides, *J. Nucl. Mater.*, 18(1): 1-30 (January 1966).

Section

III

Reactor Materials

Nuclear Poisons

Metallic Poison Materials

Investigators at Knolls Atomic Power Laboratory found that residual stresses resulting from welding of hafnium can be relieved by an anneal of 3 hr in the 1200 to 1475°F (649 to 802°C) range.[1] The degree of annealing required for stresses in the transverse direction was found to be more than that required for stresses in the longitudinal direction.

The phase diagram for hafnium–tantalum was studied[2] by dilatometric, thermal, microscopic, and X-ray analysis. The transformation temperature of hafnium is reduced to 1020°C, and at that temperature there is monotectic equilibrium. The tantalum content is 17 wt.% at the monotectoid point. Maximum solubility of hafnium in tantalum is 6 wt.% at 900°C and 33 wt.% at 1500°C. In hafnium containing 10 to 20 wt.% tantalum, a metastable omega phase is formed on quenching.

Phase diagrams for silver–europium, cadmium–europium, indium–europium, and cadmium–strontium, developed at the Max Planck Institute,[3] are shown in Figs. III-1 to III-4. (M. Kangilaski)

Dispersion and Nonmetallic Poison Materials

Boron and Boron Compounds

Two burnable-poison fuel-element designs utilizing boron were tested in the Vallecitos Boiling Water Reactor[4] for over 3930 hr at a peak heat flux of 132 watts/cm^2 [418,000 Btu/(hr)(sq ft)] to an average burnup of 8.21×10^{19} fissions/cm^3 (3000 Mwd/ton). The boron was incorporated into test-fuel rods as a 500- and 750-ppm natural-boron addition to the type 304 stainless-steel cladding tubes and as a direct

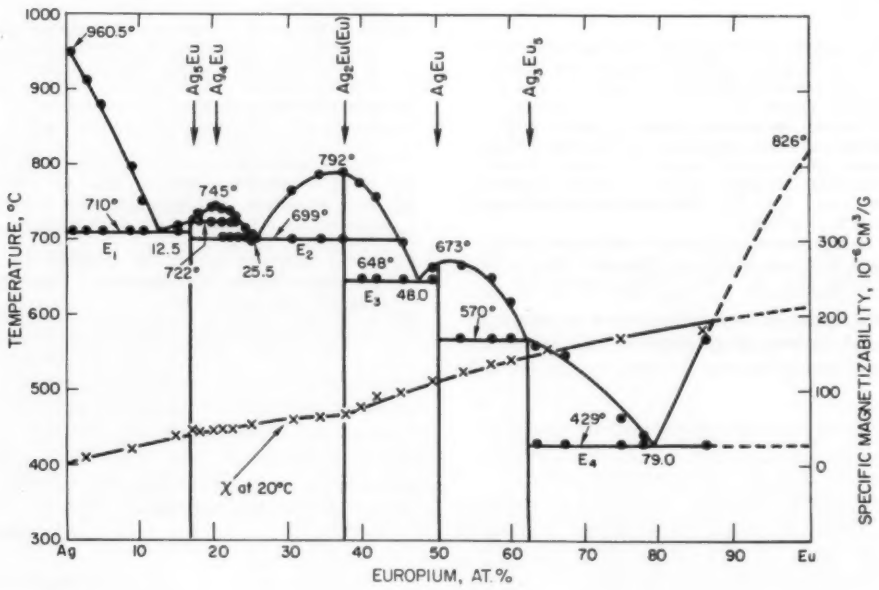

Fig. III-1 Phase diagram of silver–europium.[3]

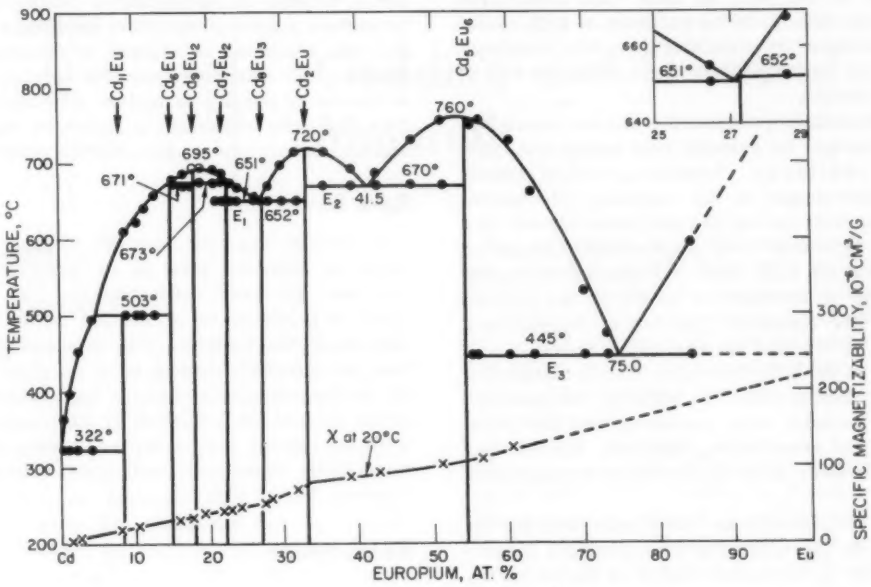

Fig. III-2 Phase diagram of cadmium–europium.[3]

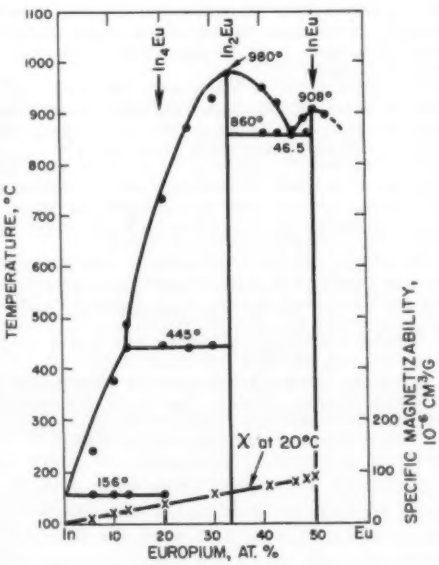

Fig. III-3 Phase diagram of indium–europium.[3]

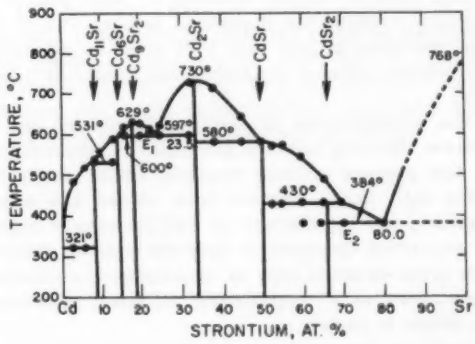

Fig. III-4 Phase diagram of cadmium–strontium.[3]

addition to the UO_2 fuel matrix in two forms. Poison was added to the fuel, as both −325-mesh ZrB_2 particles and 100- to 200-μ particles of ZrB_2 coated with molybdenum, by premixing the poison compound with the UO_2 and vibratory compacting to 85% of theoretical density.

The postirradiation examination showed no outside-diameter changes on selected rods having both types of boron additions. Room-temperature tensile strengths determined on the originally cold-worked cladding material having 750 ppm boron showed 34.2 and 28.3% increases over preirradiation measured strengths for the 0.2% yield and ultimate strengths, respectively. A decrease of 16.4% in the uniform elongation was measured. The boron depletion was 39% of the ^{10}B, or 8% of the total natural boron.

Analyses of the ZrB_2-containing rods indicated that boron migration occurred in both the molybdenum-coated and uncoated ZrB_2-containing UO_2 fuel rods. Metallographic examination, however, showed less migration in some areas of the molybdenum-coated ZrB_2 fuel.

Workers at Eagle-Picher[5] have been studying the conversion of ^{10}B, which has been produced in electrolytic cells, to crystalline boron of higher purity. In this study the amorphous boron powder was isostatically pressed in preparation for the two preferred methods of purification: sintering and float-zone refining. Sintering of the compacts, preferably in argon or vacuum at 1700 to 1800°C, reduced the impurities from the range of 35,000 to 39,000 ppm to about 20,000 ppm.

Float-zone refining was found to be the preferred method of purification. In this process the compact was first heat-treated at 800°C in vacuum. One zoning pass in argon, followed by three passes in vacuum, reduced the impurities in over 70% of the bar specimen to less than 5000 ppm. An additional two passes reduced the impurities to less than 1000 ppm.

The incorporation of B_4C in graphite for use as neutron shielding has been patented by Carborundum.[6] In this process crushed graphitic solids, finely divided B_4C, and a carbonaceous binder are mixed together, and the mixture is cold pressed in a mold at pressures designed to give the desired density. The green-pressed body is then baked in a reducing atmosphere at a temperature sufficient to convert the binder to carbon.

A Japanese patent has been granted to Hitachi Ltd.[7] for a method of fabricating a control rod. In this procedure a plate prepared by pressing a mixture of B_4C and aluminum is wrapped in aluminum foil and placed in an aluminum case. The opening of the case is closed by pouring in molten aluminum. The plate thus clad with aluminum is rolled for final shaping and for bonding of plate and cladding material.

Rare Earths

A neutron-absorber element containing 37 wt.% Eu_2O_3 in stainless steel as the absorbing material has been examined nondestructively at Oak Ridge[8] after 10.1 Mw-years of service in the Stationary Medium Power Reactor. This examination indicates that the absorber element is in excellent condition. No visible evidence of damage was apparent, gamma scans showed no indication of abnormalities in the absorber burnup distribution, and outer dimensions were found to be still well within fabrication tolerances. (D. E. Lozier)

References

1. P. T. Lovejoy and F. E. Baldwin, The Stress-Relaxation Behavior of 85-15 Hafnium Between 700 and 1700°F, USAEC Report KAPL-3120, Knolls Atomic Power Laboratory, November 1965.
2. V. N. Svechnikov, A. K. Shurin, and G. P. Dmitrieva, Phase Equilibrium Diagram of the Hf-Ta System in the Solid State, *Sb. Nauch. Tr. Inst. Metallofiz., Akad. Nauk Ukr. SSR*, 19: 206-211 (1964).
3. W. Koester and J. Meixner, The Constitution of the Systems of Europium with Silver, Cadmium, and Indium and the System Cadmium-Strontium, *Z. Metallk.*, 56: 695-703 (October 1965).
4. S. Y. Ogawa and H. E. Williamson, The Performance of Fuel Rods Containing Boron Burnable Poison, USAEC Report GEAP-4918, General Electric Company, Atomic Power Equipment Department, September 1965.
5. J. R. Musgrave, R. J. Starks, H. E. Erwin, P. E. Grayson, and L. E. Stone, Purification and Crystallization of Amorphous Boron Powder by Zone Refining; Prepurification of Boron Before Zoning, USAEC Report TID-22221, Eagle-Picher Co., February 1966.
6. D. G. Struges and G. L. Bartholomew, Neutron Shielding Using a Composition Comprising Graphite Boron Carbide and Carborized Residue, U. S. Patent No. 3,231,521, to Carborundum Co., Jan. 25, 1966.
7. T. Moxita, Fabrication of Control Rod, Japanese Patent No. 23451, Oct. 21, 1964.
8. A. E. Richt, Interim Postirradiation Examination of a Europium-Bearing Control Rod from the Stationary Medium Power Reactor, USAEC Report ORNL-TM-1407, Oak Ridge National Laboratory, March 1966.

Section IV

Reactor Materials

Cladding and Structural Materials

Corrosion

Zirconium Corrosion

Hydrogen permeation of oxide films on crystal-bar zirconium has been studied at North American Aviation, Inc.[1] The rate of permeation was found to be inversely proportional to film thickness (100 to 2500 A), exponentially related to the temperature (200 to 700°C), and related to hydrogen pressure (1 to 860 torrs) by the function $[bP/(1+bP)]$. The hydrogen permeation was postulated to occur by two diffusion processes: lattice interstitial diffusion via anion vacancies, which allow movement from interstice to interstice, and line defect diffusion along dislocation lines or grain boundaries.

The effect of electron-beam welding and annealing at 1450°F (788°C) on the 750°F (399°C) steam-corrosion behavior of Zircaloy-4 and nickel-free Zircaloy-2 has been studied at Bettis Atomic Power Laboratory.[2] Large-grained structures produced by these techniques corroded at essentially the same rates and absorbed about the same quantity of hydrogen as fine-grained structures. In other studies, it was demonstrated that silicon additions to Zircaloy-4 and nickel-free Zircaloy-2 produced the same beneficial effect of reducing hydrogen absorption during corrosion in 680°F (360°C) water as observed previously with Zircaloy-2 (Ref. 3).

The corrosion and hydrogen uptake of zirconium–2.5 niobium–0.5 copper alloy in water and steam at 600, 680, 750, and 950°F (316, 360, 399, and 510°C) have been investigated at Bettis.[4] When quenched from 1515°F (824°C) and subsequently aged at 932°F (500°C), the alloy corroded initially at a higher rate than Zircaloy-4 but, upon long-time exposure, exhibited thinner oxide films and lower hydrogen pickup values than Zircaloy-4.

The effect of welding and postwelding anneals on the aqueous corrosion behavior of zirconium–2.5 wt.% niobium alloys has been reported by German scientists.[5] It was found that the weld metal and heat-affected zone corroded more than the base metal in steam at 400°C. The reverse was true in 350°C water. Postwelding anneals at 585 or 700°C eliminated these differences and produced similar corrosion behavior in both the steam and water tests.

The in-reactor corrosion behavior of Zircaloy-2 and zirconium–3 wt.% niobium–1 wt.% tin has been studied in Germany.[6] Specimens were exposed 850 hr to 400°C steam at an integrated fast flux (> 1 Mev) of 3×10^{19} neutrons/cm^2. The corrosion behavior of both alloys was similar—weight gains and hydrogen pickup with irradiation were two to three times those without irradiation.

In-reactor corrosion studies of zirconium-base alloys are continuing at Battelle–Northwest.[7] Exposure of nickel-free Zircaloy-2, Zircaloy-4, and zirconium–3 wt.% niobium–1 wt.% tin alloy to 530°F (277°C) water containing about 1 ppm oxygen at neutron fluxes (>1 Mev) of up to 1×10^{14} neutrons/(cm^2)(sec) supported previous results that showed enhanced oxidation rates over those observed out-of-pile. The zirconium–3 wt.% niobium–1 wt.% tin alloy exhibited a low susceptibility toward flux-induced oxidation. Contrary to previous experience, these tests indicated no accelerated corrosion at out-of-flux positions 1 sec and 1 min downstream from the core. (W. E. Berry)

Stainless-Steel Corrosion

The beneficial effect of silicon additions on the oxidation resistance of stainless steels in steam has been shown in experiments conducted in France.[8] High-purity 18 chromium–10 nickel stainless steels exhibited the weight gains indicated below after 854-hr exposure to steam at 500°C and 45 kg/cm^2:

Silicon, wt.%	Weight gain, mg/dm^2
None added	196
1	93
4	65

An industrial grade 18 chromium–10 nickel alloy gained 130 mg/dm^2 under similar conditions. This relatively low weight gain was attributed to 0.51 wt.% silicon in this alloy.

The effect of molybdenum on the oxidation resistance of austenitic stainless steels in CO_2–CO–H_2O at 800 to 1000°C has been reported by the British.[9] Type 316L stainless steel exhibited higher weight gains and thicker oxides than did 20/25 or 20/30

alloys containing up to 3% molybdenum. However, it was found that the major portion of this gain occurred in the early stages of oxidation.

The effect of uranium and molybdenum additions on the corrosion behavior of type 430 stainless steel has been studied by the Canadians.[10] It was found that optimum additions of 0.25 to 0.5 wt.% uranium had a beneficial effect upon corrosion resistance in non-oxidizing H_2SO_4 and HCl solutions, in oxidizing $FeCl_3$ solution, and in crevice corrosion in oxygenated 3 wt.% NaCl solutions. The effects of molybdenum additions at the 1 to 2 wt.% level were similar to, but more beneficial than, those of uranium additions.

A detailed examination has been made at Battelle–Columbus[11] of one of the type 304 stainless-steel steam generators that had been in service for more than 5 years in the Shippingport Atomic Power Station. Widespread cracking was found in the tubes within the tube sheet. The cracks were intergranular in sensitized portions and transgranular in annealed portions of the tubes. The cracking was attributed to caustic stress corrosion that apparently occurred during the initial 150 hr of operation when the boiler water contained free caustic. (W. E. Berry)

Corrosion of Base Metals and Miscellaneous Alloys

The air oxidation of Hastelloy X has been studied at Aerojet-General Nucleonics.[12,13] Results of exposures of 5450 hr at 1750°F (954°C) and 4000 hr at 1850°F (1010°C) indicated that a low-cobalt (0.07 wt.%) alloy scaled at a higher rate, but behaved more consistently when thermally cycled from 1850°F (1010°C), than did a high-cobalt (1.9 wt.%) alloy. Oxidation rates for the low-cobalt alloy were 1×10^{-5} and 2.9×10^{-5} $(mg/cm^2)/sec$ for exposures at 1750°F (954°C) and 1850°F (1010°C), respectively. Oxide penetration at grain boundaries was greater in the high-cobalt alloy than in the low-cobalt alloy. Preliminary results from exposure of these alloys to air at 1900 and 2000°F (1038 and 1093°C) revealed trends similar to those obtained at the lower temperatures.

The corrosion behavior of Hastelloy N and Inconel 600 has been studied in static isothermal 52.9 mole % UCl_3–47.1 mole % KCl at Los Alamos Scientific Laboratory.[14] Maximum penetration rates were 2 mils after 84 days' exposure at 900°C. The corrosion appeared to be impeded by a metallic reaction layer on the specimen surface which was principally uranium and nickel.

The use of ammonia to reduce oxygen concentration in boiling-water reactors has been studied by Chalk River.[15] Out-of-reactor specimens of carbon steel, low-alloy steels, stainless steels, Monel 400, and Inconel 600 were exposed to the coolant of two-phase in-reactor loops that were operated neutral or with ammonia additions. It was found that ammonia in the coolant eliminated oxygen production from radiolysis of the coolant; thus mild steel could be used for circuit construction.

Crack growth rates of titanium alloys during low-cycle fatigue in air and 3.5% saltwater solution have been studied at the Naval Research Laboratory.[16] An increase in crack growth rate at all strain ranges was noted for titanium–7 aluminum–2 niobium–1 tantalum alloys in the saltwater environment. On the other hand, titanium–6 aluminum–4 vanadium alloys did not appear sensitive to the aqueous environment. Fractographic studies revealed that the increase in crack growth rate was accompanied by a change from the ductile mode of fatigue fracture to a brittle quasi-cleavage mode of fracture indicative of stress-corrosion cracking.

The mechanism of hot-salt stress-corrosion cracking of titanium alloys has been studied at Materials Research Laboratory, Inc.[17] It was concluded that cracking was not caused by a gas evolved from the salt but was the result either of a lowering of surface energy due to a creeping solid corrosion product or of hydrogen ions entering the metal during the course of the reaction. Electrochemical studies indicated that cracking occurred only at the cathode of an oxygen differential cell and that anodic polarization prevented cracking. (W. E. Berry)

Corrosion of Refractory Metals

UNCOATED METALS AND ALLOYS

The Bureau of Mines has published the results of an extensive investigation on the corrosion behavior of molybdenum, tungsten, and vanadium in numerous environments.[18] These metals were found to possess generally superior chemical and galvanic corrosion properties in many aqueous corrosive media at temperatures up to the boiling points. The corrosion resistance of vanadium was further improved by alloying with niobium, tantalum, and titanium. Tungsten was susceptible to a type of crevice corrosion in mercuric chloride solutions, but no other instances of crevice corrosion were encountered. With few exceptions, molybdenum, tungsten, and vanadium were not adversely affected when coupled with dissimilar metals in galvanic corrosion experiments. When exposed to aqueous ammonia spray at 60°C, all three metals were moderately attacked. They were resistant to spray environments of simulated seawater and ammonium dihydrogen phosphate.

Russian investigators determined the corrosion resistance of binary niobium alloys in boiling aqueous solutions of H_2SO_4, HCl, and H_3PO_4 (Ref. 19). The binary alloys investigated included: 5, 10, 15, and 25 at.% tantalum, titanium, zirconium, vanadium, and molybdenum. A number of alloys were also tested at 185°C and a pressure of 15 atm. The corrosion rate of the alloys in the HCl solutions increased with increasing acid strength (5 to 20% HCl). Tantalum and molybdenum additions lowered the corrosion rate of

niobium in HCl. The corrosion rate of the alloys increased sharply with increasing sulfuric acid content, with tantalum and molybdenum additions again lowering the corrosion rate of niobium. Corrosion behavior of the alloys in phosphoric acid was similar to that in the hydrochloric and sulfuric acids. The authors suggested that niobium alloys containing 15 to 25 at.% tantalum can be readily substituted for pure tantalum for use in corrosive acid media.

Kilpatrick and Lott studied the reaction of rhenium and tungsten with flowing steam at 1 atm of pressure.[20] When rhenium reacts with steam at 850 to 1700°C, the rate of evolution of hydrogen is constant with time, and the metal remains bright. Sublimation of Re_2O_7 was suggested as the rate-determining step. The mechanism of the reaction of tungsten with steam over the temperature range of 1000 to 1450°C is similar to that of molybdenum. The rate-determining step consists of the oxidation of WO_2(solid) to the volatile $WO_2(OH)_2$ and WO_3 and its polymers. Above 1450°C the tungsten reaction is complicated by the formation of a liquid phase on the surface of the metal.

Rocketdyne conducted a program to ascertain the feasibility of using the B-66 niobium alloy (niobium–5 molybdenum–5 vanadium–1 zirconium) and tantalum–10 tungsten alloy as regeneratively cooled nozzle materials in a hydrogen-fueled engine.[21] Tensile tests conducted on specimens in a hydrogen atmosphere indicated that the ductilities of B-66 and tantalum–10 tungsten were reduced at temperatures up to 800°F (427°C) and 400°F (204°C), respectively. Exposure of B-66 or tantalum–10 tungsten to hydrogen at room temperature resulted in continuous disintegration of the alloys under certain conditions. Completely clean or newly made surfaces were especially susceptible to this gross "fragmentation" phenomenon.

Tungsten alloys containing additions of refractory-oxide particles or metallic elements that form refractory oxides were found to have improved oxidation resistance in the 1600 to 3000°C temperature range.[22] (Oxidation resistance was evaluated by measuring the surface recession of resistance-heated, ¼-in.-diameter, powder-metallurgy-produced bars in an air flow up to 136 ft/sec). Alloys containing up to 10 vol.% Al_2O_3 exhibited the best oxidation resistance. The amount of surface recession was nearly an order of magnitude less than that for pure tungsten up to 2500°C. Tungsten alloys containing ThO_2 and MgO were not as effective in inhibiting oxidation because of a fluxing action between these oxides and tungsten oxides.

COATED REFRACTORY METALS

Lockheed has conducted a comprehensive study of the behavior of protective coatings in simulated aerospace environments.[23] Eight commercial or advanced pilot-scale coatings were examined: Pfaudler PFR-6, Chromizing Durak B, and Boeing Disil coatings on molybdenum alloy TZM; Pfaudler PFR-32, Vought IV, and TRW chromium–titanium–silicon coatings on niobium alloy Cb-752; the TRW chromium–titanium–silicon coating on niobium alloy B-66; and, the GT&E tin–aluminum coating on tantalum–10 tungsten alloy. These coating systems were evaluated as follows:

1. The maximum temperature (2400 to 3300°F) (1315 to 1815°C) for coating lifetimes of 30, 60, 120, and 240 min in air at 0.01-, 0.1-, 1.0-, 5-, 20-, and 50-torr pressure was determined (base-line data).
2. Tests were conducted in air flowing over the surface at Mach 3 velocity.
3. Structural changes caused by heating the coatings in high vacuum were investigated.
4. Temperature and pressure cycling studies were performed to determine the effects of various environments and multimission use on performance capabilities.
5. The ability to predict performance of heat-shield components was evaluated by conducting step-oxidation tests (termed "Kinetic Model Tests") according to calculated reentry profiles.
6. Defect-tolerance studies were conducted which included an assessment of the coatings' resistance to defect formation caused by mechanical strain, impact, and vibration.
7. The ability to repair defective coatings was examined.
8. Compatibility studies were performed between the different coating systems and also with various insulation materials.

The report also contains an informative discussion of the environments that coated refractory metals will encounter in various aerospace applications.

A short summary of Lockheed's findings is given below. Figure IV-1 is a comparison of the 4-hr random failure limits, base-line results, for the seven coating systems.

Coating performance in the 1- to 50-torr range was controlled by random defects for the silicide-base systems. Fine hairline fissures in these coatings became sites for local failures. The chromium–titanium–silicon coatings on the niobium alloys exhibited somewhat different behavior from the other silicide coatings. The chromium–titanium–silicon coatings were more tolerant to fissures, and performance was limited by coating-composition variations that caused localized melting at temperatures above 2600°F (1427°C). Performance of the tin–aluminum coating on tantalum in the 1- to 50-torr range was relatively insensitive to pressure variations at temperatures below 3000°F (1649°C), where rapid boiling of the liquid tin did not occur. Diffusion between the coating and substrate did occur at rapid rates at temperatures above 2800°F (1538°C) in the tin–aluminum system.

In the 0.01- to 1.0-torr range, all silicide coatings on the molybdenum and niobium alloys had essen-

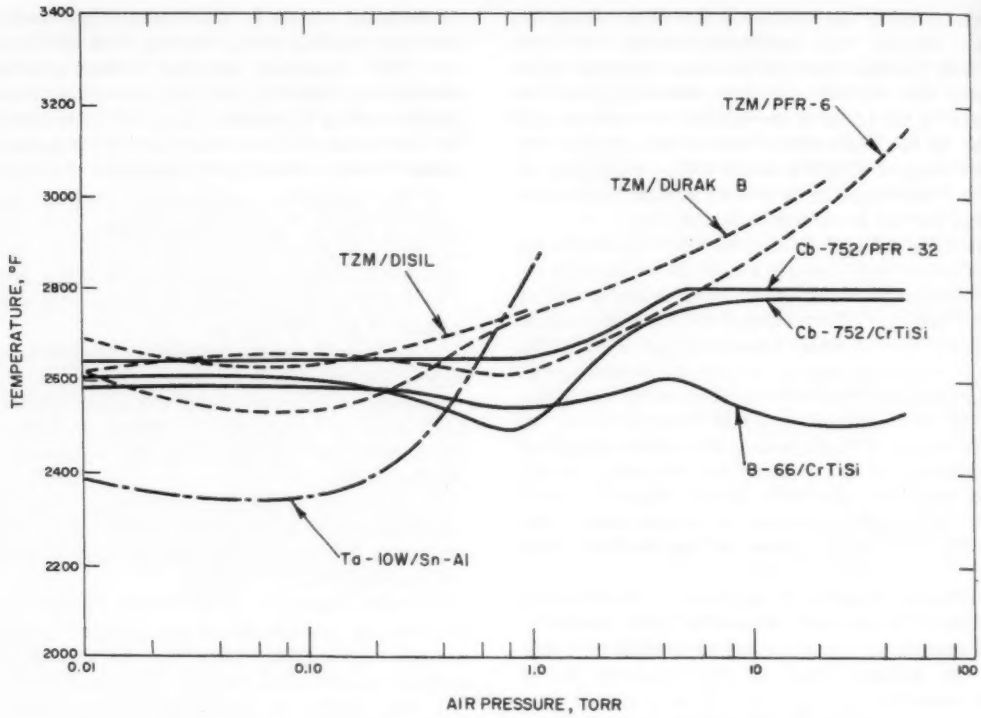

Fig. IV-1 Comparison of 4-hr random failure limits, base-line results, for six test metal-coating combinations.[23]

tially the same performance capabilities. The systems had a useful coating life of 4 hr at temperatures of 2550 to 2650°F (1399 to 1454°C) but exhibited random failure in less than 1 hr above 2650°F. The tin–aluminum coating on tantalum–10 tungsten alloy showed a marked decrease in performance at temperatures above 2200°F (1204°C) in this low-pressure range.

It was also noted that internal surfaces of reentry vehicles can be exposed to pressures below 1 torr during periods of peak heating. Structures could conceivably fail from the inside out.

Mach 3 air flow affected the performance of the coatings only when liquid or viscous conditions existed on the surface. For all coating systems with TZM as the substrate, no effect of flow was noted at temperatures below 2900°F (1593°C) and pressures of 5 to 20 torrs. The behavior of the silicide coatings on niobium was generally the same.

Silicide-base coatings on the molybdenum and niobium alloys can withstand 30-min to 1-hr preheating in vacuum at 2600 to 2800°F (1427 to 1538°C) with little change in base-line coating behavior. The tin–aluminum coating on tantalum–10 tungsten alloy poses the greatest problem with respect to vacuum exposure. Under vacuum of 10^{-5} torr, tin boils at 1600°F (871°C); at 10^{-7} torr it boils at 1325°F (718°C).

This experiment, designed to simulate the conditions characteristic of lifting reentry heat-shield panels, did not seriously degrade the protective properties of the majority of the coatings.

None of the coating systems were damaged by exposure to sinusoidal or random vibration at high intensity levels.

Most coating systems could be bent 10 to 30° at room temperature and still retain their high-temperature protectiveness. The tin–aluminum coating had the highest resistance to defect formation.

All coating systems presented compatibility problems with refractory oxides or other coating systems when liquid or semiliquid material was present. All silicide coatings reacted with Al_2O_3, ZrO_2, BeO, and SiO_2 at temperatures above 2600°F (1427°C).

The data obtained in the investigation were used successfully to make reasonable forecasts of performance capabilities and reliability under varying conditions of exposure.

Solar[24] and Vitro[25] are developing protective coatings for the tantalum alloy T-222 under the sponsorship of the National Aeronautics and Space Administration. The coatings are intended for use in protecting gas-turbine-engine nozzle vanes for a minimum of 600 hr at temperatures up to 2400°F (1315°C). Solar is examining high-pressure and

vacuum-pack cementation techniques for applying modified silicide coatings to T-222. Modifiers being investigated include combinations of titanium, tungsten, molybdenum, and vanadium. Electrophoretically deposited coatings are being applied at Vitro. In preliminary tests at Vitro, WSi_2- and $MoSi_2$-base coatings have protected T-222 for periods up to 600 hr at 1500°F (815°C) and 2400°F (1315°C).

Investigations of protective coatings for tantalum alloys for use at temperatures in excess of 3500°F (1927°C) are continuing at IITRI[26] and Solar.[27] Recent studies at IITRI have been concerned with the application of hafnium–20 to 25 tantalum alloys by cladding and slurry processes. Dense, 6- to 12-mil-thick slurry coatings were applied using a suspension of hafnium–tantalum–copper–aluminum elemental powders and sintering at about 2300°F (1260°C) in vacuum. Total copper–aluminum content in these coatings is about 4 wt.%. Coating lives in excess of 15 min have been obtained at 3500°F (1927°C) in oxygen–hydrogen torch tests. Unalloyed iridium coatings and iridium–rhodium coatings are being electrodeposited on tungsten in the studies being conducted at Solar. Tungsten is a potential diffusion barrier (to prevent liquation) between the tantalum substrate and the iridium coating. Tests of a 3-mil-thick unalloyed iridium coating on tungsten wire showed that the coating provided protection for 47 min in air at a corrected temperature of 4200°F (2316°C).

Metals and Controls, Inc., has concluded an evaluation of the use of platinum as a protective coating for niobium and molybdenum alloys.[28] The majority of this effort was directed toward the examination of potential diffusion barriers to stop the transfer of degrading substrate elements into the platinum coating. Barriers that were examined included tungsten, tungsten–25 at.% rhenium–30 at.% molybdenum alloy, rhenium, hafnium, iridium clad to tungsten, silicon carbide, zirconia, alumina, and magnesia. Test specimens consisting of these various barriers, ½ to 3 mils thick, sandwiched between niobium alloy FS-85 or molybdenum TZM and 3-mil-thick platinum were oxidation tested at 2550°F (1399°C) in air flowing at 240 in./min. The performance of these specimens was compared with that of specimens having 3- and 5-mil platinum coatings with no diffusion barriers. Many of the barrier-containing specimens had coating lives greater than 16 hr at 2550°F, which is characteristic of the 3-mil-platinum-coated specimens with no diffusion barriers. However, none of the barrier-containing systems exceeded the life of the 5-mil-platinum-coated specimens (50 to 66 hr).

The appendix of the Metals and Controls report contains a detailed analysis of the diffusion behavior of platinum–FS-85 and platinum–TZM couples and the difference in platinum-coating-failure mechanisms for solid-oxide- and gaseous-oxide-forming substrates.

(J. J. English)

Corrosion by Liquid Metals and Fused Salts

CORROSION BY SODIUM

In a continuing program at General Electric Company's Vallecitos Atomic Laboratory, it has been observed that corrosion of type 316 stainless-steel tabs in the hot legs of bimetallic sodium test loops at 1100 and 1200°F (593 and 649°C) is a "partially selective" process. This means that all metallic elements, mainly iron, chromium, nickel, manganese, and molybdenum, enter the sodium phase, but they do so in amounts different from those dictated by a given bulk-alloy composition. With the aid of electron microprobe observations of the changing concentration profiles just below the sodium-alloy interface, Brush[29] has worked out a kinetic interpretation of this partially selective corrosion process.

As pointed out in a previous review, researchers at Argonne National Laboratory found that the vanadium–20 wt.% chromium–10 wt.% aluminum alloy is attacked only about one-tenth as fast as the vanadium–20 wt.% titanium alloy by 650°C sodium containing around 30 ppm oxygen. Attempts to improve the vanadium–chromium–aluminum alloy still further by adding 1 wt.% zirconium or 0.5 wt.% yttrium were unsuccessful.[30] Reduction of the oxygen content of the flowing sodium (6.1 m/sec) to about 15 ppm resulted in a marked decrease in the rate of surface roughening of the vanadium–20 wt.% titanium alloy.

The Russians have conducted creep tests on hollow, chromium–stainless-steel specimens using air, static "liquid metal" (presumably sodium), and thermally convecting "liquid metal" in the specimen cavities.[31] Typical results are shown in Fig. IV-2, indicating that rupture life is reduced significantly under conditions conducive to mass transfer. The reductions are greatest at the lowest stresses (longest lifetimes), apparently because greater amounts of mass transfer can occur.

As part of a continuing program to evaluate materials for use in a Rankine-cycle power system with sodium as the working fluid, Brookhaven National Laboratory[32] ran 12 niobium-alloy capsules containing boiling–refluxing sodium at 1266°C for up to 8000 hr and 6 capsules at 1094°C for 10,000 hr. Variables were (1) materials (wt.%: niobium–1 zir-

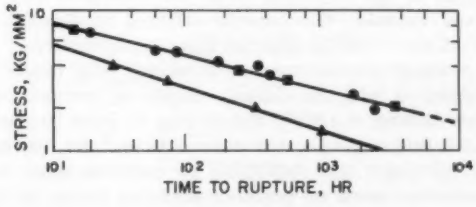

Fig. IV-2 Stress-rupture curves for chromium–stainless steel at 700°C using hollow specimens with various internal environments.[31] ●, air; ■, static liquid metal; ▲, flowing liquid metal.

conium, niobium–10 tungsten–10 tantalum, niobium–10 tungsten–1 zirconium–0.1 carbon, and niobium–5 tungsten–3 zirconium–0.1 carbon), (2) additives (calcium, magnesium, barium, yttrium, oxygen, or carbon), (3) weld contamination, and (4) use of postweld heat-treatment. No corrosion was found, except as follows:

1. One mil of transgranular and intergranular attack in niobium–1 wt.% zirconium capsule with 600 ppm added oxygen after 5000 hr
2. Twelve mils of intergranular attack in vapor region and 32 mils in seal-weld region of niobium–10 wt.% tungsten–10 wt.% tantalum capsule after 5000 hr with no additive
3. Intergranular attack to 4 mils at the liquid–vapor interface of the two 10,000-hr capsules welded with 800 ppm air added to the inert-gas welding atmosphere
4. Slight (1 mil deep) transgranular roughening at the liquid–vapor interface of the four 10,000-hr capsules welded in purified or bottled argon

The results of another series of capsule tests of refractory alloys are shown in Table IV-1. These capsules are exposed to refluxing sodium at 1315°C for 3000 hr.

Table IV-1 3000-HR TESTS OF REFRACTORY-ALLOY CAPSULES WITH 1315°C REFLUXING SODIUM[32]

Alloy	Composition, wt.%	Capsule form	Observations
FS-85	Nb–28 Ta–10 W–1 Zr	Seam-welded tubing	Surface microcracks
T-111	Ta–8 W–2 Hf	Seamless tubing	Slight pitting (<1 mil)
D-43	Nb–10 W–1 Zr–0.1 C	Seamless tubing	No detectable corrosion
X-34	Nb–5 W–3.5 Zr–0.1 C	Drilling rod	No detectable corrosion
TZM	Mo–0.5 Ti–0.06 Zr	Drilled rod	No detectable corrosion

In a similar refluxing capsule experiment with sodium boiling at 1230°C for 5000 hr, workers at Oak Ridge National Laboratory[33] found that oxygen was gettered by the niobium–1 wt.% zirconium capsule walls in a very nonuniform manner. Maximum pickups occurred at the very bottom of the capsule and in the first few inches above the liquid–vapor interface (1380 and 1200 ppm, respectively). Slight losses (20 to 30 ppm) occurred in the vapor zone at the top of the capsule. Nitrogen was gettered more or less uniformly (a 5- to 21-ppm increase over the length of the capsule). As in the analogous Brookhaven capsule, this capsule suffered no dissolutive attack that could be detected metallographically.

A small natural-convection boiling loop (made of niobium–1 wt.% zirconium), containing purified sodium boiling at 1095°C and flowing at about 10 g/min (1.5 lb/hr), was operated at Brookhaven[32] for 8007 hr. No corrosion was detectable by metallographic examination, even on polished surfaces where variations of 0.2 mil would be detectable.

Commercially Nicrobrazed joints, of a type permitting remote assembly, in ½-in. type 304 stainless-steel tubing were tested in contact with 1200°F (650°C) static sodium for 1380 hr under 44 psia pressure, with absolutely no evidence of corrosion or deterioration.[30] Such joints are promising for use in fuel-element closures, connections in a sodium loop, instrumentation connections, and other attachments in reactor components or experimental systems.

CORROSION BY POTASSIUM

It is generally agreed that refractory metals are ordinarily not susceptible to stress corrosion in the presence of alkali metals. At General Electric,[34] a program has been under way to see if there are any conditions (e.g., high stress, large creep) under which the corrosion of D-43 (or X-110) alloy (niobium–10 wt.% tungsten–1 wt.% zirconium–0.1 wt.% carbon) by potassium might be aggravated by stress. Two refluxing-potassium capsules were tested, one for 1000 hr at 2100°F (1150°C) and the other for 2000 hr at 2050°F (1120°C) to equivalent uniaxial creep strains of 7.5 and 5%, respectively. This was accomplished by thinning the capsule walls in the liquid and vapor regions so that measurable bulging would be produced by the vapor pressure of the potassium at the test temperatures. The results of metallographic, chemical, and microprobe analyses of capsule-wall specimens indicated no corrosion. This corroborates the excellent resistance of D-43 alloy to refluxing potassium and the absence of any stress corrosion, even under stresses high enough to produce substantial creep.

CORROSION BY LITHIUM

It has been established that nitrogen plays a key role in the corrosion of metals by lithium. Because titanium is an effective nitrogen getter in lithium, Argonne workers[30] made some exploratory studies of its behavior in 1200°C lithium in the hope of developing a corrosion-preventive technique. Table IV-2 shows the results, both with and without a silicon additive. The latter is a powerful oxidizing agent, is very soluble in lithium, and forms $MoSiO_2$—an effective oxidation barrier. It appears that the silicon does indeed influence the behavior of titanium in lithium, although its effects on the solubilities of nitrogen and oxygen in lithium and the nature of the layer on the molybdenum require further study.

In similar tests of the lithium–tantalum system, it was found that the addition of 0.4 at.% thorium to

the lithium resulted in a "greatly accelerated" attack of the tantalum at 1200°C.

CORROSION BY CESIUM

Short-term (on the order of 100 hr) tests have demonstrated that a number of potential construction materials for thermionic converter devices are resistant to attack by cesium up to 550°C. Hargreaves, Mayo, and Thomas[35] ran 10,000-hr capsule tests at 450 and 550°C on some of the more promising metals and metal–ceramic composites. They used austenitic stainless-steel capsules and sealed the test specimens and a small quantity of cesium inside under vacuum. Of the metals tested (titanium, niobium, tantalum, molybdenum, and copper), only niobium showed significant attack. This was in the form of a thin scale and a line of subsurface inclusions, neither of which was identified. The metallized alumina showed a wide variation in behavior—from no attack, through various degrees of tarnish, cracking, and corrosion, to complete disintegration. The damage was not related directly to overall purity, although high-density, nonporous, high-purity alumina was compatible with cesium. Also compatible were molybdenum-based metallizing compositions, copper braze, and nickel–iron–cobalt alloy used for metal–ceramic seal assemblies.

CORROSION BY MERCURY

Table IV-3 summarizes the results of thermal-convection boiling-mercury loop tests run at Brookhaven over the past several years. Salient observations from these tests and supporting studies are:

1. Unalloyed tantalum seems to be completely inert to mercury under the test conditions.
2. Niobium–1 wt.% zirconium is susceptible to stress-corrosion cracking in the presence of mercury.
3. Iron is leached from 2¼ wt.% chromium–1 wt.% molybdenum steel by hot mercury in a boiling loop and deposited in cold zones, leaving intergranular pits. These actions are effectively inhibited by a small addition of titanium to the mercury.

Table IV-2 EFFECT OF 1200°C LITHIUM ON TITANIUM IN MOLYBDENUM CAPSULE AFTER 7 DAYS' EXPOSURE[30]

Bath	Titanium weight loss, mg/cm²	Nitrogen in posttest lithium, ppm (pretest = 50 ppm)	Observations
Pure lithium	27.3	15	Titanium showed a needlelike surface structure having high microhardness
Li–1.5 at.% Si	23.3	25	No surface irregularities on titanium; brittle layer on inner molybdenum surface

Studies of the mechanism of the stress-corrosion attack of niobium–1 wt.% zirconium by mercury demonstrated that selective leaching of zirconium from the alloy was responsible. Static 1-week exposures of stressed T-111 (tantalum–8 wt.% tungsten–2 wt.% hafnium) to 650 and 752°C mercury produced similar preferential intergranular attack and evidence

Table IV-3 NATURAL-CONVECTION BOILING-MERCURY LOOP EXPERIMENTS[32]

Loop material, wt.%	Additives to mercury	Test time, hr	Estimated mercury flow rate, kg/hr	Mean temperature, °C			Corrosion results
				Boiler and condenser	Superheater	Cold leg	
100 Ta	50 ppm Mg	19,975	0.5	640	735	260	No metallographic evidence of corrosion; posttest mercury contained 64 μg of titanium and 60 μg of magnesium (13 mg of mercury had been added initially to ensure wetting)
Nb–1 Zr	None	5,712	1	760	870	240	Test was terminated by intergranular stress-corrosion failure of superheater in a bend; no other corrosion or deposition was found, except a slight roughening of a narrow band in the boiler wall
2¼ Cr–1 Mo steel	50 ppm Mg	4,968	10	593	703	270 (3900 hr) 350 (1100 hr)	Intergranular corrosion (maximum depth 1 mil) was found in liquid zone of boiler and in condenser; iron deposits (~1 g in boiler vapor zone and ~3 g in condenser) were found
2¼ Cr–1 Mo steel	50 ppm Mg; 3.0 g of Zr	5,009	10	593	703	340	Zirconium insert was completely dissolved; trace amounts of deposition were found in boiler and in condenser; spotty, whitish film was found in superheater; metallography was incomplete
2¼ Cr–1 Mo steel	50 ppm Mg; 1.31 g of Ti	4,985	10	593	703	360	Virtually no boiler corrosion; no iron deposition in either boiler or condenser; titanium insert was completely dissolved; thin layer of Fe_2Ti was found in superheater

of cracking in the stressed zones. Surprisingly, no hafnium was found in the mercury; but the zirconium impurity was leached from the hafnium and found in the mercury, which apparently accounts for the attack.

CORROSION BY OTHER NONALKALI MOLTEN METALS

Molybdenum capsules with 0.09-cm-thick walls were tested at 700 and 800°C for times up to 300 hr with molten lead, cadmium, tin, and zinc inside.[36] Ames Laboratory workers were particularly interested in the effect of oxygen (6 to 10^4 ppm) in the liquid metal on corrosion of the molybdenum. Results were as follows:

1. Lead containing 6 ppm oxygen dissolved almost 20 times as much molybdenum in 300 hr at 800°C as lead containing 25 ppm oxygen. The $PbMoO_4$ layer was protective.
2. Cadmium containing less than 17 ppm oxygen did not attack the molybdenum noticeably. High-oxygen cadmium formed a boundary layer of CdO and $CdMoO_4$.
3. Tin containing 8 ppm oxygen dissolved considerable molybdenum in 300 hr at 800°C. Tin containing greater than 125 ppm oxygen was deoxidized, and a two-phase boundary layer formed.
4. Zinc diffused through the molybdenum capsule wall and was all gone after 100 hr at 700°C. Increasing the oxygen content of the zinc reduced the diffusion rate.

Preliminary indications are that both tantalum and yttrium are promising containers for molten uranium–5 wt.% chromium alloy since neither was visibly attacked after 1500 hr at 950°C (Ref. 36).

In the sodium-cooled Experimental Breeder Reactor (EBR-II), the reactor seal is formed by the low-melting bismuth–tin eutectic alloy (42 wt.% tin) in a type 304 stainless-steel chamber. To evaluate potential corrosion problems in this system, Argonne workers[37] studied the kinetics of dissolution of type 304 stainless steel in bismuth–42 wt.% tin in a rotating-disk system at 200 to 1100°C. The dissolution process was found to be liquid-diffusion controlled at certain combinations of temperature and Reynolds number and reaction controlled after appropriate variations in either the temperature or the rotational speed of the disk. Type 304 stainless steel is not a suitable container for bismuth–42 wt.% tin above 500°C.

Argonne workers have published a report[38] that summarizes information on solubilities of the 44 elements of Table IV-4 in liquid zinc. This report, which includes many previously unpublished data, should be useful for process development, for corrosion predictions, and for theoretical studies of liquid-metal solutions.

CORROSION BY MOLTEN FLUORIDE SALTS

To study the suitability of molten fluoride salts as heat-transfer fluids in irradiation capsules at temperatures above 1500°C, workers at Battelle–Columbus[39] heated MgF_2–NaF and MgF_2–LiF binary salt mixtures in molybdenum capsules under the conditions shown in Table IV-5. The results indicate that all three salt mixtures studied are compatible with molybdenum under the test conditions. The small amount of pitting noted in the capsule walls would not be expected to interfere with high-temperature irradiation experiments up to at least 6 months' duration, because it does not seem to be progressive with time and because the pit depth (< 2 mils) would be a negligible fraction of the container wall thickness.

(E. M. Simons)

Table IV-4 ZINC-ALLOY SYSTEMS[38]

Element	System type
Silver	Intermetallic phases
Aluminum	Simple eutectic, solid solutions
Arsenic	Intermetallic phases
Gold	Intermetallic phases
Barium	Intermetallic phases
Beryllium	Unknown
Bismuth	Two immiscible liquid layers
Calcium	Intermetallic phases
Cadmium	Simple eutectic
Cerium	Intermetallic phases
Cobalt	Intermetallic phases
Chromium	Intermetallic phases
Copper	Intermetallic phases
Iron	Intermetallic phases
Gallium	Simple eutectic
Germanium	Simple eutectic
Indium	Simple eutectic
Lanthanum	Intermetallic phases
Lithium	Intermetallic phases
Magnesium	Intermetallic phases
Manganese	Intermetallic phases
Molybdenum	Intermetallic phases
Sodium	Intermetallic phases
Niobium	Intermetallic phases
Neodymium	Intermetallic phases
Nickel	Intermetallic phases
Lead	Two immiscible liquid layers
Palladium	Intermetallic phases
Praseodymium	Intermetallic phases
Platinum	Intermetallic phases
Plutonium	Intermetallic phases
Rhodium	Intermetallic phases
Ruthenium	Intermetallic phases
Antimony	Intermetallic phases
Silicon	No intermetallic phases
Tin	Simple eutectic
Strontium	Intermetallic phases
Technetium	Intermetallic phases
Thorium	Intermetallic phases
Titanium	Intermetallic phases
Uranium	Intermetallic phases
Vanadium	Intermetallic phases
Yttrium	Intermetallic phases
Zirconium	Intermetallic phases

Table IV-5 EXPERIMENTS WITH MOLTEN FLUORIDE SALTS IN MOLYBDENUM CAPSULES[39]

Salt composition, mole %	Exposure temp., °C: Hot end	Exposure temp., °C: Temperature gradient	Exposure time, hr	Maximum depth of surface pits in molybdenum, mils
MgF_2–25 NaF	1800	0	70	0.4
MgF_2–40 NaF	1570	150	100	1.8
MgF_2–40 NaF	1580	140	490	1.1
MgF_2–40 NaF	1580	140	490	1.2
MgF_2–65 LiF	1580	140	490	1.6
MgF_2–65 LiF	1580	140	490	1.4

Metal–Water Reactions

General Electric workers[40] have measured the reaction of type 304 stainless steel with steam between 1000 and 1250°C by employing a thermogravimetric technique. In this method a small disk-shaped sample undergoing the test was placed on a platinum pan suspended from a balance beam in flowing steam. The weight of oxygen gained by the sample (w) at various time intervals was determined directly. The results of these corrosion tests, plotted in Fig. IV-3, exhibit a marked temperature dependence. It is interesting to note that the results show an initial 6- to 28-min induction period in which the reaction rates are linear, i.e., the left-hand portions of the curves in Fig. IV-3 have a slope approximately equal to unity. Although no hypothesis was advanced to explain this induction period, the reaction-rate curves immediately to the right of the breaks were found to correlate with the parabolic rate law

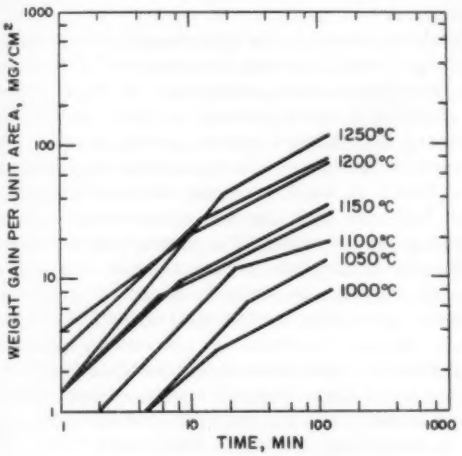

Fig. IV-3 Steam corrosion of type 304 stainless steel.[40]

$$w^2 = k_0 \exp(-E/RT) \times t = k \times t$$

where w = weight gain, mg/cm²
E = activation energy, cal/mole
k_0 = frequency factor, mg²/(cm⁴)(min)
T = temperature, °K
t = time, min
k = parabolic-rate-law constant
R = gas constant, 1.986 cal/(mole)(°K)

Figure IV-4 shows values of the reaction-rate constants calculated from the parabolic segments of the curves presented in Fig. IV-3 — the right-hand portions of the w vs. t curves. For comparison purposes, Fig. IV-4 also includes the parabolic-rate-law constants for the reaction of Zircaloy-4 with steam. At low temperatures the reaction rates for type 304 stainless steel are considerably below those for Zircaloy-4. However, at high temperatures (above 1200°C), the reaction rates for type 304 stainless steel actually become significantly greater than those for Zircaloy-4. From the Arrhenius curve shown in Fig. IV-4, an activation energy (E) of 90 kcal/mole was calculated for the type 304 stainless-steel–steam reaction.

Argonne[41] presents an analysis of the effects of the reaction between steam and 15-mil stainless-steel-clad UO_2 fuel pins for the LOFT facilities. This analysis is similar to a previous calculation[42] employing the LOFT reactor as a model, except that the latter was performed for a 25-mil-thick Zircaloy-4 cladding. Numerous assumptions were made in this calculation, most important of which were made to account for the stainless-steel–steam reaction. The primary assumption considers that the stainless-steel cladding

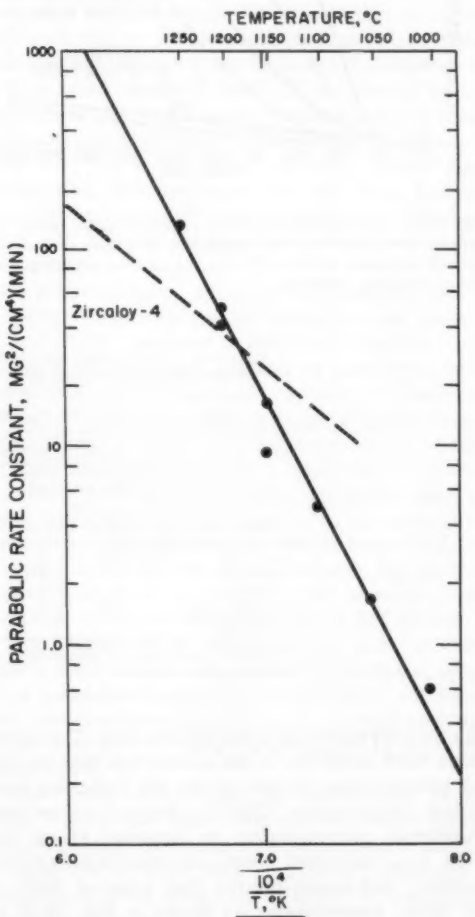

Fig. IV-4 Parabolic rate constants for type 304 stainless-steel–steam reaction vs. reciprocal absolute temperature.[40]

does not react until it has reached 1400°C, the approximate melting temperature. It was further assumed that, above 1400°C, the stainless-steel reaction rate was limited solely by the steam availability and that, for complete reaction of the metal, M_3O_4 type compounds were formed.

The calculated extent of the stainless-steel cladding–steam reaction is shown in Fig. IV-5 together with the corresponding case for Zircaloy. The curves shown were predicted on the assumption that the core had initially been cooled during the blowdown to the coolant temperature (285°C). Several cases were considered corresponding to assumed steam flow rates, i.e., unlimited steam available to the reacting cladding, and steam-limited flow rates of 1000 and 100 lb/hr, respectively. As shown in Fig. IV-5, the results for stainless-steel cladding closely parallel the corresponding case for the zirconium, although the extent of the reaction for stainless steel is somewhat less than for zirconium under all conditions. The principal difference between the behavior of the two cladding materials is attributed to the different heats of reaction.

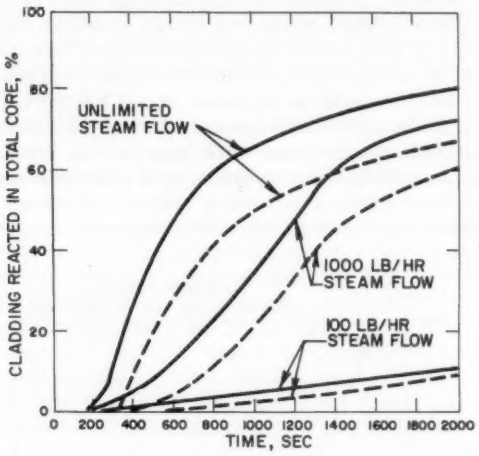

Fig. IV-5 Calculated percent of reaction–time curves for reactor core with various quantities of steam in loss-of-coolant-accident analysis.[41] —, zirconium cladding; ---, stainless-steel cladding.

Table IV-6 summarizes the calculation by presenting the extent of the stainless-steel–steam reaction and the times at which the core reached average temperatures equal to the melting point of (1) the stainless-steel cladding (1370°C) and (2) the UO_2 core (2800°C). Since no satisfactory model for the collapse of the core currently exists, the times presented in Table IV-6 were taken by the authors to represent the lower and upper limits of those required for the core to collapse onto the lower support structure.

Scale-up metal–water experiments were performed in TREAT with UO_2-core fuel clusters.[30,43] Two types of experiments were performed: (1) those intended to simulate a loss-of-coolant accident and (2) those intended to simulate a nuclear power excursion. With regard to the former, an experiment was performed in TREAT in which a cluster of three Zircaloy-2-clad UO_2-core fuel pins was melted while suspended above a pool of water. The purpose of this experiment was to simulate certain aspects of a loss-of-coolant accident in which a break in a primary-system water pipe would result in the fuel elements being exposed to steam at elevated temperatures. The results of this experiment indicated that 30 wt.% of the fuel cluster dropped into the water, although some larger particles were retained above the water by a supporting structure. The extent of the cladding–water reaction was 40% as determined by the total amount of hydrogen released. However, it was not apparent whether cladding that had dropped into the water had reacted more extensively than cladding that remained on the support structure. In this test the chemical energy contributed by the reaction corresponded to 26% of the total energy released (i.e., the contribution of the chemical reaction during the transient was 26%, approximately 197 cal per gram of UO_2 as compared with 560 cal per gram of UO_2 for the nuclear decay heat).

Table IV-6 CALCULATED TIME REQUIRED FOR COLLAPSE OF CORE AND EXTENT OF STAINLESS-STEEL–STEAM REACTION BASED ON THE AVERAGE NUCLEAR DECAY AND CHEMICAL ENERGY CONTENT[41]

(Analysis Based on LOFT Type Reactor Utilizing 15-Mil Stainless-Steel-Clad Core)

	Average core energy sufficient to melt cladding completely (1370°C)				Average core energy sufficient to begin to melt fuel (2800°C)			
	Collapse time,* sec		Metal reacted,* %		Collapse time,* sec		Metal reacted,* %	
Steam flow	Case A	Case B	Case A	Case B	Case A	Case B	Case A	Case B
Unlimited	830	350	44	38	2560	1850	80	73
1000 lb/hr	910	400	18	10	2580	1860	65	68
100 lb/hr	918	407	2.0	1.0	2700	1970	20	14
No metal–water reaction	920	410			2750	2010		

*Case A: Initial section temperatures 285°C. Case B: Initial section temperatures are those at operating power (50 Mw).

Two nuclear transient experiments were also performed in TREAT using Zircaloy-2-clad, vibratorily compacted, UO_2 fuel.[43] The primary purpose of these two experiments was to compare the meltdown behavior in water of fuel pins with and without a high internal gas pressure. These experiments also permitted a comparison of the behavior of the vibratorily compacted UO_2 fuel with that of sintered UO_2 fuel. The experiments were conducted with four-pin clusters. One cluster of pins was fabricated with a 1500-psia helium internal gas pressure to simulate fission-product gases. The helium in the other cluster was 15 psia. The data for the two runs indicated that the pressurized and unpressurized fuel pins behaved similarly. The extent of the metal–water reaction (38 and 45%, respectively) and the average particle sizes of the fragmented fuels (30 and 36 mils) were nearly identical. Also, the particle-size-frequency distributions of the fragmented fuels were nearly the same. However, temperature measurements of the two runs indicated that the fuel pins with the simulated fission-product gases (1500-psia internal pressure) failed at lower temperatures than those with an internal gas pressure of 15 psia. A thermocouple attached to the Zircaloy-2 cladding of the fuel pins having the low gas pressure indicated fuel failure at 1750°C, which is close to the melting point of the Zircaloy-2.

On the basis of these results, it was postulated that the fuel failures in the two fuel clusters with vibratorily compacted UO_2 appeared to have occurred by two different mechanisms. Fuel failure in the unpressurized (15 psia) pin cluster was thought to occur through melting of the Zircaloy-2 cladding, whereas the pressurized (1500 psia), simulated, fission-product-gas fuel pin was thought to fail because the internal gas pressure exceeded the ultimate tensile strength of the solid Zircaloy-2 cladding. In the initial case the UO_2 was thought to be molten, and in the mechanical-failure case both the UO_2 and the Zircaloy-2 cladding were thought to be solid when fuel fragmentation commenced. (J. M. Genco)

Radiation Effects in Nonfuel Materials

Stainless Steel

The elevated-temperature ductility of irradiated stainless steels continues to be of extreme interest. Many studies in both the United States and the United Kingdom are directed toward understanding the mechanism responsible for this embrittlement. Workers at Oak Ridge[44] have studied the effect of grain size on the radiation-induced embrittlement of type 304 stainless steel. They found that the embrittlement, after irradiation to about 7.0×10^{20} neutrons/cm^2 and deformation at temperatures greater than 350°C, is associated with a grain-boundary-fracture mechanism. They compared the strains at fracture of irradiated and unirradiated materials in terms of grain-boundary sliding, slip within the grain matrix, and strain associated with widening of cracks. It was found that materials having a grain size of ASTM 8 to 10 elongated nearly twice as much as those with a grain size of ASTM 3. They believe that this resulted from the reduction, in the large-grained material, of the effective length of grain boundaries, which account for much of the strength at the temperatures investigated. It was also found that irradiated materials fracture without any detectable grain-boundary sliding.

Preliminary results from a study at Oak Ridge[45] of the effect of carbon content on radiation-induced embrittlement of type 304 stainless steel at 700, 800, and 900°C show that the higher carbon content is beneficial. The (type 304) material containing 0.06 wt.% carbon has greater ductility at those test temperatures than the (type 304L) material containing 0.02 wt.% carbon. Additional improvement in ductility was obtained by aging 100 hr at 800°C, following the 1-hr solution anneal at 1036°C. The increase in ductility appeared to be related to the presence of grain-boundary carbides, which increase the stress necessary for crack nucleation and also retard crack propagation. The specimens for this study had been irradiated to 3.5×10^{20} neutrons/cm^2 ($E \geq 1$ Mev) and 4.5×10^{20} thermal neutrons/cm^2 at ambient reactor temperature.

In a surveillance study on the radiation-induced property changes in type 347 stainless steel tested at 20 and 316°C, workers at Battelle–Columbus[46] have shown that the major changes in properties occur prior to a neutron exposure of 5.0×10^{21} neutrons/cm^2 ($E \geq 1$ Mev) and that subsequent irradiation to levels as great as 2.1×10^{22} neutrons/cm^2 ($E \geq 1$ Mev) produces only slight additional changes in properties. However, when specimens are irradiated under the same conditions and tested at 750°C, the uniform and total elongations show values of only about 0.5%. The fracture mode appears to be intergranular, whereas unirradiated material tested at this same temperature fails transgranularly with about 25% total elongation. Furthermore, annealing for 1 hr at 982°C effects a recovery of the radiation damage in specimens subsequently tested at 20 and 316°C, but a similar heat-treatment produces only a slight reduction in strength with no change in elongation in specimens tested at 750°C.

Tube-burst tests made by researchers at Argonne[43] show that type 304L stainless-steel jackets taken from EBR fuel rods have a minimum in ductility in about 500°C. Tests were made over a temperature range from room temperature to 800°C. The results are shown in Figs. IV-6 and IV-7.

Workers at Karlsruhe[47] found a similar reduction in ductility at about 600°C for an austenitic steel irradiated at 70°C to about 5×10^{20} neutrons/cm^2 and

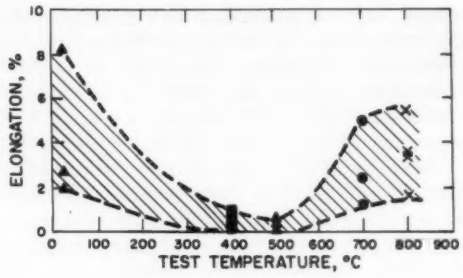

Fig. IV-6 Average elongation as a function of test temperature for irradiated type 304L stainless-steel fuel cladding.[43]

tested over the temperature range from 20 to 750°C. They also observed that recovery of the mechanical properties began at temperatures above 500°C. Oak Ridge[48] personnel attribute the low-temperature (<370°C) radiation-induced property changes to defect clusters on the order of 100 A in size. Preliminary results showed that the greatest change in properties occurred in specimens with a high density of defect clusters and that those specimens with no defect clusters (irradiated at 370°C and above) showed only very small changes in properties.

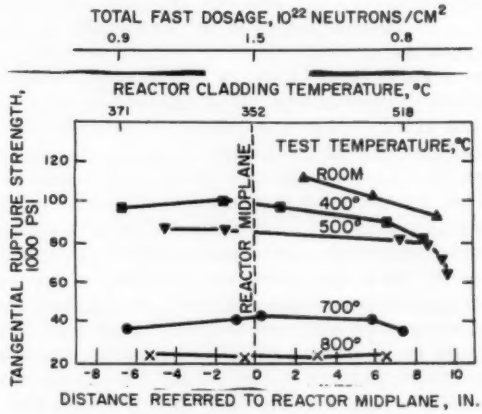

Fig. IV-7 Rupture strength along length of irradiated fuel cladding (type 304L stainless steel).

Nickel-Base Alloys

Nickel alloys irradiated by the personnel at Karlsruhe[47] in the BR-2 showed a saturation in radiation-induced property changes after an exposure of about 1×10^{21} neutrons/cm^2. They also showed evidence of elevated-temperature embrittlement, beginning at about 550°C.

Researchers at General Electric[40] report that Hastelloy N, irradiated to approximately 5×10^{20} neutrons/cm^2 ($E \geq 1$ Mev) at 760°C and tested at 760°C, showed a factor of 10 decrease in rupture life compared to the unirradiated (mill-annealed) material. Specimens irradiated to a similar level at 650°C and tested at 650°C showed a factor of 10 to 15 decrease in rupture life. Specimens stress relieved at 870°C for 4 hr before irradiation showed only a factor of 3 loss in rupture life as a result of subsequent irradiations.

An Oak Ridge study[49,50] of radiation-enhanced diffusion in alloys is being carried out with copper–nickel alloys. Previous studies suggested that the production of radiation-induced nucleation sites is an important factor in the segregation reaction. This idea was tested by bombarding a nickel–40 wt.% copper sample with 2-Mev electrons at liquid-nitrogen temperatures. The sample responded to isochronal anneals in much the same way as a sample irradiated by neutrons, and this fact suggests that diffusion enhancement is probably the dominant mechanism in the radiation-enhanced segregation process.

Zirconium Alloys

The effects of neutron irradiation on the mechanical properties and corrosion behavior of alloys zirconium–3 wt.% niobium–1 wt.% tin and Zircaloy-2 were investigated by German scientists.[6] Tensile and impact specimens received an integrated fast flux ($E \geq 1$ Mev) as great at 4.5×10^{19} neutrons/cm^2 at 45°C in contact with the pool water. Corrosion specimens were irradiated up to 820 hr in steam autoclaves at 400°C and 100 atm to a maximum integrated fast flux ($E \geq 1$ Mev) of 1.5×10^{19} neutrons/cm^2. For both alloys the irradiation produced an increase in yield strength and ultimate tensile strength and a decrease in ductility. The impact strength of zirconium–3 wt.% niobium–1 wt.% tin was increased but that of Zircaloy-2 was not altered appreciably by the irradiation. The mechanical properties of both alloys attained saturation values at an integrated fast flux of about 3×10^{19} neutrons/cm^2. The zirconium–3 wt.% niobium–1 wt.% tin alloy showed a higher strength than Zircaloy-2. With respect to the corrosion behavior in steam, both alloys were nearly equivalent. The investigators observed a hydrogen pickup and an increase in weight by a factor of 2 to 3 in the samples during irradiation.

A study made by Battelle–Northwest[51] of the effects of irradiation and environment on the mechanical properties of Inconel–Zircaloy transition joints at room temperature and at 550°F following total neutron exposures of 6.2×10^{20} neutrons/cm^2 (>1 Mev) shows that the integrity of the joints is not impaired by neutron exposure. The test indicates that the life of a transition joint will probably be limited by the properties of the irradiated Zircaloy-2 portion of the joint. A marked loss of ductility in the Zircaloy-2 portion was attributed to the hydrogen pickup. Prior fabrication history influenced both the mechanical properties and the hydrogen pickup.

Carbon and Low-Alloy Steels

Fast-neutron-irradiation hardening in steels as a function of irradiation temperature and steel type was studied by French scientists.[52] Carbon steels with carbon contents from 0.03 to 0.05 wt.%, ASTM A-302B steel, and low-alloy nickel–chromium–molybdenum steels, commonly used for reactor pressure vessels, were irradiated to 3×10^{19} neutrons/cm^2 at 100 to 500°C. Hardening occurred independently of steel type, but radiation-induced hardness was least in steels having the highest carbon content. Irradiation at temperatures of about 300°C produced negligible hardening, but secondary hardening occurred in the ASTM A-302B steel as a result of postirradiation heat-treatment. The nickel–chromium–molybdenum steels showed an initial recovery at a lower irradiation temperature than the carbon steels, but they maintained some residual hardness induced by irradiation at temperatures of 400°C.

The effect of hydrogen on the mechanical properties of steel is discussed by Oak Ridge[49] personnel, and calculations are made of the minimum neutron flux necessary to produce hydrogen attack for a 1 wt.% manganese carbon steel. It was found that attack arising from hydrogen produced in the (n,p) reaction would require fluxes greater than 10^{15} neutrons/(cm^2)(sec), which is higher than fluxes found in present-day reactors.

The results of a cooperative study[40] between two divisions of General Electric on the tensile properties of an iron–15 wt.% chromium–4 wt.% aluminum–1 wt.% yttrium alloy (1541 alloy) irradiated at 700°C to 3.5×10^{20} neutrons/cm^2 ($E \geq 1$ Mev) and tested at 600 and 700°C are given in Table IV-7. The strength was decreased by irradiation, but the ductility was only slightly affected.

The effect of radiation on precipitation of nitrides in alpha iron is being investigated by Oak Ridge personnel using internal-friction techniques.[49] In reactor studies they have indicated that low-temperature neutron irradiation enhances the rate of removal of nitrogen from supersaturated solid solution in iron. Electron irradiation under similar conditions of temperature and dose produces no change in the aging behavior. It was concluded that individual vacancies and interstitials do not act as nucleation sites for the precipitation of nitrides in alpha iron. When the electron dose is increased, some evidence for trapping of nitrogen atoms by radiation-produced defects is seen.

Initial results from another study made at Oak Ridge,[50] designed to investigate the effect of neutron-dose rate on the room-temperature tensile properties of irradiated Ferrovac E iron, show no dose-rate effect. The total dose was 1.5×10^{18} neutrons/cm^2 ($E \geq 2.9$ Mev), with fluxes of 4 to 70×10^{11} neutrons/(cm^2)(sec).

The effects of irradiation on the mechanical properties and microstructures of iron are being investigated by Brookhaven researchers.[32] They find that there is a pronounced difference in the ductile-to-brittle transition temperature between iron irradiated at 70°C (which shows embrittlement at −146°C) and iron irradiated at −70°C (which does not show embrittlement at −70°C). They also suggest that carbon is removed from alpha iron by fast-neutron irradiation. They also report the alteration of the yield strengths of iron by irradiation, without a detectable change of defect structure in electron microscopy studies. The addition of oxygen to the iron causes defects that develop into dislocation loops to become visible. Nitrogen, carbon, or hydrogen additions do not produce this conversion. The time required for complete recovery of hardness after irradiation increases with the number of visible defects.

Beryllium

Phillips Petroleum Company[53] reports that room-temperature compression tests on beryllium specimens irradiated at 750°C to 7.5×10^{20} neutrons/cm^2 (>1 Mev) showed only a very slight increase in yield strength and a reduction in ultimate strength and plastic deformation at fracture as a result of the irradiation. There was evidence of bubbles at grain boundaries in the fractographs taken of the fracture areas.

Table IV-7 EFFECT OF NEUTRON EXPOSURE ON THE TENSILE PROPERTIES OF 1541 ALLOY[40]

Exposure time at 700°C, hr	Fast-neutron exposure, neutrons/cm^2	Tensile test temp., °C	Yield stress, kg/cm^2	Ultimate stress, kg/cm^2	Uniform elongation, %	Total elongation, %
630		600	1620	1900	6	36
630	3.5×10^{20}	600	844	1124	10	37
630		700	774	844	4	61
630	3.5×10^{20}	700	633	914	5	52

Refractory Metals and Alloys

In studies of the effects of neutron exposure on the creep-rupture properties of tungsten at 1100°C and 18.28 kg/mm^2 stress, workers at General Electric[40] found that the rupture life increases as the square root of the total fast-neutron flux. Specimens were irradiated at reactor ambient temperatures to five different neutron exposures ranging from 8.5×10^{17}

to about 1.2×10^{20} neutrons/cm^2 ($E \geq 1$ Mev). The results are given in Table IV-8.

When tungsten specimens were irradiated with and without cadmium shielding (to reduce the thermal-neutron flux) and tested in creep, the unshielded specimens showed longer second-stage creep periods, greater rupture life, and more ductility at fracture than the shielded samples. The difference is attributed to the relative difference in concentrations of the transmutation products rhenium and osmium. These effects are shown in Fig. IV-8.

Table IV-8 SUMMARY OF CREEP-RUPTURE TESTS ON TUNGSTEN SPECIMENS AT 1100°C AND 18.28 kg/mm^2 (REF. 40)

Specimen*	Condition	Exposure, neutrons/cm^2 Thermal	Exposure, neutrons/cm^2 Fast ($E \geq 1$ Mev)	Linear creep rate ($\dot{\epsilon}$), sec^{-1}	Rupture life (t_r), hr	Elongation,† %	Reduction in area, %
Rod P Specimens							
1366	Control			4.46×10^{-6}	7.99		
1351	ORM-31‡	3.9×10^{19}	4.0×10^{18}	3.87×10^{-6}	12.65	35.7	90.0
1359	ORM-33	4.1×10^{19}	5.9×10^{18}	2.86×10^{-6}	15.22	29.8	94.9
1362	ORM-34	2.3×10^{20}	3.8×10^{19}	1.20×10^{-6}	43.98	24.4	92.9
1377	ORM-37§	2.5×10^{19}	3.9×10^{19}	5.0×10^{-7}	21.04	14.0	93.5
1373	ORM-36	4.9×10^{20}	7.9×10^{19}	1.23×10^{-7}	58.38	12.2	89.0
1369	ORM-35¶	7.7×10^{19}	1.2×10^{20}	2.66×10^{-6}	352.1	28.9	87.4
Rod Q Specimens							
1390	Control			5.13×10^{-6}	7.82	31.0	98.3
1391	Control			6.39×10^{-6}	6.23	30.3	98.7
1393	Control			4.52×10^{-6}	9.10	32.4	70.2
1384	ORM-32	6.8×10^{18}	8.5×10^{17}	6.26×10^{-6}	6.87	33.9	95.9
1383	ORM-31	3.9×10^{19}	4.0×10^{18}	3.60×10^{-6}	12.61	28.0	90.0
1385	ORM-33	4.1×10^{19}	5.9×10^{18}	3.0×10^{-6}	15.92	32.2	95.1
1395	ORM-34	2.3×10^{20}	2.8×10^{19}	1.08×10^{-6}	41.92	26.3	92.3
1394	ORM-37§	2.5×10^{19}	3.9×10^{19}	3.58×10^{-6}	14.64	28.0	90.0
1388	ORM-35¶	7.7×10^{20}	1.2×10^{20}	2.93×10^{-7}	194.9	33.5	92.4

*Specimens were from 0.508-cm-diameter tungsten rod postgrind annealed at 1750°C for 1 hr in hydrogen.
†In 4.54-cm gauge length.
‡ORM-31 to ORM-37 represent numbers of capsules irradiated at reactor ambient temperatures in Oak Ridge Research Reactor A2 facility.
§Specimens were shielded with 0.51-mm cadmium.
¶Exposures are estimated values.

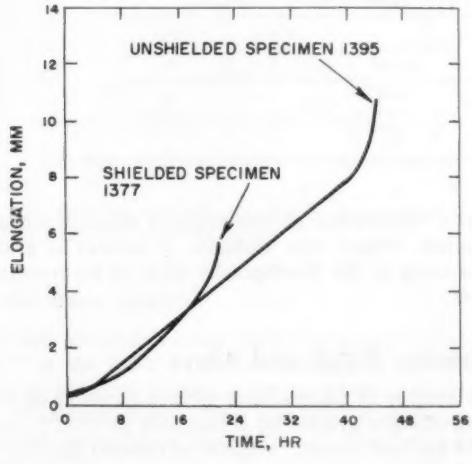

Fig. IV-8 Elongation vs. time curves for shielded and unshielded irradiated tungsten specimens[40] tested at 1100°C and 18.28 kg/mm^2. (See Table IV-8 for neutron exposures of specimens.)

Rapid recovery of the preirradiation mechanical properties of irradiated molybdenum–50 wt.% rhenium was noted in the 200 to 400°C range. Specimens had been irradiated to reactor ambient temperatures to 4.2×10^{19} neutrons/cm^2. Annealing at 700°C reduced the yield and ultimate strengths to values slightly greater than those of the controls and ductility to within 10% of the control-specimen ductility. These results are shown in Fig. IV-9. This alloy did not show thermal hardening similar to that observed for pure tungsten, molybdenum, and niobium.

A brief survey has been made by the Russians[54] on the mechanism of radiation damage and the nature of changes in the properties of metals subjected to irradiation. The possibilities of using irradiation to improve the properties of materials or to prepare materials with unusual properties (for instance, al-

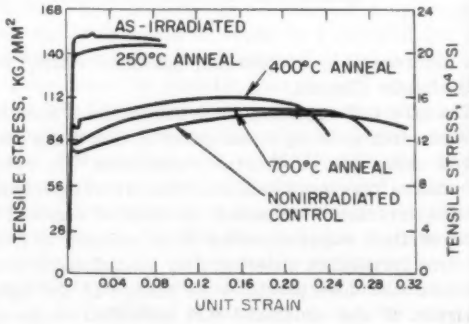

Fig. IV-9 Room-temperature engineering stress–strain curves for irradiated molybdenum–50 rhenium alloy postirradiation annealed at various temperatures.[40]

loys with elements which cannot be melted normally but which are formed by nuclear reactions under neutron irradiation) are examined. It is emphasized that, in a number of cases, a favorable effect can be obtained by combining irradiation (neutron or gamma) with subsequent heat-treatment. The surface hardening of metals and alloys by electron and heavy-ion irradiation is very promising. (F. R. Shober)

Selected Metallurgical Aspects of Cladding and Structural Materials

Aluminum and Magnesium

The plasticity of sintered-aluminum-powder (SAP) alloys was found to be dependent on two different mechanisms.[55] From room temperature to 350°C, cross slip of screw dislocations and climb of edge dislocations by diffusion were the controlling mechanisms. Above 350°C the gliding of thermally activated mobile dislocations was the dominant mechanism for plastic flow. The aluminum grain size was found to have no effect on plasticity of SAP alloys at elevated temperatures.

Thermal conductivity of SAP alloy as a function of Al_2O_3 content has been determined at 100 to 500°C (Ref. 56). Results are given in Fig. IV-10. It can be seen that extrusion results in considerable anisotropy of thermal conductivity, depending on whether the heat flow is parallel or perpendicular to the extrusion direction. This anisotropy is explained by the relative oxide cross sections in the two different directions.

The deformation mechanism of Magnox AL-80 during creep was found to be temperature dependent.[57] At 250°C creep took place by breaking down of the grains into cells, which then pulled apart. At 300, 350, and 400°C, creep cavities were nucleated by grain-boundary migration. The same deformation mechanism is also believed to operate at higher temperatures.

Zirconium

It was found that an increase in hydrogen content resulted in a decrease in the energy required to cause fracture during bend testing of zirconium.[58] The ductile-to-brittle transition temperature increased with increasing hydrogen content and strain rate during the bending tests. The hydrogen content and morphology were found to be more important than the strain rate in formulating brittle fracture.

A yield point has been found in fine-grained zirconium that had been air cooled.[59] The yield point disappears below −22°C and exists up to at least 200°C. The temperature dependence and the absence of yield point after aging of previously yielded specimens suggests that the Cottrell locking–unlocking of dislocations by solute atoms is not the dominant mechanism. The mechanism is believed to be the pileup of mobile dislocations by the fine grain size and their subsequent release at a sufficiently high stress. This theory is supported by the lack of yield point for large-grained zirconium and the disappearance of the yield point with the addition of 32 ppm hydrogen, which is believed to increase the number of mobile dislocations.

During slow cooling of Zircaloy-2, it was found that tin concentrates in the alpha grains, with tin

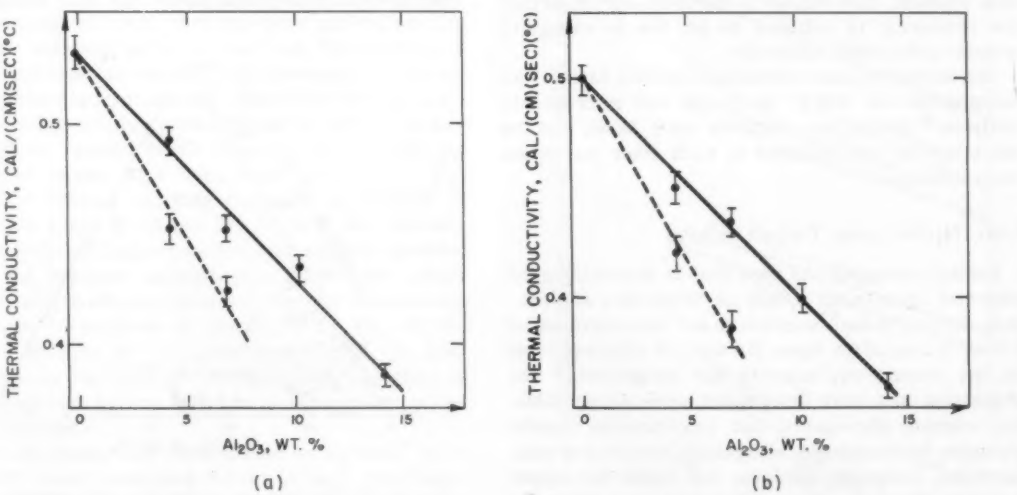

Fig. IV-10 Thermal conductivity of SAP alloy vs. alumina content.[56] Solid and dashed lines indicate heat flow in the direction parallel and normal to the extrusion axis, respectively. (a) *At 100°C.* (b) *At 500°C.*

depletion occurring in the grain boundaries.[60] Iron, chromium, and nickel were found to be distributed about equally in the grains and grain boundaries. The specific heat of Zircaloy-2 has been determined in the as-received condition and after annealing 50 hr at 800°C (Ref. 61). Results of the determinations are given in Fig. IV-11.

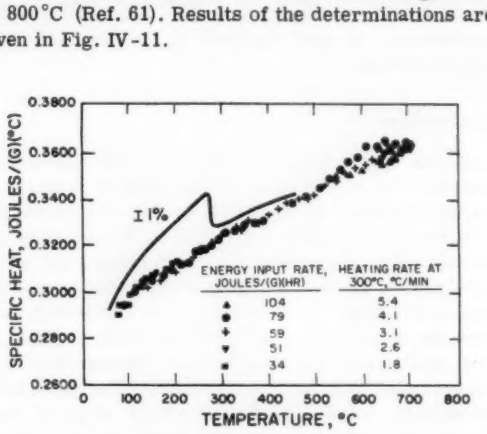

Fig. IV-11 The specific heat of Zircaloy-2 from 50 to 700°C (Ref. 61). The solid line represents the data for the as-received condition; the data points represent the data after a vacuum anneal of 50 hr at 800°C.

Water quenching of zirconium–2.5 wt.% niobium from 1000°C results in martensitic alpha-prime and niobium-rich precipitates.[62] These precipitates are at twin interfaces and grain boundaries and also are homogeneously dispersed throughout the matrix. Tempering at 500°C results in growth of the niobium-rich particles, with the particles at the twin interfaces growing the fastest. On prolonged tempering, the composition of the particles changes to that of beta niobium. The change in hardness accompanying the tempering is believed to be due to change of matrix–precipitate coherency.

The ternary system zirconium–cobalt–carbon was investigated at 800°C by X-ray and microscopic analysis.[63] No ternary carbides were found, and the solubility of the elements in each other was found to be limited.

Iron, Nickel, and Cobalt Alloys

Further research has been done in determining the effect of rare-earth metals on properties of stainless steels. Indian workers found that additions of 0.2 wt.% cerium to types 310 and 316 stainless steel do not consistently improve any properties.[64] The properties that were determined were hot workability, carbide segregation and sensitization, tensile strength, yield strength, elongation, reduction of area, hardness, austenitic stability, and sulfur and oxygen removal. However, other researchers have found that the effect of rare-earth metals on steel properties may be dependent on the presence of other elements in the steel. It has been found that additions of 0.2 wt.% rare earths improve the hot-forging properties if the lead content in steel is less than 0.018 wt.% (Ref. 65). For lead contents above that value, the hot-forging properties deteriorate with additions of 0.2 wt.% rare earths. For a rare-earth content of 0.4 wt.%, the critical lead content in the stainless steel is reduced to 0.013 wt.%. Long-term annealing studies on stainless steel have been performed by the British.[66] Specimens of 20 wt.% chromium–25 wt.% nickel–niobium austenitic stainless steel were heated for 500 and 2000 hr at 600 to 800°C. It was found that sigma formation was not serious, being a maximum at 700°C. At that temperature, isolated sigma particles at the grain boundaries made up 2% of the total volume. Particles of NbC were found in the matrix, whereas nickel-rich M_6C particles tended to be precipitated at the grain boundaries, where they probably nucleated the sigma phase.

A compilation of physical, mechanical, chemical, and irradiation properties of steels used for cladding and pressure vessels has been prepared by the British.[67] The steels included are low-carbon high-manganese steels, low-alloy chromium–molybdenum steels, 9 wt.% chromium–1 wt.% molybdenum steels, 12 wt.% chromium steels, and the austenitic stainless steels.

The highly oxidation-resistant iron–chromium–aluminum–yttrium alloy is a multiphase alloy.[68] The two constituents are the body-centered cubic alpha structure, which is a solid solution of iron, chromium, and aluminum, and the second phase is the YFe_9 intermetallic compound. Sigma-phase (CrFe) formation can be eliminated by keeping the chromium content to less than 20 wt.%. Figure IV-12 shows two other phases that must be avoided to obtain good mechanical properties, namely, Fe_3Al and the chromium-rich alpha-prime phase. The alloy composition

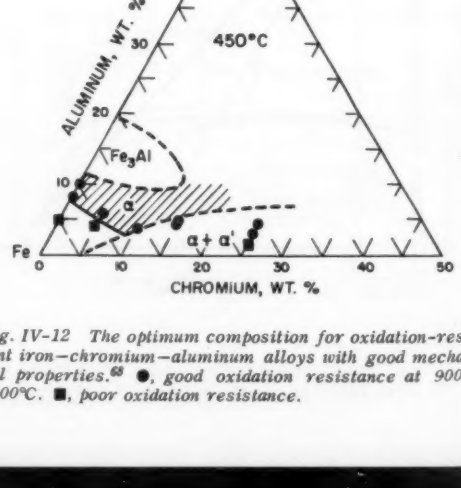

Fig. IV-12 The optimum composition for oxidation-resistant iron–chromium–aluminum alloys with good mechanical properties.[68] ●, good oxidation resistance at 900 to 1300°C. ■, poor oxidation resistance.

must be kept within the limits shown by the cross-hatching in Fig. IV-12 to obtain good oxidation resistance and to maintain good mechanical properties.

Prior cold work (5 to 40% reduction) was found to increase the room-temperature strength and ductility of L-605 (cobalt–20 wt.% chromium–15 wt.% tungsten–10 wt.% nickel) after aging at 1600°F (871°C) (Ref. 69). The ductility improvement is believed to be due to change of the Co_2W precipitates from grain boundaries to the matrix, since cold work provides precipitation sites in the matrix.

The thermal conductivity of various nickel-base alloys has been determined by workers at Oak Ridge from –270 to 1000°C (Ref. 33). Results of these determinations are given in Table IV-9.

Table IV-9 ESTIMATED THERMAL CONDUCTIVITY OF NICKEL-BASE ALLOYS[33]

Temp., °C	Estimated thermal conductivity, watt/(cm)(°C)			
	Hastelloy X	Inconel 625	Hastelloy N	Inconel 702
–270	0.020	0.020	0.020	0.020
–260	0.0295	0.0295	0.0295	0.0295
–250	0.0500	0.0532	0.0614	0.0876
–200	0.0594	0.0614	0.0690	0.0926
–100	0.0779	0.0777	0.0828	0.1031
0	0.0966	0.0937	0.0980	0.1171
100	0.1146	0.1103	0.1131	0.1290
200	0.1319	0.1259	0.1296	0.1467
300	0.1505	0.1422	0.1425	0.1644
400	0.1664	0.1593	0.1550	0.1821
500	0.1830	0.1731	0.1729	0.2000
600	0.2015	0.1926	0.1944	0.2209
700	0.2212	0.2132	0.2169	0.2433
800	0.2410	0.2342	0.2379	0.2606
900	0.2596	0.2539	0.2574	0.2815
1000	0.2772	0.2731	0.2758	0.3025

Refractory Metals

The solubility of nitrogen in niobium was found to be 0.07 at.% at 450°C and 0.55 at.% at 1000°C (Ref. 70). Excess nitrogen that has been introduced into niobium will precipitate out as Nb_2N. The addition of 1 at.% nitrogen to niobium will increase the room-temperature microhardness from 63 to 245 kg/mm^2.

The solid-solution strengthening of niobium is explained by elastic misfit of solute atoms, with the effect of atomic size being less important.[71] The effect of various alloying elements on strength is shown in Figs. IV-13 and IV-14. Note that the elements with the highest modulus of rigidity in shear have the greatest strengthening effect. The effect of the various alloying elements on room-temperature hardness of niobium is illustrated in Fig. IV-15. Creep strength at 0.5 T_m (melting point, °K) also depends on the rigidity modulus, but the effect is overshadowed by the effect of melting point on the creep strength.

A U. S. patent has been issued to Du Pont[72] for a niobium alloy containing 0.5 to 12 wt.% zirconium, 0.02 to 0.5 wt.% oxygen, carbon, or nitrogen, and one of the following metals: up to 35 wt.% tungsten, up to 10 wt.% titanium, up to 25 wt.% molybdenum, up to 25 wt.% tantalum, or up to 10 wt.% vanadium. For the test tensile properties, the alloy is solution treated at 1600 to 2100°C for times ranging from 5 min to 9 hr. After solution annealing, the alloy is age hardened above its recrystallization temperature and is then heated in the 1000 to 1500°C range from 0.5 to 40 hr.

Minor additions of yttrium to D-43 alloy (niobium–10 wt.% tungsten–1 wt.% zirconium–0.1 wt.% carbon) reduced the ductility at first but improved it considerably after aging at 2400°F (Ref. 104). The mechanism is believed to be the gettering of oxygen from

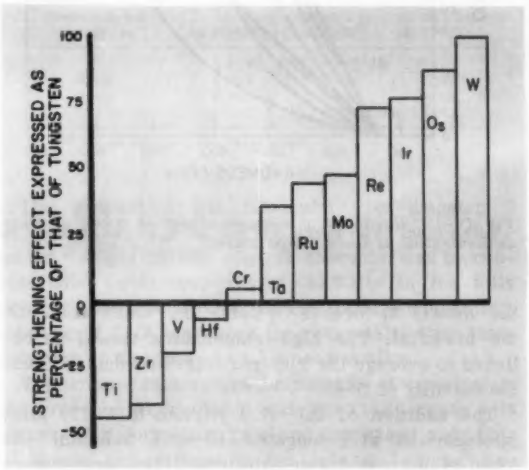

Fig. IV-13 The strengthening effect of some elements in niobium at 1200°C (Ref. 71).

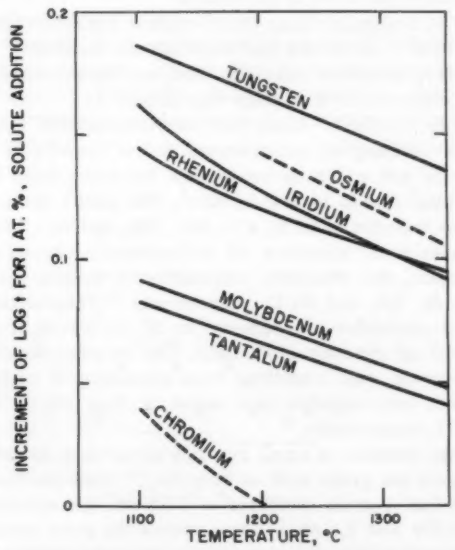

Fig. IV-14 The effect of solute additions on the strengthening of niobium at various temperatures.[71]

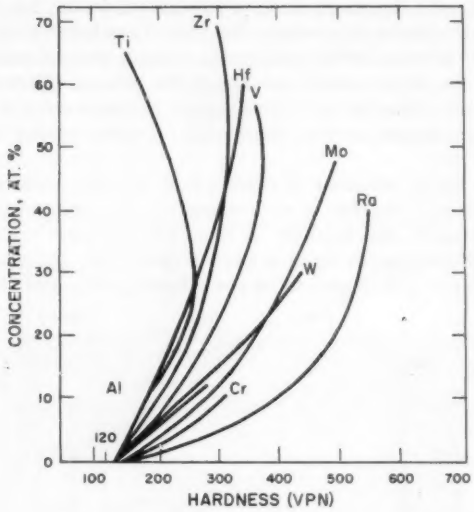

Fig. IV-15 Hardness of niobium alloys in terms of alloy concentration at room temperature.[71]

the matrix to form Y_2O_3 particles, which embrittle the material. The high-temperature anneal is believed to overage the Y_2O_3 particles and thus increase the ductility of D-43.

The addition of 0.1 wt.% yttrium to C-129 alloy (niobium–10 wt.% tungsten–10 wt.% hafnium) was found to improve the weldability and high-temperature ductility of the alloy and to maintain the high-temperature strength properties.[73] The yttrium was identified as forming a fine precipitate of rounded nonmetallic particles in the matrix.

The system niobium–iron–carbon was investigated at 1050°C by X-ray and microscopic analysis.[63] No ternary carbides were detected, and the solubility of the elements in each other was small.

The Russians[74] found that high-vacuum (10^{-7} torr) zone refining of molybdenum in the absence of oil vapors and gases decreased the hardness from 350 kg/mm^2 to 140 to 160 kg/mm^2. The gases given off were analyzed to be H_2, CO, CO_2, CH_4, and H_2O. High-temperature annealing of molybdenum, chromium, niobium, and vanadium increased the melting points 10, 40, 50, and 60°C, respectively.[75] The melting-point increases are believed to be the result of removal of gaseous impurities. The recrystallization and grain size resulting from annealing of molybdenum and tungsten are shown in Figs. IV-16 and IV-17, respectively.[76]

The addition of small amounts of boron to tungsten refines the grain size of tungsten.[77] Unalloyed tungsten has a grain diameter of 0.18 cm, and additions of 0.035 and 0.1 wt.% boron reduce the grain size to 0.04 and 0.007 cm, respectively. Boron additions of up to 0.1 wt.% induced no change in forgeability of tungsten; however, it was not possible to forge a tungsten alloy containing 0.45 wt.% boron. The recrystallization temperature was greatly increased by the addition of 0.0005 wt.% boron but was progressively reduced with further boron additions, reaching that for the unalloyed tungsten after addition of about 0.02 wt.% boron. Boron additions result in significant increases in the tensile strength of tungsten at 2500 to 3500°F (1371 to 1927°C), but this soon reaches saturation, with further boron additions having minor effect. No decrease in high-temperature ductility was noted with increasing boron content. The addition of 1 at.% tantalum to the tungsten–boron alloys resulted in an increase in the elevated-temperature tensile and creep strength along with an increase in the recrystallization temperature. The initial improvement in elevated-temperature strength is attributed to solid solution of boron in tungsten. Since the solubility is limited, being only about 0.01 wt.% at 3000°F

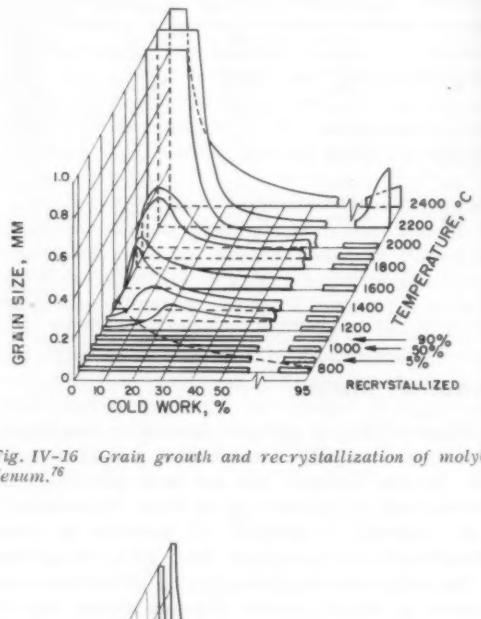

Fig. IV-16 Grain growth and recrystallization of molybdenum.[76]

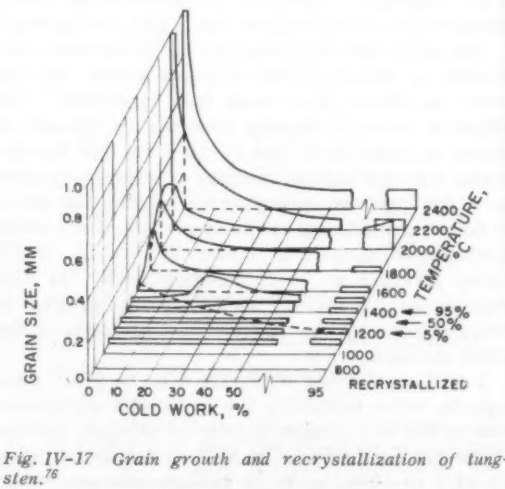

Fig. IV-17 Grain growth and recrystallization of tungsten.[76]

(1650°C), greater additions are not expected to have much effect. The boron atoms go into solution neither interstitially nor substitutionally, but somewhat in between the two mechanisms. Therefore they impart great elastic strains while in solution, and this results in large strengthening effects from minor alloying additions.

The mechanical properties of carbide-strengthened tungsten–niobium and tungsten–hafnium alloys were investigated.[78] The different degrees of strengthening were explained by the size of the carbide particles formed. Unalloyed tungsten was strengthened the least by carbon additions, whereas the tungsten–hafnium alloys were strengthened the most. The strongest alloy was tungsten–0.2 at.% hafnium–0.26 at.% carbon, which had a tensile strength of 62,500 psi at 3500°F (1927°C) and which recrystallized only after heating for 1 hr at 4200°F (2316°C).

The most effective solid-solution strengthener of tungsten was hafnium, with rhenium being the least effective. The relative solid-solution strengthening was found to be proportional to the mismatch of tungsten and solute-atom size. The strengths imparted by the ternary additions were found to be additive to those of the binary alloys.

The solubility of tungsten in rare-earth metals was found[79] to be given by the equation: $\log N = [A/T(°K)] + B$, where N is the atomic fraction of tungsten in the rare earth and A and B are constants (Table IV-10).

Table IV-10 SOLUBILITY OF TUNGSTEN AT THE MELTING TEMPERATURE OF RARE-EARTH SOLVENTS AND SOLUBILITY CONSTANTS FOR THE EQUATION LOG $N = [A/T\ (°K)] + B$ (REF. 79)

Rare-earth metal	Temp., °C	Dissolved tungsten, at.% (= 100 N)	Constants A ($\times 10^{-3}$)	Constants B
Scandium	1539	1.334	−5.405	1.108
Yttrium	1502	0.0650	−6.310	0.368
Lanthanum	920	8×10^{-4}	−11.659	1.692
Cerium	797	0.00022	−5.418	−0.588
Praseodymium	935	0.00013	−7.246	0.125
Neodymium	1024	0.00064	−6.750	0.010
Samarium	1072	0.0018	−3.949	−1.811
Europium	826	*		
Gadolinium	1312	0.0133	−6.345	0.127
Terbium	1356	0.029	−6.548	0.480
Dysprosium	1407	0.064	−5.971	0.360
Holmium	1461	0.070	−9.508	2.330
Erbium	1497	0.071	−8.724	1.799
Thulium	1545	0.322	−5.485	0.525
Ytterbium	824	*		
Lutetium	1652	0.436	−7.989	1.790

*Europium and ytterbium dissolve less than 0.0019 and 0.0007 at.% tungsten, respectively, over the temperature range of 1630 to 2100°C. The solubility at their melting temperatures could not be determined because of the scatter in the data.

Thermochemically deposited tungsten forms extremely fine grains (0.001 mm) at the original surface.[33] The grains grow with further deposition, being about 0.013 mm after 5 mils and 0.041 mm after 40 mils. Grain growth of the material deposited at different times was measured at 1800 and 2500°C. Table IV-11 shows that the first-deposited grains undergo large growth, and the grains deposited later undergo only minimal growth. The same phenomenon appears to take place for tungsten that has been vapor deposited.[80] Vapor deposition of tungsten also results in fine grains at the first-deposited surface. Removal of these fine grains by dissolution results in considerable suppression of grain growth. With the fine grains removed, no significant grain growth takes place at 2500°C.

Table IV-11 GRAIN SIZE OF THERMOCHEMICALLY DEPOSITED TUNGSTEN AND POWDER-METALLURGY SHEET TUNGSTEN[33]

Distance from first-deposited surface, in.	Average grain diameter, mm: As deposited	After 1 hr at 1800°C	After 1 hr at 2500°C
	0.001	0.063	0.120
0.005	0.013	0.022	0.042
0.040	0.041	0.056	0.065
*		0.024	0.84

*Wrought powder-metallurgy sheet.

The properties and fabricability of tungsten–5 wt.% rhenium–2.2 wt.% ThO_2 sheet have been determined.[81] Sheet of this alloy is characterized by considerable room-temperature ductility in the fully recrystallized as well as stress-relieved condition. Addition of ThO_2 increases the recrystallization temperature of tungsten–5 wt.% rhenium alloy.

The room-temperature brittleness of tantalum in the presence of hydrogen was found to increase with increased deformation rate and increased solubility of oxygen and nitrogen in the tantalum lattice.[82] Researchers at Denver Research Institute[83] have investigated tantalum–tungsten–zirconium systems at 1100 and 1600°C and the tantalum–tungsten–hafnium system at 1600°C. Isotherms of the systems are shown in Figs. IV-18 to IV-20.

Reference 84 is an English translation of a Russian book on rhenium alloys. The physical metallurgy, mechanical properties, physical properties, and corrosion resistance of rhenium and rhenium alloys are discussed. (M. Kangilaski)

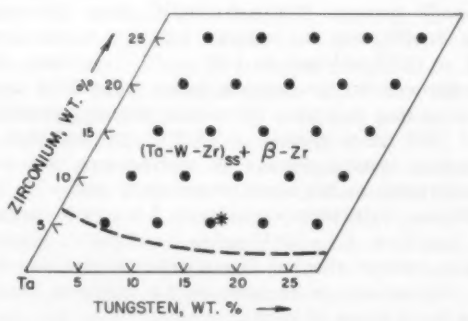

*Fig. IV-18 Isothermal section at 1100°C for the tantalum-rich region of the tantalum–tungsten–zirconium system.[83] ●, two-phase alloys; *, sample also examined by X-ray diffraction.*

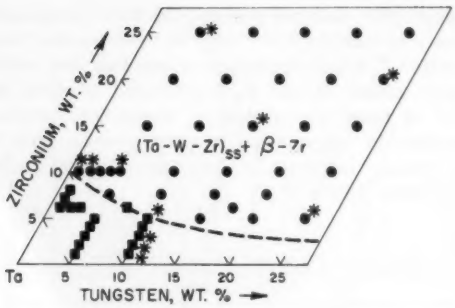

Fig. IV-19 Isothermal section at 1600°C for the tantalum-rich region of the tantalum–tungsten–zirconium system.[83] ■, essentially single-phase alloys; ●, two-phase alloys; ✱, sample also examined by X-ray diffraction.

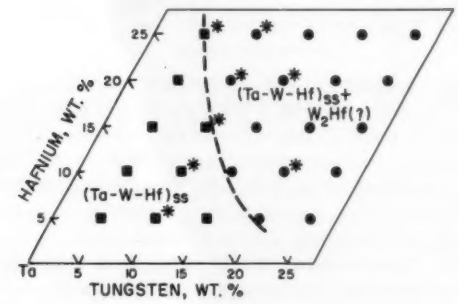

Fig. IV-20 Isothermal section at 1600°C for the tantalum-rich region of the tantalum–tungsten–hafnium system.[83] ■, single-phase alloys; ●, two-phase alloys; ✱, sample also examined by X-ray diffraction.

Diffusion Studies

A recent compilation of reports in book form contains the results of basic diffusion studies on refractory-metal systems. Coefficients for volume and boundary diffusion of tungsten in molybdenum were measured by autoradiographic methods at temperatures[85a] between 1700 and 2100°C. Over this range the coefficients for volume diffusion varied from 9.9×10^{-13} cm²/sec to 1.25×10^{-10} cm²/sec. The coefficients for boundary diffusion were 2100 times greater than they were for volume diffusion at 1850°C and 1200 times greater at 1900°C. The diffusion of rhenium isotope tracers in molybdenum was also investigated in the same temperature range.[85b] The diffusion coefficients varied from 2.8×10^{-12} cm²/sec at 1700°C to 1.7×10^{-10} cm²/sec at 2100°C. The diffusion rate of rhenium in molybdenum exceeded that of molybdenum in rhenium by 2.5 times at 1700°C and by 1.7 times at 1900°C.

In other studies the diffusion of radioactive iron and silver tracers in beryllium[86] was found to be temperature dependent according to the Arrhenius type equations:

$$D_{\text{Fe in Be}} = 0.53 \exp(-51{,}800/RT) \quad \text{cm}^2/\text{sec}$$

and

$$D_{\text{Ag in Be}} = 6.2 \exp(-46{,}100/RT) \quad \text{cm}^2/\text{sec}$$

Anisotropic diffusion of silver in beryllium was studied quantitatively on single crystals. Atoms of silver diffused more rapidly on the *c*-axis; the anisotropic effect decreased with increasing temperature. The diffusion of uranium in molybdenum, niobium, zirconium, and titanium was determined by measuring the integral activity of ^{235}U in these metals.[87] The range of temperatures studied, the frequency factors, and activation energies were reported as follows:

Metal	Temperature range, °C	Frequency factor (D_0), cm²/sec	Activation energy (Q), kcal/mole
Molybdenum	1500–2000	7.6×10^{3}	76.4
Niobium	1500–2000	8.9×10^{-2}	76.8
Zirconium	915–1200	7.77×10^{-5}	25.8
Titanium	915–1200	4.90×10^{-4}	29.3

The results of diffusion measurements of uranium out of UC pellets in porous graphite are given in a German report.[88] The UC pellets were heated in the temperature range 1400 to 2000°C. Diffusion rates showed a strong dependence on the previous treatments to UC. Uranium appears to be transported via the gaseous phase; this phase transport is greatly affected by traces of a uranium oxide compound on the pellet surface. In other foreign work the activation energy for diffusion of actinide elements 90 to 95 was measured in sintered, dense UO_2 compacts.[89] Diffusion was measured at temperatures between 1250 and 1600°C. The activation energy for plutonium diffusion in UO_2 was experimentally determined and used as a reference point. The activation energies for diffusion of the other elements in UO_2 were found by comparison with the following results:

Element	Q, kcal/mole
Thorium	98
Protactinium	108
Uranium	104
Neptunium	110
Plutonium	98
Americium	92

The final report by Peterson and Rothman on diffusion of various metal tracers in gamma uranium has been issued by Argonne.[90] Diffusion measurements were made by thin-layer sectioning techniques. Arrhenius type plots of log D vs. $1/T$ were curved at low temperatures for all elements studied, with the exception of manganese and niobium. The data do not conform to any present theory of diffusion, but several mechanisms are discussed as being responsible for the curved Arrhenius plots. The authors show

that diffusion in the body-centered cubic transition metal occurs by a defect mechanism and that very probably the defects are vacancies. A summary of the results of the measurements is given below:

Element	Annealing-temp. range, °C	Activation energy (Q), kcal/mole	Frequency factor (D_0), cm²/sec
Cobalt	786–989	12.57	3.51×10^{-4}
Chromium	822–1037	24.46	5.47×10^{-3}
Copper	786–1039	24.06	1.96×10^{-3}
Iron	701–934	12.01	2.69×10^{-4}
Manganese	787–938	13.88	1.81×10^{-4}
Nickel	787–1039	15.56	5.36×10^{-4}
Niobium	790–1102	39.65	4.87×10^{-2}

(A. N. Ashurst)

Selected Mechanical Properties of Cladding and Structural Materials

Refractory Metals

The effects of rhenium content on 1600 and 2200°C creep strength of tungsten–rhenium and tungsten–rhenium–molybdenum alloys are shown in Figs. IV-21 and IV-22, as determined by General Electric.[68] At 1600°C the tungsten–26 at.% rhenium alloy has the greatest rupture life and is the most creep resistant. Additions of 10 and 20 at.% molybdenum to tungsten–26 at.% rhenium decreased the rupture life. At 2200°C the 10 at.% molybdenum addition improved the creep resistance slightly.

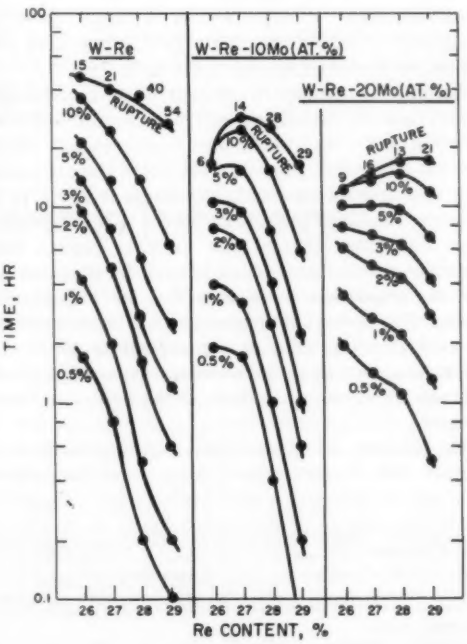

Fig. IV-21 Creep strain vs. rhenium content of tungsten–rhenium and tungsten–rhenium–molybdenum alloys at 1600°C and 4.22 kg/mm² (Ref. 68).

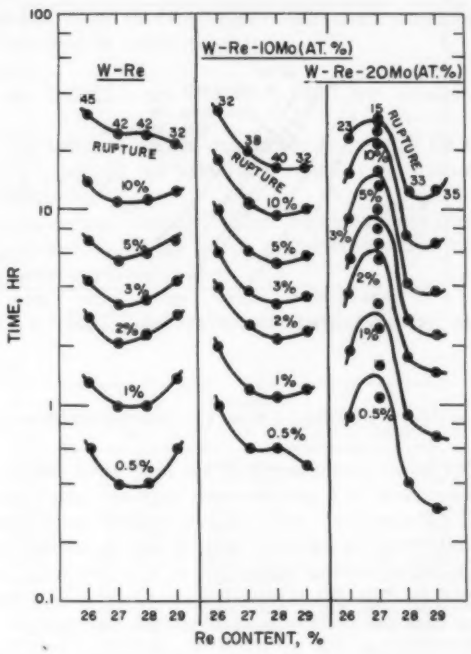

Fig. IV-22 Creep strain vs. rhenium content of tungsten–rhenium and tungsten–rhenium–molybdenum alloys at 2200°C and 0.56 kg/mm² (Ref. 68).

Figure IV-23 is a Larson–Miller plot developed by General Electric[68] for describing the short time high-temperature creep behavior of a number of refractory metals and alloys.

The Oregon Metallurgical Corp.[91] has developed a tungsten–15 wt.% molybdenum alloy and named it Oremet HPC. The alloy is vacuum-consumable-electrode melted and centrifugally cast. Room-temperature mechanical properties for a 0.105-in.-diameter bar are: tensile strength, 164,000 to 181,000 psi; 0.2% offset yield strength, 158,000 to 175,000 psi; elongation, 2.6 to 4.7%; reduction in area, 1.9% (longitudinal) and 3.9% (transverse).

Creep tests of 1000 hr and longer were conducted by the Lewis Research Center of the National Aeronautics and Space Administration (NASA–Lewis)[92] at 2000 and 2200°F on six commercially available refractory alloys at pressures of 10^{-8} to 10^{-9} torr. The creep behavior of three niobium alloys, FS-85 (niobium–28 wt.% tantalum–10 wt.% tungsten–1 wt.% zirconium), D-43 (niobium–10 wt.% tungsten–1 wt.% zirconium–0.1 wt.% carbon), and Cb-752 (niobium–10 wt.% tungsten–2.5 wt.% zirconium), and three tantalum alloys, T-222 (tantalum–0.6 wt.% tungsten–

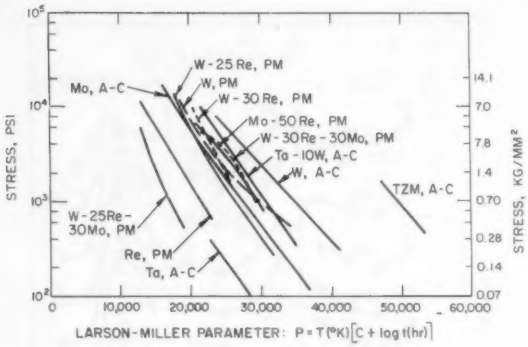

Metal	Temperature range, °C	Time range, hr	L–M constant, C
Mo (AC)*	1200–2400	0.04–580	11.87
W (AC)	1600–2800	0.78–420	11.76
W (PM)	1600–2800	0.42–62	9.42
Re (PM)	1600–2800	0.34–350	6.17
Ta (AC)	2400–2600	0.37–14	8.85
Ta–10 W (AC)	1600–2800	1.25–180	10.53
W–25 Re (PM)	1600–2800	0.05–200	8.89
W–30 Re (PM)	1600–2000	19–180	9.48
W–25 Re–30 Mo (PM)	1600–2200	15–100	5.70
W–30 Re–30 Mo (PM)	1600–2000	3.1–330	11.10
Mo–50 Re (PM)	1600–2200	1.1–230	11.47
TZM (AC)	2000–2200	1.0–6.0	20.70

*AC, arc cast; PM, powder metallurgy.

Fig. IV-23 Stress vs. Larson–Miller parameter (P) for rupture time of various refractory metals and alloys.[68]

2.4 wt.% hafnium–0.01 wt.% carbon), T-111 (tantalum–8 wt.% tungsten–2 wt.% hafnium), and tantalum–10 tungsten (90 wt.% tantalum–10 wt.% tungsten), was determined at stress-to-density ratios of 2.6×10^4 and 1.3×10^4 in., respectively, at 2000 and 2200°F. On the density-compensated basis, the tantalum alloy T-222 was the most creep-resistant material evaluated. A total creep strain of only 0.1% resulted from testing this alloy for 5000 hr at 2000°F at a stress of 15,900 psi; whereas at 2200°F and 8000-psi stress, 0.65% strain occurred in 5000 hr. The order of (decreasing) creep resistance of the materials evaluated at 2000 and 2200°F is T-222, tantalum–10 tungsten, D-43, FS-85, T-111, and Cb-752.

A study was made by NASA–Lewis[93] on the properties of tungsten fabricated from three ingots consolidated by electron-beam melting. The study included purity as a function of number of melts, recrystallization and grain-growth behavior, low-temperature ductility, and high-temperature tensile and creep strength. The level of most metallic impurities in tungsten decreased with increasing number of electron-beam melts. The levels of interstitial impurities generally were not affected by remelting. The recrystallization and grain-growth rates for worked, electron-beam-melted (EB-melted) tungsten were significantly higher than those observed for arc-melted tungsten. The ductile–brittle bend-transition temperature for EB-melted tungsten was slightly higher in the worked condition than that reported for arc-melted tungsten. This is partly associated with the large grain size of EB-melted tungsten. The high-temperature creep strength of EB-melted tungsten was less than that of arc-melted tungsten, but this appears to be entirely the result of the larger grain size of EB-melted tungsten. Step-load creep tests at 2250 to 3630°F established that, at the stress levels studied (2130 to 6870 psi), EB-melted tungsten exhibited only transient creep behavior at 2250 to 2750°F. However, at 2875°F and higher it showed the classic three-stage deformation-time behavior. The activation energies for transient and steady-state creep were 106,400 and 141,000 cal/gram mole, respectively.

An investigation was made by the Russians[94] of powdered-metal tungsten (99.95%) at 20 to 1000°C and tensile-strain rates of 2.36×10^{-2} sec^{-1} to 5.55×10^{-1} sec^{-1}. The brittle–ductile transition temperature was found to increase with increases in strain rate. In the zone of brittleness at strain rates less than 10^{-1} sec^{-1}, the ultimate strength was essentially constant; at higher strain rates the strength decreased with the decreasing temperature. At a given temperature, increasing the strain rate resulted in a slight increase in strength and a decrease in ductility.

Miscellaneous Materials

An excellent summary of strength data for Hastelloy X, shown in Table IV-12, has been presented by Aerojet-General Nucleonics.[95]

Battelle investigators studied[96] the notch impact properties of chromium and a chromium–35 at.% rhenium alloy and performed fractographic examinations on broken samples. The notch impact transition temperature of iodide chromium is 240°C in the wrought condition and up to 380°C in the recrystallized condition. Optical and electron-replica fractography show that failure occurs by cleavage and that the transition represents that for crack propagation. The transition temperature of the chromium–35 at.% rhenium alloy is approximately 260°C, and fracture occurs by grain-boundary separation, ductile parting, cleavage, or failure at the twin–matrix interface.

The results of stress-rupture measurements on Udimet 700 (a nickel-base alloy containing cobalt,

Table IV-12 DESIGN PROPERTIES OF HASTELLOY X (REF. 95)

Property	Temperature, °F						
	800	1000	1200	1400	1600	1800	2000
Ultimate tensile strength, 1000 psi	100	95	85	65	37	22	12
Yield strength, 1000 psi	44	42	41	37	27	15	8
Rupture strength at 10,000 hr, 1000 psi	70	40	23	9	4	1.5	
Elongation, %	45	45	38	40	50	40	32

chromium, and molybdenum), TZC molybdenum alloy, Ferrovac E, and Armco iron at high temperatures and high strain rates are given by Grant et al.[97] A tension type machine capable of achieving strain rates up to 10,000%/sec was used for the measurements. Typical results showing the increase in high-temperature strength with increasing strain rate for Udimet 700 are given in Fig. IV-24.

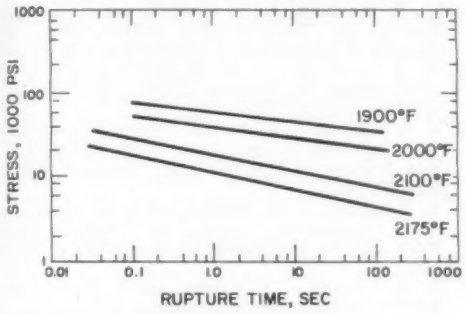

Fig. IV-24 Dependence of rupture stress on strain rate for Udimet 700 (Ref. 97).

The creep behavior, at 450°C and a stress of 350 psi, of a magnesium alloy containing 0.84 wt.% aluminum and 0.54 wt.% zirconium with smaller quantities of zinc (0.15 wt.%) and calcium (0.1 wt.%) was investigated by the British.[98] The creep rates for two specimens increased continuously during the course of the tests from minima on the order of 10^{-4} per hour. The specimens ultimately ruptured, with elongations of 60 and 69% at 820 and 600 hr, respectively. (J. A. De Mastry)

Ceramic Technology

Previously, it has been shown that dense zirconia containing 15 mole % titanium is resistant to thermal shock, even though it is not in the stable cubic structure. An investigation at NASA–Lewis[99] indicates that the titanium is present at the grain boundaries and that the stress-reducing mechanism is plastic flow of the metal. Other metal additions were found to have a comparable effect on thermal-shock resistance.

Simpson and Carter[100] have reported on the measurement of oxygen diffusion in single-crystal and polycrystalline $Zr_{0.858}Ca_{0.142}O_{1.858}$ by the sectioning technique. It was found that the diffusion coefficient, which may be represented by the equation

$$D = 0.018^{+0.1}_{-0.01} \exp -(31{,}200 \pm 4300)/RT \quad \text{cm}^2/\text{sec}$$

agrees with that calculated from the electrical conductivity and an oxygen-transport number of 1. It was also found that the oxygen surface-exchange coefficient may be represented by

$$\alpha = 0.078^{+0.4}_{-0.07} \exp -(22{,}800 \pm 4400)/RT \quad \text{cm/sec}$$

The authors discuss the effect of ignoring the exchange rate on the calculated value of the diffusion coefficient.

Rhodes and Carter[101] have reported on cationic self-diffusion in the same material. Lattice self-diffusion coefficients are:

$$D_{Ca} = 0.444^{+0.4}_{-0.2} \exp -(100{,}200 \pm 2800)/RT \quad \text{cm}^2/\text{sec}$$

and

$$D_{Zr} = 0.035^{+0.03}_{-0.02} \exp -(92{,}500 \pm 2400)/RT \quad \text{cm}^2/\text{sec}$$

It was noted that the observed lattice cation diffusion rates are approximately equal to those calculated from sintering data. This fact suggests that the sintering rate in this material is controlled by the slow (relative to the anion) diffusion rate of the cation.

Wirkus and Wilder[102] have studied the high-temperature oxidation of $MoSi_2$ in air at atmospheric pressure. The oxidation was found to occur in two modes: (1) below the boiling point of MoO_3 (about 750°C), both MoO_3 and SiO_2 form the protective layer, and (2) at higher temperatures, SiO_2 and Mo_5Si_3 are found. Evidence is presented which indicates that oxygen permeation through a silica layer controls the reaction rate and that the Mo_5Si_3 is present directly beneath this protective layer. The activation energy for the oxidation of $MoSi_2$ above 1200°C was calculated to be 81.3 kcal/mole.

The hardnesses of five borides measured at room temperature (diamond indenter, 50-g load) and at 1625°C (B_4C indenter, 2500-g load) in vacuum have been reported by Sanders and Probst.[103] The results are tabulated below:

Boride	Hardness, kg/mm²	
	Room temp.	1625°C
Hafnium diboride	2230	569
Zirconium diboride	2170	312
Niobium diboride	2140	302
Lanthanum hexaboride	2520	371
Holmium tetraboride	2220	155

(H. D. Sheets)

References

1. T. Smith, Kinetics and Mechanism of Hydrogen Permeation of Oxide Films on Zirconium, *J. Nucl. Mater.*, 18: 323-336 (1966).
2. S. Kass, The Corrosion and Hydrogen Pickup of Electron-Beam-Welded Nickel-Free Zircaloy-4, USAEC Report WAPD-TM-533, Westinghouse Electric Corporation, Bettis Atomic Power Laboratory, March 1966.

3. S. Kass, The Effect of Silicon on the Corrosion and Hydrogen Absorption Characteristics of Zircaloy-4 and Nickel-Free Zircaloy-2, USAEC Report WAPD-TM-544, Westinghouse Electric Corporation, Bettis Atomic Power Laboratory, April 1966.
4. S. Kass, The Effects of Heat Treatment on the Corrosion and Hydrogen Absorption Characteristics of Zirconium-Niobium-Copper (Zr + 2.5% Nb + 0.5% Cu) Alloy, USAEC Report WAPD-TM-500, Westinghouse Electric Corporation, Bettis Atomic Power Laboratory, March 1966.
5. H. Spindler, On the Corrosion Behavior of Welded Joints from Zirconium Alloys with Low Niobium Contents in Water and Steam at Elevated Temperatures, *Kernenergie*, 8: 679-684 (December 1965).
6. Von W. Jung-König, H. Richter, W. Spalthoff, and E. Starke, Investigation of the Effect of Neutron Irradiation on the Properties of the Alloy Zr-3Nb-1Sn, *Atomkernenergie*, 11(1/2): 47-58 (January–February 1966).
7. Battelle Memorial Institute, Pacific Northwest Laboratory, Metallurgy Research Section, Quarterly Progress Report, October–December 1965, USAEC Report BNWL-207, Jan. 17, 1966.
8. G. Chaudron, Quarterly Report No. 11 (on Stainless Steel), July 1–September 30, 1965, USAEC–Euratom Report EURAEC-1486 (EUR-2653), Centre National de la Recherche Scientifique, Dec. 27, 1965.
9. L. A. Popple, The Oxidation of Stainless Steels Containing Molybdenum—Report on Work to May 1965, British Report TRG-Report-1012, May 1965.
10. G. J. Biefer and J. G. Garrison, A Comparison of the Effects of Uranium and Molybdenum Alloying Additions on the Corrosion Resistance of AISI Type 430 Stainless Steel, Canadian file No. NP-15900, September 1965.
11. W. E. Berry, W. N. Stiegelmeyer, and W. K. Boyd, Examination of the 1B Steam Generator from the Shippingport Atomic Power Station, USAEC Report BMI-1764, Battelle Memorial Institute, Columbus Laboratories, Feb. 24, 1966.
12. R. M. Baciarelli, Army Gas-Cooled Reactor Systems Program, Isothermal Oxidation of Hastelloy X at 1750 and 1850°F in Air, USAEC Report AGN-TM-413, Aerojet-General Nucleonics, December 1965.
13. J. S. Brunhouse, Army Gas-Cooled Reactor Systems Program, Studies of Hastelloy X Corrosion in Air at 1900 and 2000°F, USAEC Report AGN-TM-414, Aerojet-General Nucleonics, December 1965.
14. B. J. Thamer, Corrosion Tests of Hastelloy N, Inconel 600, and Hymu-80 Exposed to UCl_3-KCl at 900°C, USAEC Report LA-3476, Los Alamos Scientific Laboratory, Feb. 4, 1966.
15. J. E. Le Surf, P. E. C. Bryant, and M. C. Tanner, The Use of Ammonia To Suppress Oxygen Production and Corrosion in Boiling-Water Reactors, Canadian Report AECL-2562, April 1966.
16. R. W. Judy, Jr., T. W. Crooker, R. E. Morey, E. A. Lange, and R. J. Goode, Fractographic Analysis of Ti-7Al-2Cb-1Ta and Ti-6Al-4V Fractures Developed in "Wet" Fatigue, Report NRL-6330 (AD-628277), Naval Research Laboratory, July 26, 1965.
17. E. J. Ripling, R. L. Kirchner, R. P. O'Shea, and R. G. Lingwall, Elevated-Temperature Stress Corrosion of High-Strength Sheet Materials in the Presence of Stress Concentrators, Final Report, Reports N66-16193 to N66-16195, Materials Research Laboratory, Inc., November 1965.
18. W. L. Acherman, J. P. Carter, C. B. Kenahan, and D. Schlain, Corrosion Properties of Molybdenum, Tungsten, Vanadium, and Some Vanadium Alloys, Report BM-RI-6715, Bureau of Mines, April 1965.
19. A. P. Gulyaev and I. Ya. Georgieva, Corrosion Resistance of Binary Niobium Alloys, *Zashchita Metal.*, 1: 652-657 (1965).
20. M. Kilpatrick and S. K. Lott, Reaction of Flowing Steam with Refractory Metals. II, Rhenium; III, Tungsten, *J. Electrochem. Soc.*, 113: 15-18 (January 1966).
21. R. J. Walter and W. T. Chandler, Compatibility of Tantalum and Columbium Alloys with Hydrogen, *Am. Inst. Aeron. Astronaut. J.*, 4: 302-307 (February 1966).
22. J. E. White, Development of Oxidation-Resistant Tungsten-Base Alloys, *Am. Inst. Aeron. Astronaut. J.*, 4: 307-312 (February 1966).
23. R. A. Perkins and C. M. Packer, Coatings for Refractory Metals in Aerospace Environments, Report AFML-TR-65-351, Lockheed Missiles and Space Co., September 1965.
24. O. M. Stanfield, R. T. Wimper, and A. R. Stetson, Coatings for Tantalum Alloy Nozzle Vanes, Solar, Division of International Harvester Co., Oct. 29, 1965.
25. M. H. Ortner and S. J. Klach, Development of Protective Coatings for Tantalum T-222 Alloy, Vitro Laboratories, Dec. 20, 1965.
26. V. L. Hill and J. J. Rausch, Protective Coatings for Tantalum-Base Alloys, Report IITRI-B6048-10, Illinois Institute of Technology Research Institute, Mar. 31, 1966.
27. D. T. Dickson, R. T. Wimper, and A. R. Stetson, Very High Temperature Coatings for Tantalum Alloys, Solar, Division of International Harvester Co., Apr. 29, 1966.
28. E. H. Girard, J. F. Clarke, and H. Breit, Study of Ductile Coatings for the Protection of Columbium and Molybdenum Alloys, Metals and Controls, Inc., May 1966.
29. E. G. Brush, Sodium Mass Transfer. XVI, The Selective Corrosion Component of Steel Exposed to Flowing Sodium, USAEC Report GEAP-4832, General Electric Company, Atomic Power Equipment Department, March 1965.
30. Argonne National Laboratory, Reactor Development Program Progress Report, February 1966, USAEC Report ANL-7176, Mar. 23, 1966.
31. V. I. Nikitin, Stress Rupture of Materials in Liquid Metal Under Conditions of Mass Transfer, Report FTD-TT-65-143/1 + 2, translated from *Zavodsk. Lab.* (in Russian), 30: 213-215 (1964), May 28, 1965.
32. Brookhaven National Laboratory, Nuclear Engineering Department Annual Report, December 31, 1965, USAEC Report BNL-954.
33. W. O. Harms (Comp.), High-Temperature Materials Program Quarterly Progress Report for Period Ending January 31, 1966, USAEC Report ORNL-TM-1455, Part 1, Oak Ridge National Laboratory, May 1966.
34. R. W. Harrison, The Compatibility of Biaxially Stressed D-43 Alloy with Refluxing Potassium, Report R66SD-3010, General Electric Company, Space Power and Propulsion Section, Mar. 31, 1966.
35. F. Hargreaves, G. T. J. Mayo, and A. G. Thomas, A Study of the Long-Term Compatibility of Thermionic Converter Materials with Cesium, *J. Nucl. Mater.*, 18: 212-218 (1966).
36. A. F. Voigt (Ed.), Reactor Materials Development Quarterly Report, January–March 1966, USAEC Report IS-RD-5, Ames Laboratory, Iowa State University of Science and Technology.
37. T. F. Kassner, A. Convective-Diffusion Study of the Dissolution Kinetics of 304 Stainless Steel in Bismuth-Tin Eutectic Alloy, USAEC Report ANL-6985, Argonne National Laboratory, November 1965.
38. I. Johnson and I. G. Dillon, The Solubility of Metals in Liquid Zinc, USAEC Report ANL-7083, Argonne National Laboratory, November 1965.
39. J. M. Fackelmann, Battelle Memorial Institute, Columbus Laboratories, personal communication, June 1966.
40. General Electric Company, Nuclear Materials and Propulsion Operation, High-Temperature Materials Program Progress Report No. 58, Part A, USAEC Report GEMP-58A, Apr. 29, 1966.
41. Argonne National Laboratory, Reactor Development

Program Progress Report, March 1966, USAEC Report ANL-7193, Apr. 22, 1966.
42. Argonne National Laboratory, Reactor Development Program Progress Report, April 1965, USAEC Report ANL-7045, May 19, 1965.
43. Argonne National Laboratory, Reactor Development Program Progress Report, April 1966, USAEC Report ANL-7204, May 31, 1966.
44. W. R. Martin and J. R. Weir, Influence of Grain Size on the Irradiation Embrittlement of Stainless Steel at Elevated Temperatures, *J. Nucl. Mater.*, 18: 108-118 (1966).
45. W. R. Martin and J. R. Weir, Jr., Irradiation Embrittlement of Low- and High-Carbon Stainless Steels at 700°C, 800°C, and 900°C, USAEC Report ORNL-TM-1516, Oak Ridge National Laboratory, June 1966.
46. D. L. Keller, Progress Relating to Civilian Applications During March 1966, USAEC Report BMI-1767, Battelle Memorial Institute, Columbus Laboratories, Apr. 1, 1966.
47. H. Bohm, W. Dienst, H. Hauck, and H. J. Laue, Andering der Mechanischen Eigenschaften von Chrom-Nickel-Stahlen and Nickellegierungen Durch Neutronbestrulung, *J. Nucl. Mater.*, 18: 337-347 (1966).
48. E. E. Bloom, J. O. Stiegler, W. R. Martin, and J. R. Weir, Comparison of Displacement Damage and Strength for Stainless Steel Irradiated at Intermediate Temperatures, USAEC Report ORNL-TM-1535, Oak Ridge National Laboratory, June 1966.
49. P. Patriarca (Comp.), Fuels and Materials Development Program, Quarterly Progress Report for Period Ending March 31, 1965, USAEC Report ORNL-TM-1100, Oak Ridge National Laboratory, June 1965.
50. P. Patriarca (Comp.), Fuels and Materials Development Program, Quarterly Progress Report for Period Ending September 30, 1965, USAEC Report ORNL-TM-1270, Oak Ridge National Laboratory, December 1965.
51. J. E. Irvin and T. T. Claudson, The Effects of Irradiation on the Mechanical Properties of Inconel-Zircaloy Transition Joints, USAEC Report BNWL-190, Battelle Memorial Institute, Pacific Northwest Laboratory, February 1966.
52. E. Cibois, J. Lemaire, and M. Weisz, Reactor Tanks Steels. Irradiation of Tensile-Test Pieces in EL. 3 at Different Temperatures and Postirradiation Tests, Final Report, USAEC–Euratom Report EURAEC-1502 (EUR-2660), Commissariat à l'Énergie Atomique, 1964.
53. W. C. Francis (Ed.), Annual Progress Report on Reactor Fuels and Materials Development for FY 1965, USAEC Report IDO-17154, Phillips Petroleum Company, February 1966.
54. S. T. Konobeevskii, B. M. Levitskii, Yu. N. Sokurskii, and G. A. Andreev, Possibilities and Prospects of Strengthening Metals and Alloys by Irradiation, *Protsessy Uprochneniya Detalei Mashin, Akad. Nauk SSSR*, 104-108 (1964).
55. P. Guyot, Plasticity of Dispersed-Phase-Type Al-Al_2O_3 Alloys, Euratom Report EUR-2483.f, European Atomic Energy Community, September 1965.
56. D. Nobili and M. A. De Bacci, Experimental Investigation of Thermal and Electrical Conductivity of SAP, *J. Nucl. Mater.*, 18: 187-196 (February 1966).
57. R. Nagasaki and K. Shiraishi, Metallographic Observations on Creep Deformation of Magnox AL 80, *J. Nucl. Sci. Technol. (Tokyo)*, 3: 32-40 (January 1966).
58. C. E. Coleman and D. Hardie, The Hydrogen Embrittlement of Zirconium in Slow-Bend Tests, *J. Nucl. Mater.*, 19: 1-8 (April 1966).
59. K. Weinstein, Yield Point Occurrence in Polycrystalline Alpha-Zirconium, USAEC Report CONF-651017-7, 1965.
60. R. F. Gessner, An Examination of the Effects of Thermal Treatment on the Distribution of Alloying Elements in Zircaloy-2, Thesis, USAEC Report WAPD-T-1809, Westinghouse Electric Corporation, Bettis Atomic Power Laboratory, December 1965.
61. C. R. Brooks and E. E. Stansburg, The Specific Heat of Zircaloy-2 from 50 to 700°C, *J. Nucl. Mater.*, 18: 233-234 (1966).
62. C. D. Williams and R. W. Gilbert, Tempered Structures of a Zr-2.5 Wt.% Nb Alloy, *J. Nucl. Mater.*, 18: 161-166 (February 1966).
63. T. F. Fedorov et al., Phase Equilibrium in the Ternary Zr-Co-C and Nb-Fe-C Systems, *Poroshkovaya Met., Akad. Nauk Ukr. SSR*, 12: 63-68 (December 1965).
64. L. Nemethy, Rare Earth Metals in Stainless Steelmaking, *Tech. J., Jamshedpur (India)*, 7(1): 41-48 (February 1965).
65. P. Ravizza and W. Nicodemi, Influence of Traces of Lead and Rare Earths on the Structure and Mechanical Characteristics of Stainless Steel, USAEC Report ORNL-tr-922, translated from *Rev. Met. (Paris)*, 62: 351-357 (1965).
66. R. Sumerling, J. H. Pierce, S. Freeman, and E. Dabring, The Structure of 20Cr-25Ni-Nb Steel After Aging for up to 2000 Hours in the Temperature Range 600-800°C, British Report TRG-Report-1168, 1966.
67. B. J. Seddon, Steels Data Manual, British Report TRG-Report-840, Apr. 9, 1965.
68. General Electric Company, Nuclear Materials and Propulsion Operation, High-Temperature Materials Programs, Part A, Final Annual Report, USAEC Report GEMP-400A, Feb. 28, 1966.
69. G. D. Sandrock, Effect of Cold Reduction on the Embrittlement of L-605 (HS-25), Thesis, Report X66-12625. Case Institute of Technology, 1965.
70. E. Gebhart, W. Duerrschnabel, and G. Hoertz, Study of the System Niobium-Nitrogen: I, Property Changes in Niobium by Dissolved Nitrogen, *J. Nucl. Mater.*, 18: 119-133 (February 1966).
71. G. D. McAdam, Substitutional Niobium Alloys of High Creep Strength, *J. Inst. Metals*, 93: 559-564 (December 1965).
72. C. D. Gemmell and J. E. McNutt, Method of Treating Columbium-Base Alloy, U. S. Patent 3,230,119, to E. I. du Pont de Nemours & Company, Inc., Jan. 18, 1966.
73. R. T. Torgerson and W. A. Baginski, Properties of an Yttrium-Containing Columbium Alloy, *Trans. Met. Soc. AIME*, 236: 158-164 (February 1966).
74. G. F. Ivanovskii and T. N. Zagorskaya, Zone Refining of Molybdenum in High Vacuum, *Izv. Akad. Nauk SSSR, Metal.*, No. 3: 65-69 (May–June 1965).
75. V. M. Pan, Effect of the Degree of Purity of Some Refractory Metals on Their Melting Points, *Sb. Nauchn. Tr., Inst. Metallofiz. Akad. Nauk Ukr. SSR*, 20: 130-132 (1964).
76. E. Pink, Recrystallization Diagrams for Sintered Molybdenum and Tungsten (in German), *Planseeber. Pulvermet.*, 13: 100-104 (August 1965).
77. P. L. Raffo and W. D. Klopp, Influence of Boron Additions on Physical and Mechanical Properties of Arc-Melted Tungsten and Tungsten-1 Percent Tantalum Alloy, Report N66-16420 (NASA-TN-D-3247), National Aeronautics and Space Administration, Lewis Research Center, February 1966.
78. P. L. Raffo and W. D. Klopp, Mechanical Properties of Solid Solution and Carbide Strengthened Arc-Melted Tungsten Alloys, Report NASA-TN-D-3248, National Aeronautics and Space Administration, Lewis Research Center, February 1966.
79. D. H. Dennison, M. J. Tschetter, and K. A. Gschneidner, The Solubility of Tantalum and Tungsten in Liquid Rare-Earth Metals, to be published in *J. Less-Common Metals*.
80. A. F. Weinberg, J. R. Lindgren, N. B. Elsner, and R. G. Mills, Suppression of Grain Growth in Vapor Deposited Tungsten up to 2500°C, *Nucl. Appl.*, 1: 581-583 (December 1965).
81. Battelle Memorial Institute, Columbus Laboratories,

Data Sheets for W-5 Re-2.2 ThO_2 Alloy, USAEC file No. NP-15725, July 13, 1965.

82. M. A. Clauss, Embrittlement of Tantalum by Hydrogen at Room Temperature, in *Colloq. Met. Presses Universitaires, 8e, Centre Études Nucl., Saclay, France*, pp. 29-39, 1965.
83. D. T. Klodt and A. S. Yamamoto, Phase Equilibria of the Tantalum-Rich Region of the Ta-W-Hf and Ta-W-Zr Systems, Final Report, September 1, 1964–November 30, 1965, USAEC Report DRI-1092-226, Denver Research Institute, Dec. 31, 1965.
84. E. M. Savitskii, M. A. Tylkina, and K. B. Povarova, Rhenium Alloys, Report JPRS-34566, translated from *Splavy Reniya*, Nauka Publishing House, Moscow (1965).
85. *Diffusion Processes, Structure, and Properties of Metals*, Consultants Bureau Enterprises Inc., New York, 1965.
    a. S. Z. Bokshtein, M. B. Bronfin, and S. T. Kishkin, Volume and Boundary Diffusion of Tungsten in Molybdenum, pp. 16-23.
    b. M. B. Bronfin, Diffusion of Rhenium in Molybdenum, pp. 24-26.
86. M. C. Naik, Study of the Diffusion of Iron, of Silver, and of Carbon in Beryllium Using Radioactive Tracers, French Report CEA-R-2621, 1965.
87. L. V. Paulinov, A. I. Nabonechnikov, and V. N. Bykov, Uranium Diffusion in Molybdenum, Niobium, Zirconium, and Titanium, *At. Energ.*, 521-523 (1965).
88. M. Hrovat and G. Spencer, Diffusion of Uranium in Graphite (in German), *J. Nucl. Mater.*, 19: 53-58 (April 1966).
89. F. Schmitz and R. Lindner, Diffusion of Heavy Elements in Nuclear Fuels: Actinides in UO_2, *J. Nucl. Mater.*, 17: 259-269 (November 1965).
90. N. L. Peterson and S. J. Rothman, Diffusion in Gamma Uranium, USAEC Report ANL-6568, Argonne National Laboratory, November 1965.
91. Oregon Metallurgical Corp., Oremet HPC 85W-15Mo (High-Temperature Refractory Alloy), *Alloy Digest*, W-9 (August 1965), 2 pp.
92. R. H. Titran and R. W. Hall, Ultrahigh-Vacuum Creep Behavior of Columbium and Tantalum Alloys at 2000 and 2200°F for Times Greater Than 1000 Hours, Report NASA-TN-D-3222, National Aeronautics and Space Administration, Lewis Research Center, January 1966.
93. W. D. Klopp and W. R. Witzke, Mechanical Properties and Recrystallization Behavior of Electron-Beam-Melted Tungsten Compared with Arc-Melted Tungsten, Report NASA-TN-D-3232, National Aeronautics and Space Administration, Lewis Research Center, January 1966.
94. V. P. Severdenko and R. M. Kal'nitskii, Plasticity and Strength of Tungsten During Short-Time Tests, *Issled. Stalei, i Splavov, Akad. Nauk SSSR*, pp. 114-117 (1964).
95. Aerojet-General Nucleonics, Army Gas-Cooled Reactor Systems Program. ML-1-II Fuel Element Design Report, USAEC Report AGN-TM-415, January 1966.
96. A. Gilbert and B. C. Allen, The Notch-Impact Behaviour of Chromium and a Chromium-35 At.% Rhenium Alloy, *J. Inst. Metals*, 93: 529-535 (November 1965).
97. N. J. Grant, P. Bridenbaugh, B. Greene, and R. Kane, Investigation of Fracture in Connection with Hot Deformation Processing of Metals, Final Report, Report AD-626375, Massachusetts Institute of Technology, September 1965.
98. T. C. Wells, Creep Behavior of a Magnesium-Aluminum-Zirconium Alloy at 450°C, *J. Nucl. Mater.*, 17: 274-276 (November 1965).
99. A. Arias, Investigation of the Mechanism by Which Metal Additions Impress the Thermal Shock Resistance of Zirconia, Report NASA-18383, National Aeronautics and Space Administration, Lewis Research Center, July 21, 1966.
100. L. A. Simpson and R. E. Carter, Oxygen Exchange and Diffusion in Calcia-Stabilized Zirconia, *J. Am. Ceram. Soc.*, 49(3): 139-144 (March 1966).
101. W. H. Rhodes and R. E. Carter, Cationic Self-Diffusion in Calcia-Stabilized Zirconia, *J. Am. Ceram. Soc.*, 49(5): 244-249 (May 1966).
102. C. D. Wirkus and D. R. Wilder, High Temperature Oxidation of Molybdenum Disilicide, *J. Am. Ceram. Soc.*, 49(4): 173-176 (April 1966).
103. W. A. Sanders and H. B. Probst, Hardness of Five Borides at 1625°C, *J. Am. Ceram. Soc.*, 49(4): 231-232 (April 1966).
104. G. G. Lessman and D. R. Stoner, Determination of the Weldability and Elevated Temperature Stability of Refractory Metal Alloys, Eighth Quarterly Report, March 21–June 20, 1965, Report N66-14064, Astronuclear Laboratory, 1965.

Section V

Reactor Materials

Special Fabrication Techniques

Melting, Casting, and Fabrication

The Yugoslavians[1] have developed procedures for the injection casting of uranium rods and tubes. They conducted tests to determine the best mold coating and found that the most satisfactory results were achieved when a $MgZrO_3$ ceramic coating was employed.

A method developed by Los Alamos[2] for directionally cooling during solidification has essentially eliminated piping problems in the preparation of ^{233}U castings and the need for excess material in riser–sprue type molds. The equipment and procedures used for casting ^{233}U together with the nuclear safety precautions needed, are described.

The Japanese[3] have studied the effects of carbide inclusions on the formability of metallic uranium. They compared the rolling characteristics and microstructures of commercially pure uranium and uranium containing 1000 ppm carbon. On rolling at 300°C with 12 and 19% reduction per pass, the mean specific rolling pressures were 40 and 52 kg/mm^2 for commercially pure uranium specimens, but 59 and 61 kg/mm^2 for uranium containing 1000 ppm carbon. On the other hand, upon rolling at 600°C with 33% reduction per pass, the mean specific rolling pressure for the two materials was the same, approximately 20 kg/mm^2.

The French[4] have shown that the traditional methods for the continuous casting and extrusion of metals and alloys can be extended to the shaping of certain nonmetallic materials. Continuous casting was used in the preparation of refractory carbides, UC, and alumina. Extrusion was utilized in the preparation of UC and UC_2 shapes. Graphite dies were employed in the latter work. Products obtained by continuous casting were characterized by very low impurity contents, and test pieces prepared by extrusion had highly oriented structures.

Battelle–Columbus[5] has developed an electron-beam melting and drop-casting technique for the preparation of small, high-purity (< 50 ppm total impurities), fine-grained tungsten and tungsten-alloy castings. Twenty-four cylindrical castings of tungsten and tungsten–5, 10, and 20 wt.% tantalum, tungsten–5, 15, and 23 wt.% rhenium, tungsten–2.5 and 5 wt.% osmium, and tungsten–1 and 2 wt.% iridium, $\frac{3}{4}$ in. in diameter and up to $1\frac{3}{4}$ in. long, were satisfactorily prepared by this technique.

The Russians[6] have investigated the gas content, structure, and mechanical properties of vacuum-arc-melted molybdenum, niobium, and titanium, hot rolled with a total reduction of 50% in air, argon, or a vacuum of 5×10^{-5} torr at temperatures up to 1200°C. Hot rolling in air was found to increase the gas content in titanium and niobium appreciably, especially at the higher temperatures. The greatest increase was in oxygen; increases in nitrogen and hydrogen were somewhat smaller. No noticeable increase in the gas content was observed in molybdenum rolled at 1000 to 1200°C, although the molybdenum oxidized extensively.

No noticeable gas absorption occurred during heating and rolling in vacuum. However, heating and rolling of titanium and niobium in an argon atmosphere, as well as heating in vacuum with subsequent rolling in air, resulted in gas absorption. The levels obtained were intermediate between those produced with hot rolling in vacuum and those produced in air. Niobium and titanium hot rolled in vacuum were satisfactorily cold rolled at room temperature. However, in niobium and titanium hot rolled in air, satisfactory plasticity in cold rolling was achieved only after removal of the surface gas-saturated layer, which was about 1 mm thick.

Additional hot rolling of titanium in vacuum or in air at 1100°C with a total reduction of 80% resulted in some fragmentation of the alpha-phase grains. The recrystallized structure of molybdenum and niobium with almost equiaxial grains became fibrous and elongated with additional hot rolling. Niobium and titanium hot rolled in vacuum had lower tensile and yield strengths and higher ductility than after rolling in air. The metals rolled in air failed in a brittle manner; those rolled in a vacuum had a ductile fracture. Rolling in vacuum or in air produced no significant difference in the mechanical properties of molybdenum.

Small levitation melts of vanadium–20 wt.% chromium–10 wt.% aluminum modified with additions of

1 and 2 wt.% zirconium or 0.5 and 1 wt.% yttrium were prepared and were fabricated.[7] These alloys are being studied in liquid-sodium-corrosion studies at Argonne. No improvement in fabrication ease was noted with the zirconium and yttrium additions that were made.

The ingot structure of niobium–zirconium alloys containing small amounts of oxygen solidifying as solid solutions was studied by the Germans.[8] They found that the structure was influenced principally by two factors: (1) by the solidification reaction and (2) by segregation in the solid state which leads to the precipitation of oxygen-rich phases. Both reactions could not be suppressed by the melting and cooling-down conditions (electron-beam and arc-furnace methods) employed and were observed even in cast samples containing the least amount of oxygen.

A process was developed for casting a ternary magnesium–lithium–silicon alloy by the Frankford Arsenal.[9] Because conventional magnesium-sand foundry practice was found to be unsatisfactory, a new molding material, based upon bentonite-bonded graphite powder, was employed. Melting and pouring practice was also modified to cope with the reactive nature of the alloy.

The Bureau of Mines[10] reports the satisfactory preparation by powder metallurgy of tungsten–rhenium and tungsten–rhenium–molybdenum alloy sleeves suitable for subsequent extrusion and drawing to tubing. A large number of these sleeves have been supplied to Argonne National Laboratory, General Electric (NMPO), and Oak Ridge National Laboratory for further processing and evaluation.

Two new melting and casting units have been designed and constructed by the Bureau of Mines.[11] The first is an apparatus for preparing centrifugal castings of metal–carbon alloys; the second is a furnace for preparing reactive metals in a water-cooled copper crucible by induction methods.[10] The technique used with the latter apparatus is similar to that used in electron-beam melting, the major difference being the method of heating the metal. The heating is accomplished by placing both the upper surface of the ingot and the lower end of the feed rod in the field of a work coil which is equipped with a current concentrator. This current concentrator is a split, water-cooled copper cylinder around which the work coil is wound. The effect of the concentration is to produce an intense field in a small volume at the center of the work coil and thus cause sufficient heating to melt metals placed in this field. Unique in this apparatus is the location of the concentrator with respect to the crucible. It is so arranged that the vertical axis of the crucible is perpendicular to and bisects the axis of the horizontal concentrator.

Small-diameter tungsten–26 at.% rhenium tubing and tungsten–30 at.% molybdenum–30 at.% rhenium rod were successfully fabricated at the Minnesota Mining & Manufacturing Co. by the plastic extrusion of mixtures of elemental powders and organic binders followed by sintering.[12] Both tubing and rod were ductile in the as-sintered condition.

Fabrication procedures have been developed at General Electric[13] which result in a homogeneous, sigma-free tungsten–25 at.% rhenium alloy. Sheet, tubing, and rods have been successfully fabricated with homogeneous structures. Powder-processing experiments indicated that improper metal-powder blending and sintering techniques contribute to the sigma-phase segregation and other defects. The segregation of small tungsten-powder particles and sigma-forming agglomerates of rhenium-metal powder in tungsten–25 at.% rhenium was eliminated by wet-blending the metal powders in propanol. Overnight ball milling of the metal-powder–propanol slurry in a glass jar was found satisfactory. After vacuum oven drying, the blended powders were steel-die compacted at 20,000 psia into bar and were presintered in hydrogen at 1200°C for 16 hr.

Sintering studies indicated that a 3000°C treatment for 2 hr in hydrogen was necessary to eliminate the sigma phase. Hot working of sintered tungsten–25 at.% rhenium powder compacts was accomplished by hot-press forging, hot rolling, and extrusion. For hot rolling, sintered bars were heated in hydrogen at 1450°C with the actual rolling conducted in air. A minimum of 80% reduction was preferred in hot rolling to assure full density in finished sheet. Arc-cast tungsten–26 at.% rhenium alloy was similarly worked with equivalent satisfactory results.

Tubing and rods of tungsten–25 at.% rhenium were hot extruded from both cast ingots and sintered powder compacts as starting materials. Molybdenum containers and tube mandrels were used in the extrusion process. Over 20 extrusions were completed with rapid induction heating to 1950°C in argon and loads up to 800 tons on a fast-acting extrusion press. Extrusion ratios of 4:1 and 14:1 (by area) produced acceptable tubular and solid bar shapes. The tungsten–25 at.% rhenium extrusion was recovered by dissolving the molybdenum container material in nitric acid.

Small-diameter (< 5 mm) thin-walled tubing of vanadium–20 wt.% titanium alloy was also prepared at Argonne.[14] This tubing was prepared from electron-beam and arc-melted ingots by extrusion. Tube blanks were cold finished by swaging and drawing to the final tube size with intermediate vacuum anneals.

Premium-quality tungsten sheet and strip were fabricated by rolling bar shapes prepared by a new process developed at Battelle–Columbus.[15] The process was developed for the preparation of high-purity tungsten with unusual resistance to grain growth at elevated temperatures. The hydrogen reduction of tungsten hexafluoride in a fluidized bed of tungsten seed particles was used to prepare the granular

product, and these granules were then consolidated into bar shapes by gas-pressure bonding.

Fabrication techniques were developed and employed at Battelle–Columbus[16] in the preparation of irradiation and calibration samples for a program designed to obtain equilibrium values of ^{233}U buildup in thorium in both fast and slow neutron-flux spectra. Tubular samples were prepared which consisted of cores of thorium or thorium with additions of ^{233}U, gold, or boron surrounded by zirconium cladding metallurgically bonded to the core. Fabrication consisted of (1) melting and casting the core materials; (2) hot- and cold-rolling the core materials to sheet; (3) shearing, machining, and forming the cores to tubular shapes; (4) assembling the cores into and over zirconium cladding; (5) welding the assemblies; (6) gas-pressure bonding; and (7) machining the composites to final dimensions.

Westinghouse[17] reports the preparation of B-66 niobium-alloy and T-111 tantalum-alloy tubing by extruding, rocking, and cold-drawing it to final size. The properties of the tubing are said to compare favorably with those of sheet of the same materials.

The Russians[18] studied the main parameters of rolling niobium in vacuum and in air over the temperature range 300 to 1300°C. It was found that spread, coefficient of friction, and specific pressure in rolling niobium in vacuum are somewhat higher than when rolling in air. Spread basically occurred as a result of barrel formation and the transfer of metal from the lateral to the contact edges. Specific pressure was only slightly dependent upon temperature over the temperature interval studied.

The British[19] have described results of preferred-orientation measurements on Zircaloy-2 tubing produced by 11 fabrication routes. The basic orientation of the hot-extruded stock has the basal (0 0 0 1) poles lying tangential to the circumference, whereas the poles of the prism planes (1 0 $\bar{1}$ 0) are in the axial direction. Tube reduction, cold drawing, or planetary swaging spreads the orientation of the basal poles and shifts their position of maximum intensity to either side of the tangential direction.

Preliminary screening tests of vanadium-base alloys at Argonne[7] have indicated that a vanadium–15 wt.% titanium–7.5 wt.% chromium alloy has greatly improved creep resistance and a somewhat improved sodium corrosion resistance compared with that of vanadium–20 wt.% titanium, an alloy developed earlier. Production-sized ingots of the newer alloy have been prepared by double arc melting under a helium atmosphere and have been successfully processed into tubing, rod, and sheet. Primary fabrication was by double extrusion. Billets were canned in stainless steel to prevent contamination and were extruded at 1100 to 1150°C. Secondary fabrication to rod and sheet by cold rolling presented no difficulties when as-extruded material was vacuum annealed at 850 to 900°C prior to cold working.

(S. G. Nelson)

Pressure Bonding

Gas-pressure bonding was employed as a finishing process to increase the density and tensile strength of plasma-sprayed beryllium.[20] The as-sprayed beryllium generally had a density of 86% of theoretical and exhibited a room-temperature ultimate strength of approximately 31,000 psi. For pressure bonding, beryllium platelets were encased in mild steel and bonded for 1 hr at 1400°F (760°C) and 15,000 psi. This operation increased the density to between 98 and 99% of theoretical and the ultimate strength to 67,000 psi. Ductility values were, however, not increased by pressure bonding. Metallographic examination verified the high measured densities and also showed the isotropic nature of the finished materials.

The combination of plasma-arc deposition and gas-pressure bonding has also been described for the application of refractory cermet and ceramic coatings on refractory metals and alloys.[21] When a thin cermet layer and a subsequent ceramic coating were deposited on the metal substrate, thermal-expansion mismatches across the interface were reduced. The mechanical adherence of the sprayed coatings permitted further finishing by grinding or machining. The final bonding operation served to produce metallurgical bonding to the substrate and high-density coatings. The substrate materials examined in this study included René 41, tungsten, and a TZM alloy. Coatings investigated were of two types: Al_2O_3–Cr_2O_3 combinations that would produce a spinel type structure on exposure to high temperatures, and high-melting oxides such as ZrO_2 and ThO_2. Intermediate cermet layers generally contained 50 wt.% chromium or molybdenum, with the balance as an oxide corresponding to those contained in the coating. Coatings on René 41 substrates were bonded at 2275°F (1246°C) and 10,000 psi for 3 hr. With the tungsten and TZM substrates, the coatings were bonded for 3 hr at 2900°F (1593°C) and 10,000 psi. Metallographic examination of the bonded structure showed that the coating porosity had been reduced to less than 5%, and in all cases good bonding to the substrate was achieved. Under oxyacetylene torch testing, each coating system on a cylindrical specimen afforded oxidation resistance and thermal resistance for 2 to 6 min. Coating of more complex shapes was also demonstrated in this work. (S. W. Porembka)

Canning of Particulate Fuels

A program has been conducted at Argonne[22] to find the factors influencing the economical and simplest method of fabricating entire assemblies in which particulate fuels are used. The portion of the study discussed entails the factors influencing the rate of compact formation. It was found that with the infil-

tration technique the rate of entry of particles into a matrix of larger particles was influenced by frequency of vibration, acceleration, the void fraction in the matrix, column height, and ratio of size of entering particles to size of matrix particles. Infiltration time for both spherical and angular particles decreased with increasing acceleration to about 15 g, whereas infiltration time increased with increasing frequency between 100 and 400 cps. The filtration time of a smaller component varied inversely and exponentially with the void fraction in the matrix.

For spherical particles the minimum diameter ratio of small (infiltrating) particles to large (matrix) particles to allow infiltration is about 5, whereas for angular particles the ratio is about 7. As the ratio increases, infiltration becomes faster until a limiting rate is reached. This maximum for spheres occurs when the size ratio is greater than 11. Angular particles reach a maximum infiltration rate for size ratios above 18.

A study was conducted at Battelle–Northwest[23] to analyze the stresses that cause fatigue failures in Zircaloy-2 cladding during vibratory fuel loading. The study was prompted when a number of fuel tubes cracked at the ends attached to the vibratory unit during the vibratory-compaction operation. A number of tubes were subjected to longitudinal vibrations at various frequencies and with various end-clamp arrangements until they cracked. The stresses, measured with strain gauges located near the end clamps, were found to be great enough to cause fatigue failures of the Zircaloy-2 during the final stages of fuel-powder loading. With a standard clamp the end-cap crevice acts as a stress raiser, and fatigue failure can occur at lower stress values. A modified tapered end clamp with a nylon insert was very effective in reducing fatigue failures by shifting the major stresses to the heavier cladding region of the rod.

(V. D. Linse)

Plating

Nonelectrolytic Chemical Plating

Attempts to determine the cause of the grain refinement occasionally observed in vapor-deposited tungsten were continued at Oak Ridge.[24] Small amounts (<100 ppm) of vanadium added to the tungsten by mixing VF_5 with the WF_6 feed did not produce any grain refinement. The addition did, however, cause a drastic reduction in the amount of tungsten recovery obtained with a given set of deposition conditions and also resulted, under some conditions, in the codeposition of VF_3 with the tungsten.

Oak Ridge[4,24] continued study on the deposition of tungsten–rhenium alloys in a reactor with a moving hot zone. An 8-in.-long furnace was moved along the deposition tube by ¼-in. increments every 15 min. The total movement was 4 to 5 in. A relatively high rhenium content was obtained throughout a greater length of deposit. Metal recoveries ranged from 36% at 600°C to 93% at 800°C. The fraction of tungsten recovered increased and that of rhenium decreased as the deposition temperature increased. In the deposit prepared at 800°C, the composition of the deposit near the inlet end of the tube approached the metal composition of the reacting gases. Layers of varying rhenium content were produced in the deposit by the moving hot-zone method. The grain structure was mostly columnar, although modular growths were observed. Circumferential ridges of varied height, width, and spacing continued to be a characteristic feature of these deposits. The microstructure of a ridge growth was similar to that of modular growths sometimes found in tungsten deposits. Grown-in porosity occurred along the grain interfaces in these growths. The ridges were found to form in the sharp temperature gradient on the inlet end of the hot zone.

The total interstitial impurity content of the alloy deposits[25] was found to be as low as 50 ppm. In the columnar deposits, two phases that coexisted throughout part of the composition range were found: an alpha-tungsten (bcc) structure, which was the principal phase in low-rhenium deposits, and a beta-tungsten phase favored by high-rhenium-content deposits.

The vapor deposition of cobalt–tungsten alloys by hydrogen reduction of the mixed chlorides $CoCl_2$ and WCl_6 has been studied by the Bureau of Mines.[26] Heat-treatment of the near-stoichiometric binary-metallic deposits converted nearly all to the intermetallic compound Co_3W. However, small quantities of both cobalt and tungsten remained. Deposition of cobalt–tungsten in predicted ratios may be attained by proportioning the two metal chlorides in the vapor charges, except where a greatly preponderant tungsten content is sought.

Tensile tests on specimens of the as-deposited material showed that the 75% cobalt–25% tungsten binary deposit was 10% stronger than vapor-deposited cobalt.[26] After specimens of both materials were heat-treated, the binary deposit was twice as strong as the cobalt. However, the tensile strength of the heat-treated binaries was lower than that of the materials as deposited.

The deposition of metals other than tungsten continued to be studied at Oak Ridge as part of the tungsten-alloy-deposition program.[24] The deposition of rhenium from ReF_6 was studied over the temperature range 500 to 700°C. Earlier results were substantiated. Modular growth occurred at the inlet end of the reaction zone under conditions giving high deposition rates. A ductile coating 1 to 2 mils thick and 12 in. long was deposited at 600°C using a hydrogen-to-ReF_6 ratio of 12 at a pressure of 10 torrs. Metal recovery was only 50%.

Molybdenum deposition from MoF_6 using a hydrogen-to-MoF_6 ratio of 40 was carried out over the

600 to 900°C temperature range at pressures[24] of 10 and 100 torrs. Some high-density, smooth deposits were obtained.

A patent has been issued to Brothers and Pesold[27] on the production of the metals niobium, tantalum, molybdenum, and tungsten, but particularly niobium, by reduction of the metal halides with zinc vapor in a reactor at 750 to 1100°C. The reaction mixture is condensed at 350 to 550°C, and the zinc chloride is separated by reheating to 750 to 1100°C in a flow of inert gas.

Vapor-deposition research on uranium oxide has continued at Oak Ridge[24] with a study of the effects of oxygen- and hydrogen-feed concentrations on the stoichiometry of the deposited UO_2. In addition to being influenced by the oxygen concentration, the oxygen-to-uranium ratio increased with increasing deposition rate as the gas ratio remained constant. As deposition rates were increased from 0.004 to 0.011 in./hr, the uranium oxide composition changed from $UO_{2.001}$ to $UO_{2.134}$.

The distribution of films deposited by vacuum evaporation (physical vapor deposition) has been studied at the Dow Chemical Co.[28] Copper was evaporated from two simultaneously emitting tantalum crucibles situated beneath the exterior of a 4.5-in.-radius hemispheric substrate surface. The results indicated that the thickness distributions of films deposited on plane or curved surfaces by physical vapor deposition can be precalculated using Knudsen's cosine law.

At Dow[29] a thin-film deposition-rate monitor has been developed on the basis of the change in frequency produced in a vibrating quartz crystal in an electronic circuit due to the increase in the crystal's mass by the deposit. The frequency of the monitoring crystal is compared with that of a reference crystal by an all-transistorized electronic circuit. The thickness of the film deposit is directly proportional to the change in frequency experienced by the monitoring crystal. The device covers the film-thickness range of 25 to 10,000 A with good accuracy and rapid response. The accuracy is in the range of 1% at the beat frequency of 50 kc.

The growth and annealing of aluminum–silicon films containing up to 3 wt.% silicon, formed by vacuum evaporation, has been studied by electron-microscope and electron-diffraction methods at Argonne.[30] The films were prepared by condensing the vapors from heated aluminum–silicon alloys onto rock-salt substrates. It was found that the presence of 0.1 wt.% silicon disrupted epitaxial growth of aluminum on rock salt at 450°C, and had a marked effect at grain boundaries, although some subgraining and intercrystal dislocations were also observed.

When the silicon content of the film was increased to 1 wt.%, epitaxy was reestablished with rock salt at 450°C. Dislocations were more widely dispersed through these films than they were in films of low silicon content, and dislocation networks at grain boundaries were comparatively rare.

Heating these films to temperatures in the vicinity of 550°C or above produced no structural changes unless melting occurred.

Design considerations useful in setting up and using apparatus for ion plating are discussed in a report issued by Sandia.[31] Ion plating is a modified type of plating by vacuum evaporation or physical vapor deposition in which a high d-c potential is applied between the substrate and the source of evaporating metal. Sputtering of the substrate takes place simultaneously with deposition of material, and a glow discharge also may be present. The process, which has been developed at Sandia, has the advantage of giving coatings of markedly improved adhesion and freedom from porosity as indicated by corrosion tests. The discussion is intended to aid the investigator who wishes to use ion plating in avoiding many of the difficulties frequently encountered and to describe the basic processes involved. (C. F. Powell)

Electroplating

Electroless nickel coatings greatly reduced corrosion of 6061 aluminum-alloy specimens exposed to 25 ft/sec water at 163°C, when the nickel-coated elements were heat-treated for 40 hr at 400°C, which improved the adherence of the nickel coating by diffusion alloying.[32] The aluminum-alloy surface was roughened by pickling before it was plated with about 0.5 mil of nickel in a solution of nickel and hypophosphite ions. Nickel-coated plates are being irradiated to continue the evaluation of the electroless nickel coating.

Investigators at Battelle–Northwest claim improvements in nickel plating on uranium.[33] When a sulfuric–hydrochloric acid solution was used instead of a solution of phosphoric and hydrochloric acids (or other solutions) for anodically treating the uranium, the coarseness of the etch was reduced and the porosity in 8- to 16-μ thick nickel electroplates was substantially reduced. The substitution of bromide for chloride ions in a Watts' nickel-plating bath reduced the activity of the uranium in the acid plating solution and reduced porosity in the nickel plate. Despite these improvements, some porosity was observed in the nickel deposits. There was no attempt, unfortunately, to make use of potent, pore-filling, and leveling addition agents such as coumarin, reported previously as being useful and important for eliminating porosity in nickel plate on uranium.[34]

Electrophoretic coatings that protected a tantalum–tungsten alloy at 300°F (149°C) consisted of (1) zirconia stabilized with magnesium disilicide and calcium oxide or (2) tungsten disilicide stabilized with titanium dioxide and zirconia.[35] The coatings were applied in powder dispersions of the oxides in organic solvents with a potential of 100 to 200 volts, sintered at 1400 or 1600°C with a pressure of 40,000

to 60,000 psi, and subsequently siliconized by heating at 1350°F (732°C) in silicon powder. Two oxide coatings were applied on each tungsten-alloy sample.

A translation of a fairly well-known Russian text on *The Theory and Practice of Chromium Plating* which became accessible recently[36] is worthy of review by anyone making use of chromium electrodeposits for engineering applications. One of the 16 contributors recommends two-layer chromium deposits for resisting mechanical wear and corrosion. For the first, a 20-μ-thick layer which should be nearly poreless, a high temperature of 70°C was selected. For the second, a 30- to 70-μ-thick layer was deposited in cooler solutions (50°C) to increase its hardness and wear resistance. Hardness values of 375 and 900 kg/mm^2 were reported for the first and second layers, respectively. Detailed studies of the effect of other plating conditions on hardness and wear resistance are described by other Russian authors. In a report on the effects of grinding chromium electroplate, a decrease in microhardness and an increase in the amount of cracking were minimized by limiting the thickness of chromium removed in a single pass to 0.01 mm and increasing the amount of cooling lubricant. Conditions also were disclosed for preventing grinding cracks under the chromium plate, which are frequently encountered. In another paper Russian researchers discussed advantages for chromium-plating baths containing sulfate and fluosilicate ions instead of sulfate ions only, thereby agreeing with many U.S. investigators. The addition of several cations had little influence on the chromium-plating process, however.

In a companion translation[37] of another collection of Russian-authored papers, the competing cathode reactions during chromium plating are discussed in some detail. (W. H. Safranek)

Explosive Forming

The first published account of the explosive forming of heavy steel sections has been presented by Helwig and Archibald.[38] They expanded heavy-walled forgings of several nonmagnetic steels into rings of final sizes ranging from 20 to 60 in. in diameter and 3 to 5 in. in wall thickness by a series of several standoff explosive operations. These parts serve as retaining rings in large electrical generators, and the authors report that all 50 to 60 that were explosively fabricated and put into service are performing satisfactorily thus far. Low-cycle tests indicate that fatigue strengths of the explosively formed steels are at least as high as those of conventionally fabricated steel rings.

Explosive welding of an aluminum tube (3.250 in. in outside diameter and 0.028 in. in wall thickness) to the inside of a Zircaloy-4 tube (3.25 in. in nominal inside diameter and 0.100 in. in wall thickness) has been found by Battelle–Columbus[39] to yield sound bonding if a 0.015- to 0.030-in. interface gap is employed and a central charge is detonated to expand the aluminum onto the Zircaloy. Chisel testing of the clad product showed that the unbonded region was limited to a small area at the detonation end.

The effects of irradiation on Zircaloy-2–Inconel transition joints, fabricated both by explosive welding and by coextrusion, were evaluated by Combustion Engineering.[40] Tensile testing was performed in the as-received state, after irradiation at several neutron flux levels and after heating corresponding to the thermal history of the irradiated samples.

In the as-received state and the out-of-reactor heated condition, both types of joints failed in the Zircaloy in a ductile manner and not at the joint interface. However, the irradiated samples all showed loss in ductility. For instance, after an exposure of 1.9×10^{20} neutrons/cm^2 (>1 Mev), the coextruded specimens failed in a very brittle manner with no sign of plastic flow at either room temperature or 550°F (288°C) test temperature. The explosively welded specimens exhibited a failure that was localized but quite ductile at the 550°F temperature. At room temperature the ductility was drastically reduced, but there still was evidence of both macroscopic and microscopic plastic flow. Failure in irradiated samples usually occurred in the Zircaloy very near the interface line.

This unsatisfactory irradiation behavior of both types of Zircaloy–Inconel joints has not been fully explained as yet. However, it has been determined that the hydrogen level in the Zircaloy, which is at acceptable levels in both the as-received state and after out-of-reactor heating, rises to approximately 50 ppm in the explosively welded joints and 100 ppm in the tandem extrusions. (H. S. Gurev)

Welding and Brazing

Aluminum

Much of the current development work on the welding of aluminum alloys is in support of Saturn fabrication problems for the National Aeronautics and Space Administration (NASA). The programs being conducted by several different organizations were reviewed at a conference[41] at Huntsville, Ala., in January. Presented were the current results of programs on base-metal composition–weld-defect relations, mechanisms of porosity formation, gas contaminants as a source of weld defects, effect of porosity on weld mechanical properties, welding-process-parameter transferability, time–temperature controls, nonvacuum electron-beam welding, and portable induction-brazing systems. Almost all the research is being undertaken on alloys 2219 and 2014. Recently, a program was initiated at Battelle for the Redstone Scientific Information Center which

has the objective of assimilating, correlating, and analyzing the combined results of the NASA weld-development complex.

Investigators at Southwest Research are using hydraulic-bulge and uniaxial tensile tests[42] to evaluate TIG and MIG welds in alloys X7106-T63 and 2219-T87. The tensile properties after aging as long as 19 weeks indicate that TIG welds in alloy X7106-T63 are slightly superior to MIG welds after aging for 4 weeks. Crack susceptibility (Houldcroft restraint test) in 0.090-in. X7106-T63 showed that this alloy is more susceptible to hot cracking than alloy 2219-T87. The mechanical properties of the experimental welds are shown in Fig. V-1.

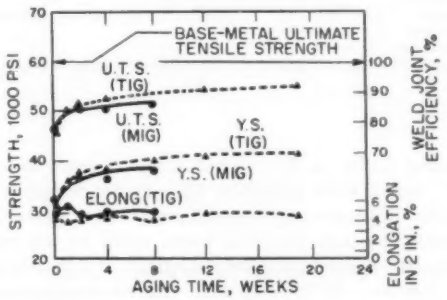

Fig. V-1 Mechanical properties of MIG and TIG X7106-T63/X5180 weldments.[42]

Design data have been developed for the use of aluminum alloy 7039-T61 at ACF Industries, Inc.[43] The data cover the range +400°F to −320°F and include thermal conductivity in addition to longitudinal and transverse, notched and unnotched tensile properties of welds and the base metal. All welds were heat-treated to the T61 condition, and three different filler metals were evaluated. The filler-metal and base-metal compositions are given in Table V-1. It was concluded from this program that 7039-T61 was less notch sensitive than 7079-T6 (NTS 7039-T61 was 59,500 psi at −320°F and 56,300 psi at −423°F vs. 43,700 and 43,400 psi for 7079-T6), but the yield strength of 7039-T61 at room temperature was low (45,000 vs. 60,000 psi for 7079-T6). Cracking occurred in welds made with filler metal D1707 but not with X5039 or D1495. The D1495 filler metal gave higher mechanical properties than the X5039 alloy.

Steel

The welding of the maraging steels, especially the most important 18% nickel (250) grade, has been the subject of much research. The major problem has been the low toughness of the weldments. One of the process variations that appears to aid in producing better toughness in maraging-steel weldments is that used by Excelco Developments and identified as BIG TIG. Not much has been published about the technique, but it is another version of high-current-density TIG welding. Large electrodes, larger than usual feed wires, and high feed rates are distinguishing features. The technique is compared to others from the viewpoint of process parameters, and the results are given in Table V-2. A net gain in weld-fabrication time of about 2% results from using BIG TIG.[44]

Beryllium

New brazing alloys with improved flow on beryllium are under development at Solar.[45] A list of the alloys under study is given in Table V-3. Flow characteristics in argon and in vacuum are being evaluated as a function of composition. The effect of beryllium oxide, in the base metal and as a result of brazing-atmosphere condition, is also under study. The flow of silver-base alloys is enhanced by the addition of phosphorus, lithium, indium, copper, and titanium. These additions also increase the tolerance of the brazing alloy for oxygen in the system. Higher levels of oxygen in both the brazing atmosphere and in the beryllium can be tolerated when the additives are present.

Molybdenum

General Electric engineers have been concerned with the development of a molybdenum welding stock that retains its ductility after heating to 1600°C or after welding.[46] Arc-cast molybdenum loses ductility above this temperature, and powder-metallurgy molybdenum is not considered weldable. Pressed powder compacts are heated to lower the carbon and oxygen to less than 10 ppm each to accomplish the objective. This is being done by heating at 1000°C in wet hydrogen for long periods of time followed by a second long-time heat in dry hydrogen at the same temperature and then at 1450°C. The times of exposure for each of the three treatments were not noted. Comparative weldability tests made by bend-

Table V-1 ALUMINUM-FILLER AND BASE-METAL COMPOSITIONS[43]

Alloy	Composition, wt.%							
	Zn	Mg	Mn	Cr	Si	Fe	Cu	Ti
X5039 filler metal	3.10	3.7	0.37			0.17	0.07	0.10
D1495 filler metal	4.37	3.2	0.36	0.10	0.10	0.07	0.05	0.03
D1707 filler metal	7.50	2.9	0.05	0.11	0.10	0.10	0.06	0.03
7039 base metal	3.5–4.5	2.3–3.3	0.01–0.40	0.15–0.25	0.30 max.	0.40 max.	0.10	

Table V-2 COMPARISON OF WELD METHODS FOR 18% NICKEL MARAGING STEEL[44]

Method	Torch speed, in./min (approx.)	No. of passes	Current av., amp	Voltage av.	Gas flow, cu ft/hr	Type of cover	Types of defects found	Method used to repair	Weld-tensile properties	Weld toughness
TIG	2 to 5	24 to 30	110	8	35	Argon	Porosity, tungsten inclusion, lack-of-fusion zones	TIG	95% plate	Equal or better than plate
Excelco ¼ TIG	12 to 15	8 to 10	340	10	40	Argon	Minor porosity, minor lack-of-fusion zones	TIG	95% plate	10% better than plate
Sub arc	8 to 12	6	400	28	Flux	Flux, no or low Si and Mn	Cracks and longitudinal cracks, lack of fusion, undercut	TIG	Erratic, depends on Ti loss	Usually less than 50% of plate
MIG	19	18	330	28	30	Argon–helium mixture	Porosity and undercut	MIG or TIG	90% plate	90% of plate
Short arc	19	26	330	28	30	Argon–helium mixture	Porosity, lack of fusion	TIG	90% plate	Equal to plate
Plasma arc	6	4	275	21	50	Argon–helium mixture	Porosity and longitudinal cracks	TIG	Not known	Not known
Electron beam	50	1 or 2		20,000/200,000	Vacuum	Vacuum	Lack of fusion	Electron beam	Not known	Not known

Table V-3 BRAZE ALLOY WETTING AND FLOW RESULTS ON SR200C BERYLLIUM–ARGON ATMOSPHERE[45]

Alloy composition, wt.%	Melt, °F	Wet, °F	Flow, °F	Max. temp., °F
Silver-Base Alloys				
Ag–1 Li	1250–1400	>1400	<1650	1750
Ag–3 Li	1250	1340	1550	1750
Ag–2 Li	1540	1650	>1650	1800
Ag–5 Li	1300	1400	>1400 <1700	1800
Ag–7 Ge	1260	1590	>1590 <1700	1700
Ag–4.5 Si	1525	1675	1725	1800
Ag–4.5 Si–0.2 Ti	1590	1660	1700	1700
Ag–4.5 Si–1.0 Cu	1530	1650	1700	1800
Ag–1 Be	1600	1750	1800	1850
Ag–1 Be–0.5 Ti	1560	1680	1720	1800
Ag–30 Be–4.0 Al–3.0 Ge	>1850			1850
Ag–15 Be–5.1 Al–3.4 Ge	>1800			1800
Ag–7.5 Cu	1580	1600	1610	1700
Ag–7.5 Cu–0.1 Li	1520	1590	1690	1820
Ag–7.5 Cu–1.0 Li	1370	1480	1520	1750
Ag–7.5 Cu–10 Li	1150	1250	1350	1700
Ag–7.5 Cu–0.3 Ti	1600	1650	1660	1750
Ag–7.5 Cu–1.0 Be	1550	1590	1610	1750
Ag–7.5 Cu–0.075 P	1460	1610	1635	1700
Ag–7.5 Cu–0.75 P	1520	1610	1670	1800
Ag–24 Cu–15 In	1180	1250	1320	1800
Ag–7.5 Cu–1 In	1530	1560	1580	1750
Ag–7.5 Cu–5 In	1515	1545	1590	1750
Ag–7.5 Cu–15 In	1480	1510	1550	1750
Ag–7.5 Cu–1 Si	1500	1580	1600	1750
Ag–7.5 Cu–5 Si	1515	(Oxide shell prevented wetting and flow)		
Ag–7.5 Cu–1 Ge	1480	1540	1620	1750
Ag–7.5 Cu–10 Ge		(Oxide shell prevented wetting and flow)		
Ag–5 Al–0.2 Mn	>1850			1850
Ag–5 Al	1720	1760	>1760	1825
Ag–6 Al–4 Ge	1150	1500	>1500	1750
Ag–1 P	1350	1490	1620	1650
Ag–1 P	1350	1550	>1550	1900
Beryllium-Base Alloys				
Be–5 Ti	>1800			1800
Be–15 Ge–10 Cu	>2000			2000
Titanium-Base Alloys				
Ti–5.6 Be (2% BeO)	1870	1900	1900	1915
Ti–5.6 Be (0.01% BeO)	1790	1800	1800	1860
Ti–47.2 Zr–5.6 Be	1470	1540	1590	1635
Ti–47.2 Zr–5.6 Be	1450	1610	1620	1800

testing welds in the treated sheet showed that 45 to 90° bends were possible. This is not possible with welds in untreated molybdenum. The welds were slightly porous. Electron-beam welds in the treated material showed good bend ductility at a temperature as low as –50°C compared with the commonly accepted 100°C ductile-to-brittle transition temperature for ordinary commercial molybdenum.

Niobium

In previous reviews of this series, research at General Electric on the stability of welds in niobium alloys was reported. Westinghouse investigators are conducting similar studies on niobium alloys, tantalum alloys, and tungsten alloys.[47] An important part of their eighth quarterly report covers the effect of the addition of yttrium to alloy D-43. As with C-129Y and AS-55, yttrium additions to D-43 resulted in improved weld ductility. Weld parameters were varied over a broad range, and welds were bend tested in both the longitudinal and transverse directions. In addition to the improved performance of yttrium-modified D-43 alloy (D-43Y), the postweld annealing response for 1-hr anneals at 1900, 2100, and 2400°F (1315°C) of D-43Y was considerably different from that of D-43. Annealing resulted in moderately improved weld ductility for D-43Y, whereas D-43 alloy responded to increased annealing temperature by displaying a severe loss and then recovery of ductility through an apparent age–overage reaction. D-43Y alloy displayed a hot-tearing tendency in TIG welding, the cause of which was not determined.

The study of embrittling aging reactions of welds in niobium alloy Cb-752 is continuing at Oak Ridge.[48] The bend-test data reported for aged Cb-752 TIG welds are plotted in Fig. V-2. (R. M. Evans)

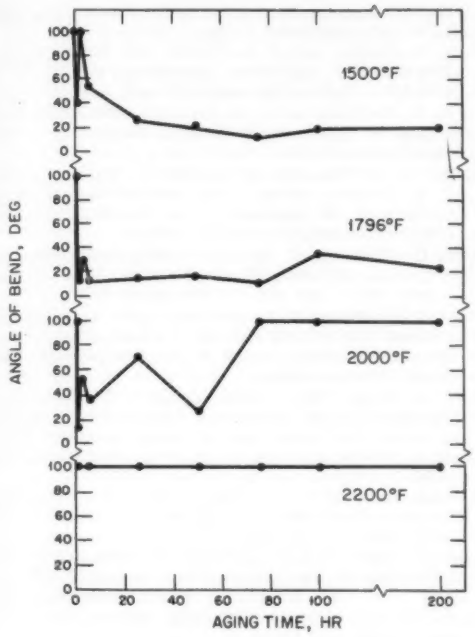

Fig. V-2 Results of room-temperature bend tests on aged Cb-752 TIG welds.[48]

Nondestructive Testing

Ultrasonic Techniques

An interesting technique for inspecting weldments has been developed by researchers at Automation Industries Inc.[49] Designated "Ultrasonic Delta Configuration Inspection Technique," the system uses a dual search unit to scan the specimen. Ultrasonic energy from the transmitting search unit impinges on the surface of the test specimen at an incidence angle. Apparently, energy undergoing mode conversion at a discontinuity caused by a defect propagates to the side of the specimen opposite the search units where it is reflected back to the receiving unit located directly over the defect.

Ultrasonic systems for evaluating the bond strength of adhesives are commercially available. These require very careful and difficult calibration procedures. The measurements give either the cohesive strength of the adhesive or they indicate lack of bond. Researchers at General American Transportation Corp. have been investigating the use of the generation of acoustical energy when stresses are applied to materials in structure tests of adhesive bonds.[50] Transducers sensitive to ultrasonic vibrations are mounted to the surface of the test specimen in the vicinity of the bond. When the bond line of the test specimen is stressed in tension, the adhesive emits many very short-duration bursts of ultrasonic energy. These bursts of energy are detected, amplified, and filtered. Frequencies before 16 khertz are rejected to eliminate noise generated in the supporting structures, and predictions are based on frequencies above 16 khertz. The amplitude of the emission increases significantly as the yield stress is approached, and the point of initiation of this emission change can be used to predict the yield point accurately without noticeable damage to the structure. For each type of adhesive, there is a large increase in noise above 16 khertz as the stress approaches the ultimate strength of the bond.

A suction-cup method has been devised to inspect honeycombs. Honeycomb panels with phenolic cores present a problem in that the phenolic material generates more ultrasonic energy than does the adhesive.

A bibliography referencing theory and application of nondestructive testing for composites has been compiled at North American Aviation.[51] This bibliography is partially annotated and contains 222 pages. It includes references to general papers in nondestructive testing, ultrasonic methods and equipment, acoustic theory, nondestructive methods of bond inspection, ultrasonic applications to QC, ultrasonic applications not to QC, standards, honeycomb materials, reinforced composites, and patents. The compilers have attempted to use fairly current information, and thus the bibliography should be of considerable value to anyone concerned with this field. (D. Ensminger)

NDT Methods Other Than Ultrasonic

An investigation of neutron imaging with the aid of a special closed-circuit television system is being continued at Argonne.[52] Tests that have been conducted on a new 15-cm-diameter input-target-intensifier tube indicate that the output brightness is much superior to that obtained on either of two tubes studied previously. The output brightness at 28-kv accelerating voltage on the tube is reported to be in excess of 100 ft-lumen for a thermal-neutron intensity of about 2×10^7 neutrons/(cm^2)(sec) at the tube window. Values measured under similar conditions for the earlier intensifier tubes were 18 and 28.5 ft-lumen. The improvement is attributed to the use of an alpha-sensitive phosphor that provides a better spectral match with the response of the photoemissive layer. Measurements indicate that gamma intensities of 4000 r/hr would cause little difficulty with the new tube, and further tests are in progress to determine if the value can be extended. The new tube can follow high-contrast object movement at least as fast as 5 m/min, and high-contrast resolution (hole size observable) is about 0.35 mm through the television system. Contrast capability is of the order of 6%.

A precision of 0.2% in measuring a 0.020-in.-wall thickness in stainless-steel tubing is reported by investigators at Oak Ridge[53] who are studying an

X-ray scintillation technique. A crystal of NaI(Tl) is mounted on the end of a quartz or Lucite light pipe and inserted into the tubing for the measurement, which is based on X-ray attenuation. A comparison of the performance of Lucite and quartz rods was made in which the rods were $^5/_{16}$ in. in diameter and 20 in. long, the crystals were $^1/_4$ by $^1/_2$ in. long, and an RCA 6342A photomultiplier tube was used to detect the light. Very little difference in the transmission efficiency of the two types of light pipe was observed, leading to the choice of Lucite for further studies of shape, size, and material.

(A. F. Leatherman)

References

1. N. Obradovic, Experiences with Uranium Rod Melting and Casting, Report CONF-207-16, presented at the Second Yugoslavian–Polish Symposium on Uranium Technology and Metallurgy, Zakopane, Poland, September 1963.
2. R. R. Gilmore and D. R. Harbur, High Yield ^{233}U Casting Operations, USAEC Report LA-DC-7510, Los Alamos Scientific Laboratory, November 1965.
3. H. Watanabe, Ductility of Metallic Uranium Containing Carbide Inclusions at Rolling, *Nippon Genshiryoku Gakkaishi*, 8: 70-75 (1966).
4. P. Magnier, M. Marchal, J. Trouve, and A. Accary, The Casting and Extrusion of Refractories, *Bull. Soc. Franc. Ceram.*, 66: 23-38 (January–March 1965).
5. S. G. Nelson and E. L. Foster, Jr., The Preparation and Evaluation of High-Purity Fine-Grained Tungsten and Tungsten Alloy Castings, Report N-65-31175 (NASA-CR-54374), Battelle Memorial Institute, July 9, 1965.
6. Y. A. Burevich and V. L. Orzhekhovski, Effect of the Conditions of Hot Plastic Deformation on the Structure and Properties of Molybdenum, Niobium, and Titanium, *Izv. Akad. Nauk SSSR, Metal.*, 4: 137-143 (July–August 1965).
7. Argonne National Laboratory, Reactor Development Program Progress Report, February 1966, USAEC Report ANL-7176, Mar. 23, 1966.
8. V. Greiter, D. Hauck, and R. Reinbach, On the Interpretation of the Ingot Structure of the Nb–25 Zr Alloy with Low Oxygen Contents, *Z. Metallk.*, 57: 113-117 (February 1966).
9. A. Saia and R. E. Edelman, Process Development of Shaped Magnesium–Lithium Castings, USAEC file No. NP-15881, Frankford Arsenal (November 1965).
10. Bureau of Mines, Albany Metallurgy Research Center, Quarterly Metallurgy Progress Report No. 30, January 1–March 31, 1966, USAEC Report USBM-RC-1232.
11. P. G. Clites, Vacuum Induction Melting of Reactive Metals in Water-Cooled Crucibles, paper to be published in the Transactions of the Ninth Annual Conference of the Vacuum Metallurgy Division of the American Vacuum Society, 1966.
12. H. G. Sowman, A. Milner, and D. D. Rowenhorst, Fabrication of Tungsten Alloy Tubing, USAEC Report COO-1518-2, Minnesota Mining & Manufacturing Co., Feb. 10, 1966.
13. W. G. Baxter, C. O. Tarr, and J. A. McGurty, Development and Evaluation of a Homogeneous W–25 At.% Re Alloy for 2600°C Applications, USAEC Report CONF-650449-1, General Electric Company, 1965.
14. W. R. Burt, W. C. Kammer, W. C. Karasek, and R. M. Mayfield, Fabrication of V–20 Wt.% Ti Alloy Tubing for Nuclear Fuel Cladding, *Nucl. Appl.*, 1: 589-596 (December 1965).
15. J. H. Oxley, E. A. Beidler, C. J. Lyons, J. M. Blocker, Jr., R. S. Park, and J. H. Pearson, Fluidized-Bed Process for Production of Tungsten, *Nucl. Appl.*, 1: 567-574 (December 1965).
16. S. G. Nelson and E. L. Foster, Jr., Development of Thorium–^{233}U Irradiation Specimens, USAEC Report BMI-1761, Battelle Memorial Institute, Feb. 10, 1966.
17. R. W. Buckman and J. L. Godshall, Refractory Alloy Tubing for Space Power Systems, *Metal Progr.*, 89(3): 105-110 (March 1966).
18. M. V. Mal'tsev, F. E. Dolzhenkov, Yu. M. Sigalow, F. R. Volchek, and Yu. I. Bat, Study of Vacuum Rolling of Niobium (In Russian), *Sb. Tr. Ukr. Nauchn-Issled. Inst. Metalloved.*, 10: 181-188 (1964).
19. E. D. Hindle and G. F. Slattery, Preferred Orientation in Zircaloy-2 Tubing Manufactured by Various Routes, *J. Inst. Metals*, 93: 565-570 (December 1965).
20. T. J. Roseberry, M. L. Headman, and F. L. Parkinson, Process Development and Evaluation of Plasma-Sprayed Beryllium, Report N-65-22107, Western Gear Corp., September 1964.
21. T. R. Wright, R. J. Diersing, and D. C. Carmichael, Ceramic Coatings for the High Temperature Protection of Refractory Metal Shapes, paper presented at the American Ceramic Society Meeting, Washington, May 1966.
22. Argonne National Laboratory, Reactor Development Program Progress Report, March 1966, USAEC Report ANL-7193, Apr. 22, 1966.
23. R. L. Gibby and R. J. Lobsinger, Stresses in Zircaloy-2 Cladding During Vibratory Fuel Loading, USAEC Report BNWL-194, Battelle–Northwest, February 1966.
24. P. Patriarca (Comp.), Oak Ridge National Laboratory, unpublished, June 1965.
25. J. I. Federer and C. F. Leitten, Jr., Vapor Deposition and Characterization of Tungsten–Rhenium Alloys, *Nucl. Appl.*, 1: 575-580 (December 1965); also USAEC Report ORNL-P-1017.
26. J. G. Donaldson, Vapor Deposition of Cobalt–Tungsten Alloys, Report BM-RI-6713, Bureau of Mines, Rolla Metallurgy Research Center, June 1965.
27. J. A. Brothers and W. F. Pesold, Production of Niobium by Vapor Phase Reduction of Niobium Pentachloride, U. S. Patent No. 3,216,822, to Wyandotte Chemicals Corp., Nov. 9, 1965.
28. R. L. Beno, Vapor-Deposited Film Distribution on Curved Substrate Surfaces, USAEC Report RFP-647, The Dow Chemical Co., Rocky Flats Division, Mar. 1, 1966.
29. T. Van Vorous, G. E. Hart, J. L. Martinez, and R. L. Beno, Thin Film Evaporation Rate Monitor, USAEC Report RFP-602, The Dow Chemical Co., Rocky Flats Division, Feb. 17, 1966.
30. R. K. Hart and D. G. Pilney, Growth and Annealing of Evaporated Aluminum–Silicon Films, USAEC Report ANL-7102, Argonne National Laboratory, November 1965.
31. D. M. Mattox, Design Considerations for Ion Plating, USAEC Report SC-R-65-997, Sandia Corp., January 1966.
32. Phillips Petroleum Company, Nuclear Technology Branches Quarterly Report, July 1–September 30, 1965, USAEC Report IDO-17147, April 1966.
33. J. R. Lundquist and R. W. Stromatt, Nickel Electroplating on Uranium: Surface Preparation and Plating Solution Studies, USAEC Report BNWL-124, Battelle–Northwest, October 1965.
34. J. G. Beach and C. L. Faust, Electroplates on Thorium and Uranium for Corrosion Protection and to Aid Joining, USAEC Report BMI-1537, Battelle Memorial Institute, Aug. 14, 1961.
35. P. F. Campbell, K. A. Cabler, and M. H. Ortner, Electrophoretic Deposition of Graduated Oxidation-Resistant Coatings on Tantalum-10 Tungsten Alloy, Report N66-19038 (NASA-CR-66068), Vitro Laboratories, June 1965.
36. A. T. Vagramyan and N. T. Kudryavtsev (Eds.), Theory and Practice of Chromium Plating, Report TT-65-50001 (English Translation from Russian), 1957.

37. Contribution to the Theory of Chromium Plating, Report TT-65-50002 (English Translation from Russian), 1959.
38. M. W. Helwig and P. A. Archibald, Explosive Forming of Heavy-Walled Forgings, *Metal Progr.*, 89(3): 65-69 (March 1966).
39. S. W. Porembka, R. H. Wittman, and R. J. Carlson, Explosively Welding Duplex Zircaloy–Aluminum Tubing, Battelle Memorial Institute, Columbus Laboratories, April 1966.
40. J. F. Gibbons, L. E. Anderson, R. W. Knapp, F. T. Grubelich, and W. Mordarski, Advanced BONUS Core Development Program. Final Report, USAEC Report CEND-265, Combustion Engineering, Inc., Nuclear Division, Feb. 28, 1966.
41. Aluminum Weld Development Complex Conference, George C. Marshall Space Flight Center, Jan. 19, 1966.
42. H. C. Burghard, Jr., N. G. Lenamond, and K. K. Speirs, Development of Welding Techniques and Filler Metals for High Strength Aluminum Alloys, Third Quarterly Report X65-15874, Southwest Research Institute, Apr. 15, 1965.
43. J. J. Dillon and L. A. Wallace, Cryogenic and Elevated Temperature Properties of 7039 Aluminum Plate and Weldments, USAEC Report ACF-14 (ACF-412-262), ACF Industries, Inc., Oct. 8, 1965.
44. W. D. Abbott and L. A. Brooks, Investigation of Sub Arc, Excelco Big TIG and Other Welding Processes on 18 Percent Nickel Maraging Steel, Report CR-57856, Excelco Development Inc., March 1965.
45. R. G. Bogowitz and A. G. Metcalfe, Brazing Beryllium by Capillary Flow, Interim Technical Documentary Progress Report No. 2, Solar, Division of International Harvester Co., Jan. 24, 1966.
46. General Electric Company, Nuclear Materials and Propulsion Operation, High-Temperature Materials Program Progress Report No. 59, Part A, USAEC Report GEMP-59A, May 31, 1966.
47. G. G. Lessmann and D. R. Stoner, Determination of the Weldability and Elevated Temperature Stability of Refractory Metal Alloys, Quarterly Report No. 8, March 21–June 20, 1965, Report WANL-PR(P)-008 (NASA-CR-54723), Westinghouse Electric Corp., Astronuclear Laboratory.
48. W. O. Harms (Comp.), Oak Ridge National Laboratory, unpublished, May 1966.
49. G. L. Cross, H. R. Ellerington, and B. T. Cross, Advancement of Ultrasonic Techniques Using Reradiated Sound Energies for Nondestructive Evaluation of Weldments, Quarterly Progress Report No. 1, Automation Industries, Inc., Nov. 15, 1965.
50. G. Schmitz and L. Frank, Nondestructive Testing for Evaluation of Strength of Bonded Material, Report N66-11761 (NASA-CR-67983), General American Research Division, General American Transportation Corp., September 1965.
51. G. Martin and J. F. Moore, Bibliography of Nondestructive Testing—Theory and Application for Composites, Report N66-13338 (NASA-CR-68604), North American Aviation, Inc., Oct. 15, 1965.
52. Argonne National Laboratory, Reactor Development Program Progress Report, April 1966, USAEC Report ANL-7204, May 31, 1966.
53. P. Patriarca (Comp.), Oak Ridge National Laboratory, unpublished, December 1965.

NUCLEAR SCIENCE ABSTRACTS

The U. S. Atomic Energy Commission, Division of Technical Information, publishes *Nuclear Science Abstracts* (*NSA*), a semimonthly journal containing abstracts of the literature of nuclear science and engineering.

NSA covers (1) research reports of the U. S. Atomic Energy Commission and its contractors; (2) research reports of government agencies, universities, and industrial research organizations on a worldwide basis; and (3) translations, patents, books, and articles appearing in technical and scientific journals.

Complete indexes covering subject, author, source, and report number are included in each issue. These are cumulated quarterly, semiannually, and annually providing a detailed and convenient key to the literature.

Availability of *NSA*

SALE *NSA* is available on subscription from the Superintendent of Documents, U. S. Government Printing Office, Washington, D. C., 20402, at $30.00 per year for the semimonthly abstract issues and $22.00 per year for the four cumulated-index issues. Subscriptions are postpaid within the United States, Canada, Mexico, and all Central and South American countries, except Argentina, Brazil, Guyana, French Guiana, Surinam, and British Honduras. Subscribers in these Central and South American countries, and in all other countries throughout the world, should remit $37.00 per year for subscriptions to semimonthly abstract issues and $25.00 per year for the four cumulated-index issues.

EXCHANGE *NSA* is also available on an exchange basis to universities, research institutions, industrial firms, and publishers of scientific information. Inquiries should be directed to the Division of Technical Information Extension, U. S. Atomic Energy Commission, P. O. Box 62, Oak Ridge, Tennessee, 37830.

Index

Reactor Materials

Volume 9

Note: The page range for each of the four issues of Vol. 9 is as follows: No. 1, pages 1 to 72; No. 2, pages 73 to 150; No. 3, pages 151 to 202; No. 4, pages 203 to 265.

A

1541 alloy (irradiated)
  tensile properties, 241
A-110 AT (irradiated)
  properties, 192
A-356 (irradiated)
  properties, 192
Actinide elements
  diffusion in UO_2 compacts, 82
Adhesives
  ultrasonic testing, 263
Alkali metals (molten)
  corrosive effects, 107
Alloy 718
  physical metallurgy, 50-51
Alloys
  brazing, corrosion of, 36
  corrosion, 107
  diffusion in, 131-32
  reactions with water, 41-43
  stress-corrosion cracking, 175
Alloys (irradiated)
  properties, 117, 192
Alloys (refractory metal)
  chemical plating of, 199
  protective coatings for, 199
  thermal properties, 184
  welding, 142-44
Alloys (refractory metal)(irradiated)
  properties, 115, 241-43
Alloys (refractory metal)(Nb-refractory metal)
Aluminum
  bonding, 68, 147, 198
  coating of Nb and Nb alloys with, 199
  corrosion, 36, 103, 177-78
  extrusion of honeycomb structure, 64
  Ni deposition on, 140
  plating on U, 151, 200
  reaction with UO_2, 82
  reaction with water, 43
  solubility in molten Zn, 236
  solubility in Y_2C, 131
  ultrasonic testing for fatigue cracks, 200
  welding, 68
Aluminum (irradiated)
  corrosion, 174
  lattice parameters, 49
  primary knock-on recoil spectrum, 192-93
Aluminum (molten)
  U diffusion in, 189
Aluminum (Ni plated)
  corrosion, 103
Aluminum (SAP)
  deformation, 123
  plasticity, 243
  thermal conductivity, 243
Aluminum alloy coatings (Al–U)
  oxidation, 66
Aluminum alloy dispersions (Al(1100)–PuO_2)
  development, 9
Aluminum alloy tubes (Al–Fe–U)(Zircaloy clad)(irradiated)
  swelling, 2-4
Aluminum alloys
  (see also A-356(irradiated))
  cavitation, 105
  chemical milling, 141-42
  Ni deposition on, 140
  ultrasonic testing for fatigue cracks, 200
  welding, 260-61
Aluminum alloys (1100)
  corrosion, 36
  fatigue behavior, 180
  use in brazing of Be, 168
Aluminum alloys (6061)
  electroplating with Ni, 259
Aluminum alloys (6061)(irradiated)
  properties, 115, 192
Aluminum alloys (6061-T6)
  corrosion, 36
Aluminum alloys (7075)(irradiated)
  properties, 192
Aluminum alloys (Al–Be)
  phase studies, 92-93
Aluminum alloys (Al–Cr–Fe–Y)
  (see also 1541 alloy)
  oxidation, 79
  properties, 244-45
Aluminum alloys (Al–Cr–Fe–Y)(irradiated)
  ductile–brittle transition temperature, 115
  hardness, 115
  tensile properties, 190
Aluminum alloys (Al–Cr–Ti–V)
  friction welding, 68
Aluminum alloys (Al–Cr–V)
  corrosion, 109, 233
Aluminum alloys (Al–Cr–V–Y)
  fabrication, 255-56
Aluminum alloys (Al–Cr–V–Zr)
  fabrication, 255-56
Aluminum alloys (Al–Hf–Nb)
  oxidation, 100
Aluminum alloys (Al–Hf–Ta)
  oxidation, 100
Aluminum alloys (Al–Fe–U)
  precipitate solution in, 73
  UAl_3 precipitates in, 151-52
Aluminum alloys (Al–Mg–Zr)
  creep properties, 251
Aluminum alloys (Al–Mo–Ti–V)
  properties, 183
Aluminum alloys (Al–Mo–U)(Al clad)(irradiated)
  properties, 203-4
Aluminum alloys (Al–Nb–Ta–Ti)
  crack growth, 230
  welding, 145
Aluminum alloys (Al–Sn)
  coating of Nb and Nb alloys with, 199
Aluminum alloys (Al–Ti–V)
  crack growth, 230
  welding, 68, 145
Aluminum alloys (Al–U)
  transformation, 1, 74
Aluminum alloys (Al–V)
  corrosion, 109
Aluminum alloys (Al–Y)
  corrosion, 103
Aluminum alloys (Al–Zn)
  corrosion, 103
Aluminum alloys (Al–Zr)
  electrodeposition of, 140-41
Aluminum alloys (high strength)
  fracture strength, 117
Aluminum alloys (irradiated)
  damage, 115
Aluminum coatings (Al–Sn)
  behavior, 231-32
Aluminum dispersion films (Al–UAl_4)(irradiated)
  fission-fragment tracks, 17
Aluminum dispersions (Al–Eu molybdate–Eu_2O_3)(Al clad)(irradiated)
  dimensional stability, 101
Aluminum dispersions (Al–U aluminide)
  fabrication, 208
Aluminum dispersions (Al–U aluminide)(irradiated)
  properties, 208
Aluminum fused slurry coatings
  development and evaluation, 106
Aluminum intermetallic compound coatings (UAl_3)
  oxidation, 66
Aluminum intermetallic compound dispersion films (Al–UAl_4)(irradiated)
  fission-fragment tracks, 17

Aluminum intermetallic compound dispersions (Al–U aluminide)
fabrication, 208
Aluminum intermetallic compound dispersions (Al–U aluminide)(irradiated)
properties, 208
Aluminum intermetallic compounds (UAl_2)
precipitation in Al–Fe–U alloys, 151-52
preparation, 208
Aluminum intermetallic compounds (UAl_3)
preparation, 208
Aluminum mixtures (Al–B_4C)(Al clad)
fabrication, 228
Aluminum mononitride powder
preparation, 13
Aluminum mononitride system compacts (AlN–UN)
fabrication, 13
Aluminum oxide
casting, continuous, 255
corrosion, 40
joining to Nb–Zr alloy, 146
sealing to Nb, 59
strength, 58-59, 193
Aluminum oxide cermets
corrosion, 235
Aluminum oxide coatings
for W, 38, 105
Aluminum oxide coatings (Al_2O_3–Cr_2O_3)
application, 257
Aluminum oxide particles
strain fields around, in Al–Al_2O_3 foils, 53
Aluminum oxide powder
coating with Mo and W, 139-40
compaction, 142
Aluminum system films (Al–Si)
annealing and growth, 259
Aluminum oxide system foils (Al–Al_2O_3)
strain fields in, 53
Aluminum oxide systems (Al–Al_2O_3)
work hardening, recovery of, 183
Aluminum system foils (Al–Al_2O_3)
strain fields in, 53
Aluminum system tubes (Al–Fe–Si–U)(Zircaloy clad)(irradiated)
swelling, 2-4
Aluminum systems (Al–Al_2O_3)
work hardening, recovery of, 183
Aluminum systems (Al–B)
fabrication, 100
Aluminum systems (Al–C–Ti–Zr)
mechanical properties at high temperatures, 123
Aluminum systems (Al–C–Y)
phase studies, 131
Aluminum systems (Al–Eu_2O_3)
fabrication, 100-1
Aluminum systems (Al–HfO_2)
fabrication, 100
Aluminum systems (Al–Fe–Mo–Si–U)
hardness, 2
Aluminum systems (Al–Fe–Ni–Si)
corrosion, 103
Aluminum systems (Al–Si)
corrosion, 103
Aluminum tubing
explosive welding to Zircaloy-4 tubing, 260
Americium
diffusion in UO_2, 82, 248
Antimony
solubility in molten Zn, 236
Antimony alloys (Sb–Zr)
H terminal solubility in, 28
Arsenic
solubility in molten Zn, 236
As-30
creep properties, 181
AS-55
corrosion, 40
welding, 143
Autoclaves
design and operation of high-pressure, 142

B

B33
corrosion, 40
B-66
coatings for, 38, 231-32
corrosion, 40, 251
diffusion bonding, 64
evaporation loss, 124-25
welding, 142-44
B-66 foils (coated)
properties, 38
B-66 tubing
fabrication, 257
Barium
diffusion in graphite, 91
phase diagrams, 186
solubility in molten Zn, 236
Bearing materials (journal)
corrosion, 40
Beryllide coatings
corrosion-resistant, 27
Beryllides
oxidation, 27
Beryllium
analysis, 93-94, 220
anodizing, 67
bonding, 68, 147, 257
brazing, 94, 146, 168, 261
compatibility studies, 25-26, 37, 94
contamination of, 23
corrosion, 177-78, 220-21
critical-resolved-shear stresses, 22-23
electrodeposition of metals on, 67
fabrication, 24-25, 167-68, 220
impurities in commercial, 23
inclusions in commercial, 23
Fe diffusion in, 248
mechanical properties, 22, 24, 93
metallography at high temperatures, 93
physical metallurgy, 167-68
properties, 22-24
purification, 22-24, 168
recrystallization, 93
Ag diffusion in, 248
solubility in molten Zn, 236
surface-recession rates, 125
vapor deposition, 66
Beryllium (irradiated)
crystal orientation, 219
oxidation, 94
properties, 115, 169
tensile properties, 241
Beryllium alloys
development, 168
Beryllium alloys (Al–Be)
phase studies, 92-93
Beryllium alloys (Be–Ca)
recrystallization, 93
Beryllium alloys (Be–Cr)
phase studies, 92-93
Beryllium alloys (Be–Cu)
fabrication, 24-25
mechanical properties, 219
phase studies, 92-93
production by splat cooling, 219
strength, 25
Beryllium alloys (Be–Fe)
mechanical properties, 219
phase studies, 92-93
production by splat cooling, 219
Beryllium alloys (Be–Ag)
phase studies, 92-93
Beryllium alloys (Be–Ni)
mechanical properties and production, 219
Beryllium alloys (Be–Ti–Zr)
use for brazing, 146
Beryllium fluoride systems (BeF_2–LiF–UF_4–ZrF_4)(molten)
corrosive effects, 110
Beryllium intermetallic compounds, 27, 168
Beryllium oxide
phase transformation, 169
strength, 26, 193, 221-23
thermal conductivity, 193
thermal diffusivity, 26
Beryllium oxide (irradiated)
behavior, 94, 96
compatibility with irradiated graphite, 217
microcracking, 223
thermal diffusivity, 26
Beryllium oxide mixtures (BeO–UO_2)
creep properties, 58
Beryllium oxide systems (Be–BeO)(irradiated)
behavior, 94
Beryllium oxide systems (BeO–MgO–SiC)
properties, 223
Beryllium oxide systems (BeO–PuO_2–ThO_2)
phase studies, 8
Beryllium oxide systems (BeO–SiC)
properties, 223
Beryllium oxide systems (BeO–ThO_2–UO_2–Y_2O_3)
UO_2 loss, 26-27
Beryllium oxide systems (BeO–ThO_2–UO_2–Y_2O_3)(irradiated)
fission-gas release, 27
Beryllium powder
gas-pressure bonding, 64
sintering, 25
Beryllium sheet
fabrication and properties, 220
Beryllium single crystals
mechanical properties, 218-19
Ag diffusion in, 248
Beryllium systems (Be–BeO)(irradiated)
behavior, 94
Beryllium tubes
use for fuel-element cladding, 25
Billets
casting for NPR fuel, 63
Bismuth
solubility in molten Zn, 236
Bismuth alloys (Bi–Sn)(molten)
corrosive effects, 236
Bismuth (molten)
U diffusion in, 188
Bismuth alloys (Bi–Pb)(molten)
wetting effects, 178
Bonding, 64, 68, 142, 147, 200, 257
Borides
hardness, 251
Boron
use in stainless-steel (304) cladding, 99
vapor deposition on Ti, 66
Boron carbide (stainless-steel (316) clad)
corrosion, 177
Boron carbide dispersions (B_4C–glass)(stainless-steel (321) clad)(irradiated)
performance, 32
Boron carbide mixtures (Al–B_4C)(Al clad)
fabrication, 228
Boron carbide mixtures (B_4C–graphite)
preparation, 228
Boron carbide spherules
preparation, 101

Boron fused slurry coatings
development and evaluation, 106
Boron nitride
corrosion, 40
Boron nitride powder
compaction, 142
Boron nitride systems
oxidation, 132
Boron oxide
melting point, 173
Boron oxide systems (B_2O_3–WO_3)
phase studies, 173
Boron powder
purification, 228
Boron system cladding (B–stainless steel)(irradiated)
performance, 226, 228
Boron systems (Al–B)
fabrication, 100
Boron systems (B–Cr–Ni)
(see CM 60)
Boron systems (B–Cr–Ni–Si)
(see CM 53)
Boron systems (B–Cu)(irradiated)
He precipitation in, 192
Boron systems (B–Ni–Si)
(see CM 52)
Boron systems (B–Nb)
mechanical properties, 127
Boron systems (B–Th)(Zr clad)
fabrication, 257
Boron systems (B–Zr)
sintering, 34
Brass 70/30
explosive cladding of mild steel with, 67
Braze joints
nondestructive testing, 70
Brazing, 142–47, 260–63
Brazing alloys
corrosion, 36
Brazing foils
nondestructive testing, 70
Brittle materials
Poisson's ratio and shear properties, 121
Bubbles (fission gas)
migration, 17, 87

C

C-129
corrosion, 40
C129Y
properties, 246
welding, 142–43
C-129Y (V-modified disilicide coated)
properties, 38
C-1294
evaporation loss, 124–25
Cadmium
solubility in molten Zn, 236
Cadmium (molten)
corrosion effects, 178, 236
U diffusion in, 188
Cadmium alloys (Cd–Eu)
phase studies, 226
Cadmium alloys (Cd–In–Ag)(plated)(irradiated)
mechanical properties, 32
Cadmium alloys (Cd–Mg)(molten)
corrosive effects, 178–79
Cadmium alloys (Cd–Mg–Zn)(molten)
corrosive effects, 178–79
Cadmium alloys (Cd–Sr)
phase studies, 226
Calcium
corrosion, 177–78
phase diagrams, 186
solubility in molten Zn, 236
Calcium alloys (Be–Ca)
recrystallization, 93
Calcium oxide systems (CaO–PuO_2–UO_2–ZrO_2)
melting points, 78
Calcium oxide systems (CaO–ZrO_2)
thermal conductivity, 193
Carbide cermets
development, 79
Carbide coatings (refractory)
for Ta, 38
Carbide fuels (clad)(irradiated)
behavior, 79
Carbides
casting, 101, 255
corrosion, 110
Carbides (Co bonded)
corrosion, 107–8
Carbides (Grade 7178)
corrosion, 40
Carbides (Mo bonded)
corrosion, 107–8
Carbides (Ni bonded)
corrosion, 107–8
Carboloy 907
corrosion, 40
Carboloy 999
corrosion, 40
Carbon
(see also Graphite)
activity in UC, 84
activity in UC_2, 84
chemical deposition, 66
corrosion, 177–78
diffusion in Cr, 132
diffusion in Nb carbide, 189
diffusion in Ta carbide, 189
diffusion in Zr, 132
self-diffusion in UC, 211–12
solubility in refractory metals, 51
solubility in UC_2, 84
Carbon (irradiated)
contraction, 218
properties of heat-treated, 217–18
Carbon (pyrolytic)(irradiated)
thermal diffusivity, annealing effects on, 20–21
Carbon coatings (pyrolytic)
characterization of, for fuel particles, 80
deposition on fuel particles, 209–10
development, 156–57
Carbon coatings (pyrolytic)(irradiated)
properties, 217
Carbon monoxide mixtures (CO–water vapor)
radiolysis, 20
Carbon system particles (C–U–Zr)(irradiated)
behavior, 13
Carbon systems (Al–C–Ti–Zr)
mechanical properties at high temperatures, 123
Carbon systems (Al–C–Y)
phase studies, 131
Carbon systems (C–Cr–Co–Fe–Ni–W)
(see Star J)
Carbon systems (C–Cr–Co–Mo–W–Y)
oxidation and strength, 131
Carbon systems (C–Cr–Co–Nb–W–Y)
oxidation and strength, 131
Carbon systems (C–Cr–Co–Ta–W–Y)
oxidation and strength, 131
Carbon systems (C–Cr–Fe–Ni–N)
stress-corrosion cracking, 104
Carbon systems (C–Cr–Zr)
phase studies, 50
Carbon systems (C–Co–Zr)
phase studies, 244
Carbon systems (C–Hf)
phase studies, 101
Carbon systems (C–Hf–Ta)
phase studies, 32
Carbon systems (C–Hf–Ta–W)
(see T-222)
Carbon systems (C–HfC)
tensile properties, 101-2
Carbon systems (C–Fe–Nb)
phase studies, 246
Carbon systems (C–metal)
melting and casting apparatus for, 256
Carbon systems (C–Mo)
phase studies, 51
Carbon systems (C–Mo–Nb–Ti–Zr)
fabrication and properties, 51
Carbon systems (C–Mo–Ti–Zr)
(see also TZC)
creep-rupture properties, 118
fabrication, 51, 138
properties, 51
Carbon systems (C–Mo–Zr)
phase studies, 50
Carbon systems (C–Ni–U)
phase studies, 211
Carbon systems (C–Nb–W–Zr)
cold working, 127
corrosion, 233–34
Carbon systems (C–Nb–Zr)
corrosion, 108
development, 52
phase studies, 128
Carbon systems (C–N–Pu)
hardness, 8
Carbon systems (C–O–Pu)
phase studies, 207
Carbon systems (C–Pu)
vapor pressure, 78
Carbon systems (C–Pu–Th)
phase studies, 12
Carbon systems (C–Ta–W)
(see K601)
Carbon systems (C–Th)
phase studies, 12
Carbon systems (C–W–Zr)
phase studies, 50, 128
Carbon systems (C–U)
aging effects, 152
casting, 83
melting, 83
melting point, 74
precipitates in, 152
Carbon tetrachloride
reaction with burning Pu, 6
Casting, 63–64, 138, 197–98, 255–57
Cb-752
coatings for, behavior of, 231–32
corrosion, 40
creep properties, 249–50
welding, 143, 262
Cb-752 foils (coated)
properties, 38
Ceramic coatings
fission-product migration through, 10
Ceramic fibers
preparation, 132
Ceramic powders (irradiated)
fission-gas release, 162
Ceramic whiskers
preparation, 132
Ceramics
fabrication, 193
joining to metals, 146–47
oxidation, 132
technology, 58–59, 251
wetting of U, by liquid Na, 110
Ceramics (irradiated)
fission-gas diffusion in, 213

Cerium
diffusion in graphite, 91
solubility in molten Zn, 236
W solubility in, 247
Cerium alloys (Ce–Fe–Pu)
phase studies, 77
Cerium alloys (Ce–Pu) (molten)
viscosities, 6, 75, 77
Cermet coatings
corrosion of plasma-sprayed, 108
Cermet fuels
development, 79
Cermet fuels (irradiated)
burnup, 79
Cermets
corrosion, 235
mechanical properties, 155
Cesium
phase diagrams, 186
Cesium (molten)
corrosive effects, 235
Cesium (vaporized)
corrosive effects, 40
Chromium
annealing on U, 67
C diffusion in, 132
compatibility with Eu molybdate, 100
compatibility with Pu–Th–U alloys, 9
compatibility with $Pu_{0.2}C$–$U_{0.8}C$ system, 8
corrosion, 177-78
deposition of, 140
diffusion in U, 248-49
electrodeposition of, 67, 260
electroplating with Cr–Re alloy, 198
ion plating on U, 200
mechanical properties, Y effects on, 53
melting point, annealing effects on, 246
Mo diffusion in, 132
notch impact properties, 250
phase diagrams, 186
reaction with PuC-UC system, 159
solubility in molten Li, 107
solubility in molten Zn, 236
stainless-steel (304) corrosion-product deposition on, 36
Chromium (irradiated)
lattice parameters, 49
Chromium alloys (Al–Cr–Fe–Y)
(see also 1541 alloy)
oxidation, 79
properties, 244-45
Chromium alloys (Al–Cr–Fe–Y)(irradiated)
ductile-brittle transition temperature, 115
hardness, 115
tensile properties, 190
Chromium alloys (Al–Cr–Ti–V)
friction welding, 68
Chromium alloys (Al–Cr–V)
corrosion, 109, 233
Chromium alloys (Al–Cr–V–Y)
fabrication, 255-56
Chromium alloys (Al–Cr–V–Zr)
fabrication, 255-56
Chromium alloys (Be–Cr)
phase studies, 92-93
Chromium alloys (Cr–Co–Fe–Ni–W)
(see L-605)
Chromium alloys (Cr–Co–Mo–Ni)
(see Udimet 700)
Chromium alloys (Cr–Co–Ni–W)
(see Haynes 25)
Chromium alloys (Cr–Hf–Ta)
oxidation, 100
Chromium alloys (Cr–Fe)(irradiated)
^{133}Xe release during heating, 190
Chromium alloys (Cr–Fe–Ni)
(see Alloy 718)
Chromium alloys (Cr–Fe–Ni–Nb)(irradiated)
ductility, B effects on, 112
Chromium alloys (Cr–Fe–Ni–Ti)(irradiated)
ductility, B effects on, 112
Chromium alloys (Cr–Fe–Sn–Zr)
corrosion and mechanical properties, 103
Chromium alloys (Cr–Fe–Zr)
corrosion and mechanical properties, 103
Chromium alloys (Cr–Ni)
compatibility with PuO_2, 207
oxidation, 174
Chromium alloys (Cr–Ni)(irradiated)
fission-fragment damage, 190
Chromium alloys (Cr–Ni–Nb)(irradiated)
fission-fragment damage, 190
stress-rupture properties, annealing effects on, 191-92
Chromium alloys (Cr–Nb)
mechanical properties, 127
Chromium alloys (Cr–Nb–U)
transformation, 1
Chromium alloys (Cr–Re)
electrodeposition on Cr, Cu, Mo, and W, 198
notch impact properties, 250
Chromium alloys (Cr–Ti–V)
corrosion, 257
creep properties, 186
fabrication, 257
Chromium alloys (Cr–U)
phase changes, kinetics of, 152
transformation, 1
Chromium alloys (Cr–U–V)
phase studies, 204
Chromium alloys (Cr–U)(molten)
corrosive effects, 236
Chromium alloys (Cr–V)
corrosion, 109
Chromium alloys (Cr–Y)
mechanical properties, 53
Chromium alloys (Cr–Y)(hydrided)(clad)
cracking, 97
Chromium alloys (Cr–Y)(hydrided)(clad)(irradiated)
behavior, 97
Chromium alloys (Cr–Zr)
corrosion, 36
Chromium coatings (Cr–Si–Ti), 38, 106, 231-32
Chromium disilicide
oxidation and thermal dilation, 106
Chromium dispersions
cladding materials for, 79
Chromium fused slurry coatings
development and evaluation, 106
Chromium intermetallic compounds ($CrBe_{12}$)
oxidation, 27
Chromium oxide coatings (Al_2O_3–Cr_2O_3)
application, 257
Chromium powder
use as binder for ZrB_2, 172
Chromium systems (B–Cr–Ni)
(see CM 60)
Chromium systems (B–Cr–Ni–Si)
(see CM 53)
Chromium systems (C–Cr–Co–Fe–Ni–W)
(see Star J)
Chromium systems (C–Cr–Co–Mo–W–Y)
oxidation and strength, 131
Chromium systems (C–Cr–Co–Nb–W–Y)
oxidation and strength, 131
Chromium systems (C–Cr–Co–Ta–W–Y)
oxidation and strength, 131
Chromium systems (C–Cr–Fe–Ni–N)
stress-corrosion cracking, 104
Chromium systems (C–Cr–Zr)
phase studies, 50
Chromium systems (Cr–SiC)
oxidation, 132
Chromium systems (Cr–stainless steel)
stress rupture in liquid metal, 233
Chromium trioxide powder
compaction, 142
Cladding, 64-67, 139-42
Cladding materials, 35-62, 103-37, 174-96, 229-54
CM 52
corrosion as brazing alloy, 176
CM 53
corrosion as brazing alloy, 176
CM 60
corrosion as brazing alloy, 176
Coast Alloy 52
corrosion of brazed joints using, 40
Coatings
(see also Films (thin))
ion plating of, 199-200, 259
oxidation-resistant, 38-39
for refractories, 38-39, 105-6, 175, 199
Coatings (ceramic)
fission-product migration through, 10
Coatings (cermet)
corrosion of plasma-sprayed, 108
Coatings (fused slurry silicide)
development and evaluation, 106
Coatings (pack-cementation)
development, 106
Coatings (silicide)
for T-222, 232-33
thermal stresses of, on refractory metals, 106
Cobalt
corrosion, 177-78
diffusion in U, 248-49
phase diagrams, 186
solubility in molten Zn, 236
tensile strength of electrodeposited, 67
Cobalt alloys
corrosion, 177-78
Cobalt alloys (Cr–Co–Fe–Ni–W)
(see L-605)
Cobalt alloys (Cr–Co–Mo–Ni)
(see Udimet 700)
Cobalt alloys (Cr–Co–Ni–W)
(see Haynes 25)
Cobalt alloys (Co–Cu)(irradiated)
precipitation, 115-16
Cobalt alloys (Co–Fe–Ni)
corrosion, 235
Cobalt alloys (Co–Ni)
tensile properties of electrodeposited, 66-67
Cobalt alloys (Co–W)
vapor deposition, 258
Cobalt alloys (U–UCo_2–UMn_2)
phase studies, 152-53
Cobalt dispersions (Co–Dy_2O_3)(stainless-steel (304) clad)(irradiated)
performance, 32
Cobalt intermetallic compounds (Pu_2Co)
physical properties, 153
Cobalt intermetallic compounds (U_6Co)
solid solubility, 153
Cobalt systems (C–Cr–Co–Fe–Ni–W)
(see Star J)
Cobalt systems (C–Cr–Co–Mo–W–Y)
oxidation and strength, 131
Cobalt systems (C–Cr–Co–Nb–W–Y)
oxidation and strength, 131
Cobalt systems (C–Cr–Co–Ta–W–Y)
oxidation and strength, 131
Cobalt systems (C–Co–Zr)
phase studies, 244
Cobalt systems (Co–O–W)
phase studies, 129

Cobalt systems (Co–TaC–WC)
(see Carboloy 907)
Cobalt systems (Co–WC)
(see Carboloy 999)
Composites
nondestructive testing, 263
Compton spectrometers
use in nondestructive-assay of fuels, 70
Coolants (organic)
corrosive and hydriding effects on Zr alloys, 36
Copper
annealing on U, 67
corrosion, 177–78, 235
corrosion of brazed joints using, 40
diffusion in U, 248–49
electrodeposition, 67, 141
electroplating with Cr–Re alloy, 198
explosive cladding of mild steel with high-conductivity, 67
friction welding, 68
Mo deposition on substrates of, 140
solubility in molten Zn, 236
surface-recession rates, 125
ultrasonic testing, 69
use in diffusion bonding of Mg and U, 67
vapor deposition, 259
Copper (Ir plated)
ductility, 141
Copper (irradiated)
lattice parameters, 49
primary knock-on recoil spectrum, 192–93
recrystallization of cold-rolled polycrystalline, 116
swelling, 16
Copper (Ta plated)
reduction, 141
Copper alloys (Be–Cu)
fabrication, 24–25
mechanical properties, 219
phase studies, 92–93
production by splat cooling, 219
strength, 25
Copper alloys (Co–Cu) (irradiated)
precipitation, 115–16
Copper alloys (Cu–Ni)
use for brazing, 146
welding, 145
Copper alloys (Cu–Ni–W)
properties, 126
Copper alloys (Cu–Nb–Zr)
corrosion and H uptake, 229
Copper alloys (Cu–Zr)
diffusion in, 132
Copper braze
corrosion, 235
Copper-braze bonds
corrosion, 40
ultrasonic testing, 69
Copper single crystals (irradiated)
defect-cluster density relation to critical-shear stress, 193
flow stress, 116
microstrain, 49
Copper systems (B–Cu)(irradiated)
He precipitation in, 192
Croloy 2 1/4
corrosion, 110, 176
Croloy 9M
corrosion, 177

D

D-11
erosion, 177
D-14
coating with silicide and Ti, 140
corrosion, 40
D-36
diffusion bonding, 64
D-43
coating with silicide and Ti, 140
coatings for, protective, 106
corrosion, 40, 234
creep properties, 249–50
diffusion bonding, 64
evaporation loss, 124–25
properties, 127
welding, 142–44
D-43 foils (coated)
properties, 38
D-43Y
ductility, 245–46
welding, 143, 262
Disil coatings
behavior, 231–32
Disilicide coatings (V modified)
properties of, on C-129Y, 38
Durak B coatings
behavior, 231–32
Dysprosium
W solubility in, 247
Dysprosium oxide
development of rod, 100
Dysprosium sesquioxide absorber columns
development, 34
Dysprosium sesquioxide dispersions Co–Dy_2O_3(stainless-steel(304) clad) (irradiated)
performance, 32

E

Eddy-current testing, 70, 148, 201
EI-437B
creep rates, 39–40
EI-851
creep rates, 39–40
EI-869
creep rates, 39–40
Electroplating, 66–67, 140–42, 198–99
Elements
corrosion, 177–78
Enrico Fermi Fast Breeder Reactor
radiation damage in graphite shield, 166
Erbium
W solubility in, 247
Ethane (1,1,1-trichloro-)
reaction with burning Pu, 6
Europium
W solubility in, 247
Europium alloys
phase studies, 226
Europium dicarbide
heat of formation and vaporization, 101
Europium molybdate
compatibility with Cr, Fe, and Ni, and corrosion, 100
Europium molybdate dispersions (Al–Eu molybdate–Eu_2O_3)(Al clad)(irradiated)
dimensional stability, 101
Europium sesquioxide dispersions (Al–Eu molybdate–Eu_2O_3)(Al clad)(irradiated)
dimensional stability, 101
Europium sesquioxide dispersions (Eu_2O_3–stainless steel)(irradiated)
properties, 228
Europium sesquioxide dispersions (Eu_2O_3–stainless steel)(stainless-steel clad) (irradiated)
examination, 171–72
Europium sesquioxide systems (Al–Eu_2O_3)
fabrication, 100–1
Explosive forming, 67, 260

F

F-48
erosion, 177
Fabrication
special techniques, 63–71, 138–50, 197–202, 255–65
Ferrovac E
stress-rupture properties, 250–51
Fertile materials, 1–19, 73–90, 151–65, 203–16
Films (thin)
deposition-rate monitor, 259
Fission-gas bubbles
migration, 17, 87
Fissium alloys (fissium–Pu–U)
compatibility with stainless steel, 5
development, 6
phase studies, 74–75
solidus temperatures, 5
Fissium alloys (fissium–Pu–U)(irradiated)
properties, 205–6
Fizzium alloys (fizzium–Pu–U)(clad) (irradiated)
burnup, 74
Fizzium alloys (fizzium–Pu–U)(irradiated)
properties, 205–6
Fluorides (liquid)
corrosive effects, 110, 236
Foils (brazing)
nondestructive testing, 70
Forming (explosive), 67, 260
FS-80
evaporation loss, 124–25
FS-85
corrosion, 40, 108, 234
creep properties, 55, 249–50
evaporation loss, 124–25
Pt coatings for, 233
welding, 143–44
FS-85 couples (FS-85–TZM)
diffusion behavior in Pt-coated, 233
Fuel cladding materials
(see Cladding materials)
Fuel materials, 1–19, 73–90, 151–65, 203–16
(see also Nonfuel materials (irradiated))
Fuel particles (ceramic coated)
development, 209–10
Fuel particles (ceramic coated)(irradiated)
fission-product release, 10
Fuel particles (coated)
development, 156–57
Fuel particles (coated)(irradiated)
evaluation, 10
performance, 81, 210
Fuel particles (PyC coated)(irradiated)
performance, 10, 210
Fuel pins (irradiated)
thermal properties, detection of changes in, 200–1
Fuel-reprocessing solutions
corrosive effects, 178
Fuel rods (stainless-steel(304) clad) (irradiated)
properties, 189
Fuel wafers
fabrication of glass-bonded, 11
Fuels
billet casting for NPR, 63
corrosion, 15
H release during SNAP 10A/2 reactor destructive test, 28
nondestructive assay, 70
production for production reactors, 63
reactions with water, 161
Fuels (bonded)
ultrasonic testing, 69

Fuels (cermet)
development, 79
Fuels (cermet)(irradiated)
burnup, 79
Fuels (intermetallic compound), 12-14
Fuels (irradiated)
inert-gas migration in, 163
nondestructive assay, 70
properties, 15-17
reactions with water, 14-15
stresses caused by swelling, 162
Fuels (particulate)
canning of, 257-58
Fuels (stainless-steel(304) clad)
ultrasonic testing, 69
Fused salts
corrosive effects, 107-10
Fused slurry silicide coatings
development and evaluation, 106

G

Gadolinium
W solubility in, 247
Gadolinium intermetallic compounds ($GdBe_{13}$)
properties, 27
Gallium
solubility in molten Zn, 236
Gas bubbles (fission-)
migration, 17, 87
Germanium
corrosion, 177-78
solubility in molten Zn, 236
Glass dispersions (B_4C–glass)(stainless-steel(321) clad)(irradiated)
performance, 32
Gold
corrosion, 177-78
solubility in molten Zn, 236
Gold (irradiated)
primary knock-on recoil spectrum, 192-93
Gold alloys (Au–Mo–Ni)
use for brazing, 146
Gold alloys (Au–Ni)
use in brazing of Be, 168
Gold alloys (Au–Th)(Zr clad)
fabrication, 257
Grade 7178
corrosion, 40
Graphite
(see also Carbon)
Ba diffusion in, 91
brazing, 146
Ce diffusion in, 91
compaction, 142
corrosion, 21-22, 40
gas-pressure bonding, 200
oxidation, $POCl_3$ effects on, 20
plastic strain, thermal induction of, 166
properties of compacted, 91
reaction with H_2, 91
Sr diffusion in, 91
thermal expansion, 22
U diffusion in, 248
Graphite (ATJ)
tensile properties, 121
Graphite (irradiated)
compatibility with irradiated BeO, 217
contraction, 20, 217-18
creep properties, 91-92, 166-67
damage, 166
dilation, liquid-Na, 22
dimensional changes, 91-92
elastic modulus, 167
oxidation, 166
properties of heat-treated, 217-18
Graphite (pyrolytic)
formation, 199
tensile properties, 121
Graphite (pyrolytic)(irradiated)
thermal diffusivity, annealing effects on, 20-21
Graphite mixtures (B_4C–graphite)
preparation, 228
Graphite systems (graphite–ThC_2)
eutectic, 12
Graphite systems (graphite–UO_2)
melting, 197

H

Hafnium
corrosion, 99-100
effects on Mo recrystallization temperature, 182
effects on W strength, 182
mechanical properties, 32
phase diagrams, 186
properties, O effects on, 171
residual stresses, annealing effects on, 226
Hafnium (irradiated)
mechanical properties, 32
Hafnium alloy coatings (Hf–Ir)
for Ta, 38
Hafnium alloy coatings (Hf–Mo–Ta)
oxidation, 106
Hafnium alloy coatings (Hf–Ta)
oxidation, 106
for Ta, 38
for Ta alloys, 233
Hafnium alloys (Al–Hf–Nb)
oxidation, 100
Hafnium alloys (Al–Hf–Ta)
oxidation, 100
Hafnium alloys (Cr–Hf–Ta)
oxidation, 100
Hafnium alloys (Hf–Nb–W)
(see C-129)
Hafnium alloys (Hf–Nb–W–Y)
(see C-129Y)
Hafnium alloys (Hf–Re–Ta)
phase studies, 129
Hafnium alloys (Hf–Ta)
phase studies, 226
Hafnium alloys (Hf–Ta–W)
(see also T-111)
cavitation, 105
corrosion, 108
phase studies, 247
Hafnium alloys (Hf–W)
mechanical properties of carbide-strengthened, 247
Hafnium alloys (Hf–Zr)
H terminal solubility in, 28-29
Hafnium boride systems
oxidation, 132
Hafnium carbide
corrosion, 110
tensile properties, 172
Hafnium carbide solid solutions
preparation and properties, 101
Hafnium diboride
hardness, 251
Hafnium dioxide
corrosion, 40
use to protect thermocouples, 105
Hafnium dioxide coatings
for W, 38
Hafnium dioxide powders (HfO_2–MgO)
sintering, 59
Hafnium dioxide solid solutions (HfO_2–ZrO_2)
thermal expansion, 172
Hafnium dioxide systems (Al–HfO_2)
fabrication, 100
Hafnium intermetallic compounds ($HfBe_{13}$)
oxidation, 27
Hafnium monocarbide systems (C–HfC)
tensile properties, 101-2
Hafnium monocarbide systems (HfC–Ta)
preparation, 101
Hafnium systems (C–Hf)
phase studies, 101
Hafnium systems (C–Hf–Ta)
phase studies, 32
Hafnium systems (C–Hf–Ta–W)
(see T-222)
Hafnium systems (Hf–H–Zr)
phase studies, 29
Hafnium systems (Hf–Mo–Nb–W)
(see SU-16)
Hafnium systems (Hf–O)
hardness and phase studies, 99
Hafnium systems (Hf–SiC)
oxidation, 132
Hastelloy C
nitriding, 175
oxidation, 104
Hastelloy C (irradiated)
properties, 192
Hastelloy F
microstructural evaluation for cladding use, 51
tensile properties, temperature effects on, 180
Hastelloy N
corrosion, 177, 230
oxidation, 104
properties, 124
thermal conductivity, 245
Hastelloy N (irradiated)
mechanical properties, 45-46, 124, 191
rupture life, 240
Hastelloy R-235
properties, 124
Hastelloy R-235 (irradiated)
mechanical properties, 113, 124
Hastelloy X
compatibility with $Pu_{0.2}C$–$U_{0.8}C$ system, 8
corrosion, 37, 104
creep-rupture properties, 117, 180
microstructural evaluation for cladding use, 51
nitriding, 175
oxidation, 230
properties, 124
reaction with PuC–UC system, 159
strength, 250
tensile properties, 54-55, 180
thermal conductivity, 245
Hastelloy X (irradiated)
mechanical properties, 124
Hastelloy X-280
oxidation, 104
Hastelloy X-280 (irradiated)
mechanical properties, 46, 113
Haynes 25
oxidation, 104
welding, 145
High-energy-release-rate (HERR) bonding, 68, 147
Holmium
W solubility in, 247
Holmium tetraboride
hardness, 251
Honeycombs
ultrasonic testing, 263
Hydrides (solid), 27-30, 96-98

Hydrocarbons (fluorinated)
corrosion, 36
Hydrogen
reaction with graphite, 91
Hydrogen systems
(see specific hydrides)
Hydrogen systems (Hf–H–Zr)
phase studies, 29
Hydrogen systems (H–Nb)
phase studies, 29
tensile properties, strain-rate effects on, 56
Hydrogen systems (H–V)
ductility, 56

I

Incoloy 800
corrosion, 37, 104
microstructural evaluation for cladding use, 51
nitriding, 175
oxidation, 174
tensile properties, temperature effects on, 180
welding, 145–46
Incoloy 800 (irradiated)
mechanical properties, 46, 191
Incoloy 800 (modified)
microstructural evaluation for cladding use, 51
Incoloy 800 tubes
strength, 117
Incoloy 801
microstructural evaluation for cladding use, 51
tensile properties, temperature effects on, 180
Incoloy 804
microstructural evaluation for cladding use, 51
Incoloy 825
corrosion, 37, 104
microstructural evaluation for cladding use, 51
tensile properties, temperature effects on, 180
Inconel
compatibility with Th, 9
corrosion, 37
joining to Zircaloy, 68
stainless-steel (304) corrosion-product deposition on, 36
Inconel transition joints (Inconel–Zircaloy-2)(irradiated)
mechanical properties, 240
properties, 260
Inconel 600
corrosion, 37, 104, 230
oxidation, 104
nitriding, 175
welding, 145
Inconel 600 (irradiated)
mechanical properties, 46, 113
Inconel 625
corrosion, 37, 104
microstructural evaluation for cladding use, 51
oxidation, 104
tensile properties, temperature effects on, 180
thermal conductivity, 245
welding, 145–46
Inconel 625 (irradiated)
mechanical properties, 113
tensile properties, 46
Inconel 702
thermal conductivity, 245
Inconel 702 (irradiated)
mechanical properties, 113
Inconel 713C (irradiated)
properties, 192
Inconel 718
microstructural evaluation for cladding use, 51
tensile properties, temperature effects on, 180
Inconel X-750 (irradiated)
properties, 192
Indium
corrosion, 177–78
solubility in molten Zn, 236
Indium alloys (Cd–In–Ag)(plated)(irradiated)
mechanical properties, 32
Indium alloys (Eu–In)
phase studies, 226
Indium alloys (In–Th)
tensile properties, 9
Indium alloys (In–Zr)
H terminal solubility in, 28
INOR-8
brazing and welding, 146
INOR-8 (irradiated)
rupture properties, 113
Iridium
electrodeposition of, 141
phase diagrams, 186
Iridium alloy coatings
for Ta, 38
for W, 233
Iridium alloys (Ir–Nb)
mechanical properties, 127
Iridium alloys (Ir–W)
casting, 255
Iridium coatings (Ir–Rh)
for W, 233
Iridium intermetallic compounds (Pu_2Ir_3)
physical properties, 153
Iron
compatibility with Eu molybdate, 100
corrosion, 177–78
diffusion in Be, 248
diffusion in U, 248–49
electrodeposition on Be and Zn-plated Be, 67
fatigue-limit behavior, 181
oxidation, 37, 104
phase diagrams, 186
reaction with steam, 42–43
solid solubility in U, 203
solubility in molten Li, 107
solubility in molten Zn, 236
surface-recession rates, 125
Iron (Armco)
stress-rupture properties, 250–51
Iron (Ferrovac E)(irradiated)
tensile properties, 241
Iron (irradiated)
lattice parameters, 49
mechanical properties, 241
microstructure, 241
nitride precipitation in, 241
primary knock-on recoil spectrum, 192–93
Iron alloy tubes (Al–Fe–U)(Zircaloy clad)(irradiated)
swelling, 2–4
Iron alloys
brittleness of body-centered cubic, 50
corrosion, 177–78
mechanical properties, 54, 117–18
metallurgy, 50–51
Iron alloys (Al–Cr–Fe–Y)
(see also 1541 alloy)
oxidation, 79
properties, 244–45
Iron alloys (Al–Cr–Fe–Y)(irradiated)
ductile–brittle transition temperature, 115
hardness, 115
tensile properties, 190
Iron alloys (Al–Fe–U)
precipitate solution in, 73
UAl_3 precipitates in, 151–52
Iron alloys (Be–Fe)
mechanical properties, 219
phase studies, 92–93
production by splat cooling, 219
Iron alloys (Ce–Fe–Pu)
phase studies, 77
Iron alloys (Cr–Co–Fe–Ni–W)
(see L-605)
Iron alloys (Cr–Fe)(irradiated)
^{133}Xe release during heating, 190
Iron alloys (Cr–Fe–Ni)
(see Alloy 718)
Iron alloys (Cr–Fe–Ni–Nb)(irradiated)
ductility, B effects on, 112
Iron alloys (Cr–Fe–Ni–Ti)(irradiated)
ductility, B effects on, 112
Iron alloys (Cr–Fe–Sn–Zr)
corrosion and mechanical properties, 103
Iron alloys (Cr–Fe–Zr)
corrosion and mechanical properties, 103
Iron alloys (Co–Fe–Ni)
corrosion, 235
Iron alloys (Fe–Pu–U)
properties, 153–54
Iron alloys (Fe–U)
transformation, 1
Iron cermets (Fe–UO_2)
development, 9, 79
Iron dispersions
cladding materials for, 79
Iron dispersions (Fe–UO_2)(Al–Cr–Fe–Y alloy clad)
preparation, 79–80
Iron fused slurry coatings
development and evaluation, 106
Iron system tubes (Al–Fe–Si–U)(Zircaloy clad)(irradiated)
swelling, 2–4
Iron systems (Al–Fe–Mo–Si–U)
hardness, 2
Iron systems (Al–Fe–Ni–Si)
corrosion, 103
Iron systems (C–Cr–Co–Fe–Ni–W)
(see Star J)
Iron systems (C–Cr–Fe–Ni–N)
stress-corrosion cracking, 104
Iron systems (C–Fe–Nb)
phase studies, 246
Iron systems (Fe–SiC)
oxidation, 132
Iron systems (Fe–UC)
reaction with stainless steel (316), 159

J

Journal bearing materials
corrosion, 40

K

K501
corrosion, 40
Kennemetal K-7178 couples
corrosion, 108

L

L-605
embrittlement, 131

tensile properties, 245
Lanthanum
electrodeposition on Pt, 198
phase diagrams, 186
solubility in molten Zn, 236
W solubility in, 247
Lanthanum alloys (La–Mo)
fabrication, 51
Lanthanum alloys (La–Nb)
mechanical properties, 127
Lanthanum hexaboride
hardness, 251
Lead
solubility in molten Zn, 236
Lead (molten)
corrosive effects, 110, 178, 236
Lead alloys (Bi–Pb)(molten)
wetting effects, 178
Lead alloys (Pb–Zr)
H terminal solubility in, 28
Lithium
solubility in molten Zn, 236
Lithium (molten)
corrosive effects, 107-9, 234-35
Lithium fluoride mixtures ($LiF–MgF_2$) (molten)
corrosive effects, 236
Lithium fluoride systems ($BeF_2–LiF–UF_4–ZrF_4$)(molten)
corrosive effects, 110
Lithium hydride
casting, 97
thermodynamic properties, 170
Lithium hydride (molten)
corrosive effects, 41
Lithium systems (Li–Mg–Si)
casting, 256
Lucalox
corrosion, 40
sealing to Nb, 59
Lutetium
W solubility in, 247

M

Magnesium
cavitation during creep, 123
compatibility studies, 37
corrosion, 177-78
diffusion bonding to U using Cu and Ni, 67
Pu diffusion in, 188
solubility in molten Zn, 236
Magnesium alloys
Pu diffusion in, 188
Magnesium alloys (Al–Mg–Zr)
creep properties, 251
Magnesium alloys (Cd–Mg)(molten)
corrosive effects, 178-79
Magnesium alloys (Cd–Mg–Zn)(molten)
corrosive effects, 178-79
Magnesium alloys (irradiated)
damage, 115
Magnesium alloys (Mg–Zr)
creep properties, heat-treatment effects on, 183
Magnesium fluoride mixtures ($LiF–MgF_2$) (molten)
corrosive effects, 236
Magnesium fluoride mixtures ($MgF_2–NaF$) (molten)
corrosive effects, 236
Magnesium oxide
evaporation rates, 58
strength, 58-59, 193
Magnesium oxide coatings
for W, 38, 105
Magnesium oxide powders
coating with Mo and W, 139-40
compaction, 142
sintering, HfO_2 effects on, 59
Magnesium oxide systems (BeO–MgO–SiC)
properties, 223
Magnesium solutions (Mg–U–Zn)
corrosive effects, 178
Magnesium systems (Li–Mg–Si)
casting, 256
Magnox
compatibility studies, 37
Magnox Al-80
creep deformation, 243
Manganese
corrosion, 177-78
diffusion in U, 248-49
phase diagrams, 186
solubility in molten Zn, 236
Manganese alloys ($U–UCo_2–UMn_2$)
phase studies, 152-53
Manganese disilicide
thermal dilation, 106
Manganese fused slurry coatings
development and evaluation, 106
Manganese intermetallic compounds (U_6Mn)
solid solubility, 153
Melting, 63-64, 138, 197-98, 255-57
Mercury
corrosive effects, 39, 177-78, 235-36
Metal carbides
casting, 101
Metal foils (refractory)(coated)
properties, 38
Metal systems (C-metal)
casting and melting, 256
Metals
casting of reactive, 256
corrosion, 177-78
diffusion in, 131-32
eddy-current testing, 201
electrodeposition on Pt, 198-99
explosive working, 67
ion plating of, 199-200
joining to ceramics, 146-47
melting of reactive, 256
reactions with water, 41-43, 161, 237-39
solubility in molten Zn, 236
Metals (alkali)(liquid)
corrosive effects, 107
Metals (hexagonal)
base pole figures of close-packed, 49-50
Metals (irradiated)
properties, 115, 192
Metals (molten)
corrosive effects, 39-41, 107-10, 178
reactions with water, 110-11
solidification, 198
Metals (rare earth)
effects on Zr properties, 183
Ta solubility in, 185
W solubility in, 247
Metals (refractory)
C solubility in, 51
chemical plating of, 199
coatings for, 38-39, 105-6, 175, 199
compatibility with $PuO_2–UO_2$ system, 78
corrosion, 37-39, 107, 230-33
diffusion bonding, 64
diffusion in, 248
ductile-brittle transition in body-centered cubic, 51
mechanical properties, 55-56, 118, 120, 249-50
metallurgy, 51
properties, 175
reactions with PuC–UC system, 78
reactions with steam, 41-42
thermal properties, 184
Metals (refractory)(coated)
properties, 175
Metals (refractory)(irradiated)
properties, 115, 241-43
Moderator materials, 20-31, 91-98, 166-70, 217-25
Molybdenum
C solubility in, 51
chemical plating of, 199, 258-59
chemical plating of $MoSi_2$ on, 140
compatibility with $Pu_{0.8}C–U_{0.8}C$ system, 8
compatibility with $PuO_2–UO_2$ system, 78
compatibility with UC–ZrC system, 159
compatibility with UP, 212
corrosion, 37-38, 40, 107, 177-78, 230, 235-36
creep properties, 120
creep-rupture properties, 249
deposition on Cu substrates, 140
diffusion in Cr, 132
electrodeposition of, 141
electrodeposition of Cr on, 67
electrodeposition of Cr–Re alloy on, 198
electrodeposition of Ni on, 67
electrodeposition of Re on, 141, 198
fabrication, La addition effects on, 51
grain size, annealing effects on, 246
hardness, zone-refining effects on, 246
mechanical properties, 182
melting point, annealing effects on, 246
metallurgy, 51
oxide-dispersion hardening, 51
phase diagrams, 186
properties, 175
properties, hot plastic deformation effects on, 255
reaction with PuC–UC system, 159
reaction with steam, 42
recrystallization, 181-82, 246
Re diffusion in, 248
siliconizing of, 199
sintering effects on sprayed, 125
solubility in molten K, 107
solubility in molten Zn, 236
structure, hot plastic deformation effects on, 255
surface-recession rates, 125
thermal conductivity, 125, 185
W diffusion in, 185, 248
U diffusion in, 248
use for coating nonmetallic powders, 139-40
vapor deposition, 259
vapor pressure, 185-86
welding, 185, 261-62
Molybdenum (irradiated)
properties, 49, 116-17, 242
Molybdenum alloy coatings (Hf–Mo–Ta)
oxidation, 106
Molybdenum alloy couples (Mo–Ti)
corrosion, 108
Molybdenum alloy couples (Mo–Ti–Zr)
corrosion, 108
Molybdenum alloy films (Mo–U)(irradiated)
fission-fragment tracks, 17
Molybdenum alloy rod (Mo–Re–W)
fabrication, 256
Molybdenum alloy tubes (Mo–U)(Zircaloy clad)(irradiated)
swelling, 3-4
Molybdenum alloys
cavitation, 105
metallurgy, 51
PFR-6 coating development for, 106
Pt coatings for, 233

properties, 175
thermal properties, 184
Molybdenum alloys (Au–Mo–Ni)
use for brazing, 146
Molybdenum alloys (Al–Mo–Ti–V)
properties, 183
Molybdenum alloys (Al–Mo–U)(Al clad)
(irradiated)
properties, 203–4
Molybdenum alloys (Cr–Co–Mo–Ni)
(see Udimet 700)
Molybdenum alloys (high strength)
oxidation, 125
Molybdenum alloys (La–Mo)
fabrication, 51
Molybdenum alloys (Mo–Nb)
binary interdiffusion in, 132
corrosion, 230–31
high-temperature properties, 185
mechanical properties, 52, 127
Molybdenum alloys (Mo–Nb–Ta–Zr)
(see SCb-61)
Molybdenum alloys (Mo–Nb–Ti–Zr)
(see PWC-533)
Molybdenum alloys (Mo–Nb–W–Zr)
(see F-48)
Molybdenum alloys (Mo–Nb–V–Zr)
(see B-66)
Molybdenum alloys (Mo–Os–W)
phase studies, 128–29
Molybdenum alloys (Mo–Pu–U)
fabrication, 138
thermal expansion, 206
Molybdenum alloys (Mo–Re)
creep-rupture properties, 249
Molybdenum alloys (Mo–Re–W)
creep-rupture properties, 120, 249
creep strength, 249
powder metallurgy, 256
Molybdenum alloys (Mo–Ta–V)
phase studies, 129
Molybdenum alloys (Mo–Ti)
binary interdiffusion in, 132
chemical plating of $MoSi_2$ on, 140
ductility, 125
erosion, 177
Molybdenum alloys (Mo–Ti–V)
corrosion, 109
Molybdenum alloys (Mo–Ti–Zr)
(see also TZM)
chemical plating of $MoSi_2$ on, 140
tensile properties, 118
Molybdenum alloys (Mo–W)
corrosion, 178
mechanical properties, 249
reaction with UC, 84
Molybdenum alloys (Mo–W–Zr)
phase studies, 129
Molybdenum alloys (Mo–U)
specific heat, 204
transformation, 1
Molybdenum alloys (Mo–U)(irradiated)
swelling, 152
Molybdenum alloys (Mo–U)(stainless-steel
(304) clad)(irradiated)
behavior, 4–5
Molybdenum alloys (Mo–Zr)
binary interdiffusion in, 132
Molybdenum cermets
corrosion, 235
fracture, 79
Molybdenum couples
corrosion, 108
Molybdenum disilicide
chemical deposition of, 66, 140, 199
oxidation, 39, 251
thermal dilation, 106
Molybdenum disilicide systems ($MoSi_2$–ZrB_2)
tensile properties, 121
Molybdenum dispersions (Mo–Ni–ThO_2)
preparation, 51
Molybdenum dispersions (Mo–UO_2)
UO_2 loss, heat effects on, 79
Molybdenum fused slurry coatings
development and evaluation, 106
Molybdenum powder
use as binder for ZrB_2, 172
Molybdenum silicide (Mo_5Si_3)
thermal dilation, 106
Molybdenum silicide systems
oxidation, 132
Molybdenum system couples (Mo–Nb–Ti–
WC)
corrosion, 108
Molybdenum systems (Al–Fe–Mo–Si–U)
hardness, 2
Molybdenum systems (C–Cr–Co–Mo–W–Y)
oxidation and strength, 131
Molybdenum systems (C–Mo)
phase studies, 51
Molybdenum systems (C–Mo–Nb–Ti–Zr)
fabrication and properties, 51
Molybdenum systems (C–Mo–Ti–Zr)
(see also TZC)
creep-rupture properties, 118
fabrication, 51, 138
properties, 51
Molybdenum systems (C–Mo–Zr)
phase studies, 50
Molybdenum systems (Hf–Mo–Nb–W)
(see SU-16)
Molybdenum systems (Mo–Nb–Si)
phase studies, 128
Molybdenum systems (Mo–Si–U)
phase studies, 74
physical metallurgy, 1
properties, 1–2
Molybdenum systems (Mo–Si–U)(irradiated)
swelling, 152
Molybdenum systems (Mo–SiC)
oxidation, 132
Molybdenum systems (Mo–TiC)
corrosion, 40
Monel 400
corrosion, 230

N

NaK
corrosive effects, 107–10, 176–77
Nb 132M
creep properties, 181
Neodymium
solubility in molten Zn, 236
W solubility in, 247
Neptunium
diffusion in UO_2, 82, 248
Neutron imaging, 263
Neutron radiography, 70
New Production Reactor
billet casting for fuel, 63
Nichrome dispersions (Nichrome–PuO_2)
metallography, 208
Nickel
chemical deposition, 66, 140
compatibility with Eu molybdate, 100
corrosion, 177–78
diffusion in U, 248–49
electrodeposition, 67, 141–42
mechanical properties of carbonyl-
deposited and electrodeposited, 184
oxidation, 37
phase diagrams, 186
reaction with UN, 12–13
solubility in molten Li, 107
solubility in molten Zn, 236
tensile strength of electrodeposited, 67
use in diffusion bonding of Mg and U, 67
Nickel (ThO_2 strengthened)
mechanical properties and metallurgy,
124
Nickel alloys
(see also EI-437B, EI-869, Hastelloy,
Incoloy, Inconel, and Nimonic)
corrosion, 104, 177–78
mechanical properties, 54–55, 117–18
metallurgy, 50–51
oxidation, 174
properties, 124
tensile properties, temperature effects
on, 180
thermal conductivity, 245
ultrasonic testing for fatigue cracks, 200
welding, 145–46
Nickel alloys (Be–Ni)
mechanical properties and production, 219
Nickel alloys (Cr–Co–Fe–Ni–W)
(see L-605)
Nickel alloys (Cr–Co–Mo–Ni)
(see Udimet 700)
Nickel alloys (Cr–Co–Ni–W)
(see Haynes 25)
Nickel alloys (Cr–Fe–Ni)
(see Alloy 718)
Nickel alloys (Cr–Fe–Ni–Nb)(irradiated)
ductility, B effects on, 112
Nickel alloys (Cr–Fe–Ni–Ti)(irradiated)
ductility, B effects on, 112
Nickel alloys (Cr–Ni)
compatibility with PuO_2, 207
oxidation, 174
Nickel alloys (Cr–Ni)(irradiated)
fission-fragment damage, 190
Nickel alloys (Cr–Ni–Nb)(irradiated)
fission-fragment damage, 190
stress-rupture properties, annealing
effects on, 191–92
Nickel alloys (Co–Fe–Ni)
corrosion, 235
Nickel alloys (Co–Ni)
tensile properties of electrodeposited,
66–67
Nickel alloys (Cu–Ni)
use for brazing, 146
welding, 145
Nickel alloys (Cu–Ni–W)
properties, 126
Nickel alloys (Au–Mo–Ni)
use for brazing, 146
Nickel alloys (Au–Ni)
use in brazing of Be, 168
Nickel alloys (irradiated)
properties, 44–46, 113–15, 124, 240
Nickel alloys (Ni–Nb)
mechanical properties and phase studies,
52
Nickel alloys (Ni–Pd)
use for brazing, 146
Nickel alloys (Ni–Ti)
corrosion of brazed joints using, 40
Nickel alloys (Ni–W)
creep rates, 54
Nickel alloys (TD)
diffusion bonding, 64
properties, 124
strength, 182
Nickel alloys (TD)(irradiated)
mechanical properties, 124
Nickel brazing alloys
corrosion, 40, 176

Nickel cermets (Ni–UO_2)
development, 9
Nickel coatings
electroplating, 259
Nickel disilicide
thermal dilation, 106
Nickel dispersions (Mo–Ni–ThO_2)
preparation, 51
mechanical properties, 51
oxidation, 37
preparation, 51
Nickel single crystals (irradiated)
recovery, 116
Nickel systems (Al–Fe–Ni–Si)
corrosion, 103
Nickel systems (B–Cr–Ni)
(see CM 60)
Nickel systems (B–Cr–Ni–Si)
(see CM 53)
Nickel systems (B–Ni–Si)
(see CM 52)
Nickel systems (C–Ni–U)
phase studies, 211
Nickel systems (C–Cr–Co–Fe–Ni–W)
(see Star J)
Nickel systems (C–Cr–Fe–Ni–N)
stress-corrosion cracking, 104
Nimonic 80A springs (irradiated)
stress relaxation, 44-45
Nimonic PE16 (irradiated)
tensile properties, 45, 113-14
Niobium
coating UC_2 with, 200
coatings for, 199
compatibility with $Pu_{0.3}C$–$U_{0.8}C$ system, 8
compatibility with PuO_2, 8
compatibility with PuO_2–UO_2 system, 78
compatibility with Th, 9
compatibility with UC–ZrC system, 159
compatibility with UP, 212
contamination by N, 184
corrosion, 37-38, 107-8, 177-78, 235
diffusion in U, 248-49
electrodeposition of, 141
high-temperature properties, Mo and Ti effects on, 185
impurity-phase identification, 53
mechanical properties, 52, 127, 182
melting point, annealing effects on, 246
metallurgy, 52-53
N solubility in, 126-27, 245
N sticking factor, 184-85
oxide-dispersion hardening, 51
phase diagrams, 186
properties, 51, 175
properties, hot plastic deformation effects on, 255
reaction with PuC–UC system, 159
reaction with steam, 42
relaxation peaks, internal-friction, 52
rolling, 257
sealing to Al_2O_3, 59
sealing to Lucalox, 59
solubility in molten Li, 107
solubility in molten Pu, 153
solubility in molten K, 107
solubility in molten Zn, 236
strain aging, 52, 184
strengthening, solid-solution, 245
structure, hot plastic deformation effects on, 255
tensile properties, 55-56
U diffusion in, 248
vapor deposition, 259
Niobium (Ir plated)
brittleness and pinholes, 141
Niobium (irradiated)
annealing, 116
corrosion, 174
He production, 192
H production, 192
interstitials, 116
vacancies, 116
Niobium alloy couples (Nb–Zr)
corrosion, 109
Niobium alloy couples (Nb–Zr)(carburized)
corrosion, 108
Niobium alloy tubing (Nb–Zr)
crystal structure, 49
Niobium alloys
(see also As-30, D-36, and Nb 132M)
cavitation, 105
Cr–Si–Ti coating for, application process for, 106
coatings for, 106, 199
corrosion, 233-34
impurity-phase identification, 53
mechanical properties, 52
metallurgy, 52-53
properties, 175
reaction with UC, 84
reaction with UN, 84
thermal properties, 184
welding, 142-44, 262
Niobium alloys (Al–Hf–Nb)
oxidation, 100
Niobium alloys (Al–Nb–Ta–Ti)
crack growth, 230
welding, 145
Niobium alloys (Cr–Fe–Ni–Nb)(irradiated)
ductility, B effects on, 112
Niobium alloys (Cr–Ni–Nb)(irradiated)
fission-fragment damage, 190
stress-rupture properties, annealing effects on, 191-92
Niobium alloys (Cr–Nb)
mechanical properties, 127
Niobium alloys (Cr–Nb–U)
transformation, 1
Niobium alloys (Cu–Nb–Zr)
corrosion and H uptake, 229
Niobium alloys (Hf–Nb–W)
(see also C-129)
cavitation, 105
Niobium alloys (Hf–Nb–W–Y)
(see C-129Y)
Niobium alloys (high-strength)
oxidation, 125
Niobium alloys (Ir–Nb)
mechanical properties, 127
Niobium alloys (La–Nb)
mechanical properties, 127
Niobium alloys (Mo–Nb)
binary interdiffusion in, 132
corrosion, 230-31
high-temperature properties, 185
mechanical properties, 52, 127
Niobium alloys (Mo–Nb–Ta–Zr)
(see SCb-61)
Niobium alloys (Mo–Nb–Ti–Zr)
(see PWC-533)
Niobium alloys (Mo–Nb–W–Zr)
(see F-48)
Niobium alloys (Mo–Nb–V–Zr)
(see B-66)
Niobium alloys (Ni–Nb)
mechanical properties and phase studies, 52
Niobium alloys (Nb–refractory metal)
treatment, 245
Niobium alloys (Nb–Re)
mechanical properties, 127
Niobium alloys (Nb–Ta)
corrosion, 230-31
mechanical properties, 127
Niobium alloys (Nb–Ta–Ti–V)
creep resistance, 53
Niobium alloys (Nb–Ta–W)
(see SCb-291)
corrosion, 233-34
Niobium alloys (Nb–Ta–W–Zr)
(see FS-85)
Niobium alloys (Nb–Ta–V)
phase studies, 129
Niobium alloys (Nb–Ta–Zr)
removal of N and O, 63
Niobium alloys (Nb–Sn)
phase studies, 52
Niobium alloys (Nb–Sn–Zr)
corrosion, 36
tempering, 50
Niobium alloys (Nb–Sn–Zr)(irradiated)
corrosion, 229, 240
mechanical properties, 240
oxidation, 229
Niobium alloys (Nb–Ti)
binary interdiffusion in, 132
coating with PWK-5, 199
corrosion, 230-31
high-temperature properties, 185
Niobium alloys (Nb–Ti–V)
annealing, 53
evaluation, 138
evaporation, 128
preparation, 138
Niobium alloys (Nb–Ti–Zr)
annealing, 53
Niobium alloys (Nb–W)
mechanical properties, 52, 127, 247
reaction with UC, 84
reaction with UN, 84
Niobium alloys (Nb–W–Y–Zr)
(see AS-55 and D-43Y)
Niobium alloys (Nb–W–Zr)
(see Cb-752, D-43, and X-34)
Niobium alloys (Nb–U)
specific heat, 205
transformation, 1
Niobium alloys (Nb–U–Zr)
properties, 204
Niobium alloys (Nb–U–Zr)(irradiated)
reaction with water, 161
Niobium alloys (Nb–V)
(see also B33)
binary interdiffusion in, 132
corrosion, 108, 230-31
evaluation, 138
interdiffusion in, 188
mechanical properties, 52
preparation, 138
twinning, 52
welding, 144
Niobium alloys (Nb–V–Zr)
aging, 127-28
hardness, 128
Niobium alloys (Nb–Zn), 52
Niobium alloys (Nb–Zr)
(see also D-11, D-14, PWC-11, PWC-33, and PWC-34)
age-hardening, 183-84
annealing, 53
binary interdiffusion in, 132
brazing, 146
carburization, 140
coating with PWK-5, 106, 199
compatibility with Be, 94
corrosion, 35-36, 40, 108, 110, 177, 229-31, 233-34
electrical resistivity, 127
fracture, 58
heat treatment, 183
H segregation, 124

H terminal solubility in, 28
ingot structure, O effects on, 256
joining to Al_2O_3, 146
mechanical properties, 52, 127
N removal, 63
N solubility in, 126-27, 184
oxidation, 37
oxidative weight gain, 127
O removal, 63
properties, 57-58
recrystallization temperature, 127
strength, 35
strengthening, 127
stress-corrosion cracking, 235
tempered structures, 244
tensile properties, 118
Zr_2H_3 reorientation, stress effects on, 124
Niobium alloys (Nb–Zr)(irradiated)
annealing, 114
creep properties, 114
impact properties, 46, 192
Niobium carbide
C diffusion in, 189
corrosion, 107, 110
Niobium carbide (Mo bonded)
corrosion, 107-8
Niobium carbide films (Nb_2C)
growth on Nb—Zr alloys, 140
Niobium carbide solid solutions (Hf carbide–Nb carbide)
preparation and properties, 101
Niobium diboride
hardness, 251
Niobium disilicide
thermal dilation, 106
Niobium disilicide systems (Nb–$NbSi_2$)
intermediate-phase growth-rate kinetics, 105
Niobium dispersions
preparation, 80
Niobium hydride
tensile properties, 29-30
Niobium monocarbide films
growth on Nb–Zr alloys, 140
Niobium monocarbide systems (NbC–UC)
creep rate, 212
Niobium nitride
corrosion, 110
Niobium oxide systems (Nb_2O_5–WO_2)
phase studies, 133
Niobium silicide (Nb_5Si_3)
thermal dilation, 106
Niobium single crystals
mechanical properties, purification effects on, 182
Niobium system couples (Mo–Nb–Ti–WC)
corrosion, 108
Niobium systems (B–Nb)
mechanical properties, 127
Niobium systems (C–Cr–Co–Nb–W–Y)
oxidation and strength, 131
Niobium systems (C–Fe–Nb)
phase studies, 246
Niobium systems (C–Mo–Nb–Ti–Zr)
fabrication and properties, 51
Niobium systems (C–Nb–W–Zr)
cold working, 127
corrosion, 233-34
Niobium systems (C–Nb–Zr)
corrosion, 108
development, 52
phase studies, 128
Niobium systems (Hf–Mo–Nb–W)
(see SU-16)
Niobium systems (H–Nb)
phase studies, 29
tensile properties, strain-rate effects on, 56
Niobium systems (Mo–Nb–Si)
phase studies, 128
Niobium systems (Nb–$NbSi_2$)
intermediate-phase growth-rate kinetics, 105
Niobium systems (Nb–Si)
mechanical properties, 127
Niobium systems (Nb–TiC)
corrosion, 40
Niobium tubing
bonding to stainless steel (316), 198
Nitride coatings (refractory)
for Ta, 38
Nitrides
corrosion, 110
Nitrogen systems (C–Cr–Fe–Ni–N)
stress-corrosion cracking, 104
Nitrogen systems (C–N–Pu)
hardness, 8
Nondestructive testing, 69-70, 147-48, 200-1, 263-64
Nonfuel materials (irradiated)
(see also Fuel materials)
properties, 43-49, 111-17, 189-93, 239-43
Novodur ABS plastic
coating with Ni, 66
Nuclear poisons, 32-34, 99-102, 171-73, 228-28

O

Organic coolants
corrosive and hydriding effects on Zr alloys, 36
Osmium
phase diagrams, 186
Osmium alloys (Mo–Os–W)
phase studies, 128-29
Osmium alloys (Os–W)
casting, 255
Osmium intermetallic compounds (Pu_5Os_3)
physical properties, 153
Oxides
formation of dense, 193
Oxides (PuO_2 containing)
thermal expansion, 77
Oxygen systems (C–O–Pu)
phase studies, 207
Oxygen systems (Co–O–W)
phase studies, 129
Oxygen systems (Hf–O)
hardness and phase studies, 99
Oxygen systems (O–Pu)
phase studies, 8
Oxygen systems (O–Na–U)
phase studies, 5
Oxygen systems (O–Zr)
H terminal solubility in, 28

P

Palladium
phase diagrams, 186
solubility in molten Zn, 236
Palladium alloys (Ni–Pd)
use for brazing, 146
Palladium alloys (Pd–Ti)
corrosion, 105
Palladium intermetallic compounds (PuPd)
physical properties, 153
Particles
(see also Powders)
vibratory compaction, 64
Penetrameter
development, 148
PFR-6 coating
behavior, 231-32
development for Mo alloys, 106
PFR-32 coating
behavior, 231-32
Plastic (Novodur ABS)
coating with Ni, 66
Plastics
corrosion, 36
Plating (electro-), 66-67, 140-42, 198-99, 259-60
Plating (nonelectrolytic chemical), 65-66, 139-40, 199-200, 258-59
Platinum
corrosion, 177-78
electroplating with metals, 198-99
phase diagrams, 186
solubility in molten Zn, 236
Platinum alloys (Pt-Ta)
phase studies, 53
Platinum alloys (Pt-Ti)
binary interdiffusion in, 132
Platinum coatings
for Mo alloys and Nb alloys, 233
Platinum intermetallic compounds (Pu_3Pt_5)
physical properties, 153
Plutonium
annealing, 77
creep properties, 7, 77
diffusion in Mg, 188
diffusion in Mg alloys, 188
diffusion in UO_2, 82, 248
distribution in irradiated UO_2, 11
electrodeposition, 67
electronic structure, 6
etching, electrolytic, 77
physical metallurgy, 77
preparation of high-purity, 6
reactions of burning, with solvents, 6
solubility in molten Zn, 236
solubility in PuN, 78
solubility in Th, 79
transformation, 6-7, 77, 206
Plutonium (molten)
Nb solubility in, 153
Re solubility in, 5
Ta solubility in, 5
Plutonium alloys, 5-7, 205
Plutonium alloys (Ce–Fe–Pu)
phase studies, 77
Plutonium alloys (Ce–Pu)(molten)
viscosities, 6, 75, 77
Plutonium alloys (fissium–Pu–U)
compatibility with stainless steel, 5
development, 6
phase studies, 74-75
solidus temperatures, 5
Plutonium alloys (fissium–Pu–U)(irradiated)
properties, 205-6
Plutonium alloys (fissium–Pu–U)(clad)(irradiated)
burnup, 74
Plutonium alloys (fizzium–Pu–U)(irradiated)
properties, 205-6
Plutonium alloys (Fe–Pu–U)
properties, 153-54
Plutonium alloys (Mo–Pu–U)
fabrication, 138
thermal expansion, 206
Plutonium alloys (Pu–Th–U)
compatibility studies, 9
development, 6
Plutonium alloys (Pu–Ti–U)
casting, 138
compatibility with stainless steel, 5

creep properties, 6
ductility, 6
mechanical properties, 75
phase studies, 153
solidus temperatures, 5
thermal conductivity, 153
thermal expansion, 5–6
Plutonium alloys (Pu–Ti–U)(molten)
penetration of Ti–V alloy, 205
Plutonium alloys (Pu–U)
development, 5-6
phase studies, 75
Plutonium alloys (Pu–U–Zr)
casting, 138
compatibility with stainless steel (304), 5, 205
creep properties, 6
mechanical properties, 75
phase studies, 75, 153
solidus temperatures, 5
thermal conductivity, 153, 205
thermal expansion, 6
transformation, 75
Plutonium alloys (Pu–U–Zr)(molten)
penetration of stainless steel (304), 205
Plutonium alloys (Pu–Zr)
solidus temperatures, 75
Plutonium aluminates ($PuAlO_3$)
crystal properties, 77-78
Plutonium carbide systems (Pu carbide–Th carbide)(coated)(irradiated)
performance, 210
Plutonium carbide systems (Pu carbide–U carbide)
compatibility studies, 8
fabrication, 212
synthesis, 212
thermal diffusivity, 7
Plutonium carbide systems (Pu carbide–U carbide)(Nb clad)(irradiated)
properties, 160
Plutonium carbide systems (Pu carbide–U carbide)(stainless-steel clad)(irradiated)
properties, 160
Plutonium dioxide
compatibility with Cr–Ni alloy, 207
compatibility with Nb, 8
sintering, 78
Plutonium dioxide dispersions (Al(1100)–PuO_2)
development, 9
Plutonium dioxide dispersions (Nichrome–PuO_2)
metallography, 208
Plutonium dioxide dispersions (Nb–PuO_2 particles (coated)–Zr)
preparation, 80
Plutonium dioxide dispersions (Nb–(Pu-U) O_2 particles (coated)–Zr)
preparation, 80
Plutonium dioxide dispersions (PuO_2–stainless steel(304L))
development, 9
Plutonium dioxide dispersions (PuO_2–stainless steel(304L)(irradiated))
properties, 9
Plutonium dioxide microspheres
preparation, 206-7
properties, 78, 207
Plutonium dioxide mixtures (PuO_2–ThO_2)(irradiated)
fission-gas release, 78
Plutonium dioxide mixtures (PuO_2–UO_2–ZrO_2)
preparation, 82
preparation, 80
Plutonium dioxide particles
coating with metals, 80
Plutonium dioxide pellets
preparation of glass-bonded, 8
Plutonium dioxide system pellets (PuO_2–UO_2)
preparation of glass-bonded, 8
Plutonium dioxide system pins (PuO_2–UO_2)(irradiated)
behavior, 8
Plutonium dioxide systems (BeO–PuO_2–ThO_2)
phase studies, 8
Plutonium dioxide systems (CaO–PuO_2–UO_2–ZrO_2)
melting points, 78
Plutonium dioxide systems (PuO_2–UO_2)
compatibility with refractory metals, 78
density, 154
melting point, 154
particle-size-distribution determination, 8
preparation of spherical particles, 154
thermal expansion, 77
thermal gradient effects, 78
Plutonium dioxide systems (PuO_2–UO_2)(self-irradiated)
Plutonium dioxide systems (PuO_2–UO_2–ZrO_2)
lattice parameters and stability, 154
Plutonium intermetallic compounds
physical properties, 153
Plutonium monocarbide
free energy of formation, 78
production, 154
solubility in ThC_2, 12
Plutonium monocarbide (clad)(irradiated)
fission-gas release, 79
Plutonium monocarbide (self-irradiated)
lattice parameters, 207
Plutonium monocarbide system particles (PuC–UC)
preparation, 7-8
vibratory compaction, 64
Plutonium monocarbide systems (PuC–UC)
preparation, 207
preparation of powders, 154-55
reactions with alloys, 159
reactions with metals, 78, 159
reduction in H_2, 161
sintering, 161
Plutonium monocarbide systems (PuC–UC)(Nimonic 90 clad)(irradiated)
damage, 86
Plutonium monocarbide systems (PuC–UC) stainless-steel clad)(irradiated)
fission-gas release, 212
Plutonium mononitride
analysis for O, 8
free energy of formation, 78
heat treatment effects, 78
impaction, 8
Pu solubility in, 78
thermal expansion, 8
thermodynamic properties, 207
vapor pressure, 8
Plutonium mononitride compacts (PuN–stainless steel)
Plutonium mononitride systems (PuN–UN)
preparation, 155, 207
Plutonium monophosphide
microhardness, 79
Plutonium monosulfide
melting point, 155
microhardness, 79
Plutonium monosulfide solid solutions (PuS–US)
preparation, 155, 207
Plutonium monosulfide systems (PuS–US)
lattice constants and melting points, 207
Plutonium monoxide systems (PuO–UO)
stability, 155
Plutonium nitride systems (Pu nitride–U nitride)
properties, 8, 207
Plutonium nitride systems (Pu nitride–U nitride)(irradiated), 207
Plutonium sesquicarbide
free energy of formation, 78
reduction in H_2, 161
sintering, 161
Plutonium sesquicarbide (self-irradiated)
lattice parameters, 207
Plutonium sesquicarbide system (Pu_2C_3–UC)
reduction in H_2 and sintering, 161
Plutonium sesquioxide
preparation, 8
Plutonium sesquisulfide
microhardness, 79
Plutonium silicides (Pu_5Si_3)
physical properties, 153
Plutonium single crystals
growth, 153
preparation, 6
Plutonium systems (C–N–Pu)
hardness, 8
Plutonium systems (C–O–Pu)
phase studies, 207
Plutonium systems (C–Pu)
vapor pressure, 78
Plutonium systems (C–Pu–Th)
phase studies, 12
Plutonium systems (O–Pu)
phase studies, 8
Poisons (nuclear), 32-34, 99-102, 171-73, 226-28
Poisson's ratio
brittle materials, 121
Potassium
corrosion, 177-78
phase diagrams, 186
Potassium (molten)
corrosive effects, 40-41, 107, 109, 177, 234
Potassium (vaporized)
corrosive effects of wet, 108
Potassium alloys (NaK)
corrosive effects, 107-10, 176-77
Potassium chloride (irradiated)
rare-gas diffusion in, 163
Potassium fluoride (irradiated)
rare-gas diffusion in, 163
Potassium iodide (irradiated)
rare-gas diffusion in, 163
Powders
(see also Particles)
pressing, hot isostatic, 142
Powders (ceramic)
fabrication, 193
Powders (irradiated)
fission-gas release, 162
Powders (nonmetallic)
coating with Mo and W, 139-40
Praseodymium
solubility in molten Zn, 236
W solubility in, 247
Pressure vessels
fracture mechanics of steel, 181
Production reactors
fuel production for, 63
Protactinium
diffusion in UO_2, 82, 248
electrodeposition on Pt, 198-99
PWC-11
corrosion, 40, 108

mechanical properties, 52-53
oxidative weight gain, 127
PWC-33
corrosion, 108
mechanical properties, 52-53
PWC-34
mechanical properties, 52-53
PWC-533
corrosion, 40-41
PWK-1 coatings
use on refractories, 199
PWK-5 coatings
use on refractories, 106, 199

R

Radiation detectors
use in nondestructive assay of fuels, 70
Radiation effects
fuel materials, 15-17, 87-88, 162-63
nonfuel materials, 43-49, 111-17, 189-93
Radiography, 70
Rare-earth hydrides
properties and structure, 224-25
Reactors (boiling water)
corrosion suppression using NH_3, 230
Reactors (Enrico Fermi Fast Breeder)
radiation damage in graphite shield, 166
Reactors (production)
fuel production for, 63
Reactors (SNAP-8)
corrosion in, 176-77
Reactors (SNAP-10A/2)
H release from fuel during destructive test, 28
Reactors (sodium-graphite)
welding in maintenance of, 68
Refractories
(see Alloys (refractory metal) and Metals (refractory))
Rene' 41
coating of, 257
erosion, 177
properties, 124
Rene' 41 (irradiated)
mechanical properties, 124
Rene' 62
tensile properties, temperature effects on, 180
Reprocessing solutions
corrosive effects, 178
Rhenium
C solubility in, 51
chemical plating using, 140, 258
compatibility with UC–ZrC system, 159
corrosion, 247
creep-rupture properties, 249
diffusion in Mo, 248
electrodeposition of, 141, 198
mechanical properties, 247
phase diagrams, 186
physical metallurgy, 247
physical properties, 247
reaction with steam, 42, 231
solubility in molten Pu, 5
surface-recession rates, 125
Rhenium (irradiated)
defects, 49
Rhenium alloy rod (Mo–Re–W)
fabrication, 256
Rhenium alloy sheet (Re–W)
Young's modulus, static, 118, 120
Rhenium alloy thermocouples (Re–W vs. W)
sheathing of, 105
Rhenium alloy tubing (Re–W)
fabrication, 63, 256
Rhenium alloys, 247
Rhenium alloys (Cr–Re)
electrodeposition on Cr, Cu, Mo, and W, 198
notch impact properties, 250
Rhenium alloys (Hf–Re–Ta)
phase studies, 129
Rhenium alloys (Mo–Re)
creep-rupture properties, 249
Rhenium alloys (Mo–Re–W)
creep-rupture properties, 120, 249
creep strength, 249
powder metallurgy, 256
Rhenium alloys (Nb–Re)
mechanical properties, 127
Rhenium alloys (Re–W)
age hardening, 186
casting, 255
chemical plating using, 199
corrosion, 108
creep properties, 120, 181, 249
creep-rupture properties, 120
deposition of, 65, 140
fabrication, 256
powder metallurgy, 256
recrystallization temperature, ThO_2 effects on, 247
vapor deposition, 258
welding, 143
Rhenium disilicide
oxidation and thermal dilation, 106
Rhenium system sheet (Re–ThO_2–W)
fabricability and properties, 247
Rhodium
phase diagrams, 186
solubility in molten Zn, 236
Rhodium coatings (Ir–Rh)
for W, 233
Rhodium intermetallic compounds (Pu_3Rh_5)
physical properties, 153
Rubidium
phase diagrams, 186
Ruthenium
phase diagrams, 186
solubility in molten Zn, 236
Ruthenium intermetallic compounds (Pu_5Ru_3)
physical properties, 153

S

Salts (fused)
corrosive effects, 107-10, 236
Samarium
W solubility in, 247
SAP
(see Aluminum (SAP))
Scandium
phase diagrams, 186
W solubility in, 247
Scandium alloys (Sc–Y) (hydrided)
phase studies and thermodynamic properties, 97
Scandium hydride
H absorption, 97
Scandium intermetallic compounds
identification, 27
SCb-61
erosion, 177
SCb-291
corrosion, 40
welding, 143
Silicide coatings
thermal stresses of, on refractory metals, 106
Silicide fused slurry coatings
development and evaluation, 106
Silicides
deposition on D-14 and D-43, 140
transformation, 74
Silicon
corrosion, 177-78
solubility in molten Zn, 236
vapor deposition on Mo and Ta, 199
Silicon carbide
corrosion, 40
Silicon coatings (Cr–Si–Ti), 38, 106, 231-32
Silicon dioxide fibers (Al coated)(irradiated)
strength, 115
Silicon dioxide fibers (irradiated)
damage, 115
Silicon fused slurry coatings
development and evaluation, 106
Silicon monocarbide powder
compaction, 142
Silicon monocarbide systems
oxidation, 132
Silicon monocarbide systems (BeO–MgO–SiC)
properties, 223
Silicon monocarbide systems (BeO–SiC)
properties, 223
Silicon system films (Al–Si)
annealing and growth, 259
Silicon system tubes (Al–Fe–Si–U) (Zircaloy clad)(irradiated)
swelling, 2-4
Silicon systems
oxidation, 132
Silicon systems (Al–Fe–Mo–Si–U)
hardness, 2
Silicon systems (Al–Fe–Ni–Si)
corrosion, 103
Silicon systems (Al–Si)
corrosion, 103
Silicon systems (B–Cr–Ni–Si)
(see CM 53)
Silicon systems (B–Ni–Si)
(see CM 52)
Silicon systems (Li–Mg–Si)
casting, 256
Silicon systems (Mo–Nb–Si)
phase studies, 128
Silicon systems (Mo–Si–U)
phase studies, 74
physical metallurgy, 1
properties, 1-2
Silicon systems (Mo–Si–U)(irradiated)
swelling, 152
Silicon systems (Nb–Si)
mechanical properties, 127
Silver
corrosion, 177-78
diffusion in Be, 248
electrodeposition on Be, 67
solubility in molten Zn, 236
use for brazing, 146
Silver (irradiated)
primary knock-on recoil spectrum, 192-93
Silver alloys
use in brazing of Be, 168, 261
Silver alloys (Be–Ag)
phase studies, 92-93
Silver alloys (Eu–Ag)
phase studies, 226
Silver alloys (Cd–In–Ag)(plated)(irradiated)
mechanical properties, 32
SNAP-8
corrosion in, 176-77
SNAP-10A/2 reactor
H release from fuel during destructive test, 28
Sodium
corrosion, 177-78
solubility in molten Zn, 236
Sodium (molten)
corrosive effects, 39, 109-10, 175-76, 233-34

effects on EI-437B creep rate, 39–40
effects on EI-851 creep rate, 39–40
effects on EI-869 creep rate, 39–40
effects on ferritic steel relaxation, 39
O solubility in, 39
ultrasonic scanning in, 200
wetting of U ceramics, 110
Sodium alloys (NaK)
corrosive effects, 107–10, 176–77
Sodium fluoride mixtures (MgF_2–NaF) (molten)
corrosive effects, 236
Sodium-graphite reactors
welding in maintenance of, 68
Sodium systems (O–Na–U)
phase studies, 5
Solids (irradiated)
bubble behavior, 213–14
bubble behavior during annealing, 162
defect structure, 116
radiation saturation, 116
Solutions (fuel reprocessing)
corrosive effects, 178
Spectrometers (Compton)
use in nondestructive-assay of fuels, 70
Stainless steel
compatibility with fissium–Pu alloys, 5
compatibility with Pu–Ti–U alloys, 5
corrosion, 174–75, 230
corrosion of B-containing, 50
explosive cladding of mild steel with, 67
friction welding, 68
hot-working properties of B-containing, 50
joining, 68, 146–47
oxidation, Si effects on, 229
properties, rare-earth effects on, 244
sensitization, aging effects on, 184
tensile properties, 184
Stainless steel (irradiated)
corrosion, 174
damage, 115
ductility, 112, 239
properties, 43–44
Stainless-steel cermets (stainless steel–UO_2)
development, 9, 79
Stainless-steel cladding
reaction with steam, 237–38
Stainless-steel compacts (PuN–stainless steel)
oxidation, 8
Stainless-steel dispersions (Eu_2O_3–stainless steel)(irradiated)
properties, 228
Stainless-steel dispersions (Eu_2O_3–stainless steel)(stainless-steel clad)(irradiated)
examination, 171–72
Stainless-steel dispersions (stainless steel–UO_2)
fabrication, 155–56
Stainless-steel system cladding (B–stainless steel)(irradiated)
performance, 226, 228
Stainless-steel systems (Cr–stainless steel)
stress rupture in liquid metal, 233
Stainless-steel tubing
lining with Al, 68
mechanical properties, 118
thickness measurement, 263–64
welding, 68
Stainless steel (17-4 PH)
corrosion, 36–37
Stainless steel (17-4 PH)(irradiated)
embrittlement, 189–90
Stainless steel (18-8)(irradiated)
ductility, Ti effects on, 43
Stainless steel (20-25)(irradiated)
stress-corrosion cracking, 104
Stainless steel (25-20)
corrosion, 103–4
Stainless-steel (301) tanks
burst testing, 184
Stainless steel (302)
corrosion, 36
Stainless steel (303)
corrosion, 36
Stainless steel (304)
carburization, 176
compatibility with Pu–Th–U alloys, 9
compatibility with Pu–U–Zr, 5, 205
compatibility with $Pu_{0.2}C$–$U_{0.8}C$ system, 8
corrosion, 36–37, 103–4, 109–10, 178–79, 236
creep properties, 56, 113
development of boronated, 99
ductility, 43
nitriding, 175
nondestructive testing of brazed joints in, 70
penetration by molten Pu–U–Zr alloys, 205
reaction with PuC–UC system, 159
reaction with steam, 41, 174–75, 179–80, 237
rupture life, carburization effects on, 124
stress-corrosion cracking, 104, 230
stainless-steel (304) corrosion-product deposition on, 36
ultrasonic testing, 69
Stainless steel (304)(irradiated)
behavior of boronated, 99
creep properties, 44, 113
ductility, 43, 189
embrittlement, 43, 189–90, 239
He production, 192
H production, 192
mechanical properties, 190
microstructure, 190
Stainless-steel (304) cladding (irradiated)
properties, 189
Stainless-steel (304) tubing
collapse and creep-buckling, 118
corrosion of brazed joints, 234
Stainless-steel (304B) dispersions stainless steel(304B)–UO_2)
fabrication and mechanical properties, 209
Stainless steel (304L)
ductility, 43
Stainless steel (304L)(irradiated)
ductility, 43
Stainless-steel (304L) cladding(irradiated)
burst testing, 239
Stainless-steel (304L) dispersions (PuO_2–stainless steel(304L))
development, 9
Stainless-steel (304L) dispersions (PuO_2–stainless steel(304L)(irradiated))
properties, 9
Stainless steel (304L sensitized)
corrosion, 36
Stainless steel (310)
mechanical properties, sigma-phase effects on, 59
microstructural evaluation for cladding use, 51
properties, Ce effects on, 244
sigma-phase identification, 50
stress-corrosion cracking, 104
wetting by Bi–Pb eutectic, 178
Stainless steel (316)
brazing, 94, 146
carburization, 176
cavitation, 105
compatibility with Be, 94
corrosion, 36–37, 40–41, 233
nitriding, 175
properties, Ce effects on, 244
reaction with Fe–UC system, 159
reaction with UC, 159
Stainless steel (316)(irradiated)
ductility, B effects on, 112
embrittlement, 189–90
He production, 192
H production, 192
stress-corrosion cracking, 104
tensile properties, 112–13
Stainless-steel (316) couples
corrosion, 109
Stainless-steel (316) tubing
bonding to Nb, 198
Stainless steel (316L)
oxidation, Mo effects on, 229–30
welding, 145
Stainless steel (316L)(irradiated)
embrittlement, 189–90
Stainless steel (321)
corrosion, 41
Stainless-steel (321) couples
corrosion, 109
Stainless steel (347)
corrosion, 41
Stainless steel (347)(irradiated)
properties, 192, 239
tensile properties, 112–13
Stainless-steel (347) dispersions (stainless steel(347)–UO_2–ZrB_2)
properties, 156
Stainless-steel (347) dispersions (stainless steel(347)–UO_2–ZrB_2(Nb coated))
properties, 156
Stainless-steel (347) dispersions (stainless steel (347)–UO_2)
preparation, 208–9
Stainless-steel (347) dispersions (stainless steel (347)–UO_2)(irradiated)
swelling, 208–9
Stainless-steel (347) tubes (irradiated)
ductility, 190
Stainless-steel (348) cladding (irradiated)
evaluation, 190
Stainless steel (405)
corrosion, 178–79
Stainless steel (406)
corrosion, 37
Stainless steel (406)(irradiated)
tensile properties, 112–13
Stainless-steel (406) tubing
strength, 117
Stainless steel (410)
corrosion, 103–4
joining to Zircaloy, 68
stainless-steel (304) corrosion-product deposition on, 36
wetting by Bi–Pb eutectic, 178
Stainless steel (410)(irradiated)
properties, 192
Stainless steel (430)
corrosion, Mo and U effects on, 230
wetting by Bi–Pb eutectic, 178
Stainless steel (502)
wetting by Bi–Pb eutectic, 178
Stainless steel (A-286)(irradiated)
properties, 192
Stainless steel (austenitic)
corrosion, 174
oxidation, Mo effects on, 229–30
properties, 50, 244
Stainless steel (austenitic)(irradiated)
corrosion, 174

ductility, 112, 189
mechanical properties, 239-40
properties, 244
Stainless-steel (austenitic) tubing
strength, 117
Stainless steel (Cr–Ni)
oxidation, Si effects on, 229
Stainless steel (Cr-Ni)(irradiated)
properties, 113
Stainless-steel (Cr–Ni–Nb-stabilized) tubing (irradiated)
ductility and strength, 43-44
Stainless steel (nitrided)
corrosion, 36
Star J
corrosion, 40
Steel
corrosion inhibition, 36
explosive forming, 260
fatigue properties, creep effects on, 54
properties, 180-81
Steel (irradiated)
mechanical properties, H effects on, 241
properties, 180-81
Steel (19-9DL)
corrosion, 41
Steel (1020 carbon)
corrosion, 109-10, 178-79
Steel (1035)
friction welding, 68
Steel (3140)
friction welding, 68
Steel (4140)
friction welding, 68
Steel (A-212B)
hardenability, U addition effects on, 50
Steel (A-212B)(irradiated)
embrittlement, 190
Steel (A-302B)
fatigue properties, 181
Steel (A-302B)(irradiated)
damage, 190
hardening, 241
Steel (A-350LF1(Modified)) (irradiated)
embrittlement, 190
Steel (alloy)
mechanical properties of strain-aged, 181
Steel (austenitic)
annealing, 244
Steel (austenitic)(irradiated)
corrosion, 113
fission-fragment damage, 190
Steel (carbon)
corrosion, 37, 110, 230
friction welding, 68
Steel (carbon)(irradiated)
corrosion, 174
hardening, 241
mechanical properties, 191
Steel (Cr)
properties, 244
Steel (Cr)(irradiated)
properties, 244
Steel (Cr–Mn) sheet (irradiated)
mechanical properties, 191
Steel (Cr–Mn–Ni)
friction welding, 68
Steel (Cr–Mo)
carburization, 176
corrosion, 235
properties, 190-91, 244
wetting by Bi–Pb eutectic, 178
Steel (Cr–Mo)(irradiated)
properties, 190-91, 244
Steel (Cr–Mo–Ni)(irradiated)
hardening, 241
tensile properties, 191
Steel (Cr–Ni)
creep rates, 39-40
Steel (Cr–Ni–Nb)
annealing, 244
Steel (Ducol W30)
fatigue properties, 181
Steel (EI-851)
creep rates, 39-40
Steel (ferritic)
relaxation, 39
Steel (high strength)
development, 69
fracture toughness, 117
joining, 68-69
Steel (low alloy)
corrosion, 230
Steel (low alloy)(irradiated)
hardening, 241
properties, 190-91
Steel (Mn)
properties, 244
Steel (Mn)(irradiated)
properties, 244
Steel (Mn–Mo)
mechanical properties, 124
Steel (maraging)
welding, 261
Steel (maraging)(irradiated)
brittle–ductile transition temperature, 112
tensile properties, 191
Steel (mild)
corrosion, 37
explosive cladding of, 67
fatigue-limit behavior, 181
ultrasonic testing for fatigue cracks, 200
Steel (mild)(irradiated)
mechanical properties, 111-12
Steel (Ni)(irradiated)
properties, 46, 49
Steel (18Ni maraging)
welding, 69
Steel (Soudotenax 56)
fatigue properties, 181
Steel (T-1)
friction welding, 68
Steel (ZA)
fatigue properties, 181
Steel (ZD)
fatigue properties, 181
Steel (ZS)
fatigue properties, 181
Steel pressure vessels
fracture mechanics, 181
Stellite 6B
erosion, 177
Strontium
diffusion in graphite, 91
phase diagrams, 186
solubility in molten Zn, 236
Strontium alloys (Cd–Sr)
phase studies, 226
Strontium hydride systems (Sr–SrH_2)
phase studies, 224
Strontium systems (Sr–SrH_2)
phase studies, 224
Structural materials, 35-62, 103-37, 174-96, 229-54
SU-16
properties, 53
Sylvania "A"
creep properties, 181
welding, 143
Systems for Nuclear Auxiliary Power (see SNAP...)

T

T-111
corrosion, 40, 108, 234
creep properties, 249-50
diffusion bonding, 64
erosion, 177
evaporation loss, 124-25
stress-corrosion cracking, 235-36
welding, 143-44
T-111 tubing
fabrication, 257
T-222
coatings for, 232-33
corrosion, 40
creep properties, 181, 249-50
welding, 143
Tantalum
C in, interstitial ordering of, 53
coatings for, 38
compatibility with $Pu_{0.7}C$–$U_{0.3}C$ system, 8
compatibility with PuO_2–UO_2 system, 78
compatibility with Th, 9
compatibility with UC–ZrC system, 159
compatibility with UP, 212
corrosion, 37-38, 40, 177-79, 234-36
creep-rupture properties, 249
deposition by sputtering, 66
electrodeposition of, 141
H embrittlement, 247
metallurgy, 53
oxidation, 105
oxide-dispersion hardening, 51
phase diagrams, 186
properties, 175
reaction with PuC–UC system, 159
reaction with steam, 42
reaction with UO_2, 211
recrystallization temperature, Y effects on, 185
siliconizing of, 199
solubility in molten Pu, 5
solubility in rare earths, 185
surface-recession rates, 125
thermal expansion, 53
use to protect thermocouples, 105
vapor deposition of, 65-66, 199, 259
work hardening, strain-aging effects on, 126
Tantalum (Ir plated)
brittleness, 141
Tantalum (irradiated)
corrosion, 174
Tantalum alloy coatings (Hf–Mo–Ta)
oxidation, 106
Tantalum alloy coatings (Hf–Ta)
oxidation, 106
for Ta, 38
for Ta alloys, 233
Tantalum alloys
cavitation, 105
coatings for, 38, 233
metallurgy, 53
properties, 175
reactions with UC, 84
reactions with UN, 84
thermal properties, 184
welding, 142-43, 262
Tantalum alloys (Al–Hf–Nb)
oxidation, 100
Tantalum alloys (Al–Hf–Ta)
oxidation, 100
Tantalum alloys (Al–Nb–Ta–Ti)
crack growth, 230
welding, 145
Tantalum alloys (Cr–Hf–Ta)
oxidation, 100

Tantalum alloys (Hf–Re–Ta)
phase studies, 129
Tantalum alloys (Hf–Ta)
phase studies, 226
Tantalum alloys (Hf–Ta–W)
(see also T-111)
cavitation, 105
corrosion, 108
phase studies, 247
Tantalum alloys (high-strength)
oxidation, 125
Tantalum alloys (Mo–Nb–Zr)
(see SCb-61)
Tantalum alloys (Mo–Ta–V)
phase studies, 129
Tantalum alloys (Nb–Ta)
corrosion, 230-31
mechanical properties, 127
Tantalum alloys (Nb–Ta–Ti–V)
creep resistance, 53
Tantalum alloys (Nb–Ta–W)
(see also SCb-291)
corrosion, 233-34
Tantalum alloys (Nb–Ta–W–Zr)
(see FS-85)
Tantalum alloys (Nb–Ta–V)
phase studies, 129
Tantalum alloys (Nb–Ta–Zr)
removal of N and O, 63
Tantalum alloys (Pt–Ta)
phase studies, 53
Tantalum alloys (Ta–W)
cavitation, 105
coatings for, behavior of, 231-32
corrosion, 40, 178, 231
creep properties, 249-50
electroplating with WSi_2 and ZrO_2, 259-60
mechanical properties, B effects on, 246-47
physical properties, B effects on, 246-47
welding, 143
Tantalum alloys (Ta–W–Zr)
phase studies, 247
Tantalum alloys (Ta–V)
corrosion, 230
Tantalum carbide
C diffusion in, 189
corrosion, 110
interstitial ordering of C in, 53
Tantalum carbide solid solutions (Hf carbide–Ta carbide)
preparation and properties, 101
Tantalum carbide systems (Ta–Ta_2C)
whisker reinforcement, 185
Tantalum couples
corrosion, 108-9
Tantalum disilicide
thermal dilation, 106
Tantalum disilicide systems (Ta–$TaSi_2$)
intermediate-phase growth-rate kinetics, 105
Tantalum monocarbide
thermal expansion, 133
Tantalum monocarbide systems (Co–TaC-WC)
(see Carboloy 907)
Tantalum silicide (Ta_5Si_3)
thermal dilation, 106
Tantalum silicide systems
oxidation, 132
Tantalum systems (C–Cr–Co–Ta–W–Y)
oxidation and strength, 131
Tantalum systems (C–Hf–Ta)
phase studies, 32
Tantalum systems (C–Hf–Ta–W)
(see T-222)
Tantalum systems (C–Ta–W)
(see K601)
Tantalum systems (HfC–Ta)
preparation, 101
Tantalum systems (SiC–Ta)
oxidation, 132
Tantalum systems (Ta–Ta_2C)
whisker reinforcement, 185
Tantalum systems (Ta–$TaSi_2$)
intermediate-phase growth-rate kinetics, 105
Technetium
phase diagrams, 186
solubility in molten Zn, 236
Technetium alloys (Tc–W)
hardness and solid-solution formation, 52
Technetium alloys (Tc–U)
phase studies, 152
Television (infrared sensitive)
use in nondestructive testing, 70
Testing (nondestructive), 69-70, 147-48, 200-1, 263-66
Terbium
W solubility in, 247
Thermalox 995A (irradiated)
behavior, 94, 96
Thorium
compatibility studies, 9
diffusion in UO_2, 82, 248
electrical resistivity, 155
electrodeposition on Pt, 198-99
Pu solubility in, 79
production, 207
properties, 79
solubility in molten Zn, 236
thermal conductivity, 155
thermoelectric power, 155
uses, potential, 79
Thorium (irradiated)
physical properties, annealing effects on, 9
Thorium (Zr clad)
fabrication, 257
Thorium alloys
properties, 79
tensile properties, 9
Thorium alloys (Au–Th)(Zr clad)
fabrication, 257
Thorium alloys (In–Th)
tensile properties, 9
Thorium alloys (Pu–Th–U)
compatibility studies, 9
development, 6
Thorium alloys (Th–U)(Zircaloy clad)
coextrusion, 198
Thorium alloys (Th–U)(Zr clad)
fabrication, 257
Thorium alloys (Th–Zr)
tensile properties, 9
Thorium carbide systems (Pu carbide–Th carbide)(coated)(irradiated)
performance, 210
Thorium compounds
properties, 79
Thorium couples
corrosion, 108-9
Thorium dicarbide
crystal structure, 12
PuC solubility in, 12
production by sol-gel process, 8-9
Thorium dicarbide particles
fabrication of spherical, 13
Thorium dicarbide system particles (ThC_2–UC_2)
fabrication of spherical, 13
Thorium dicarbide system particles (ThC_2–UC_2)(coated)(irradiated)
evaluation, 156-57
Thorium dicarbide systems (graphite–ThC_2) eutectic, 12
Thorium dicarbide systems (ThC_2–UC_2)
production by sol-gel process, 8-9
thermal expansion, 86
Thorium dioxide
surface energy, 13
thermal expansion, 77
Thorium dioxide coatings
application, 257
for W, 38
Thorium dioxide dispersions (Mo–Ni–ThO_2)
preparation, 51
Thorium dioxide dispersions (Ni–ThO_2)
mechanical properties, 51
oxidation, 37
preparation, 51
Thorium dioxide mixtures (PuO_2–ThO_2)
(irradiated)
fission-gas release, 78
Thorium dioxide particles
coating with porous C, 80
coating with PyC, 156
Thorium dioxide pellets
fabrication, 157
Thorium dioxide system particles (ThO_2–UO_2)(PyC coated)(irradiated)
evaluation, 157
Thorium dioxide system rods (ThO_2–UO_2) (clad)(irradiated)
performance, 13
Thorium dioxide systems sheet (Re–ThO_2–W)
fabricability and properties, 247
Thorium dioxide systems (BeO–PuO_2–ThO_2)
phase studies, 8
Thorium dioxide systems (BeO–ThO_2–UO_2–Y_2O_3)
UO_2 loss, 26-27
Thorium dioxide systems (BeO–ThO_2–UO_2–Y_2O_3)(irradiated)
fission-gas release, 27
Thorium dioxide systems (Th–ThO_2)
tensile properties, 9
Thorium dioxide systems (Th–ThO_2–Zr)
tensile properties, 9
Thorium dioxide systems (ThO_2–Y_2O_3) (irradiated)
^{133}Xe release, 162
Thorium monophosphide
preparation, 14
Thorium systems
tensile properties, 9
Thorium systems (B–Th)(Zr clad)
fabrication, 257
Thorium systems (C–Pu–Th)
phase studies, 12
Thorium systems (C–Th)
phase studies, 12
Thorium systems (Th–ThO_2)
tensile properties, 9
Thorium systems (Th–ThO_2–Zr)
tensile properties, 9
Thulium
W solubility in, 247
Tin
corrosion, 177-78
electrodeposition, 67
solubility in molten Zn, 236
Tin (molten)
corrosive effects, 178, 236
Tin alloys (Bi–Sn)(molten)
corrosive effects, 236
Tin alloys (Cr–Fe–Sn–Zr)
corrosion and mechanical properties, 103
Tin alloys (Nb–Sn)
phase studies, 52
Tin alloys (Nb–Sn–Zr)
corrosion, 36
tempering, 50

Tin alloys (Nb–Sn–Zr)(irradiated)
corrosion, 229, 240
mechanical properties, 240
oxidation, 229
Tin alloys (Sn–Zr)
corrosion, 36
Tin coatings (Al–Sn)
behavior, 231-32
for Nb and Nb alloys, 199
Titanium
bonding, 68, 147
B vapor deposition on, 66
compatibility with UP, 212
corrosion, 39, 104-5, 177-78, 235
deposition on D-14 and D-43, 140
effects on Mo recrystallization temperature, 182
mechanical properties, 182
phase diagrams, 186
properties, hot plastic deformation effects on, 255
solubility in molten Li, 107
solubility in molten Zn, 236
U diffusion in, 248
use in brazing of Be, 168
Titanium alloy couples (Mo–Ti)
corrosion, 108
Titanium alloy couples (Mo–Ti–Zr)
corrosion, 108
Titanium alloy tubing (Ti–V)
fabrication, 198, 256
Titanium alloys
(see also A-110 AT (irradiated))
corrosion, 105
friction welding, 68
stress-corrosion cracking, 230
Titanium alloys (Al–Cr–Ti–V)
friction welding, 68
Titanium alloys (Al–Mo–Ti–V)
properties, 183
Titanium alloys (Al–Nb–Ta–Ti)
crack growth, 230
welding, 145
Titanium alloys (Al–Ti–V)
crack growth, 230
welding, 68, 145
Titanium alloys (Be–Ti–Zr)
use for brazing, 146
Titanium alloys (Cr–Fe–Ni–Ti)(irradiated)
ductility, B effects on, 112
Titanium alloys (Cr–Ti–V)
corrosion, 257
creep properties, 186
fabrication, 257
Titanium alloys (high strength)
fracture toughness, 117
Titanium alloys (Mo–Nb–Ti–Zr)
(see PWC-533)
Titanium alloys (Mo–Ti)
binary interdiffusion in, 132
chemical plating of $MoSi_2$ on, 140
ductility, 125
erosion, 177
Titanium alloys (Mo–Ti–V)
corrosion, 109
Titanium alloys (Mo–Ti–Zr)
(see also TZM)
chemical plating of $MoSi_2$ on, 140
tensile properties, 118
Titanium alloys (Ni–Ti)
corrosion, 230-31
corrosion of brazed joints using, 40
Titanium alloys (Nb–Ta–Ti–V)
creep resistance, 53
Titanium alloys (Nb–Ti)
binary interdiffusion in, 132
coating with PWK-5, 199
high-temperature properties, 185
Titanium alloys (Nb–Ti–V)
annealing, 53
evaluation, 138
evaporation, 128
preparation, 138
Titanium alloys (Nb–Ti–Zr)
annealing, 53
Titanium alloys (Pd–Ti)
corrosion, 105
Titanium alloys (Pt–Ti)
binary interdiffusion in, 132
Titanium alloys (Pu–Ti–U)
casting, 138
compatibility with stainless steel, 5
creep properties, 6
ductility, 6
mechanical properties, 75
phase studies, 153
solidus temperatures, 5
thermal conductivity, 153
thermal expansion, 5-6
Titanium alloys (Pu–Ti–U)(molten)
penetration of Ti–V alloys, 205
penetration by molten Pu–Ti–U alloy, 205
Titanium alloys (Ti–U)
ductility and thermal expansion, 6
Titanium alloys (Ti–V)
compatibility studies, 8-9
corrosion, 39, 109, 230, 233
creep, Na effects on, 176
tensile properties, 118
thermal conductivity, 186
thermal expansion, 186
Titanium alloys (Ti–V)(irradiated)
He and H production, 192
Titanium alloys (Ti–Zr)
electrodeposition of, 140-41
H terminal solubility in, 28
Titanium diboride
corrosion, 40
Titanium carbide
corrosion, 107
Titanium carbide (Mo bonded)
corrosion, 107-8
Titanium carbide (Ni bonded)
corrosion, 107-8
Titanium carbide solid solutions (Hf carbide–Ti carbide)
preparation and properties, 101
Titanium coatings (Cr–Si–Ti), 38, 106, 231-32
Titanium dioxide
reaction with UO_2, 82
Titanium disilicide
oxidation and thermal dilation, 106
Titanium fused slurry coatings
development and evaluation, 106
Titanium hydride
mechanical properties, 97
Titanium monocarbide
corrosion, 40
Titanium monocarbide systems
corrosion, 40
Titanium silicide (Ti_5Si_3)
thermal dilation, 106
Titanium system couples (Mo–Nb–Ti–WC)
corrosion, 108
Titanium systems (Al–C–Ti–Zr)
mechanical properties at high temperatures, 123
Titanium systems (C–Mo–Nb–Ti–Zr)
fabrication and properties, 51
Titanium systems (C–Mo–Ti–Zr)
(see also TZC)
creep-rupture properties, 118
fabrication, 51, 138
properties, 51
Titanium systems (SiC–Ti)
oxidation, 132
Titanium systems (Ti–ZrO_2)
thermal shock, 251
Tracers
diffusion in metals and alloys, 131-32
Transducers
use in ultrasonic testing, 147-48
Trichloroethane (1,1,1-)
reaction with burning Pu, 6
Tubing
bowing measurement, 148
reductions, 138
ultrasonic testing, 147, 200
Tungsten
C solubility in, 51
casting, 255
coatings for, 38, 105, 233, 257
compatibility with molten UO_2, 211
compatibility with PuO_2–UO_2 system, 78
compatibility with UC–ZrC system, 159
compatibility with UP, 212
corrosion, 40, 177-78, 230
creep properties, 181
creep-rupture properties, 120, 249
diffusion in Mo, 248
electrodeposition of, 141
electroplating on, 67, 141, 198
grain properties, 246-47, 258
hardness, tensile strength relation to, 126
mechanical properties, 52, 182, 246-47, 250
metallurgy, 51-52
oxide-dispersion hardening, 51
phase diagrams, 186
physical properties, B effects on, 246
properties, 175
reaction with PuC–UC system, 159
reaction with steam, 42, 231
reaction with UC, 84
recrystallization, 246-47
solubility in molten UC, 211
solubility in rare earths, 247
strength metal-addition effects on, 182
strengthening, solid solution, 247
surface-recession rates, 125
tensile properties, interstitial effects on, 186
thermal conductivity, 126, 208
use for coating nonmetallic powders, 139-40
vapor deposition, 65, 139, 259
vapor pressure, 186
welding, 143-45
zone refining, 126
Tungsten (arc melted)
properties, 126
Tungsten (irradiated)
creep-rupture properties, 241-42
Tungsten alloy rod (Mo–Re–W)
fabrication, 256
Tungsten alloy sheet (Re–W)
Young's modulus, static, 118, 120
Tungsten alloy thermocouples (Re–W vs. W)
sheathing of, 105
Tungsten alloy tubing (Re–W)
fabrication, 63, 256
Tungsten alloys
metallurgy, 51-52
oxidation, 231
properties, 175
welding, 262
Tungsten alloys (Cr–Co–Fe–Ni–W)
(see L-605)
Tungsten alloys (Cr–Co–Ni–W)
(see Haynes 25)

Tungsten alloys (Co–W)
vapor deposition, 258
Tungsten alloys (Cu–Ni–W)
properties, 126
Tungsten alloys (Hf–Nb–W)
(see also C-129)
cavitation, 105
Tungsten alloys (Hf–Nb–W–Y)
(see C-129Y)
Tungsten alloys (Hf–Ta–W)
(see also T-111)
cavitation, 105
corrosion, 108
phase studies, 247
Tungsten alloys (Hf–W)
mechanical properties, 247
Tungsten alloys (high strength)
oxidation, 125
Tungsten alloys (Ir–W)
casting, 255
Tungsten alloys (Mo–Nb–W–Zr)
(see F-48)
Tungsten alloys (Mo–Os–W)
phase studies, 128-29
Tungsten alloys (Mo–Re–W)
creep-rupture properties, 120
creep strength, 249
powder metallurgy, 256
Tungsten alloys (Mo–W)
corrosion, 178
mechanical properties, 249
reaction with UC, 84
Tungsten alloys (Mo–W–Zr)
phase studies, 129
Tungsten alloys (Ni–W)
creep rates, 54
Tungsten alloys (Nb–Ta–W)
(see also SCb-291)
corrosion, 233-34
Tungsten alloys (Nb–Ta–W–Zr)
(see FS-85)
Tungsten alloys (Nb–W)
mechanical properties, 52, 127, 247
reaction with UC, 84
reaction with UN, 84
Tungsten alloys (Nb–W–Y–Zr)
(see AS-55 and D-43Y)
Tungsten alloys (Nb–W–Zr)
(see Cb-752, D-43, and X-34)
Tungsten alloys (Os–W)
casting, 255
Tungsten alloys (Re–W)
age hardening, 136
casting, 255
chemical plating using, 199
corrosion, 108
creep properties, 181, 249
creep-rupture properties, 120, 249
deposition of, 65, 140
fabrication, 256
powder metallurgy, 256
recrystallization temperature, ThO_2 effects on, 247
vapor deposition, 258
welding, 143
Tungsten alloys (Ta–W)
casting, 255
cavitation, 105
coatings for, 231-32, 259-60
corrosion, 40, 178, 231
creep properties, 249-50
mechanical properties, 246-47
physical properties, 246-47
welding, 143
Tungsten alloys (Ta–W–Zr)
phase studies, 247
Tungsten alloys (Tc–W)
hardness and solid-solution formation, 52
Tungsten carbide
corrosion, 107
Tungsten carbide (Co bonded)
corrosion, 107-8
Tungsten carbide (Mo bonded)
corrosion, 107-8
Tungsten carbide (Ni bonded)
corrosion, 107-8
Tungsten disilicide
chemical deposition, 66
oxidation, 106
thermal dilation, 106
Tungsten disilicide coatings
electroplating on Ta–W alloy, 259-60
Tungsten dispersions (W–UO_2)
density, 208
preparation, 207-8
thermal conductivity, 207-8
Tungsten fused slurry coatings
development and evaluation, 106
Tungsten monocarbide
solubility in molten Zr, 128
Tungsten monocarbide system couples (Mo–Nb–Ti–WC)
corrosion, 108
Tungsten monocarbide system (Co–TaC-WC)
(see Carboloy 907)
Tungsten monocarbide systems (Co–WC)
(see Carboloy 999)
Tungsten oxide systems (Nb_2O_5–WO_3)
phase studies, 133
Tungsten powder
use as binder for ZrB_2, 172
Tungsten rod
Young's modulus, static, 118, 120
Tungsten sheet
fabrication, 256-57
Young's modulus, static, 118, 120
Tungsten silicide (W_5Si_3)
thermal dilation, 106
Tungsten silicide systems
oxidation, 132
Tungsten single crystals
deformation and fracture, 120
Tungsten strip
fabrication, 256-57
Tungsten system sheet (Re–ThO_2–W)
fabricability and properties, 247
Tungsten systems (C–Cr–Co–Fe–Ni–W)
(see Star J)
Tungsten systems (C–Cr–Co–Mo–W–Y)
oxidation and strength, 131
Tungsten systems (C–Cr–Co–Nb–W–Y)
oxidation and strength, 131
Tungsten systems (C–Cr–Co–Ta–W–Y)
oxidation and strength, 131
Tungsten systems (C–Hf–Ta–W)
(see T-222)
Tungsten systems (C–Nb–W–Zr)
cold working, 127
corrosion, 233-34
Tungsten systems (C–Ta–W)
(see K601)
Tungsten systems (Co–O–W)
phase studies, 129
Tungsten systems (C–W–Zr)
phase studies, 50, 128
Tungsten systems (Hf–Mo–Nb–W)
(see SU-16)
Tungsten systems (SiC–W)
oxidation, 132
Tungsten systems (W–UC)
solidus temperature, 84
Tungsten thermocouples (Re–W vs. W)
sheathing of, 105
Tungsten trioxide
melting point, 173
Tungsten trioxide systems (B_2O_3–WO_3)
phase studies, 173
Tungsten tubing
fabrication, 63
Tungsten wire
cavities in sintered, 186
TZC
creep properties, 181
creep-rupture properties, 118
erosion, 177
fatigue properties, 181
stress-rupture properties, 250-51
TZM
coatings for, 231-33, 257
corrosion, 40-41, 234
creep properties, 181
creep-rupture properties, 249
diffusion bonding, 64
ductile–brittle transition temperature, 125
ductility, 125
erosion, 177
fatigue properties, 181
mechanical properties, 56
PFR-6 coating development for, 106
properties, 124
reactions with UC and UN, 84
recrystallization temperature, 125
strength, C effects on, 125
tensile properties, 118
TZM (irradiated)
mechanical properties, 124
TZM couples
corrosion, 108
diffusion behavior in Pt-coated, 233

U

Udimet 700
stress-rupture properties, 250-51
Ultrasonic testing, 69-70, 147-48, 200, 263
Unidyne bonding, 68, 147
Uranium
annealing, 203
carbide removal using HNO_3, 74
casting, 255
Cr diffusion in, 248-49
coatings for, 66-67
Co diffusion in, 248-49
compatibility studies, 37
Cu diffusion in, 248-49
corrosion, 74
diffusion bonding to Mg using Cu and Ni, 67
diffusion in materials, 82, 188, 248
ductile–brittle transition temperature, 203
ductility, 203, 255
electrodeposition of metals on, 141-42, 259
electrodeposition on Pt, 198
fatigue properties, 73
fracture, 151
ion plating on, 151, 200
Fe diffusion in, 248-49
Fe solubility in, 203
Mn diffusion in, 248-49
melting point, C effects on, 74
metallography, 203
metallurgy, physical, 151
Ni diffusion in, 248-49
Nb diffusion in, 248-49
nitride removal using HNO_3, 74
oxidation, 73, 212-13
phase changes, kinetics of, 152
preferred orientation, 1

production by skull-reduction process, 138
purification by zone melting, 203
rolling, carbide-inclusion effects on, 255
self-diffusion in UO_2, 158-59
self-diffusion in UC, 211-12
solubility in molten Zn, 236
structure, network, 151
tensile deformation, 203
texture, 74
thermal expansion, 203
x-ray diffraction studies, 74
Uranium (adjusted)
intermetallic compounds in, distribution and identification of, 73
Uranium (irradiated)
annealing effects on swelling, 1
damage, 213
fission-gas bubbles in, 15-16, 87, 162
fission-gas release, 163
growth, prediction of, 162
Kr diffusion in, 87
mass transport by fission fragments, 16
reaction with water, 15, 161
swelling, 1, 15, 87
thermal conductivity, 151
Xe diffusion in, 87, 213
Uranium (molten)
corrosive effects, 110
UC solubility in, 84
Uranium (Ni plated)
porosity, 142
Uranium (Zircaloy clad)
coextrusion, 198
Uranium alloy coatings (Al–U)
oxidation, 66
Uranium alloy films (Mo–U)(irradiated)
fission-fragment tracts, 17
Uranium alloy tubes (Al–Fe–U)(Zircaloy clad)(irradiated)
swelling, 2-4
Uranium alloy tubes (Mo–U)(Zircaloy clad)(irradiated)
swelling, 3-4
Uranium alloys, 1-5
corrosion, 74
particle studies in, 73-74
rolling, 63
x-ray diffraction studies, 74
Uranium alloys (Al–Fe–U)
precipitate solution in, 73
UAl_4 precipitates in, 151-52
Uranium alloys (Al–Mo–U)(Al clad)(irradiated)
properties, 203-4
Uranium alloys (Al–U)
transformation, 1, 74
Uranium alloys (Cr–Nb–U)
transformation, 1
Uranium alloys (Cr–U)
phase changes, kinetics of, 152
transformation, 1
Uranium alloys (Cr–U–V)
phase studies, 204
Uranium alloys (fissium–Pu–U)
compatibility with stainless steel, 5
development, 6
phase studies, 74-75
solidus temperatures, 5
Uranium alloys (fissium–Pu–U)(clad)(irradiated)
burnup, 74
Uranium alloys (fissium–Pu–U)(irradiated)
properties, 205-6
Uranium alloys (fizzium–Pu–U)(irradiated)
properties, 205-6
Uranium alloys (Fe–Pu–U)
properties, 153-54
Uranium alloys (Fe–U)
transformation, 1
Uranium alloys (irradiated)
microstructure effect on cavitational swelling of dilute, 2
reactions with water, 15
Uranium alloys (Mo–Pu–U)
fabrication, 138
thermal expansion, 206
Uranium alloys (Mo–U)
specific heat, 204
transformation, 1
Uranium alloys (Mo–U)(irradiated)
swelling, 152
Uranium alloys (Mo–U)(stainless-steel(304) clad)(irradiated)
behavior, 4-5
Uranium alloys (Nb–U)
specific heat, 205
transformation, 1
Uranium alloys (Nb–U–Zr)
properties, 204
Uranium alloys (Nb–U–Zr)(irradiated)
reaction with water, 161
Uranium alloys (Pu–Th–U)
compatibility studies, 9
development, 6
Uranium alloys (Pu–Ti–U)
casting, 138
compatibility with stainless steel, 5
creep properties, 6
ductility, 6
mechanical properties, 75
phase studies, 153
solidus temperatures, 5
thermal conductivity, 153
thermal expansion, 5-6
Uranium alloys (Pu–Ti–U)(molten)
penetration of Ti–V alloy, 205
Uranium alloys (Pu–U)
development, 5-6
phase studies, 75
Uranium alloys (Pu–U–Zr)
casting, 138
compatibility with stainless steel (304), 5, 205
creep properties, 6
mechanical properties, 75
phase studies, 75, 153
solidus temperatures, 5
thermal conductivity, 153, 205
thermal expansion, 6
transformation, 75
Uranium alloys (Pu–U–Zr)(molten)
penetration of stainless steel (304), 205
Uranium alloys (Tc–U)
phase studies, 152
Uranium alloys (Th–U)(Zircaloy clad)
coextrusion, 198
Uranium alloys (Th–U)(Zr clad)
fabrication, 257
Uranium alloys (Ti–U)
ductility and thermal expansion, 6
Uranium alloys (U–UCo_2–UMn_2)
phase studies, 152-53
Uranium alloys (U–Zr)
metallography of hydrided, 170
Uranium alloys (U–Zr)(irradiated)
decomposition, 2
swelling, 153
Uranium alloys (U–Zr)(Zircaloy clad)
coextrusion, 198
Uranium alloys (Zircaloy clad)
coextrusion, 198
Uranium carbide
casting, 197
fabrication, 212
melting, 197
synthesis, 212
yield strength, 159-60
Uranium carbide (irradiated)
fission-gas release, 163
Uranium carbide cermets
fracture, 79
Uranium carbide particles (PyC coated)
development, 156
Uranium carbide single crystals (irradiated)
point-defect clusters, 213
Uranium carbide systems (Pu carbide–U carbide)
compatibility studies, 8
fabrication, 212
synthesis, 212
thermal diffusivity, 7
Uranium carbide systems (Pu carbide–U carbide)(Nb clad)(irradiated)
properties, 160
Uranium carbide systems (Pu carbide–U carbide)(stainless-steel clad)(irradiated)
properties, 160
Uranium carbide systems (U carbide–Zr carbide)
fabrication and synthesis, 212
Uranium carbonitride
preparation and sintering, 13-14
Uranium ceramics
wetting by liquid Na, 110
Uranium dicarbide
C activity and solubility in, 84
coating with Nb, 200
extrusion, 255
thermodynamic properties, 13
US solubility in, 84
Uranium dicarbide particles
fabrication of spherical, 13
Uranium dicarbide particles (PyC coated)
evaluation, 210
Uranium dicarbide particles (PyC coated)(irradiated)
analysis, x-ray microprobe, 10
evaluation, 10, 157
Uranium dicarbide single crystals (irradiated)
point-defect clusters, 87-88
Uranium dicarbide solid solutions (UC_2–YC_2)
phase studies, 159
Uranium dicarbide system particles (ThC_2–UC_2)
fabrication of spherical, 13
Uranium dicarbide system particles (ThC_2–UC_2)(coated)(irradiated)
evaluation, 156-57
Uranium dicarbide systems (ThC_2–UC_2)
production by sol-gel process, 8-9
thermal expansion, 86
Uranium dicarbide systems (UC_2–UC)
phase studies, 84
Uranium dioxide
enthalpy, 11
heat of sublimation, latent, 211
loss from Mo–UO_2 dispersions, heat effects on, 79
mechanical properties, H effects on, 82
melting point, 157
metal diffusion in, 248
point defects in, 11
reaction with Al, 82
reaction with Ta, 211
reaction with TiO_2, 82
reaction with water, 82-83
reaction with Zircaloy-2, 81-82
thermal conductivity, 208
thermal expansion, 77, 211
U self-diffusion in, 158-59
vapor deposition, 140, 259
vapor pressure, 157

wetting by liquid Na, 110
Uranium dioxide (irradiated)
fission-gas bubble distribution in, 16-17, 87
fission-product distribution in, 11
fission-product release, 163, 210-11, 214
Pu distribution in, 11
self-diffusion in, 11
void migration, 17
Xe diffusion in, 10-11, 16
Xe release from doped, 16
Uranium dioxide (molten)
compatibility with W and vapor pressure, 211
Uranium dioxide (stainless-steel clad)
reaction with steam, 237-38
Uranium dioxide (stainless-steel clad) (irradiated)
fission-gas pressure in, 158
Uranium dioxide (stainless-steel(304) clad)
ultrasonic testing, 69
Uranium dioxide (stainless-steel(304) clad) (irradiated)
reaction with water vapor in, 157-58
Uranium dioxide (stainless-steel(304) clad) (molten)
reaction with water, 110-11
Uranium dioxide (Zircaloy-2 clad)
reaction with water, 238-39
Uranium dioxide (Zircaloy-2 clad)(molten)
reaction with water, 110-11
Uranium dioxide (Zr clad)
reaction with steam, 238
Uranium dioxide cermets
development, 9, 79
Uranium dioxide compacts
actinide-element diffusion in, 82
preparation, 11, 211
Uranium dioxide dispersions
cladding materials for, 79
thermal stability, 209
Uranium dioxide dispersions (Fe–UO_2) (Al–Cr–Fe–Y alloy clad)
preparation, 79-80
Uranium dioxide dispersions (Mo–UO_2)
UO_2 loss, heat effects on, 79
Uranium dioxide dispersions (Nb–(Pu-U)O_2 particles (coated)–Zr)
preparation, 80
Uranium dioxide dispersions (stainless steel–UO_2)
fabrication, 155-56
Uranium dioxide dispersions (stainless steel (304B)–UO_2)
fabrication and mechanical properties, 209
Uranium dioxide dispersions (stainless steel (347)–UO_2)
preparation, 208-9
Uranium dioxide dispersions (stainless steel (347)–UO_2)(irradiated)
swelling, 208-9
Uranium dioxide dispersions (stainless steel(347)–UO_2–ZrB_2)
properties, 156
Uranium dioxide dispersions (stainless steel(347)–UO_2–ZrB_2)(Nb coated)
properties, 156
Uranium dioxide dispersions (W–UO_2)
density, 208
preparation, 207-8
thermal conductivity, 207-8
Uranium dioxide films (irradiated)
fission-fragment tracks, 17
grain growth in, 163
mass transport in, 163
Uranium dioxide mixtures (BeO–UO_2)
creep properties, 58
Uranium dioxide mixtures (PuO_2–UO_2–ZrO_2)
preparation, 82
Uranium dioxide mixtures (UO_2–ZrB_2) (irradiated)
performance, 226, 228
Uranium dioxide mixtures (UO_2–ZrO_2) (Zircaloy clad)(irradiated)
homogenization of two-phase, 214
Uranium dioxide particles
production of spherical, 11-12
Uranium dioxide particles (Al_2O_3 coated) (irradiated)
evaluation, 10
Uranium dioxide particles (PyC coated) (irradiated)
evaluation, 10, 156-57, 210
Uranium dioxide pellets
fabrication, 157
preparation, 82
properties, 82
Uranium dioxide powder
compaction, 142
Uranium dioxide single crystals
creep, 211
Uranium dioxide single crystals (irradiated)
fission-gas release, 214
Xe diffusion from, 210-11
Uranium dioxide system particles (ThO_2–UO_2)(PyC coated)(irradiated)
evaluation, 157
Uranium dioxide system pellets (PuO_2–UO_2)
preparation of glass-bonded, 8
Uranium dioxide system pins (PuO_2–UO_2) (irradiated)
behavior, 8
Uranium dioxide system rods (ThO_2–UO_2) (clad)(irradiated)
performance, 13
Uranium dioxide systems (BeO–ThO_2–UO_2–Y_2O_3)
UO_2 loss, 26-27
Uranium dioxide systems (BeO–ThO_2–UO_2–Y_2O_3)(irradiated)
fission-gas release, 27
Uranium dioxide systems (CaO–PuO_2–UO_2–ZrO_2)
melting points, 78
Uranium dioxide systems (graphite–UO_2)
melting, 197
Uranium dioxide systems (PuO_2–UO_2)
compatibility with refractory metals, 78
density, 154
melting point, 154
particle-size-distribution determination, 8
preparation of spherical particles, 154
thermal expansion, 77
thermal gradient effects, 78
Uranium dioxide systems (PuO_2–UO_2)(self irradiated)
lattice parameters, 207
Uranium dioxide systems (PuO_2–UO_2–ZrO_2)
lattice parameters and stability, 154
Uranium dioxide systems (UO_2–Y_2O_3) (irradiated)
^{133}Xe release, 162
Uranium dioxide systems (UO_2–ZrO_2) (irradiated)
homogenization, 163
Uranium fluoride systems (BeF_2–LiF–UF_4–ZrF_4)(molten)
corrosive effects, 110
Uranium fuel materials (irradiated)
properties, 153
Uranium hydride systems (U hydride–Zr hydride)
pulse-heating effects, 28
thermal behavior, 224
Uranium intermetallic compound coatings (UAl_3)
oxidation, 66
Uranium intermetallic compound dispersion films (Al–UAl_4)(irradiated)
fission-fragment tracks, 17
Uranium intermetallic compound dispersions (Al–U aluminide)
fabrication, 208
Uranium intermetallic compound dispersions (Al–U aluminide)(irradiated)
properties, 208
Uranium intermetallic compounds (UAl_2)
precipitation in Al–Fe–U alloys, 1[illegible]-52
preparation, 208
Uranium intermetallic compounds (UAl_3)
preparation, 208
Uranium intermetallic compounds (U_6Co)
solid solubility, 153
Uranium intermetallic compounds (U_6Mn)
solid solubility, 153
Uranium monoarsenide powder
ignition, 160
Uranium monocarbide
C activity in, 84
C self-diffusion in, 211-12
casting, 255
coating, 197
corrosion, Fe effects on, 161-62
creep rate, 84, 212
dynamic modulus, U effects on, 13
extrusion, 255
free energy of formation, 84
hot hardness, C effects on, 159
hydrolysis, 15
melting, 197-98
preparation, 14
preparation, 83
properties, 84
reaction with Mo–W alloy, 84
reactions with Nb alloys, 84
reaction with stainless steel (316), 159
reactions with Ta alloys, 84
reaction with W, 84
reaction with TZM, 84
reduction in H_2, 161
sintering, 161
slip, 212
solubility in liquid U, 84
strength, W effects on, 159
thermal conductivity, 84, 211-12
U diffusion, 211-12, 248
wetting by liquid Na, 110
Uranium monocarbide (irradiated)
CO release, 212
lattice parameters, 213
^{133}Xe diffusion in, 163
Uranium monocarbide (molten)
W solubility in, 211
Uranium monocarbide particles (irradiated)
behavior, 13
Uranium monocarbide single crystals (irradiated)
point-defect clusters, 87-88
Uranium monocarbide (stainless-steel clad)(irradiated)
damage, 160
Uranium monocarbide (stainless-steel)(304) clad)(irradiated)
damage, 86
Uranium monocarbide powder
ignition, 160
synthesis, 161

Uranium monocarbide system particles (PuC–UC)
preparation, 7–8
vibratory compaction, 64
Uranium monocarbide systems (Fe–UC)
reaction with stainless steel (316), 159
Uranium monocarbide systems (NbC–UC)
creep rate, 212
Uranium monocarbide systems (PuC–UC)
preparation, 207
preparation of powders, 154–55
reactions with alloys, 159
reactions with metals, 78, 159
reduction in H_2, 161
sintering, 161
Uranium monocarbide systems (PuC–UC) (Nimonic 90 clad)(irradiated)
damage, 86
Uranium monocarbide systems (PuC–UC) (stainless-steel clad)(irradiated)
fission-gas release, 212
Uranium monocarbide systems (Pu_2C_3–UC)
reduction in H_2 and sintering, 161
Uranium monocarbide systems (W–UC)
solidus temperature, 84
Uranium monocarbide systems (UC_2–UC)
phase studies, 84
Uranium monocarbide systems (UC–UP)
phase studies, 12
Uranium monocarbide systems (UC–ZrC)
compatibility with metals, 159
thermal expansion, 86
Uranium mononitride
creep rate, 84
hydrolysis, 212
N partial pressure over, 84
N self-diffusion in, 84
production, 83
properties, 84
reaction with Ni, 12–13
reaction with Nb alloy, 84
reactions with Ta alloys, 84
reactions with W alloys, 84
reaction with TZM, 84
sintering, 161
thermal conductivity, 84
wetting by liquid Na, 110
yield from UO_2 reduction, 83–84
Uranium mononitride (stainless-steel clad) (irradiated)
damage, 86
Uranium mononitride dispersions
cladding materials for, 79
Uranium mononitride microspheres
preparation, 84
Uranium mononitride powder
ignition, 160
preparation, 13
synthesis, 161
wetting by Na, 176
Uranium mononitride solid solutions (PuN–UN)
preparation, 155
Uranium mononitride system compacts (AlN–UN)
fabrication, 13
Uranium mononitride systems (PuN–UN)
preparation, 207
Uranium mononitride systems (UN–UP)
phase studies, 12
Uranium monophosphide
compatibility with metals, 212
density, 12
melting point, 12
production, 83
thermal conductivity, 211
wetting by liquid Na, 110
Uranium monophosphide powder
oxidation, 160
Uranium monophosphide solid solutions UP–US)
melting points, 160
Uranium monophosphide systems (UC–UP)
phase studies, 12
Uranium monophosphide systems (UN–UP)
phase studies, 12
Uranium monosulfide
melting point, 155
preparation, 14
production, 83
solubility in UC_2, 84
thermal conductivity, 12, 211
thermal diffusivity, 160
transient-heating effects, 212
wetting by liquid Na, 110
Uranium monosulfide powder
ignition, 160
Uranium monosulfide solid solutions (PuS–UN)
preparation, 155, 207
Uranium monosulfide solid solutions (UP–US)
melting points, 160
Uranium monosulfide systems (PuS–US)
lattice constants and melting points, 207
Uranium monoxide systems (PuO–UO)
stability, 155
Uranium nitride systems (Pu nitride–U nitride)
properties, 8, 207
Uranium nitride systems (Pu nitride–U nitride)(irradiated), 207
Uranium oxide fuels
behavior and properties, 81–83
Uranium rod
casting, 255
Uranium sesquicarbide
thermodynamic properties, 13
Uranium sheet
pole-figure measurements, 74
Uranium silicide (U_3Si_2)
properties, 86
Uranium silicide (U_3Si_2)(irradiated)
behavior, 86–87
Uranium silicides (U_3Si)
transformation, 74
Uranium single crystals
elastic moduli, 203
Kossel diffraction patterns, 74
plastic deformation, 203
Uranium single crystals (irradiated)
plastic deformation, 162, 203
Uranium solutions (Mg–U–Zn)
corrosive effects, 178
Uranium system particles (C–U–Zr) (irradiated)
behavior, 13
Uranium system tubes (Al–Fe–Si–U) (Zircaloy clad)(irradiated)
swelling, 2–4
Uranium systems
aging effects, 152
Uranium systems (Al–Fe–Mo–Si–U)
hardness, 2
Uranium systems (C–Ni–U)
phase studies, 211
Uranium systems (C–U)
aging effects, 152
casting, 83
melting, 83
melting point, 74
precipitates in, 152
Uranium systems (Mo–Si–U)
phase studies, 74
physical metallurgy, 1
properties, 1–2
Uranium systems (Mo–Si–U)(irradiated)
swelling, 152
Uranium systems (O–Na–U)
phase studies, 5
Uranium trialuminide coatings
application and properties, 66
Uranium tubing
casting, 255
Uranium tubing (Zircaloy clad)(irradiated)
swelling, 3–4

V

Vanadium
compatibility with $Pu_{0.2}C$–$U_{0.8}C$ system, 8
corrosion, 177–78, 230
ductility, 56
melting point, annealing effects on, 246
phase diagrams, 186
reaction with PuC–UC system, 159
solubility in molten Zn, 236
Vanadium alloy tubing (Ti–V)
fabrication, 198, 256
Vanadium alloys (Al–Cr–Ti–V)
friction welding, 68
Vanadium alloys (Al–Cr–V)
corrosion, 109, 233
Vanadium alloys (Al–Cr–V–Zr)
fabrication, 255–56
Vanadium alloys (Al–Mo–Ti–V)
properties, 183
Vanadium alloys (Al–Ti–V)
crack growth, 230
welding, 68, 145
Vanadium alloys (Al–V)
corrosion, 109
Vanadium alloys (Cr–Ti–V)
corrosion, 257
creep properties, 186, 257
fabrication, 257
Vanadium alloys (Cr–U–V)
phase studies, 204
Vanadium alloys (Cr–V)
corrosion, 109
Vanadium alloys (Mo–Nb–V–Zr) (see B-66)
Vanadium alloys (Mo–Ta–V)
phase studies, 129
Vanadium alloys (Mo–Ti–V)
corrosion, 109
Vanadium alloys (Nb–Ta–Ti–V)
creep resistance, 53
Vanadium alloys (Nb–Ta–V)
phase studies, 129
Vanadium alloys (Nb–Ti–V)
annealing, 53
evaluation, 138
evaporation, 128
preparation, 138
Vanadium alloys (Nb–V) (see also B33)
binary interdiffusion in, 132
corrosion, 108, 230–31
evaluation, 138
interdiffusion in, 188
mechanical properties, 52
preparation, 138
twinning, 52
welding, 144
Vanadium alloys (Nb–V–Zr)
aging, 127–28
hardness, 128
Vanadium alloys (Ta–V)
corrosion, 230
Vanadium alloys (Ti–V)
compatibility studies, 8–9

corrosion, 39, 109, 230, 233
creep, Na effects on, 176
penetration by molten Pu–Ti–U alloy, 205
tensile properties, 118
thermal conductivity, 186
thermal expansion, 186
Vanadium alloys (Ti–V)(irradiated)
He and H production, 192
Vanadium fused slurry coatings
development and evaluation, 106
Vanadium systems (H–V)
ductility, 56
Vought IV coatings
behavior, 231-32

W

Welding, 67-69, 142-47, 260-63

X

X-34
corrosion, 234
X-110
corrosion, 234
X-315
erosion, 177
X-ray radiography, 70

Y

Ytterbium
W solubility in, 247
Yttrium
compatibility with Th, 9
corrosion, 236
effects on Ta recrystallization temperature, 185
phase diagrams, 186
solubility in molten Zn, 236
W solubility in, 247
Yttrium alloy coatings (Ir–Y)
for Ta, 38
Yttrium alloys (Al–Cr–Fe–Y)
(see also 1541 alloy)
oxidation, 79
properties, 244-45
Yttrium alloys (Al–Cr–Fe–Y)(irradiated)
ductile–brittle transition temperature, 115
hardness, 115
tensile properties, 190
Yttrium alloys (Al–Cr–V–Y)
fabrication, 255-56
Yttrium alloys (Al–Y)
corrosion, 103
Yttrium alloys (Cr–Y)
mechanical properties, 53
Yttrium alloys (Cr–Y)(hydrided)(clad)
cracking, 97
Yttrium alloys (Cr–Y)(hydrided)(clad)
(irradiated)
behavior, 97
Yttrium alloys (Hf–Nb–W–Y)
(see C-129Y)
Yttrium alloys (Nb–W–Y–Zr)
(see AS-55 and D-43Y)
Yttrium alloys (Sc–Y)(hydrided)
phase studies and thermodynamic properties, 97
Yttrium alloys (Y–Zr)
H terminal solubility in, 28
Yttrium carbide (Y_3C)
Al solubility in, 131
Yttrium dicarbide solid solutions (UC_2–YC_2)
phase studies, 159
Yttrium hydride
H absorption and thermodynamic properties, 96-97
Yttrium oxide
effects on Zr stress rupture, 183
thermal conductivity, 193
Yttrium sesquioxide systems (BeO–ThO_2–UO_2–Y_2O_3)
UO_2 loss, 26-27
Yttrium sesquioxide systems (BeO–ThO_2–UO_2–Y_2O_3)(irradiated)
fission-gas release, 27
Yttrium sesquioxide systems (ThO_2–Y_2O_3)(irradiated)
^{133}Xe release, 162
Yttrium sesquioxide systems (UO_2–Y_2O_3)(irradiated)
^{133}Xe release, 162
Yttrium sesquioxide systems (Y_2O_3–Zr–ZrO_2)
thermal conductivity, 193
Yttrium systems (Al–C–Y)
phase studies, 131
Yttrium systems (C–Cr–Co–Mo–W–Y)
oxidation and strength, 131
Yttrium systems (C–Cr–Co–Nb–W–Y)
oxidation and strength, 131
Yttrium systems (C–Cr–Co–Ta–W–Y)
oxidation and strength, 131

Z

Zinc
corrosion, 177-78
electrodeposition on Be and Zn-plated Be, 67
Zinc (molten)
corrosive effects, 178, 236
metal solubility in, 236
U diffusion in, 188
Zinc alloys (Al–Zn)
corrosion, 103
Zinc alloys (Cd–Mg–Zn)(molten)
corrosive effects, 178-79
Zinc alloys (Nb–Zn), 52
Zinc solutions (Mg–U–Zn)
corrosive effects, 178
Zircaloy
bonding to stainless steel, 68
corrosion, 37
ductility, Zr hydride effects on, 49
joining, 68, 146
reaction with steam, 41
stress-corrosion cracking, 103
Zircaloy tubing
lining with Al using explosive welding, 68
Zircaloy-2
alloying-element distribution, 243-44
bonding to Al by extrusion, 198
corrosion, 36, 103, 174, 229
creep properties, 56, 58
fracture, 58
hardness, O effects on, 50
hydriding, 28, 33-36, 174
H charging of, 224
H segregation, 124
mechanical properties, 103
microstructure, 28
pole figure of hydride plates, 49-50
preferred orientation, 50
properties, 124
reaction with steam, 41
reaction with UO_2, 81-82
specific heat, 244
Zircaloy-2 (irradiated)
annealing, 114
corrosion, 35, 229, 240
creep properties, 114
dislocation loops, 117
He production, 192
H production, 192
impact properties, 46, 192
mechanical properties, 114, 240
oxidation, 229
Zircaloy-2 cladding
stresses during vibrating fuel loading, 258
Zircaloy-2 transition joints (Inconel–Zircaloy-2)(irradiated)
mechanical properties, 240
properties, 260
Zircaloy-2 tubing
crystal structure, 49
ductility, H effects on, 28
grain growth, 49
preferred orientation, fabrication effects on, 257
properties, 120
properties of welded, 183
strength, 117-18
stresses during fuel loading, 64-65
weld cracking, 65
Zircaloy-4
corrosion, 103, 229
fatigue-strength reduction factors, 56-57
hydride habit, 183
mechanical properties, 103
physical properties, 183
properties, 124
reaction with steam, 237
Zircaloy-4 (irradiated)
mechanical properties, 114
oxidation, 229
tensile properties, 114
Zircaloy-4 single crystals
physical properties, 183
Zircaloy-4 tubing
explosive welding to Al tubing, 260
properties, 120
Zircoa 1027
corrosion, 40
Zirconium
C diffusion in, 132
compatibility with UP, 212
corrosion, 177-78
creep properties, 182
damping capacity, 124
effects on Mo recrystallization temperature, 182
electrodeposition of, 140-41
embrittlement, ZrH_2 effects on, 124
hydride habit, 183
H embrittlement, 169, 243
H permeation of oxide films on, 229
H terminal solubility in, O effects on, 27
oxidation, 35, 174
phase diagrams, 186
properties, rare-earth effects on, 183
reaction with steam, 41-42
recovery, 123
self-diffusion in Zr hydride, 96, 169
solubility in molten Zn, 236
stress rupture, Y_2O_3 effects on, 183
tensile properties, hydriding effects on, 124
U diffusion in, 248
work hardening, 123
yield point, 243
Zirconium (irradiated)
corrosion, 174
Zirconium (molten)
WC solubility in, 128
Zirconium alloy coatings (Ir–Zr)
for Ta, 38
Zirconium alloy couples (Mo–Ti–Zr)
corrosion, 108
Zirconium alloy couples (Nb–Zr)
corrosion, 109

Zirconium alloy couples (Nb–Zr)(carburized)
corrosion, 108
Zirconium alloy tubing (Nb–Zr)
crystal structure, 49
Zirconium alloys
corrosion, 36
embrittlement, Zr_2H_3 effects on, 124
hydriding, 36, 169–70
H terminal solubility in, 28–29
H uptake, 174
mechanical properties, 56–58, 182
metallurgy, 49–50
Zirconium alloys (Al–Cr–V–Zr)
fabrication, 255–56
Zirconium alloys (Al–Mg–Zr)
creep properties, 251
Zirconium alloys (Al–Zr)
electrodeposition of, 140–41
Zirconium alloys (Be–Ti–Zr)
use for brazing, 146
Zirconium alloys (Cr–Fe–Sn–Zr)
corrosion and mechanical properties, 103
Zirconium alloys (Cr–Fe–Zr)
corrosion and mechanical properties, 103
Zirconium alloys (Cr–Zr)
corrosion, 36
Zirconium alloys (Cu–Nb–Zr)
corrosion and H uptake, 229
Zirconium alloys (Cu–Zr)
diffusion in, 132
Zirconium alloys (irradiated)
properties, 46, 115
Zirconium alloys (Mg–Zr)
creep properties, heat-treatment effects on, 183
Zirconium alloys (Mo–Nb–Ta–Zr)
(see SCb-61)
Zirconium alloys (Mo–Nb–Ti–Zr)
(see PWC-533)
Zirconium alloys (Mo–Nb–W–Zr)
(see F-48)
Zirconium alloys (Mo–Nb–V–Zr)
(see B-66)
Zirconium alloys (Mo–Ti–Zr)
(see also TZM)
chemical plating of $MoSi_2$ on, 140
tensile properties, 118
Zirconium alloys (Mo–W–Zr)
phase studies, 129
Zirconium alloys (Mo–Zr)
binary interdiffusion in, 132
Zirconium alloys (Nb–Ta–W–Zr)
(see FS-85)
Zirconium alloys (Nb–Ta–Zr)
removal of N and O, 63
Zirconium alloys (Nb–Sn–Zr)
corrosion, 36
tempering, 50
Zirconium alloys (Nb–Sn–Zr)(irradiated)
corrosion, 229, 240
mechanical properties, 240
oxidation, 229
Zirconium alloys (Nb–Ti–Zr)
annealing, 53
Zirconium alloys (Nb–W–Y–Zr)
(see AS-55 and D-43Y)
Zirconium alloys (Nb–W–Zr)
(see Cb-752, D-43, and X-34)
Zirconium alloys (Nb–U–Zr)
properties, 204
Zirconium alloys (Nb–U–Zr)(irradiated)
reaction with water, 161
Zirconium alloys (Nb–V–Zr)
aging, 127–28
hardness, 128
Zirconium alloys (Nb–Zr)
(see also D-11, D-14, PWC-11, PWC-33, and PWC-34)
age-hardening, 183–84
annealing, 53
binary interdiffusion in, 132
brazing, 94, 146
carburization, 140
coating with PWK-5, 106, 199
compatibility with Be, 94
corrosion, 35–36, 40, 108, 110, 177, 229–31, 233–34
electrical resistivity, 127
fracture, 58
heat treatment, 183
H segregation, 124
H terminal solubility in, 28
ingot structure, O effects on, 256
joining to Al_2O_3, 146
mechanical properties, 52, 127
N removal, 63
N solubility in, 126–27, 184
oxidation, 37
oxidative weight gain, 127
O removal, 63
properties, 57–58
recrystallization temperature, 127
strength, 35
strengthening, 127
stress-corrosion cracking, 235
tempered structures, 244
tensile properties, 118
Zr_2H_3 reorientation, stress effects on, 124
Zirconium alloys (Nb–Zr)(irradiated)
annealing, 114
creep properties, 114
impact properties, 46, 192
Zirconium alloys (Pu–U–Zr)
casting, 138
compatibility with stainless steel (304), 5, 205
creep properties, 6
mechanical properties, 75
phase studies, 75, 153
solidus temperatures, 5
thermal conductivity, 153, 205
thermal expansion, 6
transformation, 75
Zirconium alloys (Pu–U–Zr)(molten)
penetration of stainless steel (304), 205
Zirconium alloys (Pu–Zr)
solidus temperatures, 75
Zirconium alloys (Ta–W–Zr)
phase studies, 247
Zirconium alloys (Th–Zr)
tensile properties, 9
Zirconium alloys (Sn–Zr)
corrosion, 36
Zirconium alloys (Ti–Zr)
electrodeposition of, 140–41
H terminal solubility in, 28
Zirconium alloys (U–Zr)
metallography of hydrided, 170
Zirconium alloys (U–Zr)(irradiated)
decomposition, 2
swelling, 153
Zirconium alloys (U–Zr)(Zircaloy clad)
coextrusion, 198
Zirconium alloys (Y–Zr)
H terminal solubility in, 28
Zirconium boride powder
coating with Mo and W, 139–40
sintering, 34
Zirconium boride systems
oxidation, 132
Zirconium carbide cermets
fracture, 79
Zirconium carbide hydrides
lattice constants, 170
Zirconium carbide powder
coating with Mo and W, 139–40
Zirconium carbide solid solutions (Hf carbide–Zr carbide)
preparation and properties, 101
Zirconium carbide systems (U carbide–Zr carbide)
fabrication and synthesis, 212
Zirconium cladding
reaction with steam, 238
Zirconium diboride
corrosion, 110
hardness, 251
electrodeposition of, 140–41
Zirconium diboride dispersions (stainless steel(347)–UO_2–ZrB_2)
properties, 156
Zirconium diboride (Nb coated) dispersions (stainless steel(347)–UO_2–ZrB_2 (Nb coated))
properties, 156
Zirconium diboride mixtures (UO_2–ZrB_2) (irradiated)
performance, 226, 228
Zirconium diboride powder
metallic binders for, 172
sintering, 34
Zirconium diboride systems ($MoSi_2$–ZrB_2)
tensile properties, 121
Zirconium dihydride systems (ZrH_2–ZrC)
lattice constants, 170
Zirconium dioxide
cationic self-diffusion in CaO-stabilized, 251
corrosion, 40
O diffusion in CaO-stabilized, 251
thermal shock, metal addition effects on, 251
Zirconium dioxide (MgO stabilized)
corrosion, 40
Zirconium dioxide coatings
application, 257
electroplating on Ta–W alloy, 259–60
for W, 38
Zirconium dioxide films
structure, 174
Zirconium dioxide mixtures (PuO_2–UO_2–ZrO_2)
preparation, 82
Zirconium dioxide mixtures (UO_2–ZrO_2) (Zircaloy clad)(irradiated)
homogenization of two-phase, 214
Zirconium dioxide powders
coating with Mo and W, 139–40
Zirconium dioxide single crystals
O diffusion in CaO-stabilized, 251
Zirconium dioxide solid solutions (HfO_2–ZrO_2)
thermal expansion, 172
Zirconium dioxide systems (CaO–PuO_2–UO_2–ZrO_2)
melting points, 78
Zirconium dioxide systems (CaO–ZrO_2)
thermal conductivity, 193
Zirconium dioxide systems (PuO_2–UO_2–ZrO_2)
lattice parameters and stability, 154
Zirconium dioxide systems (Ti–ZrO_2)
thermal shock, 251
Zirconium dioxide systems (UO_2–ZrO_2) (irradiated)
homogenization, 163
Zirconium dioxide systems (Y_2O_3–Zr–ZrO_2)
thermal conductivity, 193
Zirconium dispersions (Nb–PuO_2 particles (coated)–Zr)
preparation, 80
Zirconium dispersions (Nb–(Pu–U)O_2 particles (coated)–Zr)
preparation, 80

Zirconium fluoride systems (BeF_2–LiF–UF_4–ZrF_4)(molten)
corrosive effects, 110
Zirconium hydride
fracture, 27-28
lengthening, heat effects on, 169
microstructure, 28
rare-gas diffusion in, 96
stability, 96
structure, 96
tensile properties, 124
Zr self-diffusion in, 96, 169
Zirconium hydride platelets
reorientation, stress effects on, 124
Zirconium hydride systems (U hydride–Zr hydride)
pulse-heating effects, 28
thermal behavior, 224
Zirconium monocarbide systems (UC–ZrC)
compatibility with metals, 159
thermal expansion, 86
Zirconium monocarbide systems (ZrH_2–ZrC)
lattice constants, 170
Zirconium silicide systems
oxidation, 132
Zirconium single crystals
growth, 123-24
Zirconium systems (Al–C–Ti–Zr)
mechanical properties at high temperatures, 123
Zirconium systems (C–Cr–Zr)
phase studies, 50
Zirconium systems (C–Co–Zr)
phase studies, 244
Zirconium systems (C–Mo–Nb–Ti–Zr)
fabrication and properties, 51
Zirconium systems (C–Mo–Ti–Zr)
(see also TZC)
creep-rupture properties, 118
fabrication, 51, 138
properties, 51
Zirconium systems (C–Mo–Zr)
phase studies, 50
Zirconium systems (C–Nb–W–Zr)
cold working, 127
corrosion, 233-34
Zirconium systems (C–Nb–Zr)
corrosion, 108
development, 52
phase studies, 128
Zirconium systems (C–W–Zr)
phase studies, 50, 128
Zirconium systems (Hf–H–Zr)
phase studies, 29
Zirconium shstems (O–Zr)
H terminal solubility in, 28
Zirconium systems (SiC–Zr)
oxidation, 132
Zirconium systems (Th–ThO_2–Zr)
tensile properties, 9
Zirconium systems (Y_2O_3–Zr–ZrO_2)
thermal conductivity, 193
Zirconium tubing
grain growth, 49

LEGAL NOTICE

This journal was prepared under the sponsorship of the U. S. Atomic Energy Commission. Neither the United States, nor the Commission, nor any person acting on behalf of the Commission:

A. Makes any warranty or representation, expressed or implied, with respect to the accuracy, completeness, or usefulness of the information contained in this journal, or that the use of any information, apparatus, method, or process disclosed in this journal may not infringe privately owned rights; or

B. Assumes any liabilities with respect to the use of, or for damages resulting from the use of any information, apparatus, method, or process disclosed in this journal.

As used in the above, "person acting on behalf of the Commission" includes any employee or contractor of the Commission, or employee of such contractor, to the extent that such employee or contractor of the Commission, or employee of such contractor prepares, disseminates, or provides access to, any information pursuant to his employment or contract with the Commission, or his employment with such contractor.

TECHNICAL PROGRESS REVIEWS may be purchased from Superintendent of Documents, U. S. Government Printing Office, Washington, D. C., 20402. *Nuclear Safety* at $3.00 per year for each subscription or $1.00 per issue; each of the other journals at $2.50 per year or $0.70 per issue. The use of the coupon below will facilitate the handling of your order.

POSTAGE AND REMITTANCE: Postpaid within the United States, Canada, Mexico, and all Central and South American countries except Argentina, Brazil, Guyana, French Guiana, Surinam, and British Honduras. For these Central and South American countries and all other countries, add $0.75 for each annual subscription or $0.20 for a single issue. Payment should be by check, money order, or document coupons, and MUST accompany order. Remittances from foreign countries should be made by international money order or draft on an American bank payable to the Superintendent of Documents or by UNESCO book coupons.

order form

SUPERINTENDENT OF DOCUMENTS
U. S. GOVERNMENT PRINTING OFFICE
WASHINGTON, D. C., 20402

Enclosed:
document coupons ☐ check ☐ money order ☐

Charge to Superintendent of Documents No. _____

Please send a one-year subscription to

☐ ISOTOPES AND RADIATION TECHNOLOGY

☐ POWER REACTOR TECHNOLOGY

☐ REACTOR MATERIALS

(Each subscription $2.50 per year; $0.70 per issue.)

☐ NUCLEAR SAFETY

(Each subscription $3.00 per year; $1.00 per issue.)

SUPERINTENDENT OF DOCUMENTS
U. S. GOVERNMENT PRINTING OFFICE
WASHINGTON, D. C., 20402

(Print clearly)

_____
Name

_____
Street

_____
City, State, ZIP Code